SIGNAL PROCESSING AND COMMUNICATIONS GROUP
DEPARTMENT OF SIGNAL THEORY AND COMMUNICATIONS
UNIVERSITAT POLITÈCNICA DE CATALUNYA

ENERGY-DRIVEN TECHNIQUES FOR MASSIVE MACHINE-TYPE COMMUNICATIONS

A PhD dissertation submitted in partial fulfilment
of the requirements for the Doctoral Degree in
Signal Theory and Communications

Author

Sergi Liesegang Maria

Advisors

Dr. Olga Muñoz Medina

Dr. Antonio Pascual Iserte

Barcelona, July 2022

L'essencial és invisible als ulls...
- ANTOINE DE SAINT-EXUPÉRY

Abstract

In the last few years, a lot of effort has been put into the development of the fifth generation of cellular networks (5G). Given the vast heterogeneity of devices coexisting in these networks, new approaches have been sought to meet all requirements (e.g., data rate, coverage, delay, etc.). Within that framework, massive machine-type communications (mMTC) emerge as a promising candidate to enable many Internet of Things applications.

mMTC define a type of systems where large sets of simple and battery-constrained devices transmit short data packets simultaneously. Unlike other 5G use cases, in mMTC, a low cost and power consumption are extensively pursued. Due to these specifications, typical human-type communications (HTC) solutions fail in providing a good service.

In this dissertation, we focus on the design of energy-driven techniques for extending the lifetime of mMTC terminals. Both uplink (UL) and downlink (DL) stages are addressed, with special attention to the traffic models and spatial distribution of the devices. More specifically, we analyze a setup where groups of randomly deployed sensors send their (possibly correlated) observations to a collector node using different multiple access schemes. Depending on their activity, information might be transmitted either on a regular or sporadic basis.

In that sense, we explore resource allocation, data compression, and device selection strategies to reduce the energy consumption in the UL. To further improve the system performance, we also study medium access control protocols and interference management techniques that take into account the large connectivity in these networks. On the contrary, in the DL, we concentrate on the support of wireless powered networks through different types of energy supply mechanisms, for which proper transmission schemes are derived. Additionally, for a better representation of current 5G deployments, the presence of HTC terminals is also included.

Finally, to evaluate our proposals, we present several numerical simulations following standard guidelines. In line with that, we also compare our approaches with state-of-the-art solutions. Overall, results show that the power consumption in the UL can be reduced with still good performance and that the battery lifetimes can be improved thanks to the DL strategies.

Resum

En els últims anys, s'han dedicat molts esforços al desenvolupament de la cinquena generació de telefonia mòbil (5G). Donada la gran heterogeneïtat de dispositius coexistint en aquestes xarxes, s'han buscat nous mètodes per satisfer tots els requisits (velocitat de dades, cobertura, retard, etc.). En aquest marc, les *massive machine-type communications* (mMTC) sorgeixen com a candidates prometedores per fer possible moltes aplicacions del *Internet of Things*.

Les mMTC defineixen un tipus de sistemes en els quals grans conjunts de dispositius senzills i amb poca bateria, transmeten simultàniament paquets de dades curts. A diferència d'altres casos d'ús del 5G, en mMTC es persegueix un cost i un consum d'energia baixos. A causa d'aquestes especificacions, les solucions típiques de les *human-type communications* (HTC) no aconsegueixen proporcionar un bon servei.

En aquesta tesi, ens centrem en el disseny de tècniques basades en l'energia per allargar la vida útil dels terminals mMTC. S'aborden tant les etapes del *uplink* (UL) com les del *downlink* (DL), amb especial atenció als models de trànsit i a la distribució espacial dels dispositius. Més concretament, analitzem un escenari en el qual grups de sensors desplegats aleatòriament, envien les seves observacions (possiblement correlades) a un node col·lector utilitzant diferents esquemes d'accés múltiple. Depenent de la seva activitat, la informació es pot transmetre de manera regular o esporàdica.

En aquest sentit, explorem estratègies d'assignació de recursos, compressió de dades, i selecció de dispositius per reduir el consum d'energia en el UL. Per millorar encara més el rendiment del sistema, també estudiem protocols de control d'accés al medi i tècniques de gestió d'interferències que tinguin en compte la gran connectivitat d'aquestes xarxes. Per contra, en el DL, ens centrem en el suport de les *wireless powered networks* mitjançant diferents mecanismes de subministrament d'energia, per als quals es deriven esquemes de transmissió adequats. A més, per una millor representació dels desplegaments 5G actuals, també s'inclou la presència de terminals HTC.

Finalment, per avaluar les nostres propostes, presentem diverses simulacions numèriques seguint pautes estandarditzades. En aquesta línia, també comparem els nostres enfocaments amb les solucions de l'estat de l'art. En general, els resultats mostren que el consum d'energia en el UL pot reduir-se amb un bon rendiment i que la durada de la bateria pot millorar-se gràcies a les estratègies del DL.

Resumen

En los últimos años, se han dedicado muchos esfuerzos al desarrollo de la quinta generación de telefonía móvil (5G). Dada la gran heterogeneidad de dispositivos coexistiendo en estas redes, se han buscado nuevos métodos para satisfacer todos los requisitos (velocidad de datos, cobertura, retardo, etc.). En este marco, las *massive machine-type communications* (mMTC) surgen como candidatas prometedoras para hacer posible muchas aplicaciones del *Internet of Things*.

Las mMTC definen un tipo de sistemas en los cuales grandes conjuntos de dispositivos sencillos y con poca batería, transmiten simultáneamente paquetes de datos cortos. A diferencia de otros casos de uso del 5G, en mMTC se persigue un coste y un consumo de energía bajos. A causa de estas especificaciones, las soluciones típicas de las *human-type communications* (HTC) no consiguen proporcionar un buen servicio.

En esta tesis, nos centramos en el diseño de técnicas basadas en la energía para alargar la vida útil de los terminales mMTC. Se abordan tanto las etapas del *uplink* (UL) como las del *downlink* (DL), con especial atención a los modelos de tráfico y a la distribución espacial de los dispositivos. Más concretamente, analizamos un escenario en el cual grupos de sensores desplegados aleatoriamente, envían sus observaciones (posiblemente correladas) a un nodo colector utilizando diferentes esquemas de acceso múltiple. Dependiendo de su actividad, la información se puede transmitir de manera regular o esporádica.

En este sentido, exploramos estrategias de asignación de recursos, compresión de datos, y selección de dispositivos para reducir el consumo de energía en el UL. Para mejorar todavía más el rendimiento del sistema, también estudiamos protocolos de control de acceso al medio y técnicas de gestión de interferencias que tengan en cuenta la gran conectividad de estas redes. Por el contrario, en el DL, nos centramos en el soporte de las *wireless powered networks* mediante diferentes mecanismos de suministro de energía, para los cuales se derivan esquemas de transmisión adecuados. Además, para una mejor representación de los despliegues 5G actuales, también se incluye la presencia de terminales HTC.

Finalmente, para evaluar nuestras propuestas, presentamos varias simulaciones numéricas siguiendo pautas estandarizadas. En esta línea, también comparamos nuestros enfoques con las soluciones del estado del arte. En general, los resultados muestran que el consumo de energía en el UL puede reducirse con un buen rendimiento y que la duración de la batería puede mejorarse gracias a las estrategias del DL.

Agraïments

Arribats a aquest punt, què més puc dir? Ha estat un camí llarg, complicat, i plè d'emocions. Tot i això, ho tornaria a fer (sense cap mena de dubte). Gràcies al doctorat, he crescut molt, tant a nivell personal com professional. És increïble com en tan "poc" temps et poden canviar la visió del món i la manera d'afrontar les coses. Mirant enrere, i amb llàgrimes de felicitat als ulls, ara finalment puc dir-ho: ho he aconseguit!

Ho sé, moltes vegades *m'enrollo* i no vaig al gra. Tothom que em conegui ho sap. És per això que em resulta difícil nombrar a totes les persones que han fet possible aquesta tesi. En realitat, qui s'hagi creuat en el meu camí durant aquests darrers quatre anys i *pico* hi ha contribuit (d'una manera o altra). Intentaré ser breu i no deixar-me a ningú...

M'agradaria dedicar aquestes primeres linies als meus dos supervisors Olga Muñoz i Toni Pascual, per donar-me l'oportunitat de realitzar aquesta tesi. Sense ells res d'això hagués estat possible. Voldria agrair-vos tota la paciència que heu tingut amb mi durant aquest procés i tots els coneixements que m'heu transmès. Em vareu obrir les portes al món de la investigació, en el qual no tenia (gairebé) experiència, i m'hi heu fet quedar... Gràcies!

No puc oblidar-me tampoc dels meus companys de doctorat, Jordi Borràs, Ferran De Cabrera, Miquel Àngel India, i Francesc Molina, per donar-me una mà sempre que ho he necessitat. Sé que no és fàcil entendre a un mallorquí, però (casi) sempre ho heu aconseguit.

Seguidament, m'agradaria nombrar a tots els altres membres del grup de recerca que han pogut aportar el seu granet d'*arena*: Adrián Agustín, Marga Cabrera, Juan Fernández, Montse Najar, i Josep Vidal. També voldria agrair als professors Josep Salavedra i Gregori Vàzquez, per les bromes i les *xerrades* (entre hores) que han ajudat a fer més amè aquest trajecte.

Per últim, i no menys important, m'agradaria agraïr especialment als meus pares Fernando i Magdalena, a la meva germana Paula, i a la meva parella Anna, pel seu suport incondicional. Sempre heu estat allà, *no matter what*. M'heu portat a ser qui sóc i m'heu ajudat en els moments més difícils (que no han estat pocs). De veres, mil gràcies per tot. Aquesta tesi va per *voltros*!

This work has been funded through the projects 5G&B-RUNNER-UPC (Agencia Estatal de Investigación and Fondo Europeo de Desarrollo Regional, TEC2016-77148-C2-1-R / AEI / FEDER, UE) and ROUTE56 (Agencia Estatal de Investigación, PID2019-104945GB-I00 / MCIN / AEI / 10.13039 / 501100011033); the FPI grant BES-2017-079994 (Ministerio de Ciencia e Innovación); and the grant 2017 SGR 578 (AGAUR, Generalitat de Catalunya).

Contents

Acronyms

3GPP	3rd Generation Partnership Project.
5G	Fifth Generation of Cellular Networks.
AN	Access Node.
AoA	Angle of Arrival.
AWGN	Additive White Gaussian Noise.
BD	Block Diagonalization.
BER	Bit Error Rate.
BS	Base Station.
CCDF	Complementary Cumulative Distribution Function.
CDF	Cumulative Distribution Function.
CF	Characteristic Function.
CLT	Central Limit Theorem.
CN	Collector Node.
CPP	Cluster Point Process.
CSI	Channel State Information.
D2D	Device-to-Device.
DCP	Difference of Convex Programming.
DFT	Discrete Fourier Transform.
DL	Downlink.
EH	Energy Harvesting.
eMBB	Enhanced Mobile Broadband.
FD	Full Duplex.
FI	Fairness Index.
HCPP	Hard-Core Point Process.
HD	Half Duplex.
HPPP	Homogeneous Poisson Point Process.

HTC	Human-Type Communications.
I-CSI	Imperfect Channel State Information.
IFFT	Inverse Fast Fourier Transform.
IoT	Internet of Things.
ITU	International Telecommunication Union.
LoS	Line of Sight.
LTE	Long-Term Evolution.
LTE-A	Long-Term Evolution Advanced.
LTE-M	Long-Term Evolution for Machines.
MA	Multiple Access.
MAC	Medium Access Control.
MCP	Matérn Cluster Process.
MCS	Modulation and Coding Scheme.
MHCPP	Matérn Hard-Core Point Process.
MIMO	Multiple-Input Multiple-Output.
MMSE	Minimum Mean Squared Error.
mMTC	Massive Machine-Type Communications.
mmWave	Millimeter Wave.
MR	Multiple Resource.
MSE	Mean Squared Error.
NB-IoT	Narrowband Internet of Things.
NLoS	Non-Line of Sight.
NMSE	Normalized Mean Squared Error.
NOMA	Non-Orthogonal Multiple Access.
NR	New Radio.
OFDM	Orthogonal Frequency-Division Multiplexing.
OFDMA	Orthogonal Frequency-Division Multiple Access.
OMA	Orthogonal Multiple Access.
PCP	Poisson Cluster Process.
PDF	Probability Density Function.
PER	Packet Error Rate.
PF	Proportional Fair.
PMF	Probability Mass Function.
PP	Point Process.

PPP	Poisson Point Process.
PRB	Physical Resource Block.
QoS	Quality of Service.
QPSK	Quadrature Phase-Shift Keying.
RA	Resource Allocation.
RACH	Random Access Channels.
RCP	Repulsive Cluster Process.
RIS	Reconfigurable Intelligent Surface.
RV	Random Variable.
SDP	Semi-Definite Programming.
SIC	Successive Interference Cancelation.
SINR	Signal-to-Interference-plus-Noise Ratio.
SNR	Signal-to-Noise Ratio.
SQUM	Successive Quadratic Upper-Bound Minimization.
SR	Single Resource.
SWIPT	Simultaneous Wireless Information and Power Transfer.
TDM	Time-Division Multiplexing.
UCA	Uniform Circular Array.
UL	Uplink.
UPA	Uniform Planar Array.
URLLC	Ultra-Reliable Low Latency Communications.
UT	User Terminal.
WPN	Wireless Powered Network.
WPT	Wireless Power Transfer.
WSN	Wireless Sensor Network.

Figures

Notation

Basic

x	Scalar.
$\boldsymbol{x}$	Column vector.
$\boldsymbol{X}$	Matrix.
$[\boldsymbol{x}]_m$	m-th element of vector $\boldsymbol{x}$.
$[\boldsymbol{X}]_{m,n}$	(m,n)-th entry of matrix $\boldsymbol{X}$.
$\boldsymbol{X} \succ \mathbf{0}$	Positive definite matrix.
$\boldsymbol{X} \succeq \mathbf{0}$	Positive semi-definite matrix.
$\mathbf{I}_m$	Identity matrix of size $m \times m$.
$\mathbf{0}_m$	All-zeros vector of length m.
$\mathbf{1}_m$	All-ones vector of length m.
e	Euler's number.
i	Imaginary unit.
$\mathcal{X}$	Set.
$\cup$	Union.
$\emptyset$	Empty set.
$\cap$	Intersection.
$\in$	Element of (vector or set).
$\mathbb{R}^{m\times n}$	Real space of dimension $m \times n$.
$\mathbb{N}^{m\times n}$	Natural space of dimension $m \times n$.
$\mathbb{C}^{m\times n}$	Complex space of dimension $m \times n$.
$\triangleq$	Defined as.
$\propto$	Proportional to.
$\approx$	Approximately equal.

Functions

$\arg(\cdot)$	Argument function.
$\min(\cdot)$	Minimum function.
$\max(\cdot)$	Maximum function.
$\exp(\cdot)$	Exponential function.
$Q(\cdot)$	Gaussian Q-function.
$\ln(\cdot)$	Natural logarithm.
$\log(\cdot)$	Base-2 logarithm.

Operators

$(\cdot)^{\mathrm{T}}$	Transpose operator.
$(\cdot)^{*}$	Complex conjugate operator.
$(\cdot)^{\mathrm{H}}$	Complex conjugate transpose (Hermitian) operator.
$\boldsymbol{X}^{-1}$	Inverse of matrix $\boldsymbol{X}$.
$\mathrm{tr}(\boldsymbol{X})$	Trace of matrix $\boldsymbol{X}$.
$\det(\boldsymbol{X})$	Determinant of matrix $\boldsymbol{X}$.
$\mathrm{Det}(\boldsymbol{X})$	Pseudo-determinant of matrix $\boldsymbol{X}$.
$\mathrm{diag}(\boldsymbol{x})$	Diagonal matrix with entries specified by vector $\boldsymbol{x}$.
$\lvert x\rvert$	Absolute value of scalar x.
$\lVert\boldsymbol{x}\rVert_p$	l_p-norm of vector $\boldsymbol{x}$.
$\lVert\boldsymbol{X}\rVert_F$	Frobenius norm of matrix $\boldsymbol{X}$.
$\mathrm{vec}(\boldsymbol{X})$	Vectorized form of matrix $\boldsymbol{X}$.
$\otimes$	Kronecker product.
$\odot$	Hadamard product.
$\lvert\mathcal{X}\rvert$	Cardinality of set $\mathcal{X}$.
$\nabla_x f(\cdot)$	Gradient of function f with respect to x.
$\frac{\partial f(\cdot)}{\partial x}$	Partial derivative of function f with respect to x.
$\int f(\cdot)dx$	Indefinite integral of function f with respect to x.
$\int_{\mathcal{D}} f(\cdot)dx$	Definite integral of function f with respect to x in the domain $\mathcal{D}$.

Statistics

$\Pr[\cdot]$	Probability.
$\sim$	Distributed as.
$\mathbb{E}[\cdot]$	Mathematical expectation.
$p_X(x)$	Probability mass function of random variable X.
$f_X(x)$	Probability density function of random variable X.
$F_X(x)$	Cumulative distribution function of random variable X.
$\bar{F}_X(x)$	Complementary cumulative distribution function of random variable X.
$\mathcal{U}(a, b)$	Uniform distribution between a and b.
Ber(p)	Bernoulli distribution with parameter p.
$\mathcal{N}(\mu, \sigma^2)$	Real scalar Gaussian distribution with mean μ and variance σ^2.
$\mathcal{CN}(\mu, \sigma^2)$	Complex scalar Gaussian distribution with mean μ and variance σ^2.
$\Gamma(\kappa, \theta)$	Gamma distribution with shape parameter κ and scale parameter θ.
$\mathcal{N}(\boldsymbol{\mu}, \boldsymbol{C})$	Real vector Gaussian distribution with mean $\boldsymbol{\mu}$ and covariance matrix $\boldsymbol{C}$.
$\mathcal{CN}(\boldsymbol{\mu}, \boldsymbol{C})$	Complex vector Gaussian distribution with mean $\boldsymbol{\mu}$ and covariance matrix $\boldsymbol{C}$.

Part I

Introduction

Chapter 1

Introduction

1.1 Motivation

During the past decade, both academic and industrial communities have been devoted to the evolution of the fifth generation of cellular networks (5G) [1]. The exponential growth in the number of connected terminals, together with the increasing demand for heterogeneous data services, shed light on the need for the development of novel solutions [2–4]. Within the new era of wireless communications, 5G systems have contributed to the advent of a myriad of unprecedented applications. The emergence of augmented virtual reality, the tactile internet, and smart cities are only a few examples of the impact that 5G technologies are having on modern societies [5]. Not surprisingly, 5G has constituted part of the *digital revolution*.

Compared to its predecessors, which focus solely on human-type communications (HTC), the current release of 5G (at the time of writing), also known as New Radio (NR) [6], addresses three different use cases: enhanced mobile broadband (eMBB), ultra-reliable low latency communications (URLLC), and massive machine-type communications (mMTC). According to the 3rd Generation Partnership Project (3GPP) [7,8], these services can be characterized by their requirements. In eMBB, user terminals pursue high data rates (e.g., tens of Gbps), URLLC systems seek low delays (e.g., 1 ms) and small error probabilities (e.g., 99.999% success), and mMTC networks require vast connectivity (e.g., 10^6 devices/km^2) and low power consumption (e.g., 10 years of battery lifetime). Providing simultaneous support to these three cornerstones becomes, therefore, a challenging problem and represents the main purpose of 5G [9].

More recently, the increasing popularity of the Internet of Things (IoT) has put special attention on mMTC systems [10,11]. Thanks to their easy deployment and large scalability, IoT is nowadays a reality. In a nutshell, mMTC can be defined as a type of networks where a large set of low-cost devices try to communicate with barely or even no human supervision [12,13]. A common example is a setup where a group of sensors[1] collects information from the environment and sends it to a base station (BS) or collector node (CN). This opens the door for a plethora of applications like weather forecasting, surveillance systems, and health monitoring.

Unfortunately, in many practical scenarios, mMTC devices can be power constrained, especially if the replacement or charging of their batteries is difficult [14,15]. Therefore, in order to meet the long autonomy of these networks, it is imperative to develop energy-aware strategies

---

[1] From now on, the terms device and sensor will be used indistinguishably to refer to mMTC terminals.

that improve their power consumption. Along with these concerns, these large networks are also characterized by other key factors like complexity and latency (like in URLLC) [16].

In general, mMTC transmissions consist of short data packets, for which a small overhead is required [17]. Conventional medium access solutions, such as dedicated random access channels (RACH), are, therefore, no longer valid given the amount of signaling and the large number of devices [18,19]. That is why, as pointed out in the NR standard [6,20], approaches based on grant-free access are usually pursued. However, since these schemes entail a large number of collisions, appropriate resolution mechanisms are needed to avoid network failure [21].

Additionally, unlike typical HTC networks (where data traffic is usually scheduled), some mMTC applications present a sporadic activity, i.e., devices send their information depending on some event [22]. In that sense, dealing with non-predictable patterns is crucial for many mMTC services (e.g., emergency scenarios) [23]. Even in the case of transmissions on an approximately regular basis (e.g., industrial control networks), their coordination is still a major issue and the design of new access protocols becomes essential [24].

Moreover, given the high spatial density of these devices, the collected data (e.g., temperature) can be highly correlated [25]. Hence, a question arising is how to manipulate this information to reduce the overall payload. In fact, this redundancy entails the waste of a significant amount of transmit power. Compressing this data and working only with relevant information would then help to decrease the energy consumption and extend the battery lifetimes [13].

In addition to that, in some cases, the exact positions of the mMTC devices can be unknown, and statistical modeling is often required, i.e., their locations are considered to be random and following a certain spatial distribution [26,27]. Since these uncertainties condition the ultimate performance, taking this model into account to evaluate their impact becomes mandatory.

As mentioned before, coexistence with other cellular services (e.g., eMBB and mMTC), also plays an important role in the development of the next mobile generations [28,29]. Long-Term Evolution for Machines (LTE-M) and narrowband-IoT (NB-IoT) are two well-known solutions elaborated by the 3GPP to address this issue [30,31]. Other standards proposed by different entities can be found in [32]. As a result, compatibility with existing cellular networks must be extensively revisited during the investigation of new mMTC approaches.

Based on this framework, in this thesis, we explore novel techniques to improve the autonomy and performance of mMTC networks. The design of these strategies will encompass both uplink (UL) and downlink (DL) scenarios. In the UL, we focus on the reduction of power consumption, with special emphasis on medium access control (MAC), resource allocation (RA), and inference of parameters (i.e., retrieval of the information measured by the devices). On the other hand, based on energy supply mechanisms, the support of wireless powered networks (WPNs) and coexistence with HTC systems are the principal objects of study of the DL setup.

Mathematical tools like optimization theory, estimation theory, and stochastic geometry, will be fundamental for the development of this thesis. Our proposals will be based on state-of-the-art technologies and will take into account practical implementation aspects in their design. Accordingly, to faithfully represent a realistic scenario, we follow the parameters and guidelines specified by the 3GPP and International Telecommunication Union (ITU) standards.

1.2 Outline

The contents of this dissertation are divided into two main parts, each one describing the techniques used for power reduction and interference management in the UL, and the energy supply mechanisms and transmission schemes employed in the DL. This is referred to as Part II and Part III, respectively. A detailed summary of each part is listed below, where we present the scenarios under evaluation, design problems, and research contributions. To avoid redundancy, the review of the current state of the art will be provided at the beginning of each chapter.

For the sake of completeness, prior to both parts, we dedicate an initial chapter to describe the system overview, upon which the rest of the thesis is constructed. That chapter, together with the present introduction, constitute Part I.

1.2.1 System Overview

In this chapter, we establish the basic assumptions considered in this dissertation. Three main areas will be discussed, namely, traffic models, multiple access (MA) schemes, and spatial distributions. Depending on the setup, UL or DL, we might adopt different points of view. Thus, this overview will serve as a theoretical reference for the system models in Parts II and III.

In **Section 2.2**, we present the traffic models constantly used throughout this dissertation. This section will be structured into two main subsections: data transmission and network communication. For each of them, we characterize the different figures of merit that will be studied in the upcoming parts (e.g., error probability, throughput, etc.).

In the former, we distinguish between the case of event-driven (non-scheduled) and regular (scheduled) transmissions. Recall that both patterns can be found in many mMTC applications. Accordingly, for the event-driven (or sporadic) activity, we model the statistics of the transmission with the help of binary random variables (RVs). Differently, in the regular case, we focus mainly on the type of scheduling approach, since the communication follows a predictable behavior. For both traffic types, we also discuss some appropriate mechanisms for MAC.

On the other hand, the latter deals with the network communication, which can be either continuous or packet-based. In that sense, given that sensors usually send short data packets, the continuous case is only used as a first approximation in Chapter 3 to work with a tractable scenario. This way, the system performance can be analyzed by means of the outage probability. Nevertheless, for a more realistic analysis, we later consider the packet-based setup and study the effect of noise, interference, and channel in terms of packet error rate (PER).

In **Section 2.3**, we describe the types of MA schemes used in this thesis, i.e., orthogonal MA (OMA) and non-orthogonal MA (NOMA), and derive the resulting signal-to-noise ratio (SNR) and signal-to-interference-plus-noise ratio (SINR). Note that both cases are closely related to Section 2.2 since they depend on the data transmission (event-driven or regular).

In **Section 2.4**, we expose the spatial distributions employed to model the locations of the mMTC devices. Given that these terminals are usually organized in clusters, we focus on cluster point processes (CPPs) and, regarding the minimum distance between sensing devices, we also study repulsive or hard-core point processes (HCPPs). To analyze the impact on our scenario, the necessary stochastic geometry tools are thoroughly presented.

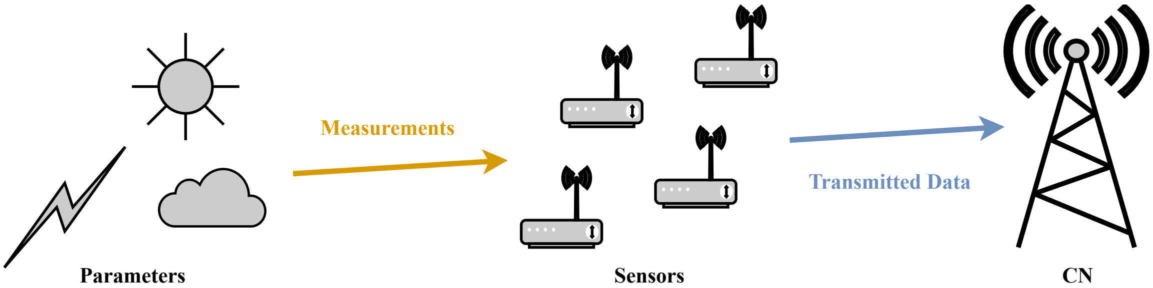

Figure 1.1: UL reference scenario. Sensors transmit the observed (and possibly correlated) parameters to the CN.

1.2.2 Techniques in the Uplink

As mentioned earlier, in this dissertation, we investigate novel techniques to improve the battery lifetime of mMTC devices. In this part, we focus our attention on the UL setup, which is depicted in Figure 1.1. As we can see, in this illustration, we consider that the different sensors measure a set of (possibly correlated) parameters, and send the collected data to the CN.

This part is structured into three chapters: resource allocation, device selection, and data quantization, and robust design of reconfigurable intelligent surfaces (RISs).

In **Chapter 3**, we concentrate on the popular and still open RA problem and propose a graph-based approach that minimizes the outage probability. Since the number of retransmissions increases with this metric, designing a proper resource distribution scheme can help to reduce the energy consumption (i.e., fewer retransmissions imply less transmit power). For that task, we consider a network with a sporadic (or intermittent) activity and model the statistics of the aggregate interference. Given its discrete nature and the large number of sensors, we propose several continuous approximations based on Gaussian kernels. These approximations are then used to derive an analytic closed-form expression for the outage probability.

The results presented in Chapter 3 have been published in one journal paper [J1] and one conference paper [C1] (see next section).

In **Chapter 4**, we present a device selection scheme and a quantization approach that optimizes the inference of parameters, considering the energy limitations of mMTC terminals. This problem is tackled from two different perspectives: entropy and estimation error. Intuitively, both approaches can be seen from the point of view of data compression since we reduce the overall payload by exploiting the correlation among the sensors' observations[2].

In the former, we design a sensing scheme that maximizes the joint entropy of a quantized Gaussian source (which represents the set of observations taken by the sensors) under power-related constraints. Given that the measurements can be expressed with the data covariance matrix, and that in mMTC systems these matrices may be well approximated as rank deficient, we leverage this singularity to design the device selection technique.

On the contrary, the latter focuses on a transmission scheme that minimizes the error in the estimation of the (quantized) parameters. Different from before, the sensors' observations can be corrupted by measurement noise, and the number of quantization bits can be adapted.

---

[2] In this dissertation, the concept of observation and measurement will be used interchangeably.

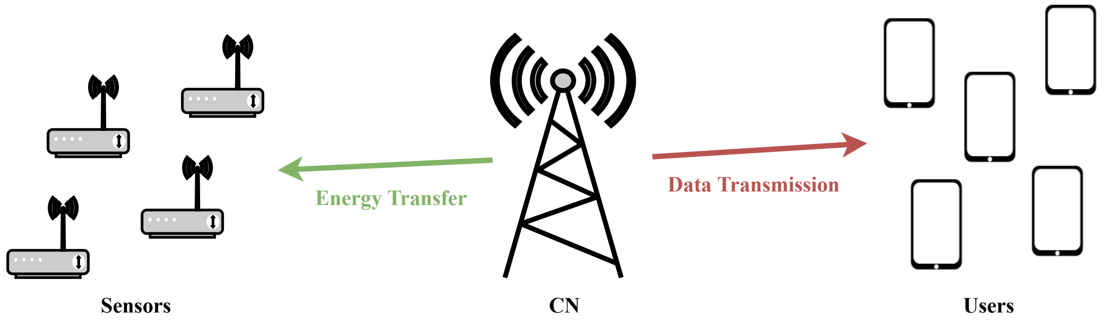

Figure 1.2: DL reference scenario. The CN transfers power to the sensors and information to the users.

Additionally, considering an OMA scheme, the actual transmission of information is also taken into account by averaging the estimation error over the decoding error probabilities. Apart from the spatial correlation, the proposed approach is also extended to the case of temporal evolution. Based on that, we present a device selection strategy to reduce the number of active sensors and a quantization scheme with an adjustable number of bits to minimize the overall payload. The set of selected sensors and quantization levels are, therefore, designed to minimize the resulting error in the parameter estimation.

The results presented in Chapter 4 have been published in two journal papers [J2] and [J3].

In **Chapter 5**, we continue with the estimation of parameters (cf. Chapter 4) and introduce the use of a RIS to support the data transmission and enhance the ultimate performance. Unlike the previous chapter, here we consider a NOMA scheme and study successive interference cancelation (SIC) as a decoding procedure. In addition, given that channel state information (CSI) is essential in this kind of environment, we investigate different methodologies for acquiring this knowledge and include the effects of channel estimation errors in the communication. Accordingly, the RIS is designed to minimize the average error in the parameter estimation, taking into account the imperfect CSI errors. Thus, a robust estimation scheme is derived.

The results presented in Chapter 5 will be submitted to one journal paper [J4] (currently in preparation).

1.2.3 Techniques in the Downlink

Likewise, in order to satisfy the energy requirements of mMTC networks, in this part, we concentrate on the design of energy-driven techniques for the DL setup. An illustrative scenario is shown in Figure 1.2, where the CN is responsible for providing a sufficient amount of energy to all sensors in the network[3]. In addition, in this case, we also include the presence of HTC devices or user terminals (UTs), which usually demand high data rates (cf. eMBB). As a result, the CN will also play the role of a common cellular BS since it is in charge of transferring information to UTs in the DL.

This part is structured into two main chapters, according to the two scenarios under evaluation: energy transfer (pure mMTC setup), and information and power transfer (coexisting mMTC and HTC setup).

---

[3] Different from the UL case, here we omit the transmission of DL data since it consists of signaling [33].

In **Chapter 6**, we address the analysis of wireless powered mMTC networks when considering energy harvesting (EH) and wireless power transfer (WPT) as energy supply mechanisms. Assuming that the CN is equipped with multiple antennas, we characterize the collected energy coming from both procedures with the help of stochastic geometry tools (cf. Section 2.4) and binary RVs. This allows us to model the random positions and sporadic activities of the sensors. Based on that, we derive an energy allocation scheme under a proportional fair policy to guarantee a fair battery recharging for all sensors over time.

The results presented in Chapter 6 have been published in one conference paper [C2].

In **Chapter 7**, we follow a similar approach to the previous one, yet we include the presence of HTC devices. As mentioned before, in this situation, the CN is responsible for providing energy to the sensors and data to the UTs. To that end, depending on the type of HTC, half duplex (HD) or full duplex (FD), we consider that both can be transferred through the same signals, i.e., simultaneous wireless information and power transfer (SWIPT), or separate signals, respectively. Accordingly, we design transmission schemes that maximize the throughput for the UTs while guaranteeing all sensors receive enough energy to avoid depleted batteries.

The results presented in Chapter 7 have been published in one conference paper [C3].

1.3 Chapter Relationships

For the sake of clarity in the explanation, in Figure 1.3 we establish the connections between the aforementioned chapters. For better readability, these relationships are listed in the following:

- The event-driven transmissions from Section 2.2 are used in Chapters 3, 6, and 7.
- The regular transmissions from Section 2.2 are used in Chapters 4 and 5.
- The continuous communication from Section 2.2 is used in Chapters 3 and 7.
- The packet-based communication from Section 2.2 is used in Chapters 4, 5, 6, and 7.
- The OMA schemes from Section 2.3 are used in Chapter 4.
- The NOMA schemes from Section 2.3 are used in Chapters 3 and 5.
- The CPPs and HCPPs from Section 2.4 are used in Chapters 6 and 7.
- The estimation approach from Chapter 4 is used in Chapter 5.
- The energy characterization from Chapter 6 is used in Chapter 7.

As a matter of fact, the distributions from Section 2.4 are also used in Chapters 3, 4, and 5, yet only in the simulations. That is why their connections are not shown in Figure 1.3.

1.4 Research Contributions

The research performed during this dissertation has led to the following publications that are either accepted, submitted, or in preparation for submission in the near future:

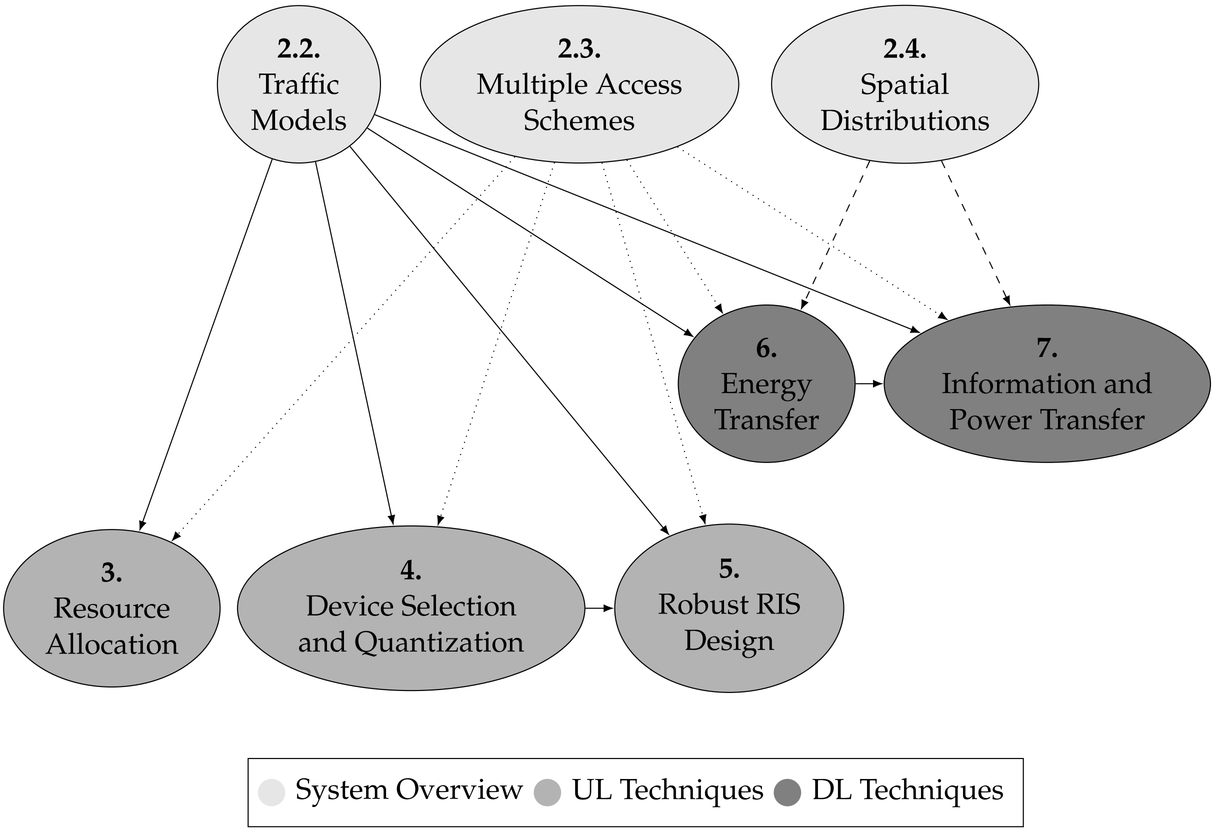

Figure 1.3: Chapter relationships.

Journals

[J4] **S. Liesegang**, A. Pascual-Iserte, and O. Muñoz, ”Robust Design of Reconfigurable Intelligent Surfaces for Parameter Estimation in mMTC,” in preparation for submission to *IEEE Transactions on Wireless Communications*.

[J3] **S. Liesegang**, O. Muñoz, and A. Pascual-Iserte, ”Sensor Selection and Distributed Quantization for Energy Efficiency in Massive MTC,” *IEEE Transactions on Communications*, vol. 69, no. 12, pp. 8518-8533, December 2021.

[J2] **S. Liesegang**, A. Pascual-Iserte, and O. Muñoz, ”Entropy-Based Sensing Schemes for Energy Efficiency in Massive MTC,” *IEEE Wireless Communications Letters*, vol. 9, no. 8, pp. 1173-1177, August 2020.

[J1] **S. Liesegang**, A. Pascual-Iserte, and O. Muñoz, “Approximations of the Aggregated Interference Statistics for Outage Analysis in Massive MTC,” *Sensors*, vol. 19, no. 24, p. 5448, December 2019.

Conference Proceedings

[C3] **S. Liesegang**, A. Pascual-Iserte, and O. Muñoz-Medina, ”Energy Driven Transmission Schemes for Coexistence between HTC and MTC,” in *2021 European Wireless Conference (EW)*, Verona (Italy), November 2021.

[C2] **S. Liesegang**, O. Muñoz-Medina, and A. Pascual-Iserte, ”Stochastic Geometry Analysis and Design of Wireless Powered MTC Networks,” in *2020 IEEE 21st International Workshop on Signal Processing Advances in Wireless Communications (SPAWC)*, Atlanta (GA, USA) - Virtual Conference, May 2020, pp. 1-5.

[C1] **S. Liesegang**, O. Muñoz, and A. Pascual-Iserte, ”Interference Statistics Approximations for Data Rate Analysis in Uplink Massive MTC,” in *2018 IEEE Global Conference on Signal and Information Processing (GlobalSIP)*, Anaheim (CA, USA), November 2018, pp. 176-180.

Other Presentations

[P2] **S. Liesegang**, O. Muñoz-Medina, and A. Pascual-Iserte, ”Stochastic Geometry Analysis and Design of Wireless Powered MTC Networks,” in *2021 IEEE Signal Processing, Information Theory and Communications Webinar (SIC)*, Virtual Webinar, July 2021.

[P1] **S. Liesegang**, O. Muñoz-Medina, and A. Pascual-Iserte, ”Modeling and Optimization of Wireless Powered MTC Networks with Stochastic Geometry,” in *2021 IEEE Communication Theory Workshop (CTW)*, Banff (AB, Canada) - Virtual Conference, June 2021.

Chapter 2

System Overview

2.1 Introduction

Throughout this dissertation, we consider a packet-based communication, in which a set of M sensors transmit their data to the CN on a time-division basis [7]. We assume that time is divided into frames, each consisting of N time slots. Accordingly, one slot will correspond to one packet of n_i transmit symbols or channel uses (cus), which are mapped from k_i source (or observation) symbols through the source-channel code of sensor i, with $i \in \{1, \ldots, M\}$.

Following the separation theorem [34], we consider that source and channel codes are constructed separately. This is illustrated in Figure 2.1, where the k_i symbols observed from source i[1] are first encoded into l_i information bits (inf. bits) and later transformed into n_i cus. In that sense, the first stage (source coding) represents the data compression with rate $S_i \triangleq l_i/k_i$, and the second one (channel coding) defines the modulation and coding scheme (MCS) with data rate $R_i \triangleq l_i/n_i$. For the latter, we consider the l_i inf. bits are first protected and converted into c_i coded bits (cod. bits), and later modulated into n_i cus. This way, the rate R_i is decomposed into (error) coding rate $R_i^{\mathcal{C}} \triangleq l_i/c_i$ and modulation size $R_i^{\mathcal{M}} \triangleq c_i/n_i$ such that $R_i = R_i^{\mathcal{C}} R_i^{\mathcal{M}}$.

Depending on the application, sensors will either send their information during one or several slots, following a random or deterministic pattern. Recall that, given the large number of devices and lack of coordination in the MAC, interference in mMTC networks can be critical. Besides, since resources are usually limited, assuming orthogonality between received signals can be unrealistic. Therefore, in this thesis, we also study the use of OMA and NOMA schemes and compare the benefits of both approaches. Finally, we consider that devices are randomly located and analyze the impact of their spatial distribution on the system performance. With the help of stochastic geometry tools, we are able to model this behavior feasibly.

All these issues play an important role in the design criteria for energy consumption and data transmission. That is why we present this chapter as the backbone for Parts II and III.

The remainder of this chapter is structured as follows. In Section 2.2, we discuss the traffic models corresponding to the different types of data transmissions and network communications considered in this dissertation, along with some thoughts on MAC protocols. In Section 2.3, we describe the MA schemes used in this thesis. Finally, in Section 2.4 we characterize the spatial distributions of the sensors by means of stochastic geometry.

---

[1] Each sensor observes a different source, which might be correlated with the other sources (cf. Chapter 4).

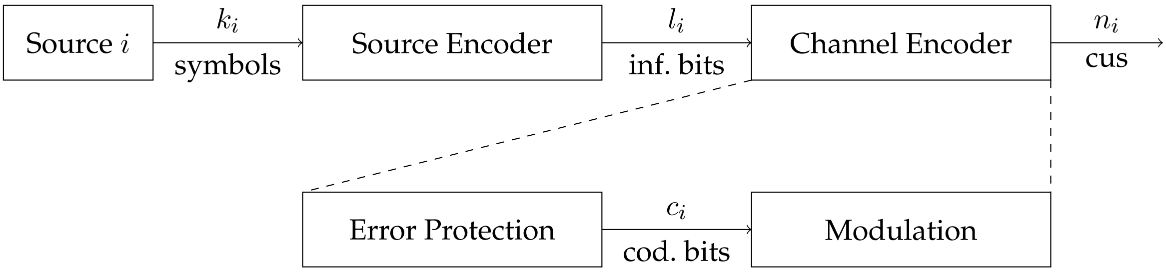

Figure 2.1: Communication scheme of sensor i: source and channel coding are applied sequentially with rates S_i (inf. bits/symbols) and R_i (inf. bits/cus), respectively. The channel encoder is decomposed into error protection (or correction) and modulation with rates $R_i^{\mathcal{C}}$ (inf. bits/cod. bits) and $R_i^{\mathcal{M}}$ (cod. bits/cus), respectively. For more details on the separation theorem, we encourage the interested reader to refer to [34] and references therein.

2.2 Traffic Models

2.2.1 Data Transmission

As pointed out in Chapter 1, mMTC systems can be classified according to the type of data traffic generation, event-driven or regular [12]. In the following, we analyze both types and model the communication between the sensors and the CN.

2.2.1.1 Event-driven

In some mMTC scenarios, sensors can transmit sporadically and the exact transmission time be difficult to know [22]. This is the case, for instance, of sensors reporting power failure or tamper notifications. In these kinds of applications, the devices are triggered by a certain event and remain in a sleep mode (or idle state) for most of the time. This can complicate the prediction of the exact transmission time and, hence, it is imperative to include their (unpredictable) state when evaluating the system performance.

To facilitate the analysis, particularly in the case of a massive number of sensors, we model the sporadic transmissions as Bernoulli RVs with known probability (or activity factor) p_i. As a result, we assume that these devices are either active or asleep (on/off), i.e.,

$$\beta_i \sim Ber(p_i), \tag{2.1}$$

is the RV capturing the intermittent behavior of sensor i, i.e., $\beta_i = 0$ and $\beta_i = 1$ refer to the idle and active states, respectively. As mentioned earlier, this will condition the communication between sensors and the CN. For instance, in Chapter 3 we will evaluate the impact of the resulting (random) aggregate interference with the help of the outage probability.

Contrarily to the case of regular (scheduled) traffic, in event-driven applications, contention-based communication (e.g., ALOHA) is usually preferred [20]. Instead of allocating resources in advance, sensors choose one of the available slots at random. In that sense, as discussed in Chapters 3 and 5, the resulting collisions will be treated as interference (rather than transmission failure) and, thus, the MAC protocol will enable multi-packet reception at the CN [23].

2.2.1.2 Regular

Other mMTC applications, such as those under the umbrella of IoT, can be characterized by periodic patterns (e.g., information is retrieved by polling the sensors every certain time) or deterministic arrivals (e.g., data is communicated within a given time frame) [24]. Some examples can be smart utility metering, smart agriculture, and smart environment, among others.

In other words, transmissions are predictable and the use of conflict-free access mechanisms, such as configured scheduling [35], becomes more suitable than random access strategies (which are widely used in setups with a low traffic load or sporadic transmissions). That is why in some parts of this dissertation (e.g., Chapter 4), we consider a time-division multiplexing (TDM) scheduling mechanism, in which sensors will transmit through a pre-allocated (temporal) resource. This MAC procedure will be fully implemented by the CN.

2.2.2 Network Communication

As mentioned earlier, mMTC transmissions are generally characterized by small data packets [4]. That is why in this dissertation, we mainly focus on packets of finite length. However, since the corresponding analysis can be challenging, we start by considering the classical Shannon approach, i.e., continuous communication (used in Chapters 3 and 7). This is discussed in the following, where we also provide the expressions for the data rate and error probability.

2.2.2.1 Continuous

In the case of continuous communications ($n_i \to \infty$), we are able to transmit with an arbitrarily small error probability as long as the data rate R_i is below the channel capacity C_i [36]. Hence, the communication channel has a binary behavior, i.e., the transmission either succeeds or fails.

For the additive white Gaussian noise (AWGN) channel, this capacity reads as

$$C_i \triangleq \log(1 + \rho_i), \tag{2.2}$$

where ρ_i is the SNR or SINR of the received signal at the CN, later discussed in Section 2.3.

Nevertheless, this assumption does not hold when considering fading access channels or random interference. In those situations, the transmitter is unable to adapt the throughput to the resulting (random) capacity and, thus, the receiver fails to decode the original message properly. In other words, error-free communication is not possible and we need to deal with a non-zero error probability. This is commonly referred to as outage probability and represents the event of the SNR (in the case of OMA schemes) or SINR (in the case of NOMA schemes) being below a detection threshold. Accordingly, we can express this metric as follows:

$$P_i^{\text{out}} \triangleq \Pr\{R_i > C_i\} = \Pr\{\rho_i < \delta_i\}, \tag{2.3}$$

where $\delta_i \triangleq 2^{R_i} - 1$ is the minimum SNR/SINR for the message to be successfully decoded.

Note that expressions (2.2) and (2.3) are normally used as ultimate performance limits since in real scenarios we work with packets of finite lengths. In fact, to reach these upper bounds, Gaussian constellations (or codewords) are also required at the transmitters' side [36].

However, these conditions imply transmitting symbols with continuous alphabets (i.e., infinite codebooks), which can not be achieved in practice (only a few bits are available per channel use, especially in mMTC), apart from an unfeasible latency and complexity. That is why in the following, we present the case of packets of finite length (considered in Chapters 4 and 5).

2.2.2.2 Packet-based

Even when considering (deterministic) AWGN channels, a zero-error probability is only attainable when the number of transmit symbols n_i goes to infinity [34]. Otherwise, we need to face a certain PER, which can be distinguished from the outage probability. The reason behind this is that, unlike before, the condition upon which a communication (or decoding) error occurs is no longer $R_i > C_i$ (i.e., the channel has a non-binary behavior). Instead, now the error probability depends on the MCS and decision boundaries of the decoding procedure [36].

The PER corresponding to all bits transmitted by sensor i in a single slot reads as

$$\mathrm{PER}_i \triangleq \mathcal{C}_i\left(\mathrm{PER}_i^{\mathrm{raw}}\right), \tag{2.4}$$

where $\mathrm{PER}_i^{\mathrm{raw}} \geq \mathrm{PER}_i$ is the (raw) PER computed at the output of the channel and before the channel decoder for the set of coded bits. Accordingly, $\mathcal{C}_i(\cdot)$ is the function that relates both probabilities and that depends exclusively on the coding rate $R_i^{\mathcal{C}}$ and the structure of the channel encoder [37]. Some examples of these functions are discussed in [38].

Assuming independent bit errors (due to channel and noise effects)[2], we have

$$\mathrm{PER}_i^{\mathrm{raw}} \triangleq 1-\left(1-\mathrm{BER}_i^{\mathrm{raw}}\right)^{c_i}, \tag{2.5}$$

where $\mathrm{BER}^{\mathrm{raw}}$ is the raw bit error rate (BER), which is independent of the channel code and only depends on the modulation scheme and ratio ρ_i. For instance, in the case of quadrature phase-shift keying (QPSK), widely employed in mMTC networks[3], this BER is known, i.e.,

$$\mathrm{BER}_i^{\mathrm{raw}}(\mathrm{QPSK}) = Q\left(\sqrt{2\rho_i B_i/R_i}\right), \tag{2.6}$$

where $Q(\cdot)$ is the Gaussian Q-function and B_i is the bandwidth of sensor i. However, for higher-order modulations, only an upper bound of the BER can be derived [36]. In addition, since the mappings $\mathcal{C}_i(\cdot)$ are usually found by numerical evaluation, an analytic closed-form expression of the PER is available in the case of only modulation and no error protection coding.

Contrarily, as we will see in some parts of this thesis, using the approximation from [39], we can work with an expression for the PER as a function of ρ_i (even for coded transmission):

$$\mathrm{PER}_i \approx Q\left(\sqrt{n_i}\frac{C_i - R_i}{\sqrt{V_i}}\right), \tag{2.7}$$

where $V_i \triangleq (1-(1+\rho_i)^{-2})\log^2 e$ is the so-called channel dispersion.

---

[2] In the case of slowly varying channels, this condition can be easily met with the help of bit interleavers [36].

[3] To commit to the mMTC requirements (massive connectivity, short packet lengths, and limited power consumption), 3GPP standards consider the use of low order constellations [22].

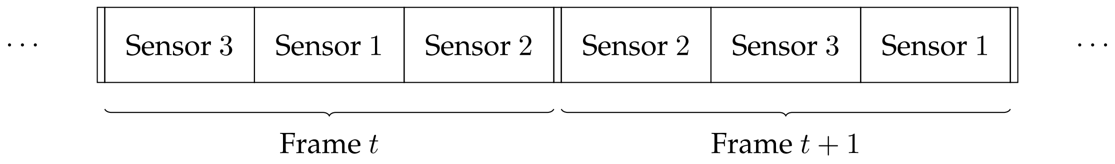

Figure 2.2: Example of two consecutive transmission frames for $M = N = 3$ (OMA case). Sensors 1, 2, and 3 are allocated slots 2, 3, and 1 during frame $t \in \{1, \ldots, \}$, respectively, and slots 3, 1, and 2 during frame $t + 1$, respectively. Note that resources can be differently distributed across time frames.

2.3 Multiple Access Schemes

Due to the vast number of devices, interference can be a limiting factor in mMTC networks [21]. To counteract its impact, a first approach is to consider an OMA scheme and distribute orthogonal resources, also known as physical resource blocks (PRBs) in 3GPP standards, to all sensors. For instance, orthogonal frequency-division MA (OFDMA) is extensively used in current cellular deployments, i.e., LTE, LTE-Advanced (LTE-A), and early stages of NR [38].

However, since the number of resources is usually limited (e.g., in LTE-M, only 6 PRBs are available [22, 40]), some efficient reuse is needed to serve all devices. This leads to a NOMA-based strategy, where mMTC terminals transmit without any scheduling [41–43]. Compared to contention-based protocols, where collisions represent a packet loss, dealing with interference can result in lower latency (in exchange for a higher decoding complexity), given the reduction in the number of (re)transmissions. As we will see in Chapter 5, a well-known example is the use of SIC, which allows the decoding of multiple packets [44–46].

As mentioned before, dedicated approaches are used in setups with regular traffic (e.g., Chapters 4 and 5), whereas random access schemes are suited for low traffic loads or sporadic activities (e.g., Chapters 3, 6, and 7). Nevertheless, although OMA schemes are normally used for the former, the NOMA approaches can be applied to both cases.

In this section, we provide the expressions for the SNR and SINR in the case of OMA and NOMA schemes, respectively. Accordingly, we incorporate the type of traffic pattern and study its impact on the system performance.

2.3.1 Orthogonal Resources

In the case of orthogonal resources, sensors will use separate time slots[4] to send their data to the CN. If all devices are active, we need $N \geq M$ slots to ensure all sensors can transmit without sharing resources. An illustrative example of two consecutive transmission frames is shown in Figure 2.2, where, for simplicity, we assume that there are no empty slots (i.e., $M = N = 3$).

In line with that, the ratio ρ_i will represent the SNR of the received signal from sensor i at the CN. Considering an effective channel h_i and a transmit power P_i, we have

$$\rho_i^{\text{OMA}} \triangleq \frac{P_i |h_i|^2}{N_o B_i}, \quad i \in \{1, \ldots, M\}, \tag{2.8}$$

---

[4] From now on, we assume that all transmission slots are aligned in time (i.e., synchronized, like in slotted ALOHA [47, 48]) such that no overlapping among packet transmissions is permitted.

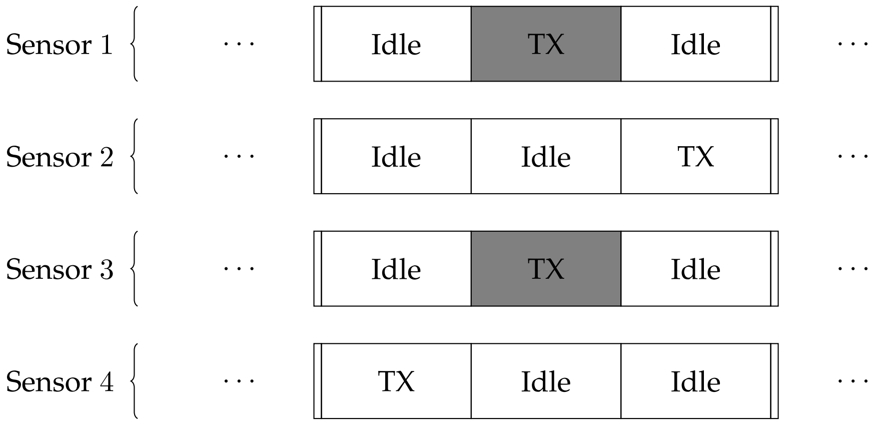

Figure 2.3: Example of transmission frame for $M = 4$ and $N = 3$ (NOMA case). Here, sensors 1 and 3 communicate through slot 2, which yields interference between their packets (marked in gray). On the contrary, since sensors 2 and 4 use resources 3 and 1, respectively, no collision occurs.

where N_o is the AWGN spectral density [36]. Note that h_i depends on the characteristics of the link between transmitter and receiver (e.g., number of antennas, path loss, frequency bands, etc.). This information will be specified in each chapter accordingly. Also, since this model is used for regular data traffic, the devices' activity will not affect the randomness in the scenario.

2.3.2 Non-Orthogonal Resources

Contrarily, when all sensors are active and share resources (i.e., $N < M$)[5], we face a certain interference. This means that the ratio ρ_i will correspond to the SINR of the desired signal and, depending on the type of traffic (regular or intermittent), we will have different expressions.

An illustrative example is depicted in Figure 2.3, where a set of $M = 4$ sensors transmit their packet[6] over $N = 3$ slots. In the regular case, despite a RA is performed prior to transmission (cf. Chapter 3), some interference will still be generated given the limited number of time slots. Likewise, for the sporadic pattern, due to the random selection of resources and the intermittent activity, some sensors might transmit through the same slots, thus creating interference.

In the case of a regular (predictable) activity, we can write the SINR as follows (cf. (2.8)):

$$\rho_i^{\text{NOMA, regular}} \triangleq \frac{P_i|h_i|^2}{N_o B_i + \sum_{j \neq i} P_j |h_j|^2}, \quad i \in \{1, \ldots, M\}, \tag{2.9}$$

where $P_j|h_j|^2$ represents the interference coming from the transmit signal of sensor j. As we will see in Chapter 5, by means of SIC decoding, the CN is able to remove (or mitigate) some of these terms (which increases the robustness against interference). For the sake of clarity in the explanation, we keep this expression generic and reserve that discussion for later on.

When considering a low or sporadic traffic load, the expression of the SINR yields

$$\rho_i^{\text{NOMA, sporadic}} \triangleq \frac{P_i|h_i|^2}{N_o B_i + \sum_{j \neq i} \beta_j P_j |h_j|^2}, \quad i \in \{1, \ldots, M\}, \tag{2.10}$$

---

[5] For the moment, we assume that sensors use the same frequency carriers and bandwidth B_i.

[6] In this dissertation, we consider that each sensor generates and sends only one packet per frame.

Figure 2.4: General construction procedure of a RCP Φ. By means of clustering operations, a CPP Π is obtained from a parent PP Ξ. Later, thinning is applied to the CPP in order to retrieve the RCP.

where the RVs β_j (cf. (2.1)) are introduced to model the (unpredictable) states of the devices (on/off). Thus, the resulting aggregate interference will follow a random behavior that will condition the data transmission. In other words, the communication can be hard to adapt and the CN might struggle to decode some messages. This is further discussed in Chapter 3.

2.4 Spatial Distributions

In the scenario under evaluation, the positions of the sensors are considered to be random and normally unknown [27]. That is why in this dissertation, we make use of stochastic geometry to characterize their spatial distribution and include this uncertainty in the system model [49].

As mentioned in Chapter 1, throughout this thesis we consider that all mMTC devices are organized in K clusters, each one spatially represented by a disk of radius r_k centered at $\boldsymbol{c}_k \in \mathbb{R}^2$, with $k \in \{1, \dots, K\}$. Both r_k and $\boldsymbol{c}_k$ are assumed to be known, yet not the sensors' positions. Each cluster has a density of sensors λ_k and sensors in the same cluster are at a minimum distance d_{min} between each other. We also assume that no devices are located outside these delimited regions. Note that clustering is essential to structure mMTC networks and improve their performance, e.g., coverage, throughput, scalability, and energy consumption [50].

The positions of the sensors can then be represented by a repulsive cluster process (RCP) $\Phi \triangleq \{\Phi_1, \dots, \Phi_K\}$. Each individual process Φ_k has an intensity λ_k and minimum distance d_{min}, and devices are distributed in the circle of radius r_k around the center $\boldsymbol{c}_k$ [51].

To construct these point processes (PPs), or set of randomly located points, some ingredients are needed, namely, CPPs and HCPPs. Both processes can be derived from a parent PP through clustering (gathering points) and thinning (removing points), respectively [52]. Finally, these strategies are combined to obtain the RCP Φ. The whole procedure is summarized in Figure 2.4, where Φ results from thinning a CPP Π that originates from clustering a parent PP Ξ.

In this section, we describe all these PPs, along with the necessary construction tools, and concentrate on the Poisson case since it provides a baseline model for most works in the literature [26,53]. That is why we dedicate an initial subsection to introducing this process.

2.4.1 Poisson Point Processes

In short, a PP $\Psi \triangleq \{\boldsymbol{p}_i : i = 1, 2, \dots\} \in \mathbb{R}^2$ is a Poisson PP (PPP) with measure $\mu(\cdot)$ if, and only if, the number of points $\boldsymbol{p}_i$ lying in a compact set B, denoted by $|\Psi|$, is a Poisson RV with mean $\mu(B)$, and for any disjoint sets $B_1, B_2, \dots$, the RVs $|\Psi_1|, |\Psi_2|, \dots$ are independent [54].

In this thesis, we focus on the stationary case, the so-called homogeneous PPP (HPPP), with uniform intensity λ, i.e., $\mu(B) \triangleq \mathbb{E}\left[|\Psi|\right] = \lambda|B|$ where $|B|$ is the area of B. This means that, in an HPPP, all points are independently and uniformly distributed within B [53].

2.4.2 Cluster Point Processes

If the points in a PP can be characterized by random (disjoint) clusters, the resulting process is a CPP. As mentioned above, the CPP Π is obtained from clustering a parent PP Ξ. In our case, the parent is the set of cluster centers, i.e., $\Xi \triangleq \{\boldsymbol{c}_k : k = 1, \ldots, K\}$, and, thus, we have [52]

$$\Pi \triangleq \bigcup_k \Pi_k, \tag{2.11}$$

where Π_k are the positions of the sensors in cluster k around the center $\boldsymbol{c}_k$.

When considering the Poisson case, Ξ is defined as an HPPP with intensity (or density[7]) δ such that $K \triangleq |\Xi| \sim \mathit{Poisson}(\delta|A|)$, where A is the area of the mMTC scenario (defined later on). This way, by applying homogeneous independent clustering to Ξ, we obtain a Neyman-Scott process Π, which is a type of Poisson cluster process (PCP). As a result, we can express each process Π_k with the following shift:

$$\Pi_k \triangleq \boldsymbol{c}_k + \Omega_k, \tag{2.12}$$

where $\Omega_k \triangleq \{\boldsymbol{q}_{k,l} : l = 1, 2, \ldots\}$ are the daughter points in cluster k centered at the origin (independent from the parent process Ξ). By definition, the set of points in Ω_k are random in number and independently scattered according to a certain distribution. In that sense, $\boldsymbol{c}_k$ can be interpreted as the set of germs and $\boldsymbol{\Omega}_k$ as the set of grains that generate the PCP [52].

Throughout this dissertation, we consider that each cluster is itself an HPPP of intensity δ_k, i.e., $|\Omega_k| \sim \mathit{Poisson}(\delta_k \pi r_k^2)$. These processes are also known as doubly Poisson cluster process or doubly Poisson point process [55]. Two main cases are studied, namely, Matérn and Thomas CPPs, which correspond to uniformly and Gaussian distributed points, respectively.

In Matérn cluster processes (MCPs), the points in Ω_k are drawn following a uniform distribution. Accordingly, the (shifted) positions of the sensors in cluster k are given by

$$\boldsymbol{q}_{k,l} = r_k \sqrt{\varphi}[\cos(\omega)\ \sin(\omega)], \tag{2.13}$$

where $\varphi \sim \mathcal{U}(0, 1)$ and $\omega \sim \mathcal{U}(0, 2\pi)$. On the contrary, points in a Thomas process are Gaussian distributed with zero mean and covariance matrix $r_k^2\mathbf{I}_2$, i.e., $\boldsymbol{q}_{k,l} \sim \mathcal{N}(\mathbf{0}_2, r_k^2\mathbf{I}_2)$.

2.4.3 Hard-Core Point Processes

In the case of HCPP, no two points are allowed to lie closer than a certain minimum distance $d_{\min}$. Similar to before, an HCPP results from thinning a parent PP [52]. In this dissertation, we focus on a specific case, the Matérn HCPP (MHCPP) of type II, where a dependent thinning is applied to a parent HPPP. For other examples, the reader is referred to [55].

Recall that we are interested in networks where the distance between sensors in the same cluster is at least $d_{\min}$. Hence, in this case, the parent HPPP will be the aforementioned MCP Π, which consists of the set of processes Π_k (or, equivalently, Ω_k). In that sense, we apply dependent thinning to each Ω_k to obtain a set of MHCPPs Υ_k.

---

[7] In this dissertation, the concept of intensity and density will be used interchangeably.

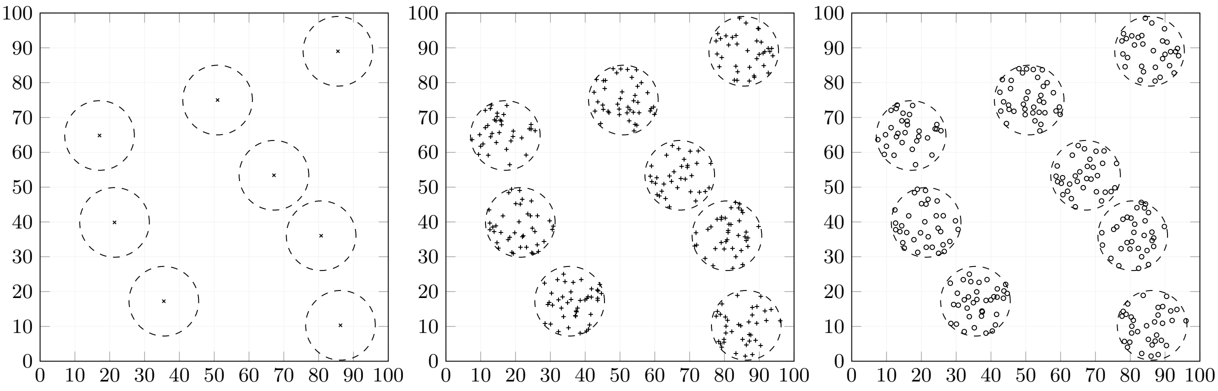

(a) Parent HPPP $\Xi = [\boldsymbol{c}_1, \ldots, \boldsymbol{c}_8]$. **(b)** MCP $\Pi = [\Pi_1, \ldots, \Pi_8]$. **(c)** Repulsive MCP $\Phi = [\Phi_1, \ldots, \Phi_8]$.

Figure 2.5: Construction procedure of a mMTC network based on the Poisson model. In this realization, $K = 8$ clusters are generated, the deployment areas of which are represented by the dashed disks centered at the points in Ξ. Accordingly, Π is generated by clustering Ξ and Φ by thinning Π.

To construct these repulsive processes, all points in each Ω_k are marked with RVs uniformly distributed within the interval $(0, 1)$. Then, the points $\boldsymbol{q}_{k,l}$ with mark $m(\boldsymbol{q}_{k,l})$ are kept only if no other points at distance $d_{\min}$ have marks smaller than $m(\boldsymbol{q}_{k,l})$. Otherwise, these points are removed. Under these constraints, the processes Υ_k are still stationary with intensities λ_k [52]:

$$\lambda_k = \frac{1 - \exp(-\delta_k \pi d_{\min}^2)}{\pi d_{\min}^2}. \tag{2.14}$$

2.4.4 Repulsive Cluster Point Processes

The combination of the previous processes yields a PCP Υ, where the individual clusters are MHCPPs, i.e., $\Upsilon \triangleq \{\Upsilon_1, \ldots, \Upsilon_K\}$. However, given the nature of MHCPP, the resulting PCP may not be mathematically tractable. For that reason, we introduce the PPP approximation.

Following the approach in [49], it can be shown that, for $d_{\min} \to 0$, each Υ_k can be safely approximated by a (cluster) process Φ_k with the same boundaries (disk of radius r_k centered at $\boldsymbol{c}_k$) and density of sensors λ_k. Since in real scenarios these densities tend to be large, devices will be very close and, therefore, this approximation can be reasonably applied. Besides, note that the number of points in each cluster will be a Poisson RV with mean $\lambda_k \pi r_k^2$, i.e., $|\Phi_k| \sim \mathit{Poisson}(\lambda_k \pi r_k^2)$, and that processes modeling different clusters will be independent. Thereby, the total number of sensors in the network will be $M \triangleq \sum_k |\Phi_k| \sim \mathit{Poisson}(\sum_k \lambda_k \pi r_k^2)$.

As a result, merging all these processes, we end up with the RCP $\Phi \triangleq \{\Phi_1, \ldots, \Phi_K\}$, which captures the structure of mMTC (i.e., clusters with large heterogeneous densities). In fact, given the Poisson assumption, Φ can be denoted as a repulsive MCP: cluster process formed by independent HPPPs Φ_k with uniform intensities λ_k and hard-core parameter $d_{\min}$.

For the sake of clarity in the explanation, in Figure 2.5 we depict an illustrative example of the construction steps (i.e., parent, clustering and thinning) for $\delta = 10^{-3}$ clusters/m^2, $r_k = r = 10$ m, $\lambda_k = \lambda = 0.1$ sensors/m^2, and $d_{\min} = 1$ m.

Part II

Techniques in the Uplink

Chapter 3

Resource Allocation

3.1 Introduction

As mentioned in the introduction, one of the main characteristics of event-driven mMTC networks is the intermittent activity of the devices [22]. Once sensors measure the phenomenon, an exception report is sent to the CN (e.g., smoke alarm detection). Since this type of communication is normally supported by NOMA and random access strategies (cf. Section 2.2), collisions are likely to take place. In general, authors advocate for contention-based transmissions to resolve these collisions [19]. However, instead of communication failure, an alternative is to treat these collisions as interference and design proper interference management techniques.

Accordingly, due to these sporadic transmissions (i.e., on/off states of the mMTC terminals), the received signal at the CN from each device will be affected by a random aggregate interference coming from the other active sensors. Then, the communication for a given sensor can be sometimes in outage, which means the interference level is high enough to make the correct detection of the signal unfeasible. In this framework, it is desirable to characterize the statistics of the aggregate interference in order to evaluate the system performance and design resource allocation (RA) strategies that mitigate the impact of this random interference.

In that sense, the outage probability, defined as the probability that the CN is unable to decode the transmitted message properly (cf. (2.3)), represents an adequate metric. It captures the random nature of the sensors' activity and is completely defined by the statistical distribution of the aggregate interference. Unfortunately, given its discrete nature and the large number of devices, an analytic closed-form expression of this distribution can be difficult to find.

Finally, recall that lower values of this probability will lead to fewer retransmissions and, thus, a smaller power consumption. Besides, the energy used in these kinds of systems during the idle state is very small compared to that when the device is active [11]. Thereby, the optimization of the outage probability can also help to improve this figure of merit.

With the above considerations, the goal of this chapter will be to model and derive analytical (continuous) approximations of the aggregate interference statistics. This way, a tractable expression of the outage probability can be obtained. Based on that, we will propose a MAC mechanism and a RA scheme that minimize this probability.

3.1.1 Related Work

The statistical modeling of the aggregate interference has been studied in several cellular wireless networks considered in the literature (see, e.g., [56–60]). For example, the authors of [56] described its distribution in the context of cognitive radio with the help of the cumulants and a truncated-stable model. Likewise, in [57], an approximation and an analytic closed-form expression were derived for the moment generating function of the aggregate interference. Other works (e.g., [58, 59]), also for cellular communications, studied the modeling in the presence of wireless channel imperfections and imperfect channel knowledge. In these works, authors considered clusters and sets of BSs that cooperate in the DL to improve the system performance and studied the effect on the aggregate interference of different transmission schemes. A more comprehensive review of modeling approaches can be found in [60].

The scenario under evaluation in [56–60] considered cellular and continuous communications (i.e., HTC). Hence, the previous works do not capture the intrinsic nature of event-driven mMTC, i.e., sporadic transmission and massive access. Because of this difference with common HTC, the existing analysis and solutions for cellular schemes (e.g., RACH-based approaches) cannot be directly applied to the mMTC system considered in this chapter.

On the other hand, the outage probability has been widely used to study the performance of wireless sensor networks (WSNs), especially using tools such as stochastic geometry [26]. As introduced in Section 2.4, this mathematical tool allows the analysis of these systems in a spatially statistical manner, i.e., the devices' positions are considered to be random and following a certain distribution [61,62]. In turn, the activity of the sensors is usually considered deterministic, which is a simplistic assumption in mMTC. Hence, the outage probability is formulated to capture the variations in the received signal power due to the random positions only. For instance, the authors of [63] derived analytic closed-form expressions for the SINR, which led to the outage probability, using HPPPs for Nakagammi-m and Rayleigh fading.

In the scenario under study (i.e., networks with sporadic traffic), the task of coordinating the interactions between devices is typically resolved through grant-free MAC protocols (cf. Subsection 2.2.1). To cope with the increasing number of collisions that arise with these strategies, the authors of [64] introduced the use of compressive sensing for (event-driven) mMTC systems. In [65], authors proposed a scheme based on the distribution of grants by means of a multiple-antenna technology. An algorithm relying on the maximization of the random access efficiency and the estimation of the number of devices was described in [66]. In [67], authors presented a methodology relying on queues and the observed traffic load to guarantee a certain statistical quality of service (QoS). An overview of more alternatives can be found in [18].

Regarding the RA problem, different methodologies can be found within the literature. As an example, the authors of [68] proposed a graph-based technique to optimize the maximum average resource utilization in the network. Differently, a dynamic scheduling solution that relied on devices' priorities in the framework of mMTC was presented in [69], where the impact on the outage probability was also studied. Moreover, in [70], authors analyzed the scheduling of resources using stochastic geometry under a NOMA transmission scheme. A similar point of view can be found in [71], where random and channel-aware allocation strategies were also investigated. For more approaches, please refer to the survey in [72] (and references therein).

3.1.2 Contributions

The main contributions of this chapter are listed in the following:

- Derivation of several analytic closed-form approximations of the statistics of the aggregate interference that include the random activity of the sensors.

Our approach is firstly formulated for a generic scenario and later particularized for an UL multiple-antenna mMTC setup in order to present the second novelty of this chapter:

- Derivation of an analytic closed-form expression of the outage probability of the sensors. This metric is used to evaluate the performance of these types of systems.

Finally, in this chapter, the following issues are also addressed:

- A MAC scheme with spatial beamforming.
- A graph-based RA strategy that minimizes the average outage probability.

3.1.3 Organization

The remainder of this chapter is organized as follows. In Section 3.2, the system model is described. The approximations of the aggregate interference statistics are presented in Section 3.3. In Section 3.4, the outage probability is derived for an illustrative reference scenario. The resource allocation problem is formulated and solved in Section 3.5. In Section 3.6, numerical simulations are shown to illustrate the accuracy of the approximations and evaluate the performance of the proposed resource allocation strategy. Section 3.7 is devoted to conclusions.

3.2 System Model

As mentioned in Chapter 1, we start by considering a generic scenario in which a set of sensors transmit their measurements[1] towards a CN through possibly different orthogonal resources (cf. Figure 1.1). Only the sensors sharing the same resources will interfere with each other. Thus, for each resource, this scheme can be interpreted as an equivalent NOMA transmission (cf. Section 2.3). Besides, note that, under these first few assumptions, the upcoming analysis can be applied to many network topologies.

Following the discussion in Section 2.2, we assume devices to be in active or sleep mode with the help of the Bernoulli RVs $\beta_j \sim Ber(p_j)$, where j is the sensor's index, and p_j is the probability that sensor j is active and transmitting. We also consider RVs of different terminals to be independent. This practice is commonly used in the literature to describe the sporadic nature of transmissions (cf. [56, 57, 60]). Intuitively, this means all sensors can transmit autonomously, irrespective of the activity of the other sensing devices.

At the detection stage, the received signal at the CN from each sensor is affected by an aggregate interference coming from the other active sensors, the probability mass function (PMF) of which results from the sum of scaled independent Bernoulli RVs.

---

[1] In this chapter, the nature and characterization of the sensors' observations are not considered (we focus on the data transmission and omit the source compression). The joint study is thoroughly discussed in Chapter 4.

Let us consider i as the index of the sensor under analysis, the transmitted signal of which is to be detected. Additionally, to represent actual communication from sensor i perspective, we assume that this sensor is active, i.e., its activity variable β_i will be set to one.

With the above considerations, the SINR corresponding to the received signal at the CN for sensor i when it is transmitting is given by expression (2.10):

$$\rho_i = \frac{a_{i,i}}{\sigma^2_{w,i} + \Gamma_i}, \tag{3.1}$$

where we have omitted the super-index *NOMA, sporadic* to ease of notation, and $a_{i,i} \triangleq P_i |h_{i,i}|^2$ is used to denote the received power of the signal from sensor i. Accordingly, the second subindex indicates the detector in charge of detecting the signal from sensor i. In fact, $h_{i,i}$ is the effective channel and $\sigma^2_{w,i}$ (equivalent to $N_o B_i$ in (2.10)) is the power of the AWGN noise, both at the detector of sensor i. Finally, the term Γ_i represents the aggregate interference:

$$\Gamma_i \triangleq \sum_{j \in \mathcal{J}_i} \beta_j a_{j,i}, \tag{3.2}$$

where $\mathcal{J}_i$ is the set of interfering devices, i.e., those sharing resources with sensor i, and $a_{j,i} \triangleq P_i |h_{j,i}|^2$ is the received power of the signal coming from sensor j at the detector of sensor i.

The distribution of the aggregate interference Γ_i can be obtained through discrete convolutions given that all the individual addends $\beta_j a_{j,i}$ are binary and independent [73]. However, such an operation can be tedious since the complexity depends on the number of interfering devices $|\mathcal{J}_i|$ and grows exponentially with this magnitude. Hence, it becomes rapidly unfeasible, albeit with a small $|\mathcal{J}_i|$. Even if a Monte-Carlo-based numerical approach is always available, it would still carry a large computational complexity. That is why in the following, we propose three different and reasonable alternatives to express the previous statistics using analytic closed-form approximations. Additionally, thanks to having these expressions, and not only numerical ones, an optimization of the RA can be carried out, as shown below.

3.3 Approximations of the Aggregate Interference Statistics

The purpose of this section is to provide an analytic closed-form expression approximating the PMF of the aggregate interference Γ_i, i.e., $p_{\Gamma_i}(\gamma_i)$. To this end, we propose three alternatives. The first one is based on the characteristic function (CF) of Γ_i, the second one makes use of the Chernoff upper bound, whereas the third one relies on the Gram-Charlier series expansion of a Gaussian kernel. The latter is employed in Section 3.4 to derive an analytic closed-form expression for the outage probability, which is later optimized in Section 3.5.

Note that the approximations for the statistics of the aggregate interference that we develop in this section can be used in many different applications. Some illustrative examples are:

- *Outage Probability*: Thanks to the approximation of the interference statistics, we can find an analytic closed-form expression for the outage probability. Based on that, and considering a communication scheme with a limited number of resources, a RA strategy can be designed to minimize this magnitude and, accordingly, improve the system performance.

- *Throughput*: The approximated statistics of the aggregate interference can also be useful to obtain an analytic closed-form expression for the throughput of the sensors. This is indeed related to the outage probability, yet it represents a different communication metric.
- *Harvested Energy*: Given the large number of active devices in mMTC, the energy coming from the transmitted signals can be recycled (i.e., harvested). Then, the derived statistics could be employed to characterize the amount of harvested energy.
- *Power Consumption*: Taking into account the number of retransmissions (e.g., due to a high outage probability) and the different energy supplies (e.g., harvested energy), a power consumption model of the sensors could be derived to study and optimize the management of available energy within the network.

As already mentioned, these are only a few examples of possible uses of the approximations of the interference statistics that are developed in this section. In particular, in this chapter, we concentrate on the first application, which is first discussed in Section 3.4 (outage probability) and then in Section 3.5 (resource allocation). Besides, although not presented in this dissertation, the throughput analysis is considered in [73] (equivalent to [C1]), whereas the rest of the use cases are studied in the upcoming chapters.

3.3.1 Characteristic Function

To obtain the PMF of Γ_i, we can use the CF. For any $X \sim$ *Ber*(p), its CF reads as

$$\varphi_X(t) \triangleq \mathbb{E}[e^{\mathrm{i}tX}] = 1 - p + pe^{\mathrm{i}t}, \tag{3.3}$$

where i denotes the imaginary unit or square root of -1 (not to be confused with the sensor's index i) and $e^x \equiv \exp(x)$ refers to the exponential function (used here for a better readability). Thereby, when introducing the weights $a_{j,i}$ with the RVs β_j, the total CF of Γ_i results

$$\varphi_{\Gamma_i}(t) = \prod_{j \in \mathcal{J}_i} (1 - p_j + p_j e^{\mathrm{i}ta_{j,i}}), \tag{3.4}$$

assuming independence among individuals. Since this can be interpreted as the Fourier transform of the PMF (with opposite sign), we can just invert this transformation to obtain the PMF:

$$p_{\Gamma_i}(\gamma_i) = \mathcal{F}^{-1}\{\varphi_{\Gamma_i}(t)\} = \frac{1}{2\pi} \int_{2\pi} \varphi_{\Gamma_i}(t) e^{-\mathrm{i}t\gamma_i} dt. \tag{3.5}$$

This way, we go from a set of convolutions to simple products and the inverse Fourier transform, which can be calculated numerically with the inverse fast Fourier transform (IFFT). The number of operations is significantly reduced and, given that the number of points used in the IFFT for the discretization of the continuous inverse Fourier transform is actually limited, an approximation of the PMF can now be obtained. In fact, note that the number of necessary points for good precision in the IFFT increases with the number of interfering devices $|\mathcal{J}_i|$. This translates into a high computational cost, yet bearable in finite time. As a result, assuming that enough points are used in the IFFT routine, this method is only used as a reference to validate the accuracy of the next alternatives.

3.3.2 Chernoff Upper Bound

Another way to find a suitable and more computationally efficient expression for the PMF of Γ_i is by means of a continuous approximation. To that end, in this subsection, we use the Chernoff bound to derive a probability density function (PDF) $f_{\Gamma_i}(\gamma_i)$ approximating the PMF $p_{\Gamma_i}(\gamma_i)$.

Following the reasoning in [74], we first find the cumulative distribution function (CDF), denoted by $F_{\Gamma_i}(\gamma_i) \triangleq \Pr\{\Gamma_i \leq \gamma_i\}$, and later obtain the corresponding PDF by differentiation. Nevertheless, note that the Chernoff upper bound is not directly applied to the CDF, yet to the complementary CDF (CCDF), defined as $\bar{F}_{\Gamma_i}(\gamma_i) \triangleq \Pr\{\Gamma_i > \gamma_i\} = 1 - F_{\Gamma_i}(\gamma_i)$.

Let us start then by applying Markov's inequality [75] to the function $e^{t\Gamma_i}$ for all $t > 0$:

$$\bar{F}_{\Gamma_i}(\gamma_i) = \Pr\{e^{t\Gamma_i} > e^{t\gamma_i}\} < e^{-t\gamma_i}\mathbb{E}[e^{t\Gamma_i}]. \tag{3.6}$$

Since all β_j are independent, we have

$$e^{-t\gamma_i}\mathbb{E}[e^{t\Gamma_i}] = e^{-t\gamma_i}\prod_{j\in\mathcal{J}_i}\mathbb{E}[e^{t\beta_j a_{j,i}}] = e^{-t\gamma_i}\prod_{j\in\mathcal{J}_i}[p_j e^{t a_{j,i}} + (1-p_j)]. \tag{3.7}$$

By setting $t \triangleq \ln(1+\delta)$ with $\delta > 0$ (later defined), the previous expression yields

$$(1+\delta)^{-\gamma_i}\prod_{j\in\mathcal{J}_i}[p_j(1+\delta)^{a_{j,i}} + (1-p_j)] \leq (1+\delta)^{-\gamma_i}\prod_{j\in\mathcal{J}_i} e^{p_j[(1+\delta)^{a_{j,i}}-1]}, \tag{3.8}$$

which follows from the exponential inequality $x + 1 \leq e^x$ [75].

For $a_{j,i} \in (0,1]$ we have $(1+\delta)^{a_{j,i}} - 1 \leq \delta a_{j,i}$ and, consequently,

$$\bar{F}_{\Gamma_i}(\gamma_i) \leq (1+\delta)^{-\gamma_i} e^{\sum_{j\in\mathcal{J}_i}\delta a_{j,i} p_j} = (1+\delta)^{-\gamma_i} e^{\delta\mu_i}, \tag{3.9}$$

where μ_i is the statistical mean of Γ_i, i.e.,

$$\mu_i \triangleq \mathbb{E}[\Gamma_i] = \sum_{j\in\mathcal{J}_i} p_j a_{j,i}. \tag{3.10}$$

For the choice of δ, a reasonable option could be the first moment μ_i as it is strictly positive ($a_j > 0$) and captures the basic statistics of Γ_i. Accordingly, the upper bound on the CDF yields

$$F_{\Gamma_i}(\gamma_i) \geq 1 - e^{\mu_i^2}(1+\mu_i)^{-\gamma_i} \triangleq \tilde{F}_{\Gamma_i}(\gamma_i). \tag{3.11}$$

Finally, the approximating PDF $f_{\Gamma_i}(\gamma_i)$ is obtained by differentiation of the previous bound of the CDF, i.e., $\tilde{F}_{\Gamma_i}(\gamma_i)$, where the resulting derivative is conveniently scaled with a factor C_i to ensure $f_{\Gamma_i}(\gamma_i)$ has a unit area. Thereby, this PDF can be expressed as

$$p_{\Gamma_i}(\gamma_i) \approx f_{\Gamma_i}(\gamma_i) = C_i\frac{\partial\tilde{F}_{\Gamma_i}(\gamma_i)}{\partial\gamma_i} = C_i e^{\mu_i^2}(1+\mu_i)^{-\gamma_i}\ln(1+\mu_i). \tag{3.12}$$

Note that the previous approach only holds when all received powers $a_{j,i}$ are normalized so that the maximum value is not higher than 1, i.e., $a_{j,i} \rightarrow \frac{a_{j,i}}{\max_j a_{j,i}}\ \forall j$. This scaling factor will affect the support of the PDF, but not its shape (the probabilities remain unaltered).

3.3.3 Gram-Charlier Series Expansion

The third proposal relies on the Gram-Charlier series expansion of a Gaussian kernel [76]:

$$p_{\Gamma_i}(\gamma_i) = \phi(\gamma_i; \mu_i, \sigma_i) \sum_{l=0}^{\infty} \frac{1}{l!\sigma_i^l} E_l(0, 0, \kappa_3^i, \ldots, \kappa_l^i) H_l(\bar{\gamma}_i), \tag{3.13}$$

where $\phi(\gamma_i; \mu_i, \sigma_i)$ is the PDF of the Gaussian distribution with mean μ_i and standard deviation σ_i, and κ_l^i, E_l, and H_l are the l-th cumulant of Γ_i, Bell, and Hermite polynomials, respectively [77]. The term $\bar{\gamma}_i \triangleq (\gamma_i - \mu_i)/\sigma_i$ represents the normalized argument.

Unlike before, this approach allows the approximation of a distribution through several of its statistical moments (not just its average value μ_i). Given that these magnitudes can be easily determined for Γ_i, this inference method represents a good alternative for approximating the PMF. Recall that the first-order moment is already given in (3.11) and, due to the independence between β_j, the second one reads as

$$\sigma_i^2 \triangleq \mathrm{Var}[\Gamma_i] = \sum_{j \in \mathcal{J}_i} p_j (1 - p_j) a_{j,i}^2. \tag{3.14}$$

The expression in (3.13) leads to a perfect approximation for infinite addends as it converges to the actual distribution [76]. Since adding more terms reduces the error in the approximation, we truncate the series up to a finite number of addends to work with a tractable expression. The resulting accuracy is further discussed in the simulations section.

As a result, similar to the work described in [56], here we obtain an expression based on the cumulants of the aggregate interference, which can be found recursively in terms of the first l-th non-centralized order moments $\mu'_{i,l} \triangleq \mathbb{E}\left[\Gamma_i^l\right] = \sum_{j \in \mathcal{J}_i} p_j a_{j,i}^l$ [78]:

$$\kappa_l^i = \mu'_{i,l} - \sum_{m=1}^{l-1} \binom{l-1}{m-1} \kappa_m^i \mu'_{i,l-m}. \tag{3.15}$$

It is noteworthy to mention that other kernels can also be employed for the expansion. The reason for choosing the Gaussian case follows from the proof of Lyapunov's central limit theorem (CLT), which states that Γ_i converges to a Gaussian distribution[2] when the number of addends l is very high (true for mMTC networks [12]), and these addends are independent but not necessarily equally distributed. This is precisely the case of our scenario, where we assume that the added RVs $a_{j,i}\beta_j$ are independent and, since they correspond to terminals located at different distances from the CN, they are not equally distributed.

The previous claim is true as long as the following condition is fulfilled [79]:

$$\lim_{|\mathcal{J}_i| \to \infty} \frac{1}{\sigma_i^{2+\epsilon}} \sum_{j \in \mathcal{J}_i} \mathbb{E}\left[|a_{j,i}\beta_j - a_{j,i}p_j|^{2+\epsilon}\right] = 0, \tag{3.16}$$

for some $\epsilon > 0$. As shown in Appendix 3.A, (3.16) is satisfied for equal p_j not close to zero and a large number of interfering devices $|\mathcal{J}_i|$. In that case, the Gaussian kernel with $l = 0$ suffices.

---

[2] Note that the Gaussian distribution is a particular case of the Gram-Charlier series expansion defined in (3.13) when the number of addends l is limited to 0 (cf. [73]).

However, as here the probabilities are different and can be small, the simple Gaussian distribution may not be enough for good accuracy. That is why we propose an extension of that approach, i.e., an expansion of a Gaussian kernel with l higher than 0.

Up to now, we have assumed that the PMF of Γ_i has infinite support. It is actually lower and upper bounded by 0 and $J_i \triangleq \sum_{j\in\mathcal{J}_i} a_{j,i}$, respectively. These are the extreme possible values for the aggregate interference. Hence, for analytic consistency, we must use a truncated Gaussian kernel with unit area [80]. The same applies in the case of the Chernoff bound, where we also need to normalize the expression in (3.12) by its area within the limits 0 and J_i.

Let $X \sim \mathcal{N}(\mu, \sigma^2)$ be a Gaussian RV defined between a and b with PDF

$$f_X(x;\mu,\sigma,a,b) \triangleq \frac{\phi_s(\frac{x-\mu}{\sigma})}{\sigma\left(\Phi_s(\frac{b-\mu}{\sigma}) - \Phi_s(\frac{a-\mu}{\sigma})\right)} = \frac{1}{\sigma Z}\phi_s\left(\frac{x-\mu}{\sigma}\right) = \frac{1}{Z}\phi(x;\mu,\sigma), \tag{3.17}$$

in the interval $a \leq x \leq b$ and 0 otherwise. The term Z represents the normalization factor used to achieve unit area, i.e., $Z \triangleq \Phi_s(\frac{b-\mu}{\sigma}) - \Phi_s(\frac{a-\mu}{\sigma})$. Note that $\phi_s(\cdot) \equiv \phi(\cdot, 0, 1)$ refers to the PDF of the standard Gaussian RV and $\Phi_s(\cdot)$ is the corresponding CDF.

In our case, by defining $Z_i \triangleq \Phi_s(\frac{J_i-\mu_i}{\sigma_i}) - \Phi_s(\frac{0-\mu_i}{\sigma_i})$, we have that the new kernel reads as

$$f_{\Gamma_i}(\gamma_i;\mu_i,\sigma_i,0,J_i) = \frac{1}{Z_i}\phi(\gamma_i;\mu_i,\sigma_i), \tag{3.18}$$

for $0 \leq \gamma_i \leq J_i$. Thereby, it can be shown that a similar expansion can be found for a finite support. We only need to introduce the cumulants of the truncated Gaussian distribution since they are no longer zero for l higher than 2 and the first two do not equal κ_1^i and κ_2^i, i.e.,

$$p_{\Gamma_i}(\gamma_i) = \frac{1}{Z_i}\phi(\gamma_i;\mu_i,\sigma_i)\sum_{l=0}^{\infty}\frac{1}{l!\sigma_i^l}E_l(\eta_1^i,\ldots,\eta_l^i)H_l(\bar{\gamma}_i), \tag{3.19}$$

where we define $\eta_l^i \triangleq \kappa_l^i - \lambda_l^i$ with λ_l^i the cumulants of the new truncated kernel. As mentioned, they are related to the non-centralized moments, which can be obtained in an analytic closed-form manner [80]. In particular, for a general $X \sim \mathcal{N}(\mu, \sigma^2)$ with support $[a, b]$, we have

$$\mu_l' = \sum_{i=0}^{l}\binom{l}{i}\sigma^i\mu^{l-i}L_i, \tag{3.20}$$

where $L_i \triangleq (\bar{x}^{i-1}\phi_s(\bar{x}) - \bar{y}^{i-1}\phi_s(\bar{y}))/Z + (i-1)L_{i-2}$, $\bar{x} \triangleq (x-\mu)/\sigma$, $\bar{y} \triangleq (y-\mu)/\sigma$ and $L_0 = 1$.

Finally, when truncating the series up to order O_i, we obtain the continuous approximation for the PMF of the aggregate interference, denoted by $f_{\Gamma_i}^{O_i}(\gamma_i)$:

$$p_{\Gamma_i}(\gamma_i) \approx f_{\Gamma_i}^{O_i}(\gamma_i) \triangleq \frac{1}{Z_i}\phi(\gamma_i;\mu_i,\sigma_i)\sum_{l=0}^{O_i}\frac{1}{l!\sigma_i^l}E_l(\eta_1^i,\ldots,\eta_l^i)H_l(\bar{\gamma}_i). \tag{3.21}$$

For instance, considering $O_i = 5$, we have

$$f_{\Gamma_i}^{5}(\gamma_i) = \frac{1}{Z_i}\nu_i(\bar{\gamma}_i)\phi(\gamma_i;\mu_i,\sigma_i), \tag{3.22}$$

where

$$\nu_i(\bar{\gamma}_i) = 1 + \frac{\eta_1^i}{\sigma_i} H_1(\bar{\gamma}_i) + \frac{\eta_2^i}{2\sigma_i^2} H_2(\bar{\gamma}_i) + \frac{\eta_3^i}{6\sigma_i^3} H_3(\bar{\gamma}_i) + \frac{\eta_4^i}{24\sigma_i^4} H_4(\bar{\gamma}_i) + \frac{\eta_5^i}{120\sigma_i^5} H_5(\bar{\gamma}_i). \tag{3.23}$$

In the next section, this approximation is used to express the outage probability of the sensors (i.e., the probability of the SINR being below a certain predefined threshold).

3.4 Outage Probability

This section is devoted to presenting an analytic closed-form expression for the outage probability taking into account the massive UL communication in mMTC systems. This figure of merit represents the probability that the receiver is unable to decode the transmitted message and can also be interpreted as the portion of time during which the communication fails. Thereby, this magnitude can be used as a valuable performance indicator in these kinds of systems (cf. [60]). As stressed in the introduction, lower values of the outage probability yield less retransmissions and, thus, a lower power consumption and lower delays. That is why in Section 3.5, for better performance, we aim to find an allocation that minimizes this metric.

Recall that the usage of the outage probability is valid for continuous communications (cf. Section 2.2), which is the case we consider in this section. This probability is already defined in (2.3), i.e., $P_{\text{out}}^i = \Pr\{\rho_i < \delta_i\}$. Accordingly, we will be in outage whenever the quality of the communication is not good enough for correct decoding. This may happen in cases of large interference, either due to high channel gains, and/or high activities of non-intended sources (represented by the set of interfering sensors $\mathcal{J}_i$).

As mentioned above, we use the Gram-Charlier approximation derived in Subsection 3.3.3 to find an analytic closed-form expression for P_{out}^i. Since this magnitude may be reduced when mitigating the interference, we consider a scenario with a set of multiple-antenna access nodes (ANs), each one equipped with a set of predefined spatial beams. This way, we can help the CN to overcome the problem of massive access and obtain reasonable outage values.

For the sake of clarity in the explanation, we start our analysis from a simple setup, and we then sophisticate it towards the more generalized multiple-antenna ANs scenario. Note that each scenario is a particular case of the following one, but we decide to present the setups in this constructive way to avoid any possible confusion in the description of the notation and the developments. Therefore, all previous setups are particular cases of the last scenario. In that sense, although at each step we characterize the system model, the expression of P_{out}^i is only presented for the general case in order to avoid redundancy.

3.4.1 Single-Antenna CN

Let us consider a single-antenna CN collecting the information from the set of M transmitting single-antenna sensors using the same access resources. In that case, the received signal is

$$z \triangleq \sum_{j=1}^{M} g_j \beta_j x_j + \omega \in \mathbb{C}, \tag{3.24}$$

where $g_j \in \mathbb{C}$ is the channel of sensor j, x_j is the transmit signal with zero mean and power P_j, independent for each sensor, and $\omega \sim \mathcal{CN}(0, \sigma_\omega^2)$ is the AWGN, independent of x_j.

Since no further processing is performed at the CN, the effective channels h_i will be directly g_i. Also, given that all sensors share the same resources, the interfering set results $\mathcal{J}_i = \{j \neq i\}$. Finally, note that the noise at the detection stage is the same for all sensors, i.e., $\sigma_{w,i}^2 = \sigma_\omega^2 \; \forall i$.

3.4.2 Multiple-Antenna CN

To reduce the interference coming from the rest of the sensors, we now consider that the CN is equipped with L antennas. As a result, the received signal can be expressed as follows:

$$\boldsymbol{y} \triangleq \boldsymbol{G}\boldsymbol{\beta}\boldsymbol{x} + \boldsymbol{\omega} \in \mathbb{C}^L, \tag{3.25}$$

where $\boldsymbol{x} = [x_1, \ldots, x_M]^\mathrm{T} \in \mathbb{C}^M$ is the vector containing the (independent) transmit signals x_j, $\boldsymbol{\omega} \sim \mathcal{CN}(\mathbf{0}_L, \sigma_\omega^2 \mathbf{I}_L)$ is the corresponding noise vector, $\boldsymbol{G} = [\boldsymbol{g}_1, \ldots, \boldsymbol{g}_M] \in \mathbb{C}^{L\times M}$ is the matrix containing the set of individual channels $\boldsymbol{g}_j$ of each sensor with respect to (w.r.t.) the CN, and $\boldsymbol{\beta} \triangleq \mathrm{diag}(\beta_1, \ldots, \beta_M)$ is the matrix containing the different RVs β_j of all sensors.

Given the degrees of freedom provided by the multiple-antenna technology, linear processing is used in this setup. Now the CN has S predefined spatial beams implemented through a spatial filter represented by matrix $\boldsymbol{F} = [\boldsymbol{f}_1, \ldots, \boldsymbol{f}_S] \in \mathbb{C}^{L\times S}$. A possible design option is to construct the different beams so that their pointing directions are equispaced. However, for the sake of generality, we keep the filtering scheme generic and represented by $\boldsymbol{F}$.

The signal coming from each sensor is then detected at the output of a given spatial beam. The S outputs at the S beams can be collected in a single vector given by

$$\boldsymbol{z} \triangleq \boldsymbol{F}^\mathrm{H}\boldsymbol{y} = \boldsymbol{F}^\mathrm{H}\boldsymbol{G}\boldsymbol{\beta}\boldsymbol{x} + \boldsymbol{w} \in \mathbb{C}^S, \tag{3.26}$$

where $\boldsymbol{z} = [z_1, \ldots, z_S]^\mathrm{T}$ is the processed signal and $\boldsymbol{w} \triangleq \boldsymbol{F}^\mathrm{H}\boldsymbol{\omega} \in \mathbb{C}^S$ is the filtered noise.

For simplicity, we assume that the signal from a given sensor is decoded using the output signal of a single beam. To determine which is the detecting beam, a possible criterion can be to choose the one leading to the largest SNR at the output of the spatial beam. Intuitively, it represents the beam where the quality of the signal might be better (irrespective of the interference). Let $s(i)$ represent the index of the beam used to detect the signal from sensor i:

$$s(i) = \underset{s}{\mathrm{argmax}} \; \frac{|\boldsymbol{f}_s^\mathrm{H}\boldsymbol{g}_i|^2}{\sigma_\omega^2 \|\boldsymbol{f}_s\|_2^2}. \tag{3.27}$$

Accordingly, we denote $\boldsymbol{f}_{s(i)}$ as the spatial filter employed for the detection of sensor i. If a different beam selection strategy is employed, we would have a different expression for $s(i)$. For the sake of generality, from now on we just use $s(i)$; hence, the upcoming analysis holds regardless of the beam selection criterion.

This way, the effective channels are given by $h_{i,i} = \boldsymbol{f}_{s(i)}^\mathrm{H}\boldsymbol{g}_i$ and $h_{j,i} = \boldsymbol{f}_{s(i)}^\mathrm{H}\boldsymbol{g}_j$, where the second sub-index is used to indicate where the sensor is actually detected, i.e., at beam $s(i)$. In addition, assuming there is still a complete reuse of resources, the interfering set is again $\mathcal{J}_i = \{j \neq i\}$. Besides, the power of the noise affecting sensor i is given by $\sigma_{w,i}^2 = \sigma_\omega^2 \|\boldsymbol{f}_{s(i)}\|_2^2$.

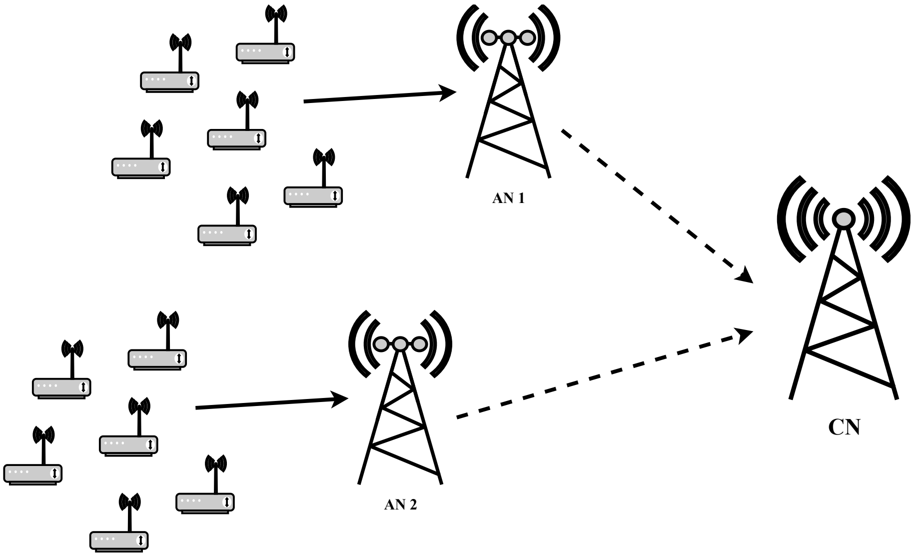

Figure 3.1: System setup for $K = 2$, $L = 3$ and $M_k = 6 \; \forall k$.

3.4.3 Multiple-Antenna ANs and CN

To further enhance the performance of the system, we now consider an extension of the previous setup with K data ANs, all equipped with L antennas. Each of them is responsible for collecting the information from a subset (cluster) of M_k single-antenna sensors for later retransmitting it to a CN, with $M = \sum_{k=1}^{K} M_k$. Thereby, we have a two-hop communication system, as illustrated in Figure 3.1. Such a multi-hop scheme is largely exploited in the literature [69, 71] and in standards such as LTE-M [81, 82]. In this chapter, we focus on the communication in the first hop (solid line) and leave the second stage (dashed line) for further studies.

Each AN has S predefined spatial beams, represented with the spatial filter matrix $\boldsymbol{F}_k = [\boldsymbol{f}_{k,1}, \ldots, \boldsymbol{f}_{k,S}] \in \mathbb{C}^{L \times S}$, with $k \in \{1, \ldots, K\}$. Accordingly, now the signal coming from each sensor is detected at the output of a given spatial beam of a given AN, i.e., at a given AN-beam pair or tuple. In addition to that, we also assume that there is no cooperation among beams and no cooperation among ANs during the signal detection stage.

The signal received at AN k can be written as

$$\boldsymbol{y}_k \triangleq \boldsymbol{G}_k \boldsymbol{\beta} \boldsymbol{x} + \boldsymbol{\omega}_k \in \mathbb{C}^L, \tag{3.28}$$

where $\boldsymbol{\omega}_k \sim \mathcal{CN}(\mathbf{0}_L, \sigma_\omega^2 \mathbf{I}_L)$ is the noise vector and $\boldsymbol{G}_k = [\boldsymbol{g}_{k,1}, \ldots, \boldsymbol{g}_{k,M}] \in \mathbb{C}^{L \times M}$ is the matrix containing the channels of each sensor w.r.t. each AN (i.e., $\boldsymbol{g}_{k,i}$ is the channel between sensor i and AN k). Again, $\boldsymbol{x} \in \mathbb{C}^M$ is the vector of (independent) transmit signals with zero mean and powers P_j, independent of $\boldsymbol{\omega}_k$, and $\boldsymbol{\beta}$ is the matrix of RVs β_j.

The S outputs at the S beams of AN k can be collected in a single vector given by

$$\boldsymbol{z}_k \triangleq \boldsymbol{F}_k^{\mathrm{H}} \boldsymbol{y}_k = \boldsymbol{F}_k^{\mathrm{H}} \boldsymbol{G}_k \boldsymbol{\beta} \boldsymbol{x} + \boldsymbol{w}_k \in \mathbb{C}^S, \tag{3.29}$$

with $\boldsymbol{z}_k = [z_{k,1}, \ldots, z_{k,S}]^{\mathrm{T}}$ the processed signal at AN k and $\boldsymbol{w}_k \triangleq \boldsymbol{F}_k^{\mathrm{H}} \boldsymbol{\omega}_k \in \mathbb{C}^S$ the filtered noise. The channels and filters are specified in Section 3.6 for an exemplifying scenario.

Similar to above, for each sensor, we focus on the detection at the AN-beam pair leading to the largest SNR after the spatial filter. Recall that other criteria to choose the detecting pair could be used. Let now $k(i)$ and $s(i)$ represent the indexes of the AN and beam, respectively, used to detect the signal coming from sensor i using the previous criterion:

$$(k(i), s(i)) = \underset{(k,s)}{\operatorname{argmax}} \frac{|\boldsymbol{f}_{k,s}^{\mathrm{H}} \boldsymbol{g}_{k,i}|^2}{\sigma_\omega^2 \|\boldsymbol{f}_{k,s}\|_2^2}. \tag{3.30}$$

Hence, $\boldsymbol{f}_{k(i),s(i)}$ will represent the spatial filter used for the detection of sensor i. In addition, here the noise power is given by $\sigma_{w,i}^2 = \sigma_\omega^2 \|\boldsymbol{f}_{k(i),s(i)}\|_2^2$.

Note that, until now, we have considered that all sensors use the same orthogonal resource, thus, creating total interference among them. Nevertheless, in real systems, more than one resource is usually available. That is why we consider that we dispose of Q orthogonal resources with indexes $\{1, \ldots, Q\}$, and that they are allocated to the different AN-beam tuples.

In that sense, the sensor that is detected at a certain AN-beam pair will use the resources allocated to that tuple. For the moment, we consider that sensors know which resources they can employ, and we ignore the way this information is acquired. An example of a mechanism that provides this knowledge at the sensors' side is described in Section 3.6.

Moreover, we distinguish between the case where only one resource is allocated to each AN-beam pair and the case where these tuples can use more than one. They are referred to as single resource (SR) and multiple resource (MR), respectively. In the latter, each sensor chooses one of the resources available for their pair, defined in (3.30), at random. In both setups, resources are allocated to reduce the impact of the interference, as discussed in Section 3.5.

With the above considerations, and assuming $\beta_i = 1$, the received signal from sensor i at tuple $(k(i), s(i))$ can be written as (cf. (3.29))

$$z^{(i)} \triangleq \boldsymbol{f}_{k(i),s(i)}^{\mathrm{H}} \boldsymbol{g}_{k(i),i} x_i + I_i + w^{(i)} \in \mathbb{C}, \tag{3.31}$$

where $z^{(i)} \equiv z_{k(i),s(i)}$ is the received signal, $\boldsymbol{f}_{k(i),s(i)}$ and $\boldsymbol{g}_{k(i),i}$ are the filter and channel of sensor i, respectively, and $w^{(i)} \triangleq \boldsymbol{f}_{k(i),s(i)}^{\mathrm{H}} \boldsymbol{w}_{k(i)} \in \mathbb{C}$ is the noise at that tuple, with power $\sigma_{w,i}^2$.

Each of the $z^{(i)}$ signals experiences an interference I_i coming from the sensors that transmit through the same orthogonal resources. This interference can be decomposed into what follows: (i) the interference coming from the sensors to be detected at the same beam and AN, namely, intra-beam I_i^{intra}, and (ii) the interference coming from the sensors to be detected at the rest of the beams and ANs that share the same resources, namely, inter-beam I_i^{inter}, i.e.,

$$I_i \triangleq \underbrace{\sum_{j \in \mathcal{I}_{k(i),s(i)} \setminus \{i\}} \boldsymbol{f}_{k(i),s(i)}^{\mathrm{H}} \boldsymbol{g}_{k(i),j} \beta_j x_j}_{\triangleq I_i^{\text{intra}}} + \underbrace{\sum_{\substack{(k,s) \neq (k(i),s(i)) \\ t_i \in \mathcal{T}_{k,s}}} \sum_{j \in \mathcal{I}_{k,s}} \boldsymbol{f}_{k(i),s(i)}^{\mathrm{H}} \boldsymbol{g}_{k(i),j} \beta_j x_j}_{\triangleq I_i^{\text{inter}}}. \tag{3.32}$$

The set $\mathcal{I}_{k,s}$ represents all sensors detected at the AN-beam pair (k, s), i.e.,

$$\mathcal{I}_{k,s} \triangleq \{j : (k(j), s(j)) = (k, s)\}. \tag{3.33}$$

To be consistent, we need to extract the signal from sensor i from the set $\mathcal{I}_{k(i),s(i)}$, as shown in (3.32). The term $t_i \in \{1, \dots, Q\}$ in (3.32) denotes the identifier of the resource used by sensor i, and the set $\mathcal{T}_{k,s}$ contains the resources allocated to the AN-beam pair (k, s).

Overall, the aggregate interference Γ_i from (3.2) is decomposed as follows:

$$\Gamma_i = \underbrace{\sum_{j \in \mathcal{I}_{k(i),s(i)} \backslash \{i\}} \beta_j a_{j,i}}_{\triangleq \Gamma_i^{\text{intra}}} + \underbrace{\sum_{\substack{(k,s) \neq (k(i),s(i)) \\ t_i \in \mathcal{T}_{k,s}}} \sum_{j \in \mathcal{I}_{k,s}} \beta_j a_{j,i}}_{\triangleq \Gamma_i^{\text{inter}}}, \tag{3.34}$$

where the effective channels corresponding to the received powers $a_{i,i}$ and $a_{j,i}$ are given by $h_{i,i} = \boldsymbol{f}^{\mathrm{H}}_{k(i),s(i)} \boldsymbol{g}_{k(i),i}$ and $h_{j,i} = \boldsymbol{f}^{\mathrm{H}}_{k(i),s(i)} \boldsymbol{g}_{k(i),j}$, respectively.

As a result, now the interfering set $\mathcal{J}_i$ yields

$$\mathcal{J}_i = \underbrace{\mathcal{I}_{k(i),s(i)} \backslash \{i\}}_{\triangleq \mathcal{J}_i^{\text{intra}}} + \underbrace{\bigcup_{\substack{(s,j) \neq (k(i),s(i)) \\ t_i \in \mathcal{T}_{k,s}}} \mathcal{I}_{k,s}}_{\triangleq \mathcal{J}_i^{\text{inter}}}\,. \tag{3.35}$$

Based on that, we now particularize the outage probability P^i_{out} from (3.16) for the SR and MR scenarios. This is done in the following.

3.4.3.1 Single-Resource Scenario

In this case, only a single resource is allowed per AN-beam tuple. This means that the resource sets $\mathcal{T}_{k,s}$ contain one element and sensor i only uses a certain resource t_i, which constitutes the set $\mathcal{T}_{k(i),s(i)}$, i.e., $\mathcal{T}_{k(i),s(i)} = \{t_i\}$. Thus, sensors detected at tuples (k, s) with that resource, i.e., $\mathcal{T}_{k,s} = \{t_i\}$, create interference when detecting the signal from sensor i (cf. (3.35)).

As a result, P^i_{out} from (3.16) is completely defined by the PMF of the aggregate interference Γ_i, regardless of resource t_i, which only determines the interfering set:

$$P^i_{\text{out}} = \Pr\{\Gamma_i > \xi_i - \sigma^2_{w,i}\} = \sum_{\gamma_i > \xi_i - \sigma^2_{w,i}} p_{\Gamma_i}(\gamma_i), \tag{3.36}$$

where $\xi_i \triangleq a_{i,i}/\delta$ is used for the sake of brevity in the notation.

Note that, using the CF method, a numerical approximation of P^i_{out} can be found. However, we use the continuous approximation $f^{O_i}_{\Gamma_i}(\gamma_i)$ of the PMF $p_{\Gamma_i}(\gamma_i)$ to express the outage probability from (3.16) in an analytic closed-form, i.e.,

$$P^i_{\text{out}} = \sum_{\gamma_i > \xi_i - \sigma^2_{w,i}} p_{\Gamma_i}(\gamma_i) \approx \int_{\xi_i - \sigma^2_{w,i}}^{J_i} f^{O_i}_{\Gamma_i}(\gamma_i) d\gamma_i. \tag{3.37}$$

For instance, using $f^5_{\Gamma_i}(\gamma_i)$ from (3.14), the approximation in (3.37) yields

$$P^i_{\text{out}} \approx \frac{1}{Z_i} \int_{\xi_i - \sigma^2_{w,i}}^{J_i} \nu_i(\bar{\gamma}_i) \phi(\gamma_i; \mu_i, \sigma_i) d\gamma_i = \frac{1}{Z_i} \sum_{l=0}^{5} A_l \int_{\xi_i - \sigma^2_{w,i}}^{J_i} \bar{\gamma}_i^l \phi_s(\bar{\gamma}_i) d\bar{\gamma}_i = \frac{1}{Z_i} \sum_{l=0}^{5} A^i_l G^i_l, \tag{3.38}$$

Table 3.1: A_l^i terms used in (3.38), listed from $l = 0$ to $l = 5$.

l	0	1	2	3	4	5
A_l^i	$1 - E_2^i + 3E_4^i$	$E_1^i - 3E_3^i + 15E_5^i$	$E_2^i - 6E_4^i$	$E_3^i - 10E_5^i$	E_4^i	E_5^i

where the integral terms G_l^i can be found via Owen's T function [83] and the terms A_l^i are listed in Table 3.1, where $E_l^i \triangleq E_l(\eta_1^i, \dots, \eta_l^i)/(l!\sigma_i^l)$ includes the set of Bell polynomials.

It is important to highlight that this approximation allows us to work directly with the statistical moments of the aggregate interference instead of the instantaneous power values $a_{j,i}$. In fact, the cumulants needed for the Gram-Charlier series expansion are also obtained with these statistical moments. Therefore, the outage probability defined in (3.37) is completely characterized by those parameters together with the received power $a_{i,i}$.

3.4.3.2 Multiple-Resource Scenario

The expression in (3.37) is valid only when a single resource is allowed per AN-beam tuple. However, when considering multiple resources can be allocated to each tuple, we need to generalize. Up to now, β_j has been a Bernoulli RV modeling the activity of sensor j. In the MR case, β_j is also a RV modeling the activity of sensor j when it is actually creating interference (cf. (3.35)). Accordingly, when $t_i \in \mathcal{T}_{k(j),s(j)}$, β_j can be decomposed as

$$\beta_j = \alpha_j \tau_j, \tag{3.39}$$

where $\alpha_j \sim$ *Ber*(p_j^{act}) represents the event of being active and transmitting. This RV depends only on the sensor itself and is equivalent to the RV in the SR setup. On the other hand, τ_j is a Bernoulli RV, independent of α_j, that is equal to 1 whenever sensor j selects randomly the same resource that is using sensor i, i.e., t_i. Then, in the cases where $t_i \in \mathcal{T}_{k(j),s(j)}$, we have $\tau_j \sim$ *Ber*(p_j^{res}), where $p_j^{\text{res}} = 1/|\mathcal{T}_{k(j),s(j)}|$ assuming that sensors choose one of the resources within $\mathcal{T}_{k(j),s(j)}$ with equal probability. Hence, τ_j depends on the number of possible resources that sensor j can equally choose, i.e., $1 \leq |\mathcal{T}_{k(j),s(j)}| \leq Q$, and, thus, on the tuple $(k(j), s(j))$ and the actual RA. The case $|\mathcal{T}_{k(j),s(j)}| = 0$ is not considered since it corresponds to the situation when no resources are allocated to the tuple $(k(j), s(j))$. Thereby, sensors detected at that pair are not included in the interfering set since $t_i \notin \mathcal{T}_{k(j),s(j)}$ in that case. Besides, all RVs τ_j are assumed to be independent, including those from sensors detected at the same AN-beam tuple and that share the same parameter $1/|\mathcal{T}_{k(j),s(j)}|$.

As a result, given that both Bernoulli RVs are independent, β_j is still a Bernoulli RV with parameter $p_j \triangleq \mathbb{E}[\beta_j] = p_j^{\text{act}} p_j^{\text{res}}$. In this case, p_j represents the probability of being active and also of transmitting through resource t_i within the set $\mathcal{T}_{k(j),s(j)}$. Thus, the use of multiple resources entails a reduction of sensors' activity which, in turn, reduces interference. In addition, note that, for the SR case, we only need to set $\tau_j = 1\,\forall j$ or, equivalently, $|\mathcal{T}_{k(j),s(j)}| = 1\,\forall j$. That is why the MR can be seen as a generalization of the SR setup.

Moreover, now interference may take place whenever there is non-null intersection between the resource sets, i.e., $\mathcal{T}_{k(i),s(i)} \cap \mathcal{T}_{k(j),s(j)} \neq \emptyset$. In fact, since $t_i \in \mathcal{T}_{k(i),s(i)}$ might no longer be unique, the interfering set $\mathcal{J}_i$ changes accordingly (cf. (3.35)). Let us denote this sets by $\mathcal{J}_i(t_i)$ to include the dependence with resource t_i. Therefore, although the expression of the SINR in (3.1) is still valid when resource t_i is used, we have $|\mathcal{T}_{k(i),s(i)}|$ different SINRs, one for each resource available for sensor i that is detected at the AN-beam tuple $(k(i), s(i))$.

Overall, since the reference sensor i decides equally among $|\mathcal{T}_{k(i),s(i)}|$ resources, we need to include this random selection in the outage probability. To that end, we average over the different possibilities, where resource t_i changes and so does the interfering set $\mathcal{J}_i(t_i)$:

$$P_{\text{out}}^{i} = p_i^{\text{res}} \sum_{t_i \in \mathcal{T}_{k(i),s(i)}} \sum_{\gamma_i(t_i) > \xi_i - \sigma_{w,i}^2} p_{\Gamma_i(t_i)}(\gamma_i(t_i)) = p_i^{\text{res}} \sum_{t_i \in \mathcal{T}_{k(i),s(i)}} P_{\text{out}}^{i}(t_i), \tag{3.40}$$

where now $\Gamma_i(t_i)$ also depends on the resource chosen by sensor i from the set of resources available at the AN-beam tuple $(k(i), s(i))$. Note that $P_{\text{out}}^{i}(t_i)$ is used to denote the outage probability when resource $t_i \in \mathcal{T}_{k(i),s(i)}$ is used and can be approximated using (3.37). Thus, we also end up with an analytic closed-form approximation for P_{out}^{i} formulated in (3.40).

The previous analysis is of special interest in the next section, where we formulate and describe a possible solution for the RA problem. This task consists in deciding which resources from the set $\{1, \ldots, Q\}$ are allocated to each AN-beam pair (k, s), which will ultimately define the resource sets $\mathcal{T}_{k,s}$. To do so, we use a graph-based approach that minimizes the average outage probability of all sensors within the network.

3.5 Resource Allocation

Once the outage probability has been defined, we can design a strategy based on this magnitude to allocate the available resources and enhance the performance of the mMTC network. For that task, in the following, we present a graph-based approach that relies on the previous approximation to minimize the outage probability P_{out}^{i}.

Note that the implementation of the proposed algorithm is possible thanks to the analytic closed-form expression of the outage probability found in the previous section (which relies on the statistical moments of the aggregate interference). In addition, a good performance of the resulting RA emphasizes the accuracy of the proposed Gram-Charlier approximation. Besides, given its relation to the sensors' transmit power, lower values of P_{out}^{i} result in better energy consumption, which is crucial in mMTC.

As mentioned earlier, we distinguish two scenarios: single resource and multiple resource. In both setups, we seek for RAs that minimize P_{out}^{i}. In particular, we adopt a strategy where the average network performance is optimized. However, any other approach could be used, e.g., a fair strategy where a minimum QoS is satisfied for all sensors.

For the sake of simplicity, in this chapter, we assume that the positions of the sensors are fixed and, hence, the AN-beam tuples where sensors are detected are known. Recall that they correspond to the pair with the highest received SNR according to (3.25). To represent these tuples, let us consider a CN equipped with a uniform circular array (UCA).

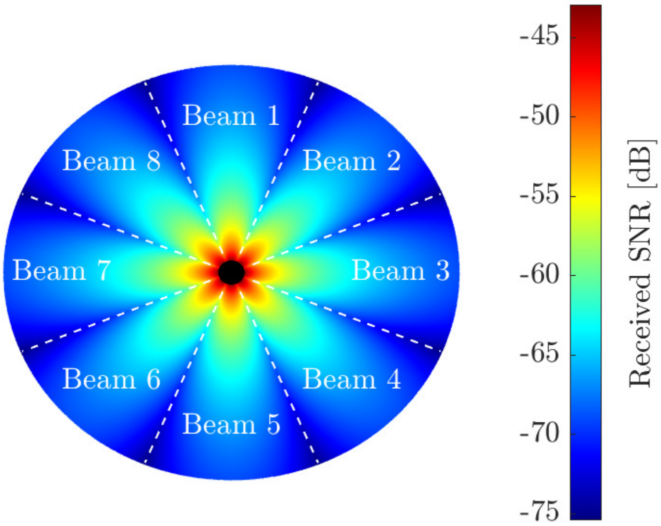

Figure 3.2: Received SNR and spatial beams. A minimum distance (black area) is set to avoid unrealistic high SNRs.

Note that this specific configuration is used here as an illustrative example, but any other structure could be used. Besides, to better understand the graphical representation, we assume channels to be the steering vectors computed with the angle of arrival (AoA) of the sensors' signals. Accordingly, a simple set of spatial beam filters is constructed with equispaced pointing directions. For a different array configuration and beamforming scheme, the shape of the beams (i.e., the radiation pattern) changes and so do the portions in which the whole space is divided. This is ultimately represented by the set of tuples and, thus, once they are defined, the following formulation is valid and the RA mechanism remains the same. In Figure 3.2, the received SNR at the beams of the CN is depicted for $L = S = 8$, unit transmit and noise powers, and a free-space path-loss model. Sensors are deployed uniformly in a circle of radius 100 m centered at the location of the CN.

3.5.1 Problem Formulation

Let us start by defining an allocation matrix $\boldsymbol{C} \in \mathbb{N}^{K\times S}$ containing the resources allocated to each AN-beam tuple. The rows and columns represent the ANs and beams, respectively, and each element $[\boldsymbol{C}]_{k,s}$ corresponds to the resources of the pair (k, s).

In the SR scenario, this matrix takes values within the set $\{0, \ldots, Q\}$, where the zero refers to the case where no resource is allocated. Recall that here the sets $\mathcal{T}_{k,s}$ have a unique element. Therefore, given that $\mathcal{T}_{k(i),s(i)} = \{t_i\}$, the element $[\boldsymbol{C}]_{k(i),s(i)}$ is directly t_i. As before, t_i represents the identifier of the resource that sensor i is employing.

We can relate the allocation matrix $\boldsymbol{C}$ to the interfering sets $\mathcal{J}_i$ in the following way:

$$\mathcal{J}_i = \{j : [\boldsymbol{C}]_{k(j),s(j)} = t_i\}\backslash\{i\}. \tag{3.41}$$

On the other hand, a different notation must be used in the MR scenario. Now, the sets $\mathcal{T}_{k,s}$ can have more than one element. To represent all possible combinations of resources, the elements in matrix $\boldsymbol{C}$ take values between 0 and $2^Q - 1$. Each element $[\boldsymbol{C}]_{k,s}$ corresponds to the decimal value of the binary vector $\boldsymbol{c}_{k,s} \in \{0,1\}^Q$, i.e.,

$$[\boldsymbol{C}]_{k,s} = \sum_{l=1}^{Q} 2^l [\boldsymbol{c}_{k,s}]_l. \tag{3.42}$$

Thereby, the specific resources allocated to the tuple (k,s) are indicated by the positions of the nonzero elements of the vector $\boldsymbol{c}_{k,s}$. For instance, for $Q = 6$ and $\boldsymbol{c}_{k,s} = [101001]$, the element $[\boldsymbol{C}]_{k,s}$ would be 37. In that case, we would use the first, third, and sixth resource, i.e., $\mathcal{T}_{k,s} = \{1,3,6\}$. Note that the all zero vector is also allowed, because the solution might switch off completely some AN-beam tuples by no allocating resources to them.

Regarding the interfering sets $\mathcal{J}_i$, we have

$$\mathcal{J}_i = \bigcup_{t_i \in \mathcal{T}_{k(i),s(i)}} \{j : [\boldsymbol{C}]_{k(j),s(j)} \in \mathcal{R}_{t_i}\} \backslash \{i\}, \tag{3.43}$$

where $\mathcal{R}_{t_i}$ contains all elements in the set $\{0,\ldots,2^Q - 1\}$ that include the usage of t_i, i.e.,

$$\mathcal{R}_{t_i} \triangleq \{q : q = \sum_{l=1}^{Q} 2^l [\boldsymbol{c}(t_i)]_l\}, \tag{3.44}$$

with $\{\boldsymbol{c}(t_i)\}$ the set of binary vectors for which resource t_i is being used, i.e., $[\boldsymbol{c}(t_i)]_{t_i} = 1$. For instance, for $Q = 3$ and $t_i = 1$, these vectors would be $\{\boldsymbol{c}(1)\} = \{[100],[110],[101],[111]\}$ and, thus, the corresponding set $\mathcal{R}_1$ would be $\{1,3,5,7\}$.

Finally, since the purpose of this chapter is to optimize the overall performance of the network, we look for allocation strategies that minimize the average outage probability of all sensors. Consequently, the RA can be formulated as the following optimization problem:

$$\boldsymbol{C}^\star = \underset{\boldsymbol{C}}{\operatorname{argmin}} \ \frac{1}{M} \sum_{i=1}^{M} P_{\text{out}}^i = \underset{\boldsymbol{C}}{\operatorname{argmin}} \ \bar{P}_{\text{out}}, \tag{3.45}$$

where P_{out}^i follows the definition in (3.36) and (3.39) for the SR and MR cases, respectively. Given the previous definitions, the outage probability is completely defined by the RA matrix $\boldsymbol{C}$. Note that, even though our approach has been formulated based on the objective function defined in (3.45), any other objective function could have been considered. For instance, we could have also used the maximum P_{out}^i, i.e.,

$$\boldsymbol{C}^\star = \underset{\boldsymbol{C}}{\operatorname{argmin}} \max_i \ P_{\text{out}}^i. \tag{3.46}$$

It is straightforward to see that the problem formulated in (3.45) is combinatorial and finding the optimal solution has an exponential complexity: $\mathcal{O}((Q+1)^{SK})$ and $\mathcal{O}(2^{RSK})$ for the SR and MR cases, respectively. Therefore, a brute force approach is not affordable as trying all possibilities becomes quickly unfeasible.

That is why we need to seek sub-optimal strategies that provide a suitable solution with far less complexity. In the forthcoming subsection, we derive a graph-based RA scheme that uses coloring techniques to achieve a feasible distribution of the limited resources.

3.5.2 Proposed Solution

One way to solve the problem stated in (3.45) is by means of graph coloring methods. In this subsection, we present an approach that relies on graph structures that capture the previous setup. We denote the AN-beam tuples as the nodes or vertices, and an edge or connection is established whenever two pairs can potentially interfere (i.e., whenever the sensors' signals detected at a pair can potentially interfere with the other pair). The resulting graph is represented with an adjacency matrix $\boldsymbol{A} \in \{0,1\}^{D \times D}$ [84], where $D \triangleq SK$ is the number of nodes, and each entry $[\boldsymbol{A}]_{l,m}$ is 1 for connecting nodes l and m. Accordingly, we use geometrical measures to determine whether the interference is large enough to create a connection.

Given that ANs might be deployed at the center of areas where the sensor concentration is high, we define a circle of radius R_{dep} around each AN to represent these regions. Thereby, with the help of an interference radius $R_{\text{int}} \triangleq cR_{\text{dep}}$, we decide which of the interference coming from sensors UL signals might be significant. The factor $c \geq 1$ essentially determines how far the interfering sensors should be to be considered negligible (e.g., when the power of their received signal is orders of magnitude lower than that of sensor i).

Whenever the distance between two ANs is smaller than $R_{\text{int}} + R_{\text{dep}}$, we label them as potentially interfering [68]. This is the condition for the intersection between the circle describing the deployment area around one AN (R_{dep}) and that representing the range of interference coming from sensors deployed around another AN (R_{int}). Their beams are denoted as interfering if one of them is pointing towards the other and all beams in the same AN are connected to each other. The reason is that sensors detected by an AN-beam pair are probably close to that AN. Thus, it is likely that they create a large interference to the other beams in that AN (due to the secondary lobes of the beam radiation pattern). This procedure determines $\boldsymbol{A}$.

An example of the previous procedure is shown in Figure 3.3 for $S = L = 4$, $K = 2$, and $c = 2$. In addition, we consider a simple beamforming where the spatial filters are constructed with the steering vectors computed at equispaced pointing directions. However, the following approach does not depend on the filtering scheme. From now on, we consider that ANs use a generic beamforming. For a different scheme, a similar procedure can be used to find $\boldsymbol{A}$.

Once the graph is created, we color it with Q resources. In the SR case, the colors are directly the resource identifier. On the contrary, in the MR, they refer to the decimal value from (3.42) that represents the set of resources of each pair. As a result, we have $Q + 1$ and 2^Q colors for each scenario, respectively. In both cases, we try to find an allocation such that two neighbors, i.e., connected nodes, do not share resources.

In the SR scenario, having different resources at neighboring nodes is equivalent to having different colors. However, in the MR, not only do we need different colors, but also we need to minimize the number of resources in common that they represent. For example, for $Q = 6$ and colors 37 and 53, the resource sets are $\{1, 3, 6\}$ and $\{1, 3, 5, 6\}$, respectively. As a result, even though the colors are different, the resource sets have a non-null intersection.

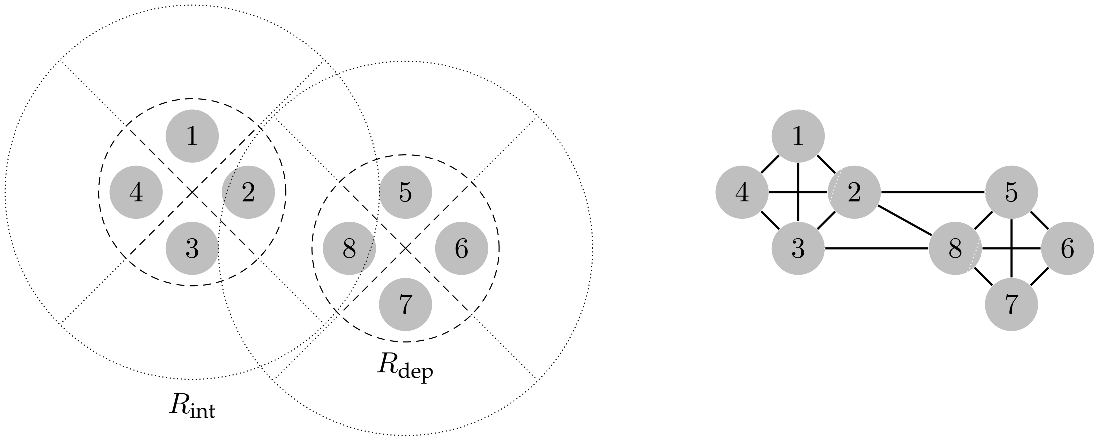

(a) Interfering nodes.

(b) Graph with resulting connections.

Figure 3.3: Construction of coloring graph for $S = L = 4$, $K = 2$, and $c = 2$. Given the positions and spatial filters of the ANs, in (a) we generate the deployment and interfering areas. Based on that, in (b) we determine which nodes (listed from 1 to $D = 8$) interfere, and connect them with edges.

As a result, we need to seek strategies that avoid any reuse of resources between neighbors (and not only colors). In the SR case, this is known as proper graph coloring [84]. However, in the MR, standard proper coloring does not guarantee there is no reuse (i.e., null intersections between resource sets of connected nodes). Given the resource limitation (e.g., in LTE-M, only $Q = 6$ resources are destined to MTC [40]), we allow two neighbors to share resources [85]. We must introduce some criteria to choose which nodes (or tuples) can reuse resources.

The proposed solution for the problem in (3.45) is the result of an iterative algorithm similar to the well-known first-fit (or greedy) approach used for graph coloring [86]. To ease of notation, we use the vectorized form of the allocation matrix $\boldsymbol{C}$, i.e., $\boldsymbol{c} \triangleq \operatorname{vec}(\boldsymbol{C})$.

The first step is to order the nodes according to the number of neighbors $\boldsymbol{v} = [v_1, \dots, v_D]$ in a descent way, where $d \in \{1, \dots, D\}$ is the node index. This magnitude is usually referred to as degree and captures roughly the amount of interference that nodes can suffer. It can be computed as $\boldsymbol{v} = \boldsymbol{A}\boldsymbol{1}_D$. This ordering is represented with the vector $\boldsymbol{o} = [o_1, \dots, o_D]$.

Next, we allocate random colors to each node (i.e., AN-beam pair) and, following the order given by $\boldsymbol{o}$, we iterate over them and assign the color that leads to the minimum average outage probability. Note that this metric takes into account the non-null intersection of resources between different colors and, thus, allows the allocation of resources in the MR scenario.

This way, we follow the criterion in (3.45), and the o_d-th element of $\boldsymbol{c}$ is updated as

$$\mathcal{P}(W, o_d) = \underset{\boldsymbol{c}(o_d) \in \{0, \dots, W\}}{\operatorname{argmin}} \; \bar{P}_{\text{out}}(\boldsymbol{c}), \tag{3.47}$$

where W is Q and $2^Q - 1$ in the SR and MR case, respectively. At each iteration, only one of the elements of vector $\boldsymbol{c}$ (that denoted by $\boldsymbol{c}(o_d)$) is allowed to change. The procedure is summarized in Algorithm 3.1, where $\bar{P}_{\text{out}}^{(u)}$ is the average outage probability at the u-th iteration. Note that we always follow the direction of $\bar{P}_{\text{out}}$ decrease and that the routine terminates when the decrease becomes smaller than a threshold χ or when a number of iterations U is exceeded.

Algorithm 3.1 Greedy optimization to solve (3.47)

```
Initialize $\boldsymbol{v}$, $\boldsymbol{o}$ and $\boldsymbol{c}$:
    $\boldsymbol{v} = [v_1, \ldots, v_D]^{\mathrm{T}} = \boldsymbol{A}\boldsymbol{1}_D$
    $\boldsymbol{o} = [o_1, \ldots, o_D]^{\mathrm{T}} = \mathrm{sort}(\boldsymbol{v})$
    $\boldsymbol{c} \leftarrow$ random
Set $u = 0$ and $\bar{P}_{\mathrm{out}}^{(u)} = \sum P_{\mathrm{out}}^{i}(\boldsymbol{c})/M$
repeat
    Update iteration: $u \leftarrow u + 1$
    for $d = 1 : D$ do
        Compute $\boldsymbol{c}(o_d)$ as indicated in (3.47)
    end for
    Update outage: $\bar{P}_{\mathrm{out}}^{(u)} = \sum P_{\mathrm{out}}^{i}(\boldsymbol{c})/M$
until $\bar{P}_{\mathrm{out}}^{(u-1)} - \bar{P}_{\mathrm{out}}^{(u)} < \chi$ or $u > U$
```

3.6 Numerical Simulations

This section is devoted to presenting several results to validate the approximations of the aggregate interference statistics introduced in Section 3.3 and, thus, sustain the adequacy of this tool for calculating the outage probability derived in Subsection 3.4.3. Later, simulations to evaluate the performance of the allocation strategy described in Subsection 3.5.2 are shown.

In particular, we compare our approximations (Chernoff and Gram-Charlier) with the experimental results obtained with the CF method from Subsection 3.3.1. Regarding the RA, we compare it w.r.t. a random allocation to highlight the performance of our approach. For both studies, we consider the system model characterized in Subsection 3.4.3.

On the other hand, we also present a practical implementation of the mechanism that informs the sensors about the resources they can use. In addition, to faithfully represent a realistic scenario, we use parameters and guidelines specified by 3GPP and ITU standards. That is why we dedicate an initial subsection to discussing all these issues.

3.6.1 Practical Issues

In LTE/LTE-A/NR [21, 87, 88], the smallest resource unit is the PRB. It corresponds to a time-frequency orthogonal resource that occupies a 0.5 ms slot and a 180 kHz bandwidth [22]. To include the coexistence of mMTC systems in cellular communications in our study, we adopt the frame structure specified by that standard (i.e., $B_i = 180$ kHz $\forall i$).

As mentioned, we assume that we dispose of Q PRBs[3], which are allocated to the different AN-beam tuples with the graph-based approach described in Subsection 3.5.2. However, the process through which sensors know the resources they can use has not been specified yet.

Given that typical RACH-based approaches are not suited for mMTC systems, we propose a methodology similar to that described in [65], where resource identifiers are distributed among the spatial beams. Once resources are allocated to the beams, they broadcast resource grants.

---

[3] Although these resources span the frequency domain for a single slot, the Q PRBs are equivalent to the N time-slots presented in Chapter 2 (where devices transmit over the same carriers). In that sense, sensors can use different frequency resources (occupying one slot), here PRBs, and those sharing the same carriers will create interference.

Table 3.2: Simulation Parameters. The transmit powers $P_j = P \; \forall j$ and the number of PRBs Q are selected following the LTE-M standard [40]. According to the 3GPP indications in [22], low order constellations are used. For a QPSK modulation, a SINR of -6.7 dB is needed to achieve block error probabilities less than 10 % [88]. The rest of the parameters (e.g., carrier frequency) can be found in [90].

M	K	L	P	p	Q	δ
$2,000$	10	10	0.1 W	0.1	6	-6.7 dB

Sensors detecting a certain grant, which means they are located in the beams pointing directions, use the associated PRBs to communicate. Recall that, in the MR scenario, sensors choose one of the available resources at random. In the event of receiving PRBs grants from more than one beam, sensors may choose that corresponding to the highest SNR (assuming normalized power per beam), i.e., the one coming from the AN-beam tuple defined in (3.30).

On the other hand, we consider that sensors are deployed uniformly in a circle of radius R_{dep} centered at the AN's location, and that M_k is approximately equal for all ANs. The ANs are also uniformly distributed in a square area of side R_t, which is set to 1 km to represent the typical dimensions of a LTE macrocell. In turn, $R_{\text{dep}} = 100$ m to match those of a microcell. As a result, the spatial distribution of sensors can be described by K MCPs of densities $M_k/(\pi R_{\text{dep}}^2)$, whereas ANs are defined by HPPP of density K/R_t^2 (cf. Section 2.4). Accordingly, all results are averaged over different realizations of these processes.

To represent the multiple-antenna technology used at the ANs, we employ a UCA configuration [89]. In addition to that, given the low mobility of the sensors [70, 71], we consider channels to change very slowly and, thus, constant and known during the data transmission. For simplicity, we assume that we have a line of sight (LoS) communication. A possible extension to this chapter could be to analyze the case where the channel includes non-LoS (NLoS) components, is not perfectly known, and/or varies over time.

Considering free-space propagation, the channels of the sensors are expressed using the steering vector and path-loss coefficient. For the sake of simplicity, we consider the previous simple beamforming with $S = L$, where the spatial filters are constructed with the steering vectors computed at equispaced pointing directions. Besides, the factor c used to generate all graphs is set to 2 since the interfering signals coming from distances $d_j \geq R_{\text{int}} = 2R_{\text{dep}}$ are received with a sufficiently large attenuation to be considered negligible.

Finally, the probability p_j^{act} is assumed to be the same for all sensors and equal to an activity factor p (not to be confused with the transmit power P_j). In the MR case, the probabilities p_j^{res} can be different as they depend on the number of resources allocated to the corresponding AN-beam tuple $(k(j), s(j))$. The rest of the simulation parameters are listed in Table 3.2.

3.6.2 Statistics Approximations

To show the accuracy of the Chernoff and Gram-Charlier approximations, we start by plotting the resulting CDF together with that obtained with the CF approach. Recall that, for a sufficient number of points in the IFFT, the method of the CF represents a more precise approximation.

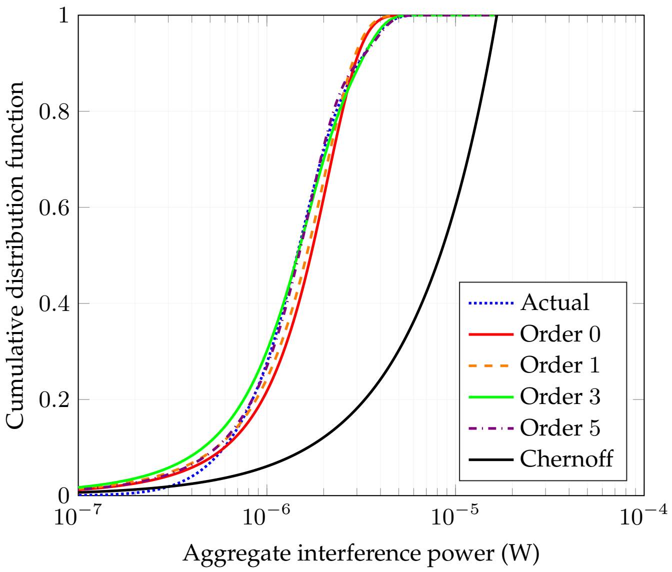

Figure 3.4: Actual and approximated CDFs.

That is why, since the real PMF of Γ_i is not available, this approach is used as a reference. Besides, all plots are done for a certain sensor i at a random location.

Note that only the SR case is shown as it is a sufficient representation of the scenario. In comparison with the SR case, in the MR case only the probabilities p_j change. Nevertheless, given that the proposed approximations already take into account that situation (i.e., they are valid for any value of the probabilities p_j), the shape of the resulting CDF in the MR does not differ from that of the SR. Thus, the MR case is omitted to avoid redundancy.

Results are depicted in Figure 3.4, where we can observe the accuracy of the approximations. Orders up to 5 are presented to illustrate the Gram-Charlier series expansion converges towards the actual PMF when using more addends. Note that the case $O_i = 0$ (zero-order) refers to the Gaussian kernel without any expansion. Hence, our approach reveals a promising performance, especially for high orders. Contrarily, the Chernoff-based approximation yields a large error. This is not surprising given that only a single statistical moment is considered.

On the other hand, to further illustrate the accuracy of our proposal, we analyze the error between the distribution obtained with the CF, i.e., $p_{\Gamma_i}(\gamma_i)$, and that provided by the Gram-Charlier and Chernoff methods, i.e., $f_{\Gamma_i}(\gamma_i)$. To compare them, we use the Jensen-Shannon divergence, which is a true distance and is bounded between 0 and 1 [91]:

$$\mathrm{JSD}(p_{\Gamma_i}(\gamma_i), f_{\Gamma_i}(\gamma_i)) \triangleq \mathrm{KL}(p_{\Gamma_i}(\gamma_i), m_{\Gamma_i}(\gamma_i))/2 + \mathrm{KL}(f_{\Gamma_i}(\gamma_i), m_{\Gamma_i}(\gamma_i))/2, \tag{3.48}$$

where $m_{\Gamma_i}(\gamma_i) \triangleq (p_{\Gamma_i}(\gamma_i) + f_{\Gamma_i}(\gamma_i))/2$ represents the average distribution of $p_{\Gamma_i}(\gamma_i)$ and $f_{\Gamma_i}(\gamma_i)$, and $\mathrm{KL}(\cdot,\cdot)$ is the standard Kullback-Leibler divergence [91].

Thereby, we can define the error in our approximation as

$$\varepsilon \triangleq \frac{1}{M}\sum_{i=1}^{M} \mathrm{JSD}(p_{\Gamma_i}(\gamma_i), f_{\Gamma_i}(\gamma_i)), \tag{3.49}$$

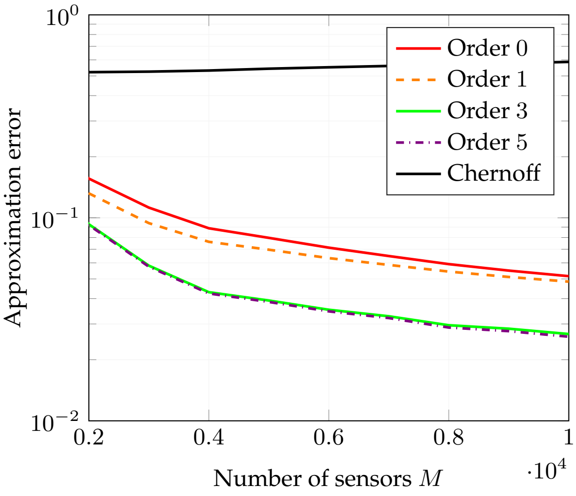

Figure 3.5: Approximation error ε versus the number of sensors M.

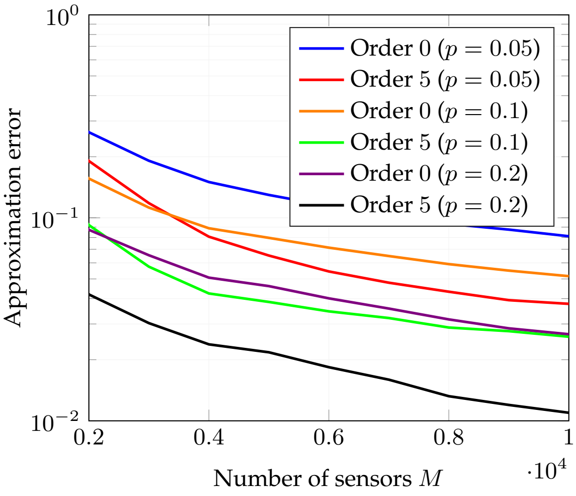

Figure 3.6: Approximation error ε versus the number of sensors M for different activity factors p.

which represents the average among all sensors. Note that, to compute the error ε numerically, the continuous approximations (Gram-Charlier and Chernoff) must be discretized. This is not necessary in the case of the CF method since it already provides a PMF.

In line with the previous discussion, we compare the different approaches for the SR scenario only. In particular, we present the error in (3.49) w.r.t. the number of sensors M. This is shown in Figures 3.5 and 3.6. In the latter, the error ε is also depicted for different values of the activity factor p. This way, we can highlight the robustness of our proposal against the probability p. To avoid redundancy, in Figure 3.6, only orders 0 and 5 are shown.

It can be observed in Figure 3.5 that the error ε diminishes with the number of sensors M. This is due to the asymptotic behavior of the sum of RVs (CLT), i.e., the more addends the aggregate interference has (which is the correct assumption in mMTC), the better the Gram-Charlier approximation becomes. Besides, the approximation error also decreases with p, as shown in Figure 3.6. The reason behind this is that larger activities can be seen as an increase in the number of sensors creating interference, which makes the actual statistics to be closer to the asymptotic behavior. As before, a finer precision is attained for higher orders and poor performance is obtained with the Chernoff method.

3.6.3 Resource Allocation

In this subsection, we present different results to assess the performance of the allocation strategy described in Subsection 3.5.2. These simulations are used to illustrate the enhancement w.r.t. the trivial allocation where the entries of $\boldsymbol{C}$ are selected randomly between 0 and W.

We first plot the average outage probability $\bar{P}_{\text{out}}$ from (3.40) obtained with both allocation strategies when changing M and p. This is depicted in Figures 3.7 and 3.8, respectively. It can be seen that a substantial improvement is obtained with our proposal. In turn, the MR yields a lower $\bar{P}_{\text{out}}$ as the activity is reduced and more degrees of freedom (i.e., colors) are available.

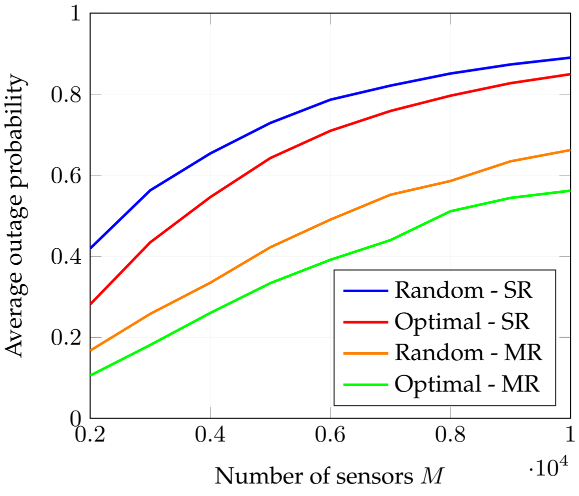

Figure 3.7: Average outage probability $\bar{P}_{\text{out}}$ versus the number of sensors M.

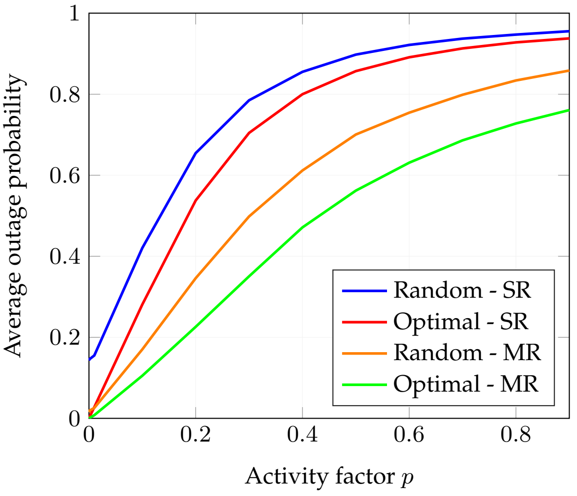

Figure 3.8: Average outage probability $\bar{P}_{\text{out}}$ versus the activity factor p.

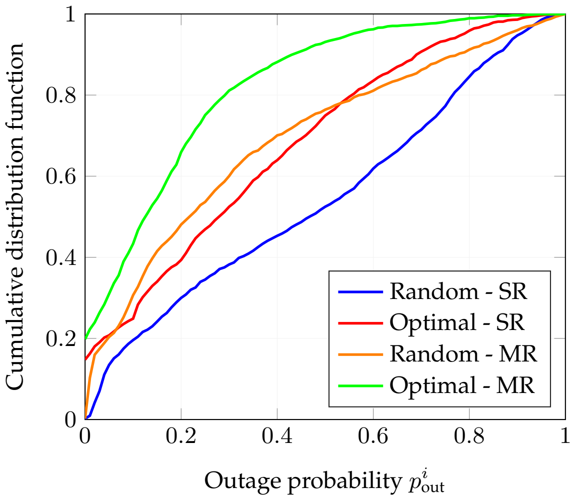

Figure 3.9: CDF of the outage probability $F_{P^i_{\text{out}}}(p^i_{\text{out}})$.

Note that the RA is always done with the Gram-Charlier approximation of order 5 and that the resulting probability values are computed using the CF method.

Moreover, to get richer insights, in Figure 3.9, we show the CDF of the outage probability:

$$F_{P^i_{\text{out}}}(p^i_{\text{out}}) \triangleq \Pr\{P^i_{\text{out}} \le p^i_{\text{out}}\}. \tag{3.50}$$

As we can see, our strategy helps to decrease considerably the outage probabilities within the network. Therefore, given the relationship between the outage probability and power consumption, our approach could also be useful to improve the energy limitations of mMTC systems and extend the battery lifetime of sensors.

3.7 Summary and Conclusions

In this chapter, we have addressed the problem of modeling the aggregate interference statistics, which captures the sporadic activity of sensors in UL mMTC. Given its discrete nature and the large number of devices, the expression of this distribution can be difficult to find. That is why we have proposed a Gram-Charlier series expansion of a truncated Gaussian kernel to approximate the aggregate interference statistics. Thanks to that, we have also derived an analytic closed-form expression for the outage probability, which is a valuable figure of merit.

We have considered a setup with several multiple-antenna ANs that receive information from a set of sensors, and each AN is equipped with a set of predefined spatial beams. We have distinguished two scenarios, SR and MR, depending on the number of resources allocated to each beam. Since the number of available PRBs is limited, we have presented a graph coloring technique that tries to minimize the average outage probability as allocation strategy. Finally, we have described a practical mechanism where resource grants are sent through the beams in a broadcast way. Sensors located at their pointing directions receive those permissions and use those resources to communicate. This non-dedicated scheduling approach can serve as an alternative to typical RACH schemes, which fail in the presence of massive requests.

Simulation results have shown that our Gram-Charlier proposal yields an accurate approximation and that our RA method can improve the overall system performance, i.e., a smaller outage probability is obtained, which translates into lower power consumption.

Based on the justifications detailed in the chapter, the random nature of the scenario comes from the sporadic activity and high number of devices, while the channel is assumed to be perfectly known. Future work will focus on the extension to the cases where these assumptions do not hold. Note, however, that the performance predicted by the results in this chapter can be taken as a valid benchmark for comparison purposes in those cases.

Appendix 3.A Proof of Lyapunov's CLT

Lyapunov's CLT is a variant of the classical CLT where the sum of a sequence of independent RVs with different statistics converges in distribution to a standard Gaussian RV under a certain condition. In particular, for some $\epsilon > 0$, the following must be fulfilled

$$\lim_{m\to\infty} \frac{1}{\sigma_i^{2+\epsilon}} \sum_{j\in\mathcal{J}_i} \mathbb{E}\left[|\beta_j a_{j,i} - p_j a_{j,i}|^{2+\epsilon}\right] = 0, \tag{3.51}$$

where $m \triangleq |\mathcal{J}_i|$ is the number of addends (i.e., number of interfering sensors).

It can be shown that the individual terms in (3.51) can be upper bounded by

$$\mathbb{E}\left[|\beta_j a_{j,i} - p_j a_{j,i}|^{2+\epsilon}\right] \leq p_j(1-p_j)a_{j,i}^{2+\epsilon}. \tag{3.52}$$

Thereby, (3.51) will be satisfied as long as the following ratio tends to zero for $m \to \infty$:

$$\frac{1}{\sigma_i^{2+\epsilon}} \sum_{j\in\mathcal{J}_i} p_j(1-p_j)a_{j,i}^{2+\epsilon} = \left(\sum_{j\in\mathcal{J}_i} p_j(1-p_j)a_{j,i}^2\right)^{-1-\epsilon/2} \sum_{j\in\mathcal{J}_i} p_j(1-p_j)a_{j,i}^{2+\epsilon}. \tag{3.53}$$

For equal transmission probabilities, i.e., $p_j = p\ \forall j$, the previous expression yields

$$\frac{1}{(p(1-p))^{\epsilon/2}} \left(\frac{\|\boldsymbol{a}_i\|_{2+\epsilon}}{\|\boldsymbol{a}_i\|_2}\right)^{2+\epsilon}, \tag{3.54}$$

where the vector $\boldsymbol{a}_i$ contains the set of interfering values $\{a_{j,i} : j \in \mathcal{J}_i\}$.

Assuming the term $p(1-p)$ is not close to 0 (which means p is neither zero or one), we prove the remaining ratio tends to zero with the help of the following relations between norms:

$$\|\boldsymbol{x}\|_s \leq \|\boldsymbol{x}\|_r \leq m^{\left(\frac{1}{r}-\frac{1}{s}\right)}\|\boldsymbol{x}\|_s, \tag{3.55}$$

for any vector $\boldsymbol{x}$ of length m and $1 \leq r < s$.

This, translated to our scenario, leads to the following inequalities:

$$1 \geq \left(\frac{\|\boldsymbol{a}_i\|_{2+\epsilon}}{\|\boldsymbol{a}_i\|_2}\right)^{2+\epsilon} \geq m^{1-(2+\epsilon)/2}, \tag{3.56}$$

where the right-hand side tends to zero with $m \to \infty$ and any positive value of ϵ. Besides, it is straightforward to see that this bound is tight for $\epsilon \to \infty$ as $\|\boldsymbol{a}_i\|_\infty = \max_j \mathrm{a}_j < \infty$, and the ratio $\|\boldsymbol{a}_i\|_\infty/\|\boldsymbol{a}_i\|_2$ will be always smaller than 1 for any $m > 1$. In fact, for $m \to \infty$ the speed of convergence is much faster as $\|\boldsymbol{a}_i\|_2 \to \infty$. This concludes the proof.

Chapter 4

Device Selection and Data Quantization

4.1 Introduction

Different from before, in this chapter, we will focus on a mMTC scenario where sensors transmit their measurements on a regular or predictable basis. Thereby, according to the discussion in Section 2.2, conflict-free access mechanisms are usually preferred for this kind of data traffic and, as in [24], we will consider a TDM scheduling mechanism (i.e., an OMA transmission).

Recall that, based on the noisy measurements (or observations) provided by the large number of devices, the CN is responsible for recovering the original set of parameters. To measure this inference of parameters (i.e., the retrieved information), two points of view will be contemplated: (i) the joint entropy of the sources, and (ii) the error of the estimate calculated by the CN. In that sense, given that the collected data can be significantly correlated (due to the potentially high spatial density in mMTC deployments) [25], in this chapter, we will propose a technique where the gathered information is manipulated to reduce the payload and power consumption of the sensors without compromising the overall performance.

Within the framework of statistical inference, parameter estimation has been widely studied in the literature and the optimal strategy depends on the scenario under study [92–94]. In the case of Gaussian sources, it is common to consider the minimum mean squared error (MMSE) estimation as the optimum approach [95]. Nevertheless, in most works, transmission errors are not taken into account, and a noiseless channel is usually considered [96,97]. Since these errors may affect significantly the system performance, in (ii) the resulting mean squared error (MSE) will be averaged over the different decoding error probabilities or PERs.

On the contrary, in (i) we will concentrate only on how much information the sensed data contains, and leave the communication aspects for future studies (we will consider that the CN can decode the messages perfectly). Then, it is desirable to establish a metric that quantifies this information. In this context, it is natural to use the multivariate entropy as a proper indicator, since it determines the minimum number of bits needed to represent a discrete source, i.e., the source rate S_i (cf. Figure 2.1) [34]. Therefore, this point of view is also related to the statistical inference, since it measures the information based on the parameters' distributions.

In order to tackle the above transformation of the sensed data, we will present a communication scheme in which only a subset of devices will be selected to transmit their observations (cf. [92]). Thereby, the decision concerning which sensors remain active will be driven by the objective of maximizing the collected information under power-related constraints [98–100]. For each perspective, this translates into: (i) maximizing the joint entropy, and (ii) minimizing the MSE in the parameter estimation. The degree of correlation between the measurements will then have an impact on the selection of sensors. In short, devices with highly correlated data will not transmit all their measurements, but some of them will remain silent. This way, as the mMTC terminals will save energy, our approach will improve the battery lifetime within the network. Note that, for a Gaussian source, the correlation between the sensors' information is captured by the (frequently ill-conditioned) covariance matrix of the observations [101, 102].

Moreover, we will consider that sensors quantize their measurements, which can also help to reduce the network traffic (due to the resulting data compression) and, hence, the overall power consumption [103]. In this chapter, we will explore the use of uniform quantizers, for which we will characterize the joint entropy in (i), and the quantization noise and its impact on the MSE in (ii) [104]. Both procedures will be based on quantized Gaussian sources. Additionally, in (ii), the different precision levels in each device (i.e., the number of quantization bits) will be also designed to minimize the MSE, leveraging the correlation in the sensed data.

Finally, in the cases where the observed parameters can vary over time (e.g., the temperature during the day), the sensors' measurements might be also temporally correlated [105]. Thereby, to take into account these situations, we will extend our study to the case of systems with memory (only in the context of parameter estimation[1]). For that task, we will make use of first-order Markov processes to model these dynamics and, since the goal in (ii) will be to minimize the average MSE, we will consider the use of Kalman filters to produce the estimates at the CN [106, 107]. Accordingly, the device selection and the number of quantization bits will be optimized over time and the resulting MSE evolution will be analyzed.

4.1.1 Related Work

The optimal selection of sensing devices has also been extensively pursued (cf. [99]). As an example, works [92] and [108] introduced this problem by reducing the message size (or dimension). On the contrary, the authors of [109] proposed the use of data censoring for reducing the information to be sent (which can be seen as an alternative to sensor selection). Besides, with the help of kernel regression, a fast and low-complexity approach based on matrix completion and extrapolation was studied in [110], accounting for prior information in the data. However, like our entropy-based strategy, these works considered negligible transmission errors, which is an unrealistic assumption in mMTC networks (where communication resources are also often limited). That is why the error-free (or noiseless) scenario will be only considered in the entropy perspective as a first tentative solution to the sensor selection problem.

Given their relevance in practical systems, data quantizers have also been considered in some of these works (e.g., [109]). The reason is that efficient compression schemes can be obtained when optimizing the quantization stage [111]. For instance, the authors of [112] derived the set of optimal quantizers when only 1-bit of resolution is available. In [107], authors studied the potential of analog mappings in a fading MA environment and optimized the precision levels of the quantizers. Another example can be found in [113], where authors relied on en-

---

[1] The temporal extension in the entropy analysis will be reserved for future studies.

coded sensing to partition the network into groups of sensors that jointly encode and transmit their information to the sink. Despite that, most of these works did not contemplate the power limitations of the devices involved (which is crucial in current mMTC deployments).

Finally, based on the fundamentals derived by S. M. Kay in 1993 [95], works like [92,108,114] approached the problem of distributed estimation in a scenario where a set of devices sent their spatially correlated data to a fusion center through a noiseless channel. In particular, considering Gaussian sources, the authors of [114] derived the optimal MMSE estimator when the measurement noise was inhomogeneous (i.e., not equally distributed for all sensors). In [92], authors extended these derivations to the case of temporally correlated data (with noiseless channels). The case of power-constrained devices (and no transmission errors) was analyzed in [108], where authors considered the presence of collaborative clusters. In the recent work [97], authors designed an estimation strategy based on distributed compression and dimensionality reduction to comply with the bandwidth constraints in an error-free environment.

4.1.2 Contributions

Considering perspectives (i) and (ii), the contributions of this chapter can also be divided into two parts. On the one hand, the entropy analysis yields the following findings:

- A sensing scheme relying on the selection of devices observing Gaussian correlated sources, which is discretized using uniform vector quantizers.
- A tractable upper bound of the entropy of the quantized joint source. This bound is used to formulate the sensor selection problem, which is non-convex.
- A sub-optimal solution of the discrete optimization problem based on convex relaxations and approximations. Simulation results justify the tightness of this approach.

On the other hand, the outcomes of the estimation approach are listed below:

- A distributed estimation scheme based on sensor selection and uniform scalar quantization with different levels of precision. Our approach is firstly formulated for a memoryless mMTC system and it only benefits from the spatial correlation in the sensed data.
- A parameter estimation based on the MMSE criterion. The MMSE estimate is derived considering actual transmission and communication errors. The analytic closed-form expression for the MSE is later characterized and a tractable upper bound is proposed.
- An iterative algorithm to optimize the set of selected devices and number of quantization bits, taking into consideration the power consumption within the mMTC network. Two strategies are presented: separate (alternating) and joint optimization.
- An extension to temporally correlated data based on the use of the Kalman filter. The resulting MSE and the MMSE estimate are derived accordingly.
- Numerical simulations for synthetically generated data and real data. In both cases, results highlight the performance of our approach and justify the selection and quantization of measurements in mMTC deployments.

4.1.3 Organization

The remainder of this chapter is structured as follows. In Section 4.2, the system model and transmission scheme (i.e., sensor selection and data quantization) are described. In Section 4.3, the source entropy and parameter estimation are characterized. The optimization problems are formulated in Section 4.4, where different approaches to finding a feasible solution are proposed. In Section 4.5, the extension to the system with memory is discussed. Numerical simulations are shown in Section 4.6 and, finally, conclusions are presented in Section 4.7.

4.2 System Model

Throughout this chapter, we consider a scenario with a set of M sensors connected to a CN. Two illustrative examples with $M = 4$ are depicted in Figure 4.1 for the entropy and estimation perspectives. Note that, since in the former we are interested in the joint source, the collected data is first sent to a fusion center (with direct access to all observations) and later to the CN.

In both setups, each sensor measures (solid lines in Figure 4.1) a noisy version x_i of a parameter θ_i, i.e., $x_i \triangleq \theta_i + \eta_i$, with η_i the observation noise and $i \in \{1, \ldots, M\}$. More specifically, in vector notation we have [115]:

$$\boldsymbol{x} \triangleq \boldsymbol{\theta} + \boldsymbol{\eta} \in \mathbb{R}^M, \tag{4.1}$$

where $\boldsymbol{x} = [x_1, \ldots, x_M]^{\mathrm{T}}$ is the set of observations of the (physically separated) devices, $\boldsymbol{\theta} = [\theta_1, \ldots, \theta_M]^{\mathrm{T}} \in \mathbb{R}^M$ is the vector containing the different (but possibly correlated) parameters, and $\boldsymbol{\eta} = [\eta_1, \ldots, \eta_M]^{\mathrm{T}} \in \mathbb{R}^M$ is the corresponding measurement noise vector. Each element in $\boldsymbol{x}$ is measured independently by each individual sensor. We assume that the parameter vector is a realization of a Gaussian process with mean $\boldsymbol{\mu_\theta} \in \mathbb{R}^M$ and covariance matrix $\boldsymbol{C_\theta} \in \mathbb{R}^{M \times M}$, i.e., $\boldsymbol{\theta} \sim \mathcal{N}(\boldsymbol{\mu_\theta}, \boldsymbol{C_\theta})$. Both mean and covariance are assumed to be known. In addition, we also consider the noise vector $\boldsymbol{\eta}$ to be independent of $\boldsymbol{\theta}$ and Gaussian distributed with zero mean and covariance matrix $\boldsymbol{C_\eta} \in \mathbb{R}^{M \times M}$, i.e., $\boldsymbol{\eta} \sim \mathcal{N}(\boldsymbol{0}_M, \boldsymbol{C_\eta})$. Note that this model also includes, as a particular case, the scenario where all sensors measure the same parameter ($\theta_i = \theta_j \ \forall i, j$), i.e., $\boldsymbol{\mu_\theta} = \mu_\theta \boldsymbol{1}_M$ and $\boldsymbol{C_\theta} = \sigma^2 \boldsymbol{1}_M \boldsymbol{1}_M^{\mathrm{T}}$ (where σ is the standard deviation).

The elements of the covariance matrix $\boldsymbol{C_\theta}$ could be modeled, for example, as [102]

$$[\boldsymbol{C_\theta}]_{i,j} = \sigma_i \sigma_j \Lambda(d_{i,j}), \quad 1 \le i \le M, \quad 1 \le j \le M, \tag{4.2}$$

where σ_i is the standard deviation of the parameter θ_i measured by sensor i. The term $\Lambda(d_{i,j})$ is the correlation factor between the parameters of sensors i and j with $|\Lambda(d_{i,j})| \le 1$, and that, usually, depends on the distance between them $d_{i,j}$. Different models can be adopted for this correlation function $\Lambda(d_{i,j})$. As an example, a well-known and accepted model for sensor networks is the exponential distance (cf. [105,113]). However, to keep our analysis general, the expression of $\Lambda(d_{i,j})$ will remain unspecified until the simulations section.

To avoid unnecessary power consumption, only a subset of sensors are selected to transmit their information to the CN. Thereby, the chosen sensors will send their observation through separate orthogonal channels (dashed lines in Figure 4.1) using different MCSs (cf. Section 2.3).

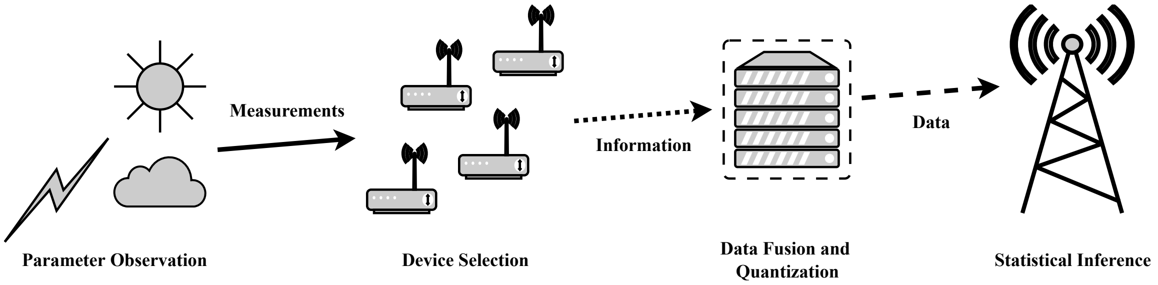

(a) Entropy perspective.

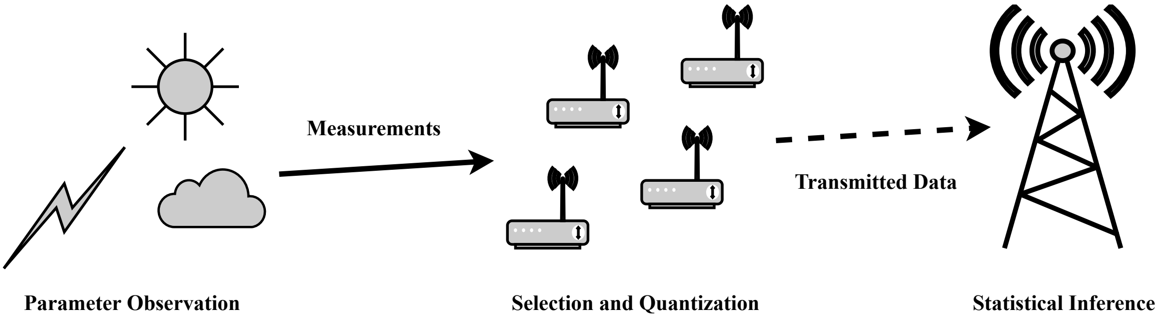

(b) Estimation perspective.

Figure 4.1: Illustrative scenarios with $M = 4$. Each sensor observes a realization of a certain parameter (solid lines), which can be different and potentially correlated with the rest. In (a), after selecting the measurements, the collected information is sent to a fusion center (dotted line), which is responsible for quantizing the data and transmitting it to the CN (dashed line). In (b), the selection and quantization are performed directly at the sensors' side, which later transmit that data to the CN (dashed line).

As previously mentioned, we adopt a communication strategy in which time is divided into frames of N slots, and we further assume that each slot has a duration of T_s seconds and a bandwidth of B_s Hertz [21,38]. Both parameters are assumed to be fixed and known. Accordingly, each sensor will be allocated a single slot (i.e., $B_i = B_s \ \forall i$) and, thus, no collisions nor interference will be experienced (cf. [24]). Hence, with this approach, only N sensors are allowed to transmit during each frame (cf. Figure 2.2). In this chapter, we consider that the rest of the sensors remain silent and discard their information.

Recall that we focus on applications where the sensors' information is generated (i.e., sensed) regularly (and will be transmitted if selected by the CN). In these scenarios, it is reasonable to assume that the CN has information regarding how many devices are sensing. Note that this assumption is valid for this type of sensor-based mMTC network, but it does not hold for systems with unpredictable, random, or sporadic traffic patterns.

Since the collected data is discretized using (uniform) quantizers, the payload and power consumption of the devices can be further reduced by adjusting the precision levels. Depending on the perspective, entropy or estimation, scalar or vector quantization will be considered. The communication scheme (prior to transmission) is depicted in Figure 4.2.

Finally, based on the correctly decoded messages, the CN will try to retrieve the parameter vector $\boldsymbol{\theta}$. As mentioned before, the resulting amount of recovered information is measured by the joint entropy and estimation error. In the latter, the possible communication failures during the data transmission are also included. This is discussed in the upcoming sections.

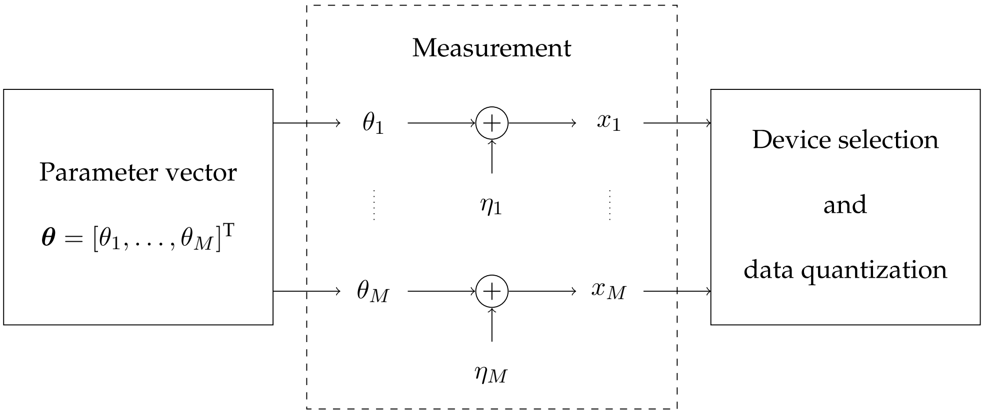

Figure 4.2: Communication scheme prior to transmission.

4.3 Statistical Inference

4.3.1 Source Entropy

In this study, the observations x_i are first selected through a selection matrix $\boldsymbol{S}$, yielding the set $\boldsymbol{y} = [y_1, \ldots, y_N]^{\mathrm{T}} \in \mathbb{R}^N$. Since this information is still continuous, an infinite number of bits are needed to represent $\boldsymbol{y}$. That is why, to work with a finite precision, the set of observations $\boldsymbol{y}$ are later discretized by means of a vector quantizer $\mathcal{Q}(\cdot)$, obtaining the set $\boldsymbol{z} = [z_1, \ldots, z_N]^{\mathrm{T}} \in \mathbb{R}^N$. For simplicity, we initially consider that there is no measurement noise, i.e., $x_i = \theta_i \; \forall i$.

Once the selected data $\boldsymbol{y}$ is jointly quantized into $\boldsymbol{z}$, it is sent through a noiseless channel to the CN, where it can be recovered perfectly (i.e., without decoding errors). Note that, since the set of measurements is not usually available at all terminals, we have assumed the presence of a fusion center that is connected to all sensors and quantizes the joint source (cf. Figure 4.1). The associated communication scheme is illustrated in Figure 4.3.

For the sake of clarity, let us start by defining the random vector $\boldsymbol{X} = [X_1, \ldots, X_M] \in \mathbb{R}^M$ with distribution $f_{\boldsymbol{X}}(\boldsymbol{x})$ to describe the original sensed data, where each element X_i is the information collected by each sensor. Accordingly, the individual x_i refer to a single realization of X_i and $\boldsymbol{x}$ to the vector of realizations (cf. Section 4.2).

The selected measurements can be expressed as $\boldsymbol{Y} \triangleq \boldsymbol{S}\boldsymbol{X}$, where $\boldsymbol{S} \triangleq \mathrm{diag}(s_1, \ldots, s_M)$ is the selection matrix with binary elements $s_i \in \{0, 1\}$. In other words, $\boldsymbol{S}$ represents an on/off activity strategy applied to the terminals. The reason behind this hard allocation scheme is the simplicity of devices, which may be unable to handle various sensing states (they can be either active or asleep, but not in intermediate phases). In Subsection 4.4.1.1, this matrix is designed to reduce power consumption while preserving the sensed information to be transmitted.

Finally, we denote the quantized version as $\boldsymbol{Z} \triangleq \mathcal{Q}(\boldsymbol{Y})$ with associated PMF $p_{\boldsymbol{Z}}(\boldsymbol{z})$. The corresponding multivariate entropy[2] (in bits) is then given by [34]

$$H(\boldsymbol{Z}) \triangleq -\sum_{\boldsymbol{z}} p_{\boldsymbol{Z}}(\boldsymbol{z}) \log p_{\boldsymbol{Z}}(\boldsymbol{z}), \tag{4.3}$$

---

[2] Note that this represents the lower bound on the number of bits necessary to describe $\boldsymbol{Z}$, which can be reached with the help of variable-rate (vector) quantizers [104].

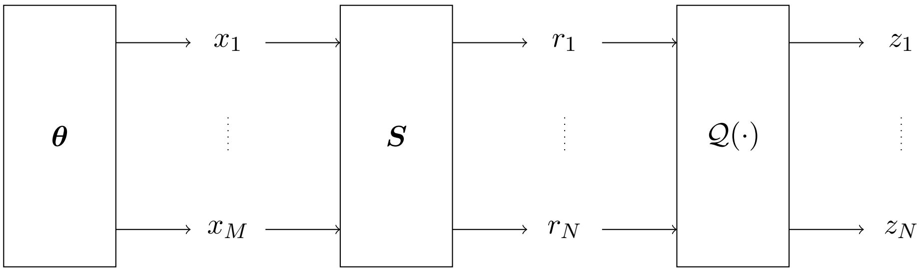

Figure 4.3: Communication scheme for the entropy perspective.

and, as shown in Appendix 4.A, it can be lower bounded by

$$H(\boldsymbol{Z}) \geq h(\boldsymbol{Y}) - M \log \Delta \triangleq \widetilde{H}(\boldsymbol{Z}), \tag{4.4}$$

where we consider the quantization regions (or cells) to be hypercubes of equal sides Δ [116]. As discussed in Subsection 4.6.1, this lower bound $\widetilde{H}(\boldsymbol{Z})$ becomes tight for $\Delta \to 0$ [34], which is why it will be used as an approximation for the actual entropy $H(\boldsymbol{Z})$. Finally, the term $h(\boldsymbol{Y})$ refers to the differential entropy of the continuous source:

$$h(\boldsymbol{Y}) \triangleq - \int_{\boldsymbol{y}} f_{\boldsymbol{Y}}(\boldsymbol{y}) \log f_{\boldsymbol{Y}}(\boldsymbol{y}) d\boldsymbol{y}, \tag{4.5}$$

which can be computed from the relation $\boldsymbol{Y} = \boldsymbol{S}\boldsymbol{X}$ and the distribution of $\boldsymbol{X}$.

Following the model in Section 4.2, $\boldsymbol{X}$ will be a Gaussian RV with mean $\boldsymbol{\mu} \triangleq \mathbb{E}[\boldsymbol{X}] = \boldsymbol{\mu_\theta}$ and (full-rank) covariance matrix $\boldsymbol{C} \triangleq \mathbb{E}\left[(\boldsymbol{X} - \boldsymbol{\mu})(\boldsymbol{X} - \boldsymbol{\mu})^{\mathrm{T}}\right] = \boldsymbol{C_\theta} + \boldsymbol{C_\eta}$, i.e., $\boldsymbol{X} \sim \mathcal{N}(\boldsymbol{\mu}, \boldsymbol{C})$. As a result, the differential entropy reads as [34]:

$$h(\boldsymbol{X}) = \frac{1}{2} \left(M \log 2\pi e + \log \det(\boldsymbol{C}) \right). \tag{4.6}$$

Note that the Gaussian distribution is taken as a reference as it requires the largest number of bits for accurate representation once quantized (hence, it can be understood as a challenging case) [34]. This assumption is typical in many sensing scenarios [101,102] and allows us to measure the amount of collected information as a function of the matrix $\boldsymbol{C}$. This matrix captures the correlation between sensors data and is often defined as a function of the distance between sensors (e.g., quadratic exponential [105]). However, the strategies developed in this chapter are valid regardless of the underlying models for $\boldsymbol{C}$ (see examples [25,101,102]).

As already mentioned, in this subsection, we consider that there is no measurement noise such that $\boldsymbol{C} = \boldsymbol{C_\theta}$. Under some assumptions, this covariance matrix $\boldsymbol{C}$ can be well approximated by a singular matrix for $M \to \infty$ [101]. Intuitively, this can be understood by the fact that its elements depend only on the distance, and, given the high spatial density, their values can be very similar. From now on, and to ease notation, $\boldsymbol{C}$ will represent the singular (rank deficient) matrix approximating the original covariance matrix.

The differential entropy of the resulting degenerate Gaussian distribution is [101]

$$h(\boldsymbol{X}) = \frac{1}{2} \left(r(\boldsymbol{C}) \log 2\pi e + \log \mathrm{Det}(\boldsymbol{C}) \right), \tag{4.7}$$

where $r(\boldsymbol{C})$ and $\mathrm{Det}(\boldsymbol{C})$ are the rank and pseudo-determinant of $\boldsymbol{C}$, respectively [117]. The latter is computed as the product of the non-zero eigenvalues of $\boldsymbol{C}$.

Similarly, since the covariance matrix of $\boldsymbol{Y}$, i.e., $\boldsymbol{SCS}$, may also be rank deficient, the corresponding differential entropy of this new quantity is

$$h(\boldsymbol{Y}) = \frac{1}{2}\left(r(\boldsymbol{SCS})\log 2\pi e + \log \mathrm{Det}(\boldsymbol{SCS})\right). \tag{4.8}$$

Finally, the entropy of the quantized vector $\boldsymbol{Z}$ yields [101]

$$H(\boldsymbol{Z}) \geq h(\boldsymbol{Y}) - r(\boldsymbol{SCS})\log\Delta = \frac{1}{2}\left(r\left(\boldsymbol{SCS}\right)\log\left(\frac{2\pi e}{\Delta^2}\right) + \log \mathrm{Det}\left(\boldsymbol{SCS}\right)\right) = \widetilde{H}(\boldsymbol{Z}), \tag{4.9}$$

which, as discussed later, will be maximized through the device selection matrix $\boldsymbol{S}$.

4.3.2 Parameter Estimation

Different from before, this subsection is devoted to characterizing the MMSE estimate in the presence of communication errors. To that end, we first study the decoding error probability, which will affect the set of correct observations at the CN and the resulting MSE.

As mentioned before, sensors quantize their measurements according to different precision levels to decrease the overall payload. In this setup, we consider uniform scalar quantizers with step size Δ_i. Note that, since the different scalar observations are available at different sensors positioned at separate locations, here vector quantization techniques cannot be applied[3]. Each sensor will use b_i bits of precision and, thus, the quantization step yields

$$\Delta_i \triangleq \mathcal{D}_i/2^{b_i}, \tag{4.10}$$

where $\mathcal{D}_i$ is the dynamic margin of the quantizer. However, given the assumption of Gaussian RVs, the support of the measurement x_i is not bounded. That is why we consider $\mathcal{D}_i$ to be 6 times the standard deviation of x_i so that 99.73% of the values lie within that interval. For a white noise with covariance matrix $\boldsymbol{C_\eta} = \sigma_\eta^2\mathbf{I}_M$, we would have $\mathcal{D}_i \approx 6\sqrt{\sigma_i^2 + \sigma_\eta^2}$.

As a result, the information to be transmitted by each sensor reads as [118]

$$y_i \triangleq q_i(x_i) = x_i + w_i \in \mathbb{R}, \quad 1 \leq i \leq M, \tag{4.11}$$

where $q_i(\cdot)$ represents the quantization function and w_i is the corresponding quantization noise.

Note that, for a sufficiently small step size Δ_i, this noise can be shown to be uncorrelated with x_i, and that the first- and second-order moments can be safely approximated by those of a noise uniformly distributed in $[-\Delta_i/2, \Delta_i/2]$. In fact, for Gaussian RVs, this approximation holds for values of Δ_i smaller than the standard deviation of x_i [118].

Here the set of N measurements from the selected sensors $\boldsymbol{z} = [z_1, \ldots, z_N]^{\mathrm{T}} \in \mathbb{R}^N$ can be expressed in terms of the following binary selection matrix (not to be confused with $\boldsymbol{S}$):

$$\boldsymbol{V} = [\boldsymbol{v}_1^{\mathrm{T}}, \ldots, \boldsymbol{v}_N^{\mathrm{T}}]^{\mathrm{T}} \in \{0,1\}^{N\times M}, \tag{4.12}$$

---

[3] Different than before, here sensors transmit directly to the CN (without the presence of a fusion center).

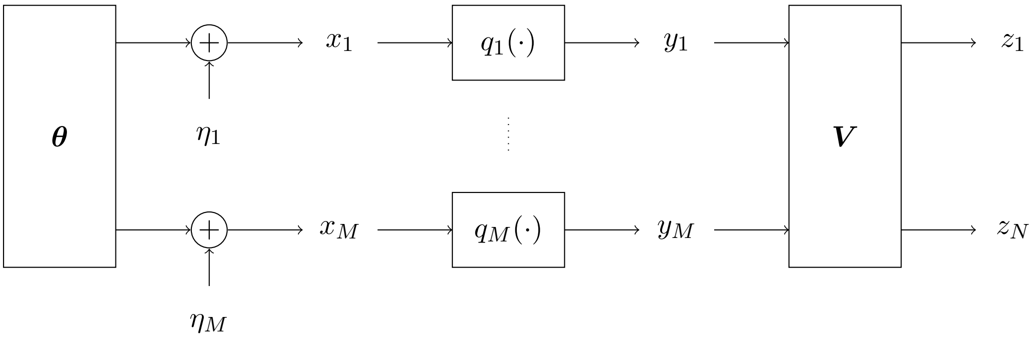

Figure 4.4: Communication scheme for the estimation perspective.

where each row $\boldsymbol{v}_i \in \{0,1\}^{1\times M}$, with $i \in \{1,\dots,N\}$, is a unit vector indicating which sensor is transmitting (i.e., the position of the non-zero element determines the active sensing device). In fact, this selection matrix is related to that in the previous subsection since $\boldsymbol{S} = \boldsymbol{V}^{\mathrm{T}}\boldsymbol{V}$.

As an illustrative example, let us consider $M = 5$, $N = 3$ and

$$\boldsymbol{V} = \begin{bmatrix} 1 & 0 & 0 & 0 & 0 \\ 0 & 0 & 1 & 0 & 0 \\ 0 & 0 & 0 & 1 & 0 \end{bmatrix}. \tag{4.13}$$

In this case, the first, third, and fourth sensors are selected to transmit their measurements. Note that all rows in $\boldsymbol{V}$ must be different, which is equivalent to the constraint $\boldsymbol{V}\boldsymbol{V}^{\mathrm{T}} = \mathbf{I}_N$.

The vector $\boldsymbol{z}$ can be written as

$$\boldsymbol{z} = \boldsymbol{V}\boldsymbol{y}, \tag{4.14}$$

where $\boldsymbol{y} = [y_1,\dots,y_M]^{\mathrm{T}}$ is the original set of quantized measurements. The associated communication scheme is shown in Figure 4.4.

4.3.2.1 Decoding Error Probability

Recall that, prior to transmission, the k_i source symbols are encoded into l_i information bits and later transformed into n_i transmit symbols (cf. Chapter 2). In that sense, given that sensors quantize their observations using b_i bits, we consider that we have $l_i = b_i$ information bits at the output of the source encoder[4] (cf. Figure 2.1). This quantity can be expressed as

$$b_i \triangleq T_s B_s R_i^{\mathcal{C}} R_i^{\mathcal{M}}, \tag{4.15}$$

where $T_s B_s$ represents the number of transmit symbols (cus) per slot, i.e., $n_i = T_s B_s \; \forall i$.

---

[4] Typically, a (simple) source encoder is constructed with scalar quantizers followed by entropy coding [104]. This way, the number of quantization bits b_i can be reduced with lossless compression. In fact, by particularizing the expression in (4.4) for $M = 1$, we find that l_i can be approximated as $h(X_i) - \log(\Delta_i) = h(X_i) + b_i - \log(\mathcal{D}_i) \leq b_i$. However, in the parameter estimation perspective, we omit this second stage and concentrate on the sole use of (fixed-rate) uniform scalar quantizers $q_i(\cdot)$. Thus, for simplicity, here we assume $l_i = b_i$.

Given that both T_s and B_s are fixed, the number of (information) bits to be transmitted b_i only depends on the MCS, i.e., the different combinations of $R_i^{\mathcal{C}}$ and $R_i^{\mathcal{M}}$. Note that the product $R_i = R_i^{\mathcal{C}} R_i^{\mathcal{M}}$ yields the spectral efficiency, that is, the ratio between the number of information bits and the number of transmit symbols (cf. Chapter 2).

With the above considerations, the CN will decode the (selected) quantized observations with individual error probabilities, which depend on the channel quality, the MCS, and the number of bits b_i of each sensor. These probabilities are already defined in Subsection 2.2.2.2:

$$\mathrm{PER}_i = \mathcal{C}_i\left(1 - (1 - \mathrm{BER}_i^{\mathrm{raw}})^{T_s B_s R_i^{\mathcal{M}}}\right), \tag{4.16}$$

which follows from (4.15) and the definition of $R_i^{\mathcal{C}}$. For the sake of generality, the coding functions $\mathcal{C}_i(\cdot)$ will not be detailed until Subsection 4.6.2.

4.3.2.2 MMSE Estimate

Once the transmitted bits are decoded, the CN will use them to estimate the parameter vector $\boldsymbol{\theta}$ from the observation vector $\boldsymbol{z}$. In that sense, the device selection and the number of quantization bits $\boldsymbol{b} = [b_1, \ldots, b_M]^{\mathrm{T}}$ will be designed to optimize the estimation accuracy.

To evaluate the whole procedure, in this subsection, we consider the MSE as a performance indicator. As a result, a suitable estimate of $\boldsymbol{\theta}$ is the linear MMSE estimate given by (we first assume that no errors occur in the communication link) [92]:

$$\hat{\boldsymbol{\theta}} \triangleq \mathbb{E}[\boldsymbol{\theta}|\boldsymbol{z}] = \boldsymbol{C}_{\boldsymbol{\theta z}} \boldsymbol{C}_{\boldsymbol{z}}^{-1} (\boldsymbol{z} - \mathbb{E}[\boldsymbol{z}]) + \boldsymbol{\mu}_{\boldsymbol{\theta}}. \tag{4.17}$$

Considering the uncorrelation between $\boldsymbol{x}$ and the quantization errors $\boldsymbol{w} = [w_1, \ldots, w_M]^{\mathrm{T}}$, the statistical terms in (4.17) yield[5]

$$\boldsymbol{C}_{\boldsymbol{\theta z}} \triangleq \mathbb{E}\left[\boldsymbol{\theta} \boldsymbol{z}^{\mathrm{T}}\right] = \mathbb{E}\left[\boldsymbol{\theta}(\boldsymbol{\theta} + \boldsymbol{\eta} + \boldsymbol{w})^{\mathrm{T}} \boldsymbol{V}^{\mathrm{T}}\right] = \boldsymbol{C}_{\boldsymbol{\theta}} \boldsymbol{V}^{\mathrm{T}}, \tag{4.18}$$

$$\boldsymbol{C}_{\boldsymbol{z}} \triangleq \mathbb{E}\left[\boldsymbol{z} \boldsymbol{z}^{\mathrm{T}}\right] = \boldsymbol{V}\left(\boldsymbol{C}_{\boldsymbol{\theta}} + \boldsymbol{C}_{\boldsymbol{\eta}} + \boldsymbol{C}_{\boldsymbol{w}}\right) \boldsymbol{V}^{\mathrm{T}}, \tag{4.19}$$

$$\mathbb{E}[\boldsymbol{z}] = \boldsymbol{V} \boldsymbol{\mu}_{\boldsymbol{\theta}}, \tag{4.20}$$

where $\boldsymbol{C}_{\boldsymbol{w}} \triangleq \mathrm{diag}\left(\Delta_1^2/12, \ldots, \Delta_M^2/12\right)$ in (4.19). Note that this expression corresponds to the second-order moments of the uncorrelated and uniformly distributed quantization errors.

Consequently, the MSE is given by the trace of the error covariance matrix $\boldsymbol{\Sigma}$ [92]

$$\boldsymbol{\Sigma} \triangleq \mathbb{E}\left[\left(\boldsymbol{\theta} - \hat{\boldsymbol{\theta}}\right)\left(\boldsymbol{\theta} - \hat{\boldsymbol{\theta}}\right)^{\mathrm{T}} \middle| \boldsymbol{z}\right] = \boldsymbol{C}_{\boldsymbol{\theta}} - \boldsymbol{C}_{\boldsymbol{\theta z}} \boldsymbol{C}_{\boldsymbol{z}}^{-1} \boldsymbol{C}_{\boldsymbol{z \theta}}, \tag{4.21}$$

where, following the derivations in (4.18), it can be seen that $\boldsymbol{C}_{\boldsymbol{z\theta}} = \boldsymbol{V} \boldsymbol{C}_{\boldsymbol{\theta}}$.

Note that, in the expressions above, we have considered that there were no errors in the communication. However, as we discussed in the previous subsection, packets might be incorrectly decoded with probability PER_i for the set of active sensors. In that case, the packet would be thrown away and the corresponding elements of $\boldsymbol{z}$ would be discarded as well.

---

[5] In the case of singular covariance matrices $\boldsymbol{C}_{\boldsymbol{\theta}}$ (cf. Subsection 4.3.1), all these expressions remain unaltered.

To formulate this, we can replace the matrix $\boldsymbol{V}$ by the following matrix:

$$\boldsymbol{U}_{\mathcal{I}} \triangleq \boldsymbol{A}_{\mathcal{I}}\boldsymbol{V} \in \{0,1\}^{|\mathcal{I}|\times M}, \tag{4.22}$$

where $\mathcal{I}$ is the set of active sensors with correctly decoded messages and $\boldsymbol{A}_{\mathcal{I}} \in \{0,1\}^{|\mathcal{I}|\times N}$ is the corresponding flat matrix indicating the absence of errors. In that sense, similar to $\boldsymbol{V}$, the non-zero positions in the (unit) rows of matrix $\boldsymbol{A}_{\mathcal{I}}$ define the (active) sensing devices with perfectly decoded messages. This way, $\boldsymbol{U}_{\mathcal{I}}$ is a binary flat matrix that represents the information finally available at the CN (after device selection and packet decoding).

Considering the decoding errors, now the set of available measurements at the CN yields

$$\boldsymbol{z}_{\mathcal{I}} \triangleq \boldsymbol{U}_{\mathcal{I}}\boldsymbol{y} \in \mathbb{R}^{|\mathcal{I}|}, \tag{4.23}$$

and, thus, the corresponding MMSE estimate can be written as

$$\hat{\boldsymbol{\theta}}_{\mathcal{I}} \triangleq \mathbb{E}[\boldsymbol{\theta}|\boldsymbol{z}_{\mathcal{I}}] = \boldsymbol{C}_{\boldsymbol{\theta}}\boldsymbol{U}_{\mathcal{I}}^{\mathrm{T}}\left(\boldsymbol{U}_{\mathcal{I}}\left(\boldsymbol{C}_{\boldsymbol{\theta}}+\boldsymbol{C}_{\boldsymbol{\eta}}+\boldsymbol{C}_{\boldsymbol{w}}\right)\boldsymbol{U}_{\mathcal{I}}^{\mathrm{T}}\right)^{-1}\left(\boldsymbol{z}_{\mathcal{I}}-\mathbb{E}[\boldsymbol{z}_{\mathcal{I}}]\right)+\boldsymbol{\mu}_{\boldsymbol{\theta}}, \tag{4.24}$$

with MSE:

$$\varepsilon_{\mathcal{I}} \triangleq \mathrm{tr}\big(\boldsymbol{C}_{\boldsymbol{\theta}}-\boldsymbol{C}_{\boldsymbol{\theta}}\boldsymbol{U}_{\mathcal{I}}^{\mathrm{T}}\left(\boldsymbol{U}_{\mathcal{I}}\left(\boldsymbol{C}_{\boldsymbol{\theta}}+\boldsymbol{C}_{\boldsymbol{\eta}}+\boldsymbol{C}_{\boldsymbol{w}}\right)\boldsymbol{U}_{\mathcal{I}}^{\mathrm{T}}\right)^{-1}\boldsymbol{U}_{\mathcal{I}}\boldsymbol{C}_{\boldsymbol{\theta}}\big). \tag{4.25}$$

Hence, we can define the overall MSE by averaging over the different error probabilities[6]:

$$\varepsilon \triangleq \sum_{m=0}^{N}\sum_{\mathcal{I}\in\mathcal{F}_m}\varepsilon_{\mathcal{I}}\prod_{i\in\mathcal{I}}(1-\mathrm{PER}_i)\prod_{j\notin\mathcal{I}}\mathrm{PER}_j, \tag{4.26}$$

where $\mathcal{F}_m$ represents all the tuples of size $N-m$ taken from the set of active sensors defined by $\boldsymbol{V}$. Thus, the subindex m indicates the number of incorrect messages. Going back to the previous example (cf. (4.13)), we have that $\mathcal{F}_1 = \{\{1,3\},\{1,4\},\{3,4\}\}$ and $\mathcal{F}_2 = \{\{1\},\{3\},\{4\}\}$. Note that $\mathcal{F}_0 = \{\{1,3,4\}\}$ always refers to the case of no errors.

4.4 Device Selection and Data Quantization

The purpose of this chapter is to present a selection strategy that minimizes the loss of information when silencing some sensors. In line with the discussions above, this loss can be measured with the source entropy from (4.9) or the error of the parameter estimation defined in (4.26). In the latter, the number of precision bits b_i in the quantization stage is also optimized.

4.4.1 Entropy Perspective

4.4.1.1 Problem Formulation

In this subsection, we explore the device selection paradigm from the entropy perspective. Accordingly, we will take advantage of the potentially high correlation within the sensed data,

---

[6] In the entropy analysis, a similar approach could be used to include the possible communication errors.

which often yields an ill-conditioned covariance matrix $\boldsymbol{C} = \boldsymbol{C}_{\boldsymbol{\theta}}$, and select as active sensors those with the highest impact on $\boldsymbol{C}$[7]. Note that as this matrix is singular, the number of sensors to keep active does not increase substantially with M [101].

The goal is to find a matrix $\boldsymbol{S}$ that maximizes $H(\boldsymbol{Z})$ under a power constraint. To that end, we consider the following optimization problem:

$$\boldsymbol{s}^{\star} = \underset{\boldsymbol{s}\in\{0,1\}^M}{\text{argmax}} \; H(\boldsymbol{Z}) \quad \text{s.t.} \quad \|f(\boldsymbol{s})\| \leq \delta, \tag{4.27}$$

where $\boldsymbol{s} = [s_1, \ldots, s_M]$ is the diagonal of $\boldsymbol{S}$, $\|f(\boldsymbol{s})\|$ represents the power-related constraint, and $\delta > 0$ determines the associated threshold. Note that the constraint can be formulated in a norm-basis thanks to the vectorized form $\boldsymbol{s}$ (which yields the optimal $\boldsymbol{S}$).

Given that the lower bound $\widetilde{H}(\boldsymbol{Z})$ becomes tight for small Δ, we can use it as the objective function in (4.27). The exact error of this approximation will be illustrated in Subsection 4.6.1.

Then, when maximizing this lower bound, the problem in (4.27) becomes

$$\boldsymbol{s}^{\star} = \underset{\boldsymbol{s}\in\{0,1\}^M}{\text{argmax}} \; \widetilde{H}(\boldsymbol{Z}) \quad \text{s.t.} \quad \|f(\boldsymbol{s})\| \leq \delta. \tag{4.28}$$

Regarding the constraint function $\|f(\boldsymbol{s})\|$, we can use different approaches. For instance, some reasonable options are:

(i) Number of active sensors: $\|\boldsymbol{s}\|_0$,

(ii) Sum of transmit powers: $\|\boldsymbol{s} \odot \boldsymbol{P}\|_1$,

(iii) Maximum transmit power: $\|\boldsymbol{s} \odot \boldsymbol{P}\|_\infty$,

where $\boldsymbol{P} = [P_1, \ldots, P_M]^{\mathrm{T}}$ is the vector containing the set of individual sensor's transmit powers[8] (cf. Section 2.3). When applied to (4.28), (i) determines the sparsity of $\boldsymbol{s}$ and, although it does not consider the power $\boldsymbol{P}$, it can reduce the consumption since it limits the number of active (sensing and transmitting) devices, i.e., $\|\boldsymbol{s}\|_0 = N$. On the other hand, since (ii) and (iii) consider transmit power, both can improve the system's energy consumption better than (i). However, since $\boldsymbol{P}$ is usually fixed, (iii) has no special interest as the solution would be a trivial thresholding irrespective of $\widetilde{H}(\boldsymbol{Z})$, i.e., $s_i = 1$ for all sensors with power P_i below δ. As a result, in this chapter, we will only focus on (i) and (ii).

Overall, given the binary nature of $\boldsymbol{s}$, we formulate a lossy information (or data compression) approach that prioritizes the relevant components of the sensed data (i.e., those with more information). This way, we end up with a system that delivers most of the relevant information with the benefit of reduced energy consumption, i.e., the battery lifetime can be extended with similar performance. Unfortunately, the solution to problem (4.28) is combinatorial and might be unfeasible to solve for large M. That is why in Subsection 4.4.1.2, we propose some simplifications to reduce computational cost.

---

[7] In the presence of a measurement noise $\boldsymbol{\eta}$, this matrix might not be rank deficient. However, as mentioned in Subsection 4.6.1, the same derivation holds and a similar analysis can be applied.

[8] In practical mMTC systems, most of the energy comes from the actual transmission of data. That is why the rest of the processes affecting the power consumption (e.g., sensing, processing, etc.) are omitted.

4.4.1.2 Proposed Solution

To reduce problem (4.28) to a feasible complexity, in this subsection, we take the following steps: relaxation of the constraint set, approximation of the objective function, and rounding of the obtained (sub-optimal) solution. Hence, we end up with a convex optimization problem, easy to solve with standard numerical methods, while still providing good performance.

We start by substituting the discrete constraint on $\boldsymbol{b}$, i.e., $\boldsymbol{b} \in \{0,1\}^M$, by a convex relaxation. More specifically, now $\boldsymbol{b}$ can take continuous values between 0 and 1, i.e., $\boldsymbol{b} \in [0,1]^M$. Thereby, we can express the new continuous problem as follows:

$$\boldsymbol{b}^\star = \underset{\boldsymbol{b}\in[0,1]^M}{\operatorname{argmax}}\ \widetilde{H}(\boldsymbol{Z}) \quad \text{s.t.} \quad \|f(\boldsymbol{b})\| \le \delta. \tag{4.29}$$

Note that the $\log \operatorname{Det}$ function in $\widetilde{H}(\boldsymbol{Z})$ is not concave in $\boldsymbol{S}$ as the Det function is discontinuous [117]. That is why, in order to deal with proper determinants, we make use of the Cholesky decomposition of the covariance matrix [119]. Since $\boldsymbol{C}$ is symmetric and positive semi-definite ($\boldsymbol{C} \succeq \boldsymbol{0}$), there exists a lower triangular matrix $\boldsymbol{L} \in \mathbb{R}^{M\times M}$ such that $\boldsymbol{C} = \boldsymbol{L}\boldsymbol{L}^{\mathrm{T}}$. Note that for rank-deficient $\boldsymbol{C}$, the matrix $\boldsymbol{L}$ will have $M - r(\boldsymbol{C})$ columns equal to zero, i.e.,

$$\boldsymbol{L} = \begin{bmatrix} l_{11} & 0 & 0 & \dots & 0 & \dots & 0 \\ l_{21} & l_{22} & 0 & \dots & 0 & \dots & 0 \\ \vdots & \vdots & \ddots & \ddots & \vdots & & \vdots \\ l_{M1} & l_{M2} & \dots & l_{Mr(\boldsymbol{C})} & 0 & \dots & 0 \end{bmatrix} = [\boldsymbol{L}_r \,|\, \boldsymbol{0}], \tag{4.30}$$

with $\boldsymbol{L}_r \in \mathbb{R}^{M\times r(\boldsymbol{C})}$ the reduced version of $\boldsymbol{L}$. This way, the covariance matrix can be expressed as $\boldsymbol{C} = \boldsymbol{L}_r\boldsymbol{L}_r^{\mathrm{T}}$. In addition, the pseudo-determinant is also invariant to matrix translations [117]:

$$\operatorname{Det}(\boldsymbol{C}) = \operatorname{Det}\left(\boldsymbol{L}_r\boldsymbol{L}_r^{\mathrm{T}}\right) = \operatorname{Det}\left(\boldsymbol{L}_r^{\mathrm{T}}\boldsymbol{L}_r\right) = \det\left(\boldsymbol{L}_r^{\mathrm{T}}\boldsymbol{L}_r\right). \tag{4.31}$$

Similarly, we can write $\operatorname{Det}(\boldsymbol{SCS}) = \operatorname{Det}(\boldsymbol{L}_r^{\mathrm{T}}\boldsymbol{SSL}_r)$, which becomes a proper determinant if the selection matrix is positive definite, i.e., $\boldsymbol{S} \succ \boldsymbol{0}$. In that case, the $\log \operatorname{Det}$ in $\widetilde{H}(\boldsymbol{Z})$ yields the (continuous) $\log\det$. Nevertheless, the $\log\det$ function is still not concave in $\boldsymbol{S}$. In what follows, we use instead the matrix $\boldsymbol{T} = \operatorname{diag}(\boldsymbol{t}) \triangleq \boldsymbol{SS} = \boldsymbol{S}^2$, and rewrite problem (4.29) as

$$\boldsymbol{t}^\star = \underset{\boldsymbol{t}\in[0,1]^M}{\operatorname{argmax}}\ \widetilde{H}(\boldsymbol{Z}) \quad \text{s.t.} \quad \|f(\boldsymbol{t})\| \le \delta, \tag{4.32}$$

where now, neglecting (iii), the constraint functions in $\boldsymbol{t}$ are given by

(i) Number of active sensors: $\|\boldsymbol{t}\|_0$,

(ii) Sum of transmit powers: $\|\boldsymbol{t} \odot \boldsymbol{T}\|_1 = \operatorname{tr}(\boldsymbol{T}\operatorname{diag}(\boldsymbol{P}))$.

As a second step, we substitute the rank in the objective function $\widetilde{H}(\boldsymbol{Z})$ from (4.32) by its nuclear norm [120], producing a lower bound of the objective function to be maximized and that can be shown to be concave in $\boldsymbol{T}$ for $\boldsymbol{T} \succ \boldsymbol{0}$ (please, refer to Appendix 4.B for more details on the derivation of this bound, denoted by $\widetilde{H}_{lb}(\boldsymbol{Z})$). Besides, we also substitute the l_0 quasi-norm in (i) by its closest convex approximation, namely, the l_1 norm $\|\boldsymbol{t}\|_1 = \text{tr}(\boldsymbol{T})$ [121].

Note that the condition $\boldsymbol{T} \succ \mathbf{0}$ can be ensured by imposing $\boldsymbol{T} - \xi\mathbf{I} \succeq \mathbf{0}$ for a sufficiently small $\xi > 0$, which is equivalent to $t_i \geq \xi \; \forall i$. In fact, since we eventually round the solution, $t_i = \xi$ or $t_i = 0$ would lead to the same binary value (i.e., the same final solution). This practice is widely used in the area of sparse sensing (see [122] and references therein).

As shown in Appendix 4.B, thanks to the previous steps, we can end up with the following convex problem (maximization of a concave function subject to convex constraints), where the optimization variable is the diagonal matrix $\boldsymbol{T}$:

$$\boldsymbol{T}^{\star} = \underset{\boldsymbol{T}=\text{diag}(\boldsymbol{t}),\ \boldsymbol{t}\in[\xi,1]^M}{\text{argmax}} \quad \widetilde{H}_{lb}(\boldsymbol{Z}) \quad \text{s.t.} \quad \text{tr}\left(f(\boldsymbol{T})\right) \leq \delta. \tag{4.33}$$

Nevertheless, due to the determinant, an analytic closed-form solution is hard to find, even for small M. That is the reason why, given the convexity of the problem, standard optimization methods are used to find the global solution numerically [123]. More specifically, in order to solve (4.33), we use the successive approximation method with the SDPT3 solver of the CVX software package and set the precision to high [124]. Finally, once the solution is found in the continuous domain, we need to return to the discrete regime. To do so, we threshold (round) the solution such that the constraints are satisfied, i.e., activate sensors with the largest $t_i^{\star}$ until (i) or (ii) are fulfilled.

4.4.2 Estimation Perspective

4.4.2.1 Problem Formulation

The purpose of this subsection is to derive a selection strategy and a quantization scheme that minimize the MSE in (4.26) so that only N sensors are active and transmitting during a single frame with limited power consumption. More specifically, we are interested in designing the optimal selection matrix $\boldsymbol{V}$ and the optimal number of quantization bits $\boldsymbol{b}$.

Note that, under the previous assumptions, the power consumption in the estimation setup can be defined as $\text{tr}(\boldsymbol{V}\text{diag}(\boldsymbol{P})\boldsymbol{V}^{\mathrm{T}})$. In that sense, $\text{tr}(\text{diag}(\boldsymbol{P}) - \boldsymbol{V}\text{diag}(\boldsymbol{P})\boldsymbol{V}^{\mathrm{T}})$ will represent the power reduction attained with the sensor selection. As mentioned earlier, $\text{tr}(\boldsymbol{V}\text{diag}(\boldsymbol{P})\boldsymbol{V}^{\mathrm{T}})$ will be constrained to a maximum value in order to limit the network power consumption.

Thereby, the optimization problem can be formulated as follows:

$$\{\boldsymbol{V}^{\star}, \boldsymbol{b}^{\star}\} = \underset{\substack{\boldsymbol{V}\in\{0,1\}^{N\times M} \\ \boldsymbol{b}\in\mathbb{N}^M}}{\text{argmin}} \; \varepsilon \quad \text{s.t.} \quad \boldsymbol{V}\boldsymbol{V}^{\mathrm{T}} = \mathbf{I}_N, \quad \text{tr}\left(\boldsymbol{V}\text{diag}(\boldsymbol{P})\boldsymbol{V}^{\mathrm{T}}\right) \leq \delta, \tag{4.34}$$

where the first constraint ensures that only N sensors are selected (equivalent to constraint (i) from Subsection 4.4.1.1), and the second one guarantees that the power consumption of the selected devices is below a given threshold δ (equivalent to constraint (ii) from Subsection 4.4.1.1). Note that the individual powers P_i are considered to be fixed (not optimized) and different among them. This way, thanks to the second constraint, we can avoid selecting simultaneously sensors with (only) high powers, yet concentrate on combining devices with high and low (or simply low) consumption. Besides, in realistic scenarios, the number of bits might be further restricted to minimum and maximum values, both depending on the capability of the sensing devices. Hence, the space dimension of $\boldsymbol{b}$ can be considerably reduced.

Unfortunately, given the expression of the objective function and the discrete nature of the optimization variables, the problem in (4.34) is combinatorial and has exponential complexity. That is why in this subsection, we will use some simplifications to reduce the optimization complexity and find a (feasible) sub-optimal solution with still good performance.

First, since we want to minimize the MSE ε, let us define the following upper bound:

$$\varepsilon \leq p_{\mathcal{F}_0}\varepsilon_{\mathcal{F}_0} + \sum_{m=1}^{G}\sum_{\mathcal{I}\in\mathcal{F}_m} p_{\mathcal{I}}\varepsilon_{\mathcal{I}} + p_G\varepsilon_{\mathcal{F}_N} \triangleq \bar{\varepsilon}_G, \tag{4.35}$$

with

$$p_{\mathcal{F}_0} \triangleq \prod_{i\in\mathcal{I},\mathcal{I}\in\mathcal{F}_0} (1-\text{PER}_i), \tag{4.36}$$

$$p_{\mathcal{I}} \triangleq \prod_{i\in\mathcal{I}} (1-\text{PER}_i) \prod_{j\notin\mathcal{I}} \text{PER}_j, \tag{4.37}$$

$$p_G \triangleq \sum_{m=G+1}^{N}\sum_{\mathcal{I}\in\mathcal{F}_m} p_{\mathcal{I}} = 1 - \left(p_{\mathcal{F}_0} + \sum_{m=1}^{G}\sum_{\mathcal{I}\in\mathcal{F}_m} p_{\mathcal{I}}\right). \tag{4.38}$$

The upper bound in (4.35) follows from the fact that $\varepsilon_{\mathcal{I}} \leq \varepsilon_{\mathcal{F}_N} = \text{tr}\left(\boldsymbol{C}_{\boldsymbol{\theta}}\right)$, where $\mathcal{F}_N = \emptyset$ represents the case of all errors. In addition, $G \in \{1, \ldots, N-1\}$ denotes the number of incorrect packets that are allowed in the decoding process before estimating $\boldsymbol{\theta}$. As an illustrative example, if $G = 2$, only two packets can contain errors; otherwise, the estimation is not carried out. Besides that, note that equality in (4.35) is achieved for $G = N - 1$.

As a result, we can rewrite problem (4.34) as the minimization of the MSE upper bound $\bar{\varepsilon}_G$:

$$\{\boldsymbol{V}^\star, \boldsymbol{b}^\star\} = \underset{\substack{\boldsymbol{V}\in\{0,1\}^{N\times M}\\ \boldsymbol{b}\in\mathbb{N}^M}}{\text{argmin}}\ \bar{\varepsilon}_G \quad \text{s.t.} \quad \boldsymbol{V}\boldsymbol{V}^{\mathrm{T}} = \mathbf{I}_N, \quad \text{tr}\left(\boldsymbol{V}\text{diag}(\boldsymbol{P})\boldsymbol{V}^{\mathrm{T}}\right) \leq \delta. \tag{4.39}$$

Considering the large number of devices involved in mMTC networks and the fact that, for practical systems, the individual error probabilities PER_i tend to be small, the terms with $G > 1$ vanish quickly. This is because the second product in $p_{\mathcal{I}}$ tends to zero for small PER_i and increasing G. Hence, working with small values of G can yield a tight approximation. The accuracy of this bound will be further studied and properly justified through simulations in Subsection 4.6.2. Thus, although problem (4.39) constitutes a worse-case scenario (minimization of an upper bound), its solution approaches that of (4.34) even for a small G.

The last step is to find the solution of the problem defined in (4.39), i.e., the optimal $\boldsymbol{V}^\star$ and $\boldsymbol{b}^\star$. Unfortunately, an analytic closed-form expression cannot be found, even for a small N and M. That is why, to find the solution to the previous problem, we make use of greedy iterative methods [125]. In that sense, first, we consider the separate optimization of $\boldsymbol{V}$ and $\boldsymbol{b}$ and, later, we concentrate on the joint optimization. Note that the latter will lead to better performance, yet at the cost of more computational complexity. This is discussed in Subsection 4.4.2.2.

4.4.2.2 Proposed Solution

4.4.2.2.1 Separate Optimization

The problem in (4.39) can be decomposed into two optimizations, where $\boldsymbol{V}$ and $\boldsymbol{b}$ are optimized separately. On the one hand, given the number of bits $\boldsymbol{b}$, (4.39) yields

$$\boldsymbol{V}^{\star} = \underset{\boldsymbol{V} \in \{0,1\}^{N \times M}}{\text{argmin}} \; \bar{\varepsilon}_G \quad \text{s.t.} \quad \boldsymbol{V}\boldsymbol{V}^{\mathrm{T}} = \mathbf{I}_N, \quad \text{tr}\left(\boldsymbol{V}\text{diag}(\boldsymbol{P})\boldsymbol{V}^{\mathrm{T}}\right) \leq \delta, \tag{4.40}$$

which can be solved sequentially. At each step, we consider that $N-1$ rows are given and, hence, the search concerns the remaining row [126].

For instance, considering the first step, the device selection matrix $\boldsymbol{V}$ can be expressed as

$$\boldsymbol{V} = [\boldsymbol{v}_1^{\mathrm{T}} \, \tilde{\boldsymbol{V}}_1^{\mathrm{T}}]^{\mathrm{T}}, \tag{4.41}$$

with $\boldsymbol{v}_1 \in \{0,1\}^{1 \times M}$ the first row and $\tilde{\boldsymbol{V}}_1 = [\boldsymbol{v}_2^{\mathrm{T}}, \ldots, \boldsymbol{v}_N^{\mathrm{T}}]^{\mathrm{T}} \in \{0,1\}^{(N-1) \times M}$ the rest of the fixed rows. As each row can only contain one non-zero element and all rows must be different (constraints imposed by $\boldsymbol{V}\boldsymbol{V}^{\mathrm{T}} = \mathbf{I}_N$), the optimal $\boldsymbol{v}_1$ is found by one-dimensional search:

$$\boldsymbol{v}_1^{\star} = \underset{\boldsymbol{v}_1 \in \{0,1\}^{1 \times M}}{\text{argmin}} \; \bar{\varepsilon}_G \quad \text{s.t.} \quad [\boldsymbol{v}_1^{\mathrm{T}} \, \tilde{\boldsymbol{V}}_1^{\mathrm{T}}]^{\mathrm{T}}[\boldsymbol{v}_1^{\mathrm{T}} \, \tilde{\boldsymbol{V}}_1^{\mathrm{T}}] = \mathbf{I}_N \quad \text{tr}\left([\boldsymbol{v}_1^{\mathrm{T}} \, \tilde{\boldsymbol{V}}_1^{\mathrm{T}}]^{\mathrm{T}}\text{diag}(\boldsymbol{P})[\boldsymbol{v}_1^{\mathrm{T}} \, \tilde{\boldsymbol{V}}_1^{\mathrm{T}}]\right) \leq \delta. \tag{4.42}$$

This operation is then repeated for all rows in the same way as it has been done with the first row, and going back to the first one until convergence is reached or when the MSE reduction is below a given threshold. Note that, as the optimization criterion is the minimization of the MSE, and one of the possibilities is to keep the same values (for $\boldsymbol{v}_i$) from the previous iteration, the new variable selection will always improve (i.e., decrease) the MSE or, in the worst case, keep the same. Thanks to that, convergence is always assured since we generate a monotonous decreasing sequence of values for the MSE.

As the search space is discrete, an analytic closed-form solution cannot be derived, yet it is found numerically by exhaustive search. In this case, the complexity grows linearly with the number of search elements since to solve (4.42), we only need to evaluate $M - N + 1$ values (i.e., the number of silent sensors that can be potentially activated).

It is noteworthy to mention that, since the MSE defined in (4.25) is invariant to row permutations of the selection matrix $\boldsymbol{V}$ [95], it can be shown that the total MSE ε and the upper bound $\bar{\varepsilon}_G$ are also invariant to row re-ordering. For instance, if $M = 3$ and $N = 2$, the results with $\boldsymbol{v}_1 = [010]$ and $\boldsymbol{v}_2 = [100]$ are equivalent to those with $\boldsymbol{v}_1 = [100]$ and $\boldsymbol{v}_2 = [010]$.

Similarly, when the selection matrix $\boldsymbol{V}$ is known, problem (4.39) reads as

$$\boldsymbol{b}^{\star} = \underset{\boldsymbol{b} \in \mathbb{N}^M}{\text{argmin}} \; \bar{\varepsilon}_G, \tag{4.43}$$

which can also be solved through a sequential (and iterative) procedure. Considering that the last $M-1$ elements in $\boldsymbol{b}$ are given, at each step the optimization becomes

$$b_1^{\star} = \underset{b_1 \in \mathbb{N}}{\text{argmin}} \; \bar{\varepsilon}_G, \tag{4.44}$$

Algorithm 4.1 Separate (alternating) optimization to solve (4.39)

```
Initialize[9] $\boldsymbol{V}$ and $\boldsymbol{b}$
repeat
    repeat
        for $i = 1 : N$ do
            Solve (4.42) through one-dimensional search to find $\boldsymbol{v}_i^\star$
            Set $\boldsymbol{v}_i = \boldsymbol{v}_i^\star$
        end for
    until Convergence is reached (or the MSE is below a given threshold)
    repeat
        for $j = 1 : M$ do
            Solve (4.44) through one-dimensional search to find $b_j^\star$
            Set $b_j = b_j^\star$
        end for
    until Convergence is reached (or the MSE is below a given threshold)
until Convergence is reached (or the MSE is below a given threshold)
```

procedure that is also repeated for all elements in $\boldsymbol{b}$ and iterated until converge is reached. As before, convergence is guaranteed because each iteration yields the same or a lower MSE (i.e., we can always keep the previous value for b_i, which will maintain the MSE, or select a new one that decreases the estimation error). Like in (4.42), we use exhaustive search to solve (4.44) given that the search space is also discrete and an analytic closed-form solution cannot be found. Additionally, since the number of quantization bits is usually limited (i.e., $b_i \leq W$, with W the maximum number of quantization bits), the number of possibilities that we actually evaluate is given by this upper bound W.

Finally, the two separate optimizations are sequentially alternated to find a (sub-optimal) stationary solution. This way, the resulting MSE will monotonically decrease until a local minimum is attained (or when the MSE is below a given threshold). The entire procedure is summarized in Algorithm 4.1.

4.4.2.2.2 Joint Optimization

Instead of considering the separate approach described above, we can search for the solution of $\boldsymbol{V}$ and $\boldsymbol{b}$ simultaneously through a similar iterative procedure. More specifically, we consider that $N-1$ rows of $\boldsymbol{V}$ and $M-1$ elements of $\boldsymbol{b}$ are given. Without loss of generality, we discuss the optimization of the first row of $\boldsymbol{V}$ like in (4.41), and the corresponding element in $\boldsymbol{b}$, which depends on the device selection. Hence, at each step, we look for the optimal solution through a two-dimensional search:

$$\left\{\boldsymbol{v}_1^\star, b^\star_{i(\boldsymbol{v}_1)}\right\} = \underset{\substack{\boldsymbol{v}_1\in\{0,1\}^{1\times M}\\ b_{i(\boldsymbol{v}_1)}\in\mathbb{N}}}{\text{argmin}} \ \bar{\varepsilon}_G \quad \text{s.t.} \quad [\boldsymbol{v}_1^{\mathrm{T}}\ \tilde{\boldsymbol{V}}_1^{\mathrm{T}}]^{\mathrm{T}}[\boldsymbol{v}_1^{\mathrm{T}}\ \tilde{\boldsymbol{V}}_1^{\mathrm{T}}] = \mathbf{I}_N, \quad \text{tr}\left([\boldsymbol{v}_1^{\mathrm{T}}\ \tilde{\boldsymbol{V}}_1^{\mathrm{T}}]^{\mathrm{T}}\text{diag}(\boldsymbol{P})[\boldsymbol{v}_1^{\mathrm{T}}\ \tilde{\boldsymbol{V}}_1^{\mathrm{T}}]\right) \leq \delta, \tag{4.45}$$

where the index $i(\boldsymbol{v}_1)$ represents the sensor selected in $\boldsymbol{v}_1$. For instance, if $M = 5$ and $\boldsymbol{v}_1 = [01000]$, then $i(\boldsymbol{v}_1) = 2$. Therefore, since we only optimize the quantization bits of the selected devices, the dimensionality of that search reduces from M to N (the same applies in the case of the separate optimization). The rest of the $M-N$ quantization bits can remain unspecified. As before, the other rows of $\boldsymbol{V}$ and elements of $\boldsymbol{b}$ can be found through the same procedure (i.e., two-dimensional search), which is sequentially repeated until the MSE converges.

Compared to the separate case, a higher computational complexity is required. For a maximum number of bits $W \geq b_i$, each iteration in the separate optimization requires $N(M-N+1)$ trials for the selection matrix and WN trials for the quantization. Contrarily, $N(M-N+1)WN$ trials are needed in the joint case. To take into account the total number of iterations, in the simulations section, we show the execution time required by each approach.

4.5 Extension to Temporal Correlation

As mentioned before, the previous analysis can be extended to scenarios where the parameters $\boldsymbol{\theta}$ vary over time with a given temporal correlation (apart from the already mentioned spatial correlation). Recall that this study is only performed in the estimation setup.

The evolution of these parameters will be modeled through first-order Markov processes [106, 107], and the estimation strategy to be designed at the CN will have memory to exploit that temporal correlation. Accordingly, given the MSE criterion, we make use of Kalman filters to estimate the parameter vector $\boldsymbol{\theta}$, which are optimum under the Gaussian assumption.

4.5.1 System Model

We start by considering an observation time of T frames (cf. Chapter 2). Thus, now the measurements x_i depend on the frame $t \in \{1, \dots, T\}$, i.e., $x_i(t) \in \mathbb{R}$ is the measurement of sensor i at frame t. Following the model in (4.1), at frame t we have:

$$\boldsymbol{x}(t) \triangleq \boldsymbol{\theta}(t) + \boldsymbol{\eta}(t) \in \mathbb{R}^M, \tag{4.46}$$

where $\boldsymbol{x}(t) = [x_1(t), \dots, x_M(t)]^{\mathrm{T}}$ is the set of measurements, $\boldsymbol{\theta}(t) \in \mathbb{R}^M$ is the parameter vector, and $\boldsymbol{\eta}(t) \in \mathbb{R}^M$ is the measurement noise vector. Like before, we assume $\boldsymbol{\theta}(t)$ to be Gaussian distributed with (known) mean $\boldsymbol{\mu}_{\boldsymbol{\theta}}(t)$ and covariance matrix $\boldsymbol{C}_{\boldsymbol{\theta}}(t)$, i.e., $\boldsymbol{\theta}(t) \sim \mathcal{N}(\boldsymbol{\mu}_{\boldsymbol{\theta}}(t), \boldsymbol{C}_{\boldsymbol{\theta}}(t))$. Besides, we assume that $\boldsymbol{\eta}(t)$ is independent of $\boldsymbol{\theta}(t)$, temporally uncorrelated, and Gaussian distributed with zero mean and (known) covariance matrix $\boldsymbol{C}_{\boldsymbol{\eta}}(t)$, i.e., $\boldsymbol{\eta}(t) \sim \mathcal{N}(\mathbf{0}_M, \boldsymbol{C}_{\boldsymbol{\eta}}(t))$.

On the other hand, the temporal evolution of $\boldsymbol{\theta}(t)$ can be expressed with the following first-order Markov model [95]:

$$\boldsymbol{\theta}(t) \triangleq \boldsymbol{F}(t)\boldsymbol{\theta}(t-1) + \boldsymbol{\nu}(t), \tag{4.47}$$

where $\boldsymbol{F}(t) \in \mathbb{R}^{M \times M}$ is the transition matrix, which is assumed to be known, and $\boldsymbol{\nu}(t) = [\nu_1(t), \dots, \nu_M(t)]^{\mathrm{T}} \in \mathbb{R}^M$ is the process noise, uncorrelated and independent of $\boldsymbol{\eta}(t)$ and $\boldsymbol{\theta}(t)$.

---

[9] One possibility is to initialize the selection matrix $\boldsymbol{V}$ randomly and set the vector of quantization bits $\boldsymbol{b}$ to $b_{\min}\mathbf{1}_M$, where $b_{\min}$ is the minimum number of quantization bits. Note that, although this will be the case considered in this chapter, our algorithm is independent of the variable initialization.

In addition, we also consider that $\boldsymbol{\nu}(t)$ follows a Gaussian distribution with zero mean and (known) covariance matrix $\boldsymbol{C}_{\boldsymbol{\nu}}(t)$, i.e., $\boldsymbol{\nu}(t) \sim \mathcal{N}(\mathbf{0}_M, \boldsymbol{C}_{\boldsymbol{\nu}}(t))$.

Thereby, now the quantized observations also depend on the frame index, i.e., $y_i(t) \in \mathbb{R}$ is the quantized version of $x_i(t)$ at frame t. Consequently, the vector of quantized observations $\boldsymbol{y}(t) = [y_1(t), \ldots, y_M(t)]^{\mathrm{T}} \in \mathbb{R}^M$ can be written as follows (cf. (4.11)):

$$\boldsymbol{y}(t) \triangleq \boldsymbol{x}(t) + \boldsymbol{w}(t) \in \mathbb{R}^M, \tag{4.48}$$

where $\boldsymbol{w}(t) = [w_1(t), \ldots, w_M(t)]^{\mathrm{T}} \in \mathbb{R}^M$ is the quantization noise vector. Like before, note that the elements $w_i(t)$ can be considered as uniformly distributed within the quantization interval $\Delta_i(t) = \mathcal{D}_i(t)/2^{b_i(t)}$, i.e., $w_i \sim \mathcal{U}(-\Delta_i(t)/2, \Delta_i(t)/2)$. In that sense, $b_i(t)$ is now the number of quantization bits, which may vary in time according to the MSE minimization.

This way, considering errors in the communication, the set of available quantized observations at the CN reads as (cf. (4.23))

$$\boldsymbol{z}_{\mathcal{I}(t)}(t) \triangleq \boldsymbol{A}_{\mathcal{I}(t)} \boldsymbol{V}(t) \boldsymbol{y}(t) \in \mathbb{R}^{|\mathcal{I}(t)|}, \tag{4.49}$$

where the selection matrix $\boldsymbol{V}(t) \in \{0,1\}^{N \times M}$ is also allowed to change over the frames to optimize the MSE. Note that $\mathcal{I}(t)$ is the set of active sensors with correctly decoded messages at frame t and $\boldsymbol{A}_{\mathcal{I}(t)}$ is the corresponding matrix indicating the absence of errors.

4.5.2 Parameter Estimation

Since we consider the MSE as the design criterion, a suitable choice for the MMSE estimator is the linear Kalman filter, which is optimum under the Gaussian assumption [109, 127, 128]. Thereby, now the estimation will consist of two steps, namely, prediction and correction.

As discussed in [95], the MMSE estimate of $\boldsymbol{\theta}(t)$ at frame t, assuming that the sensors with correctly detected signals are indexed by $\mathcal{I}(t)$, can be obtained recursively:

$$\hat{\boldsymbol{\theta}}_{\mathcal{I}(t)}(t|t) \triangleq \mathbb{E}[\boldsymbol{\theta}(t)|\bar{\boldsymbol{z}}(1), \ldots, \bar{\boldsymbol{z}}(t-1), \boldsymbol{z}_{\mathcal{I}(t)}(t)] = \underbrace{\hat{\boldsymbol{\theta}}(t|t-1)}_{\text{prediction}} + \underbrace{\mathbb{E}[\boldsymbol{\theta}(t)|\tilde{\boldsymbol{z}}_{\mathcal{I}(t)}(t)]}_{\text{correction}}, \tag{4.50}$$

where $\bar{\boldsymbol{z}}(1) \in \mathbb{R}^{C(1)}, \ldots, \bar{\boldsymbol{z}}(t-1) \in \mathbb{R}^{C(t-1)}$ are the sets of $C(1), \ldots, C(t-1)$ available observations (i.e., selected and correctly decoded) at previous frames $1, \ldots, t-1$; $\hat{\boldsymbol{\theta}}(t|t-1) \in \mathbb{R}^{|\mathcal{I}(t)|}$ is the prediction of $\boldsymbol{\theta}(t)$ given the available observations until frame $t-1$; and $\tilde{\boldsymbol{z}}_{\mathcal{I}(t)}(t) = \boldsymbol{z}_{\mathcal{I}(t)}(t) - \hat{\boldsymbol{z}}_{\mathcal{I}(t)}(t|t-1) \in \mathbb{R}^{|\mathcal{I}(t)|}$ is the innovation in $\boldsymbol{z}_{\mathcal{I}(t)}(t)$ (i.e., information provided by $\boldsymbol{z}_{\mathcal{I}(t)}(t)$ but not by the past measurements $[\bar{\boldsymbol{z}}(1), \ldots, \bar{\boldsymbol{z}}(t-1)]$). Besides, $\hat{\boldsymbol{z}}_{\mathcal{I}(t)}(t|t-1) \in \mathbb{R}^{|\mathcal{I}(t)|}$ represents the prediction of $\boldsymbol{z}_{\mathcal{I}(t)}(t)$ given the observations until frame $t-1$.

Thereby, we first wish to predict the parameters at frame t based on the observations from the previous frames, namely, the first term in (4.50). In fact, since the innovation sequences contain the same information as the original data, it can be shown that the MMSE prediction of $\boldsymbol{\theta}(t)$ is given by the following expression [95]:

$$\hat{\boldsymbol{\theta}}(t|t-1) \triangleq \mathbb{E}[\boldsymbol{\theta}(t)|\tilde{\boldsymbol{z}}(1), \ldots, \tilde{\boldsymbol{z}}(t-1)] = \boldsymbol{F}(t)\hat{\boldsymbol{\theta}}(t-1|t-1), \tag{4.51}$$

where $\tilde{\boldsymbol{z}}(1) = \bar{\boldsymbol{z}}(1) - \hat{\boldsymbol{z}}(1|0) \in \mathbb{R}^{C(1)}, \dots, \tilde{\boldsymbol{z}}(t-1) = \bar{\boldsymbol{z}}(t-1) - \hat{\boldsymbol{z}}(t-1|t-2) \in \mathbb{R}^{C(t-1)}$ are the sets of $C(1), \dots, C(t-1)$ available innovations at previous frames $1, \dots, t-1$.

Next, we need to correct the prediction with the current observation, i.e., the second term in (4.50). Based on the derivations in [95], we have

$$\mathbb{E}[\boldsymbol{\theta}(t)|\tilde{\boldsymbol{z}}_{\mathcal{I}(t)}(t)] = \boldsymbol{K}_{\mathcal{I}(t)}(t) \left(\boldsymbol{z}_{\mathcal{I}(t)}(t) - \hat{\boldsymbol{z}}_{\mathcal{I}(t)}(t|t-1) \right), \tag{4.52}$$

where $\hat{\boldsymbol{z}}_{\mathcal{I}(t)}(t|t-1) = \boldsymbol{A}_{\mathcal{I}(t)} \boldsymbol{V}(t) \hat{\boldsymbol{\theta}}(t|t-1)$ is the MMSE prediction of $\boldsymbol{z}_{\mathcal{I}(t)}(t)$ and $\boldsymbol{K}_{\mathcal{I}(t)}(t) \in \mathbb{R}^{M \times |\mathcal{I}(t)|}$ is the so-called Kalman gain [95]:

$$\boldsymbol{K}_{\mathcal{I}(t)}(t) \triangleq \boldsymbol{\Sigma}(t|t-1) \boldsymbol{V}(t)^{\mathrm{T}} \boldsymbol{A}_{\mathcal{I}(t)}^{\mathrm{T}} \left(\boldsymbol{A}_{\mathcal{I}(t)} \boldsymbol{V}(t) (\boldsymbol{\Sigma}(t|t-1) + \boldsymbol{C}_{\boldsymbol{\eta}}(t) + \boldsymbol{C}_{\boldsymbol{w}}(t)) \boldsymbol{V}(t)^{\mathrm{T}} \boldsymbol{A}_{\mathcal{I}(t)}^{\mathrm{T}} \right)^{-1}, \tag{4.53}$$

with $\boldsymbol{C}_{\boldsymbol{w}}(t) = \mathrm{diag}\left(\Delta_1^2(t)/12, \dots, \Delta_M^2(t)/12 \right)$. Note that $\boldsymbol{\Sigma}(t|t-1) \in \mathbb{R}^{M \times M}$ is the error covariance matrix of the parameter prediction (cf. (4.21)):

$$\boldsymbol{\Sigma}(t|t-1) \triangleq \boldsymbol{F}(t) \boldsymbol{\Sigma}(t-1|t-1) \boldsymbol{F}^{\mathrm{T}}(t) + \boldsymbol{C}_{\boldsymbol{\nu}}(t), \tag{4.54}$$

where $\boldsymbol{\Sigma}(t-1|t-1) \in \mathbb{R}^{M \times M}$ is the covariance matrix of the parameter estimate at frame $t-1$. In general, at frame t, the following recursive expression holds:

$$\boldsymbol{\Sigma}_{\mathcal{I}(t)}(t|t) \triangleq \left(\mathbf{I}_M - \boldsymbol{K}_{\mathcal{I}(t)}(t) \boldsymbol{A}_{\mathcal{I}(t)} \boldsymbol{V}(t) \right) \boldsymbol{\Sigma}(t|t-1). \tag{4.55}$$

As a result, considering all possibilities, the average MSE yields (cf. (4.26))

$$\varepsilon(t) \triangleq \sum_{m=0}^{N} \sum_{\mathcal{I}(t) \in \mathcal{F}_m} \varepsilon_{\mathcal{I}(t)}(t) \prod_{i \in \mathcal{I}(t)} (1 - \mathrm{PER}_i(t)) \prod_{j \notin \mathcal{I}(t)} \mathrm{PER}_j(t), \tag{4.56}$$

where $\mathrm{PER}_i(t)$ is the PER at frame t, given in (4.16) when considering $b_i(t)$ information bits. Like in (4.25), $\varepsilon_{\mathcal{I}(t)}(t)$ can be obtained by computing the trace of the matrix in (4.55).

Finally, since the goal here is to minimize the MSE in (4.56), we can simply follow the procedures described in Subsection 4.4.2.2 to obtain a sub-optimal solution for $\boldsymbol{V}(t)$ and $\boldsymbol{b}(t) = [b_1(t), \dots, b_M(t)]^{\mathrm{T}}$. In short, the MSE in (4.56) can be upper bounded by $\bar{\varepsilon}_G(t)$ (cf. (4.35)) and the resulting problem can be solved using a separate or a joint optimization procedure. Besides, note that the problem constraints could be formulated for a variable number of slots $N(t)$, i.e., $\boldsymbol{V}(t)\boldsymbol{V}(t)^{\mathrm{T}} = \mathbf{I}_{N(t)}$, and a variable vector of transmit powers $\boldsymbol{P}(t)$. Nevertheless, this analysis is beyond the scope of this section, and we only consider the case of $N(t) = N \, \forall t$ and $\boldsymbol{P}(t) = \boldsymbol{P} \, \forall t$.

4.6 Numerical Simulations

In this section, several simulations are presented to illustrate the performance of our approaches. More specifically, the resulting entropy $H(\boldsymbol{Z})$ and MSE ε after the device selection and data quantization are analyzed for different setups. Later on, we will concentrate on the results and evolution of the MSE $\varepsilon(t)$ for the case of temporally correlated data.

As mentioned in Chapter 1, we consider a realistic mMTC network for our study and make use of the parameters and guidelines specified by the 3GPP and ITU standards [35,90]. We also distinguish between the case where the measurements are generated synthetically and that where they are obtained from the database collected by the Intel Berkeley Research Lab [129]. Note that the latter is only considered in the estimation perspective (the case of the real database in the entropy setup is reserved for future works). That is why, at the beginning of each analysis (entropy and MSE), we discuss all these practical issues and describe the datasets employed.

4.6.1 Entropy Perspective

In this subsection, the relative loss ϵ in information after the device selection (not to be confused with the MSE ε), is evaluated for different sweeps where the parameters δ and M are changed. This metric corresponds to the difference between the entropy of the quantized selected data $\boldsymbol{Z}$ defined in (4.9), and that of the quantized original data $\mathcal{Q}(\boldsymbol{X})$, i.e.,

$$H(\mathcal{Q}(\boldsymbol{X})) \geq h(\boldsymbol{X}) - r(\boldsymbol{C}) \log \Delta = \frac{1}{2}\left(r\left(\boldsymbol{C}\right) \log\left(\frac{2\pi e}{\Delta^2}\right) + \log \operatorname{Det}\left(\boldsymbol{C}\right)\right) \triangleq \widetilde{H}(\mathcal{Q}(\boldsymbol{X})), \tag{4.57}$$

which is equivalent to $H(\boldsymbol{Z})$ with $\boldsymbol{S} = \mathbf{I}_M$.

This way, the relative loss ϵ can be expressed as follows:

$$\epsilon = \frac{|\widetilde{H}(\mathcal{Q}(\boldsymbol{X})) - \widetilde{H}(\boldsymbol{Z})|}{|\widetilde{H}(\mathcal{Q}(\boldsymbol{X}))|}. \tag{4.58}$$

Regarding the scenario, we consider sensors to be Gaussian distributed in a small region around the CN. This small area reduces the computational complexity of the numerical methods since we can use smaller values of M while preserving the high spatial density of sensors. Note that this spatial distribution can be interpreted as a Thomas CPP (cf. Subsection 2.4.2).

As an example of application, we consider temperature as the phenomenon to be measured, and employ the exponential quadratic-distance model from [105] with $\sigma_i = \sigma = 50\,°\mathrm{C}$ for the covariance matrix $\boldsymbol{C} = \boldsymbol{C}_{\boldsymbol{\theta}}$ defined in (4.2), i.e.,

$$\Lambda(d_{i,j}) = \exp(-(d_{i,j}/\phi)^2), \tag{4.59}$$

where $\phi > 0$ controls the degree of spatial correlation. The extreme values in (4.59) are 0 and 1 for $d_{i,j} = \infty$ and $d_{i,j} = 0$, respectively. Hence, as devices are located at different positions, the spatial dependency of the correlation is incorporated in the model. In these simulations, we set $\phi = 3.08$ and consider different levels of power consumption, i.e., $P_i \in [0.01, 0.2]$ W [40].

The sweeps over δ and M are depicted in Figures 4.5 and 4.6, respectively. Note that the values of δ represent a percentage of the constraint functions (norms 0 or 1) applied to $\boldsymbol{P}$, i.e., (i) $\delta = \kappa \mathrm{tr}(\mathbf{I}_M) = \kappa M$ and (ii) $\delta = \kappa \mathrm{tr}(\mathrm{diag}(\boldsymbol{P}))$, with $\kappa \in [0, 1]$. We use $\kappa = 0.5$ in Figure 4.6 and $M = 50$ in Figure 4.5. Additionally, we set Δ according to Appendix 4.B with $\xi = 10^{-3}$.

In order to actually represent the consumed power after the selection, in Figure 4.5 we plot the entropy loss ϵ w.r.t. the relative consumed power $\mu = \mathrm{tr}(\boldsymbol{T}\mathrm{diag}(\boldsymbol{P}))/\mathrm{tr}(\mathrm{diag}(\boldsymbol{P}))$ instead of κ. In fact, κ is equal to μ in (ii) while it is indirectly related to this ratio in (i).

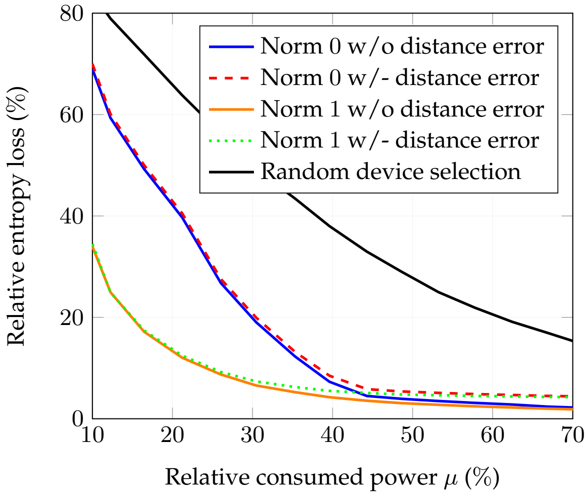

Figure 4.5: Relative entropy loss ϵ versus the relative consumed power μ with $M = 50$.

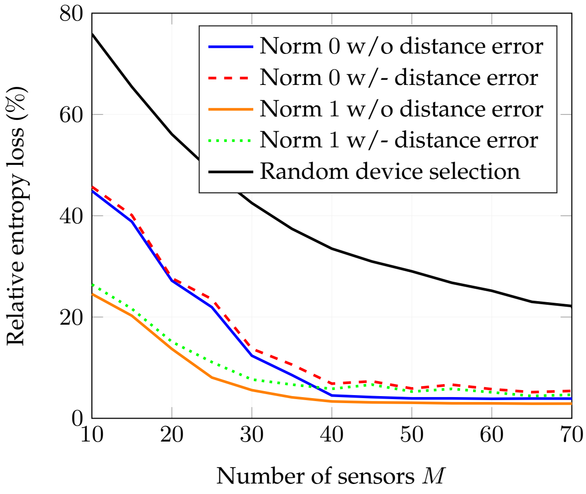

Figure 4.6: Relative entropy loss ϵ versus the number of sensors M with $\kappa = 0.5$.

Moreover, since in real scenarios the exact distances might not be known, but estimated, in Figures 4.5 and 4.6 we show the relative loss when the distances are perfectly known, i.e., norms 0 or 1 without (i.e., w/o) distance error, and also for the case of having an additive Gaussian estimation error with zero mean and standard deviation of 10% w.r.t. to the actual distances, i.e., norms 0 or 1 with (i.e., w/-) distance error.

As observed in Figure 4.5, higher values of μ (or κ) yield smaller entropy losses. This is not surprising as we allow more sensors to be active. For instance, for $\mu = 40\%$, we have a relative loss of 7.30% and 4.25% for constraints (i) and (ii), respectively. This shows that it is possible to reduce significantly the consumed power while preserving most of the relevant information.

In Figure 4.6 we can see that the entropy loss diminishes with the total number of sensors M because the dimension of the null-space of $\boldsymbol{C}$ increases with M. For an increasing M and a constant κ, a significant number of sensors can be silent while reducing the loss of information. A large error ϵ is then obtained for small M, when the covariance matrix is full-rank (all sensors provide relevant information[10]). For instance, for $M = 10$ the losses are around 45% and 25% for constraints (i) and (ii), whereas for $M = 40$, the entropy loss is only 4.5% and 3.3%.

Note that a better performance is attained for constraint (ii) because the optimal sensors (i.e., those with the highest impact on $\boldsymbol{C}$ and smaller consumption) can also be distinguished in terms of consumed energy. Hence, the difference in power consumption can play an important role in the optimization as more relevant information is taken into account in the problem.

To compare the performance of our system, the relative loss of a random selection is also illustrated in Figures 4.5 and 4.6. It represents the strategy where sensors are randomly chosen until constraint (ii) is fulfilled. As expected, a higher loss is obtained with this naive approach, especially for small κ and M, where the optimal solution (i.e., device selection) is less flexible.

---

[10] Even if the singularity of $\boldsymbol{C}$ is not exploited, our approach still applies and benefits from the spatial correlation. In that case, we simply need to replace the pseudo-determinant in (4.9) and (4.57) with the corresponding proper determinant. Accordingly, the rank functions $r(\cdot)$ should be substituted by the size of the matrices M.

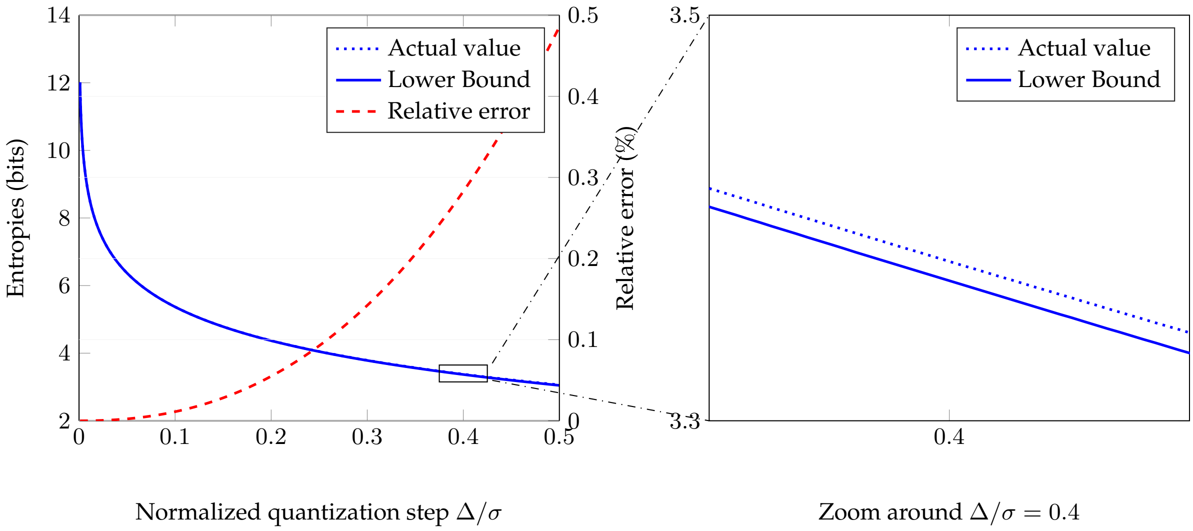

Figure 4.7: Actual entropy and lower bound (left) and relative error (right) versus the normalized quantization step Δ/σ with $M = 1$.

In contrast to the approaches described in [99, 100], where the sensor selection is based on the (deterministic) parameter to be measured, we rely on the correlation between observations (represented with the matrix $\boldsymbol{C}$). As a result, like in the estimation perspective, here the device selection is based on the statistical information. Besides, given that the optimization procedure is entirely carried out at the CN and requires low signaling (i.e., binary messages to report the on/off decisions), there is no significant additional power consumption of the sensors.

To justify the approximation of the original entropy $H(\boldsymbol{Z})$ by its lower bound $\widetilde{H}(\boldsymbol{Z})$, both magnitudes, jointly with the relative error between them, are illustrated w.r.t. the normalized quantization step (or side) Δ/σ in Figure 4.7 with $M = 1$ (i.e., $\boldsymbol{Z} = Z$). The values of $H(Z)$ are obtained numerically through simulations. As shown in the figure, the approximation is very tight, especially for low values of Δ/σ.

Finally, some practical issues should be pointed out. First, as we can observe in Figures 4.5 and 4.6, our method is robust to the uncertainty in the distance estimation since the resulting entropy loss does not increase substantially. Second, as reducing the number of active devices reduces the number of transmissions (sensors will only transmit if they are selected), our strategy can reduce the number of collisions as well.

4.6.2 Estimation Perspective

4.6.2.1 Practical Issues

Throughout these simulations, we consider the micro-urban scenario described in [90] with $P_i = P = 0$ dBm and $N_o = -174$ dBm/Hz. Accordingly, the power vector results $\boldsymbol{P} = P\boldsymbol{1}_M$ and, thus, the power consumption and reduction are given by NP and $(M - N)P$, respectively.

This way, the ratio of power consumption (i.e., ratio between consumed power and total power) and reduction (i.e., ratio between reduced power and total power) are given by the ratio of active sensors N/M and silent sensors $(M-N)/M$, respectively. In addition, for the optimization problem to be feasible, we set the threshold δ to NP[11].

Since we consider that the amount of information to be transmitted is rather small (e.g., temperature), sensors will use a single resource element (OMA), i.e., $T_s \approx 71.4\ \mu$s [35] and $B_s = 15$ kHz [40] (cf. NB-IoT). The effective channels are computed for a power-law path loss:

$$h_i = \varrho_i^{-\alpha/2}\gamma_i, \tag{4.60}$$

where ϱ_i is the distance between sensor i and the CN, $\alpha = 3$ is the decay exponent, and γ_i is the fading coefficient, Rayleigh distributed with zero mean and unit variance, i.e., $\gamma_i \sim \mathcal{CN}(0,1)$.

It is noteworthy to mention that the above model is defined for single-antenna devices but it could be extended to the multiple-antenna case by introducing the corresponding diversity gain in expression (4.60). For more information, please refer to [89].

Regarding the spatial distribution, we assume that sensors are uniformly distributed around the CN within a disk of radius 50 m, which can be seen as a single MCP with no minimum distance (i.e., $K = 1$ and $d_{\min} = 0$). Once again, this small area allows us to work with smaller values of M while preserving the high spatial correlation between the sensed data (cf. Subsection 4.6.1). This is also the case with the Intel dataset, where the exact positions of the sensors are not randomly generated but extracted from the actual deployment in the laboratory [129].

4.6.2.2 Synthetic Data

In line with the previous example, in the upcoming simulations, we also focus on a single phenomenon (temperature). Bear in mind that the parameters θ_i measured by the sensors are the different realizations of this phenomenon at the different locations of the sensors. In fact, our formulation would still be valid for the case of multiple phenomena (e.g., temperature, humidity, etc.) if each sensor only takes a single scalar measurement of just one of them. In that case, the presented technique could exploit the potential correlation between these phenomena.

Different than before, we assume a measurement noise with $\boldsymbol{C_\eta} = \mathrm{diag}(\sigma_{\eta_1}^2, \dots, \sigma_{\eta_M}^2)$ and $\sigma_{\eta_i} \in [0, 10]$°C. In addition, we make use of an exponential model for the covariance matrix $\boldsymbol{C_\theta}$ [105] with $\sigma_i = \sigma = 10\,$°C and correlation function

$$\Lambda(d_{i,j}) = \exp(-d_{i,j}/\phi). \tag{4.61}$$

For the sake of simplicity, we define $\varphi = \exp(-1/\phi) \in [0,1]$ to better study the impact of the degree ϕ, i.e., $\varphi = 0$ is the case of no correlation and $\varphi = 1$ is the case of identical parameters.

---

[11] Note that, under the assumption of equal transmit powers, we have $\mathrm{tr}(\boldsymbol{V}\mathrm{diag}(\boldsymbol{P})\boldsymbol{V}^{\mathrm{T}}) = P\cdot\mathrm{tr}(\boldsymbol{V}\mathbf{I}_M\boldsymbol{V}^{\mathrm{T}}) = NP$. Thus, in this particular case, the effect of the power constraint disappears.

In the case of a system with memory, we model the transition matrix as $\boldsymbol{F}(t) = \psi \mathbf{I}_M \, \forall t$, where $0 \leq \psi \leq 1$ represents the coefficient measuring the temporal correlation between consecutive observations. Accordingly, we consider that the covariance matrix of the process noise is given by $\boldsymbol{C}_{\boldsymbol{\nu}}(t) = (1 - \psi^2)\boldsymbol{C}_{\boldsymbol{\theta}}(t) \, \forall t$ [107]. Likewise, the impact of ψ on the MSE will be also analyzed. In all cases, we consider a period of time of $T = 21$ frames.

Finally, recall that the number of quantization bits $\boldsymbol{b}$ actually depends on the MCS available for each device, i.e., $R_i^{\mathcal{C}}$ and $R_i^{\mathcal{M}}$ (cf. (4.15)). More specifically, the set of possible values for $\boldsymbol{b}$ can be derived from Table 5.2.2.1 in [35], where the maximum number of (information) bits is limited to 8. Accordingly, the corresponding functions $\mathcal{C}_i(\cdot)$ from (4.16) are obtained following the indications of the LTE standard [88].

4.6.2.3 Real Data

To further evaluate the performance of our approach, in this subsection, we also consider the set of measurements obtained by the Intel Berkeley Research Lab [129]. This database consists of $M = 54$ deployed sensors transmitting their data (temperature) to the CN every 31 seconds (s) during $D = 38$ days. As a result, there are 2.3 million readings available.

However, since the database is not complete (not all time slots contain samples), we consider that days are divided into intervals of duration $H = 900$ s (15 minutes) so that each time instant contains at least one measurement.

Note that each of these measurements corresponds to the set of $Q \geq 1$ observations collected at day $d \in \{1, \ldots, D\}$ and time instant $t \in \{1, \ldots, I/H\}$, i.e.,

$$\boldsymbol{X}(d,t) = [\boldsymbol{x}_1(d,t), \ldots, \boldsymbol{x}_Q(d,t)] \in \mathbb{R}^{M \times Q}, \tag{4.62}$$

where I corresponds to the day duration (i.e., 86400 s), and $\boldsymbol{x}_j(d,t) \in \mathbb{R}^M$ is the j-th vector of samples, with $j \in \{1, \ldots, Q\}$, collected at day d during time instant t. Accordingly, each $\boldsymbol{x}_j(d,t)$ can be expressed with the following observation model (cf. (4.46)):

$$\boldsymbol{x}_j(d,t) = \boldsymbol{\theta}_j(d,t) + \boldsymbol{\eta}_j(d,t), \tag{4.63}$$

where $\boldsymbol{\theta}_j(d,t) = \boldsymbol{\theta}(d,t) \in \mathbb{R}^M$ and $\boldsymbol{\eta}_j(d,t) \in \mathbb{R}^M$ are, respectively, the j-th parameter vector and noise vector at day d and time instant t. Similar to before, we assume that both vectors have Gaussian distributions, i.e., $\boldsymbol{\theta}(d,t) \sim \mathcal{N}(\boldsymbol{\mu}_{\boldsymbol{\theta}}(t), \boldsymbol{C}_{\boldsymbol{\theta}}(t)) \, \forall j, d$ and $\boldsymbol{\eta}_j(d,t) \sim \mathcal{N}(\mathbf{0}_M, \boldsymbol{C}_{\boldsymbol{\eta}}(t))$ $\forall j, d$. Note that we consider stationarity over the different days.

Thereby, considering the temperature remains approximately constant over an interval of $L = 2700$ s (45 minutes), the parameter $\boldsymbol{\theta}(d,t)$ can be obtained by averaging $\boldsymbol{X}(d,t)$ with a sliding window of size $J = L/H$ intervals centered at t:

$$\boldsymbol{\theta}(d,t) = \frac{1}{JQ} \sum_{s=t-\frac{J-1}{2}}^{t+\frac{J-1}{2}} \sum_{j=1}^{Q} \boldsymbol{x}_j(d,s). \tag{4.64}$$

Accordingly, the observation noise $\boldsymbol{\eta}_j(d,t)$ can be obtained by subtracting $\boldsymbol{\theta}(d,t)$ to each of the observations in (4.62):

$$\boldsymbol{\eta}_j(d,t) = \boldsymbol{x}_j(d,t) - \boldsymbol{\theta}(d,t). \tag{4.65}$$

This way, the statistical moments of $\boldsymbol{\theta}(d,t)$ and $\boldsymbol{\eta}_j(d,t)$ can be obtained as follows:

$$\boldsymbol{\mu}_{\boldsymbol{\theta}}(t) = \frac{1}{D}\sum_{d=1}^{D}\boldsymbol{\theta}(d,t), \tag{4.66}$$

$$\boldsymbol{C}_{\boldsymbol{\theta}}(t) = \frac{1}{D}\sum_{d=1}^{D}(\boldsymbol{\theta}(d,t) - \boldsymbol{\mu}_{\boldsymbol{\theta}}(t))(\boldsymbol{\theta}(d,t) - \boldsymbol{\mu}_{\boldsymbol{\theta}}(t))^{\mathrm{T}}, \tag{4.67}$$

$$\boldsymbol{C}_{\boldsymbol{\eta}}(t) = \frac{1}{DQ}\sum_{d=1}^{D}\sum_{j=1}^{Q}\boldsymbol{\eta}_j(d,t)\boldsymbol{\eta}_j(d,t)^{\mathrm{T}}. \tag{4.68}$$

On the other hand, regarding the dynamical model, we have (cf. (4.47)):

$$\boldsymbol{\theta}(d,t) = \boldsymbol{F}(t)\boldsymbol{\theta}(d,t-1) + \boldsymbol{\nu}(d,t), \tag{4.69}$$

where $\boldsymbol{\nu}(d,t) \in \mathbb{R}^M$ is the process noise at day d and time instant t. We further assume that $\boldsymbol{\nu}(d,t) \sim \mathcal{N}\left(\mathbf{0}_M, \boldsymbol{C}_{\boldsymbol{\nu}}(t)\right)$. In addition, we consider that the transition matrix is a scaled identity, i.e., $\boldsymbol{F}(t) = \tau(t)\mathbf{I}_M$. Thereby, the factor $\tau(t)$ can be obtained as follows:

$$\tau(t) = \frac{1}{D}\sum_{d=1}^{D}\frac{\mathbf{1}_M^{\mathrm{T}}\boldsymbol{\theta}(d,t)}{\mathbf{1}_M^{\mathrm{T}}\boldsymbol{\theta}(d,t-1)}. \tag{4.70}$$

Finally, the process noise is given by

$$\boldsymbol{\nu}(d,t) = \boldsymbol{\theta}(d,t) - \tau(t)\boldsymbol{\theta}(d,t-1), \tag{4.71}$$

with covariance matrix

$$\boldsymbol{C}_{\boldsymbol{\nu}}(t) = \frac{1}{D}\sum_{d=1}^{D}\boldsymbol{\nu}(d,t)\boldsymbol{\nu}(d,t)^{\mathrm{T}}. \tag{4.72}$$

4.6.2.4 Sensor Selection and Distributed Quantization with Synthetic Data

We start this subsection by evaluating the accuracy of the MSE upper bound $\bar{\varepsilon}_G$ from (4.35). For this task, in Figure 4.8, we present this magnitude w.r.t. the number of sensors M and different values of G, together with the actual MSE ε and the corresponding relative error. Recall that G represents the number of incorrect packets we allow when computing the upper bound.

For a better visualization, both metrics are normalized by $\operatorname{tr}\left(\boldsymbol{C}_{\boldsymbol{\theta}}\right)$, i.e., the MSE is bounded between 0 and 1. As mentioned before, small values of G, e.g., $G = 3$, provide a tight bound. Therefore, for a safe and consistent analysis, from now on we consider $\bar{\varepsilon}_5$ as a suitable approximation for substituting ε in the optimization defined in (4.39). The same reasoning holds for the optimization of $\varepsilon(t)$, i.e., $G = 5$ is used when solving the corresponding problem.

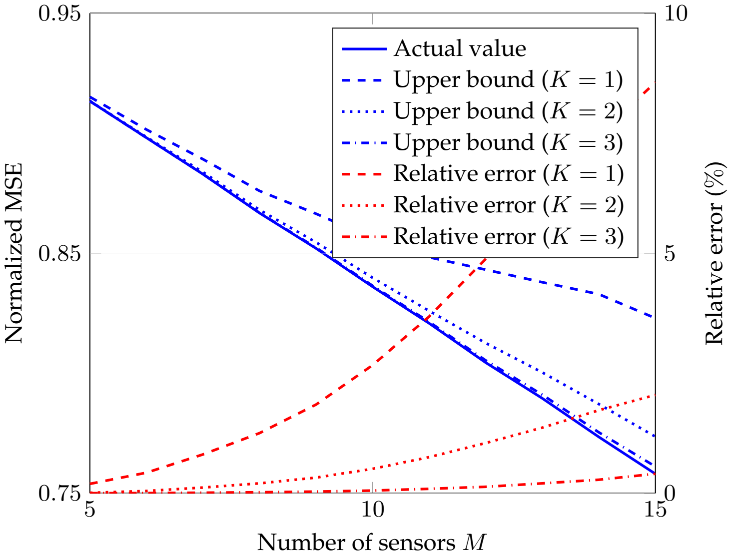

Figure 4.8: Original normalized MSE $\varepsilon/\mathrm{tr}(\boldsymbol{C}_{\boldsymbol{\theta}})$ and normalized upper bound $\bar{\varepsilon}_G/\mathrm{tr}(\boldsymbol{C}_{\boldsymbol{\theta}})$ (left) and relative error (right) versus the number of sensors M.

On the other hand, to study the performance of our estimation approach in the memoryless case, we show the normalized MSE (NMSE), i.e., $\varepsilon/\mathrm{tr}\,(\boldsymbol{C}_{\boldsymbol{\theta}})$, w.r.t. the percentage of active sensors, i.e., $N/M \cdot 100$, and different values of φ. The results are depicted in Figures 4.9, 4.10, 4.11, and 4.12 for $\varphi = 0.1$ (low correlation), $\varphi = 0.9$, $\varphi = 0.95$ (high correlation), and $\varphi = 0.99$ (almost identical observations), respectively. In all plots, we consider $M = 30$ sensors. The separate and joint optimizations are denoted by (S) and (J), respectively. Also, recall that $\bar{\varepsilon}_G$ is only used in the optimization step, while ε is the value we actually show in all figures.

It can be seen that, in both cases (S and J), a better performance (in terms of NMSE) is obtained when the percentage of active sensors increases. This is not surprising as more sensors are allowed to transmit and, thus, more data can be retrieved. For instance, with $\varphi = 0.9$, the NMSE decreases from 0.76 to 0.48 for 10% and 40% of active sensors (or consumed power), respectively. The same effect can be observed when the coefficient φ that measures correlation increases, i.e., a smaller loss is attained for the same ratio N/M. This is because most of the relevant information is contained in fewer sensors. For example, at $N/M = 0.1$ (i.e., 10% of power consumption), the NMSEs with $\varphi = 0.1$ and $\varphi = 0.99$ are 0.79 and 0.38, respectively.

To compare the performance of our system, the NMSE of a random selection with a fixed number of quantization bits is also illustrated in Figures 4.9, 4.10, 4.11, and 4.12. As expected, a higher error is obtained with this naive approach, especially for a large percentage of active sensors. Besides, note that, when increasing a lot the number of quantization bits (e.g., 8 bits), the NMSE also increases. The reason is that given the presence of communication errors, a higher precision (i.e., more quantization bits) implies weaker codeword protection (cf. (4.15)). This translates into poorer decoding and, therefore, into larger BER and PER. A larger NMSE is also achieved when the number of bits is too low (e.g., 1 bit), since the information sent by the sensors is not precise enough for a good estimation. Like before, when the correlation increases, the random approach yields less error since more sensors contain the same information.

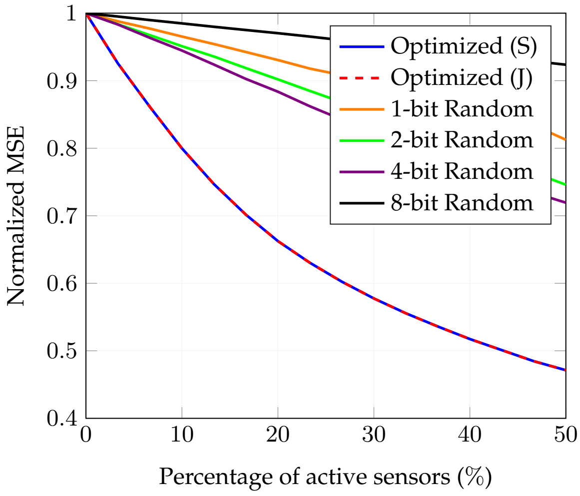

Figure 4.9: NMSE $\varepsilon/\text{tr}(\boldsymbol{C}_{\boldsymbol{\theta}})$ versus the percentage of active sensors $N/M \cdot 100$ with $\varphi = 0.1$.

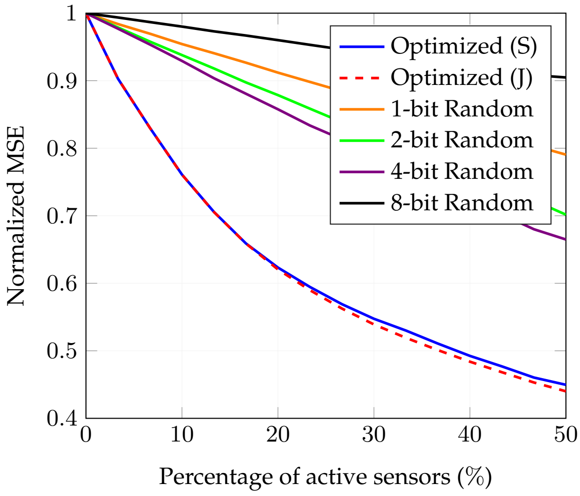

Figure 4.10: NMSE $\varepsilon/\text{tr}(\boldsymbol{C}_{\boldsymbol{\theta}})$ versus the percentage of active sensors $N/M \cdot 100$ with $\varphi = 0.9$.

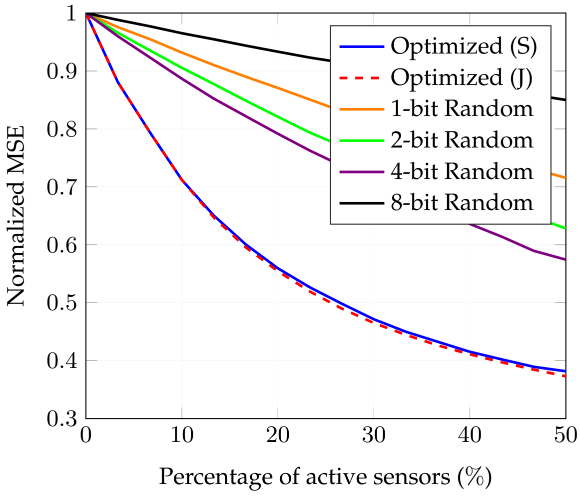

Figure 4.11: NMSE $\varepsilon/\text{tr}(\boldsymbol{C}_{\boldsymbol{\theta}})$ versus the percentage of active sensors $N/M \cdot 100$ with $\varphi = 0.95$.

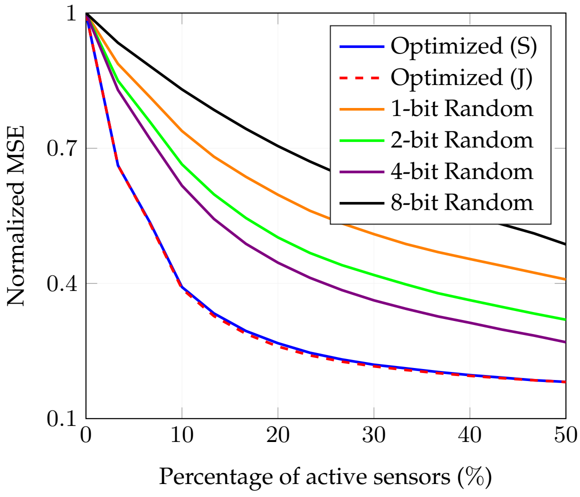

Figure 4.12: NMSE $\varepsilon/\text{tr}(\boldsymbol{C}_{\boldsymbol{\theta}})$ versus the percentage of active sensors $N/M \cdot 100$ with $\varphi = 0.99$.

Following the previous discussion, in Figure 4.13 ($\varphi = 0.9$) and Figure 4.14 ($\varphi = 0.99$) we include some additional comparisons to highlight the performance of our approach. On the one hand, we consider a selection strategy, denoted by (E), in which the number of quantization bits (or MCS indexes) is chosen to ensure an (almost) error-free communication, i.e., PER $\to 0$. This way, we reduce the problem complexity since we only optimize the selection matrix $\boldsymbol{V}$. Nevertheless, reliable communication might be difficult to ensure in scenarios with poor channel conditions, which usually require strong codeword protections. Recall that this condition translates into a low number of information bits and, hence, into high quantization errors (which increase the overall NMSE). Additionally, considering the error-free policy, in both figures, we also illustrate the results obtained with the selection strategy proposed in [97],

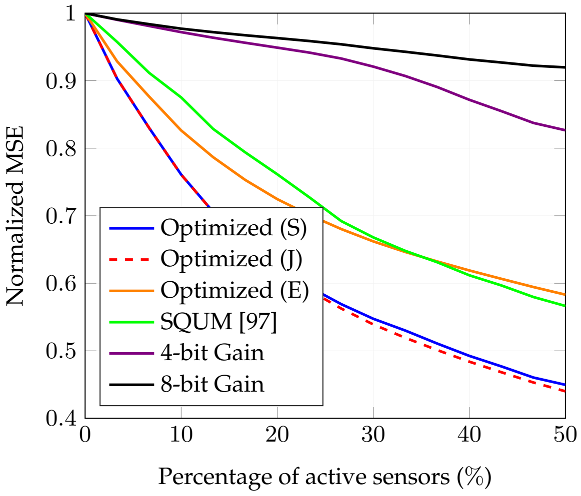

Figure 4.13: NMSE $\varepsilon/\text{tr}(\boldsymbol{C}_{\boldsymbol{\theta}})$ versus the percentage of active sensors $N/M \cdot 100$ with $\varphi = 0.9$.

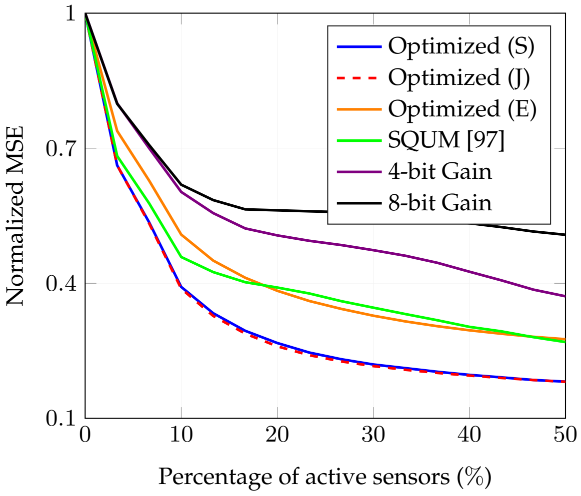

Figure 4.14: NMSE $\varepsilon/\text{tr}(\boldsymbol{C}_{\boldsymbol{\theta}})$ versus the percentage of active sensors $N/M \cdot 100$ with $\varphi = 0.99$.

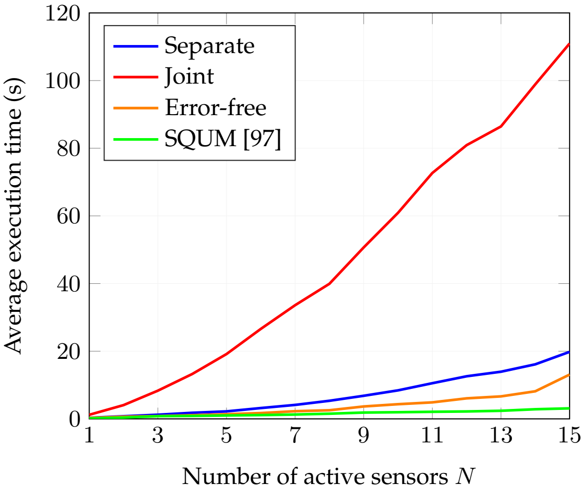

Figure 4.15: Average execution time versus the number of active sensors N.

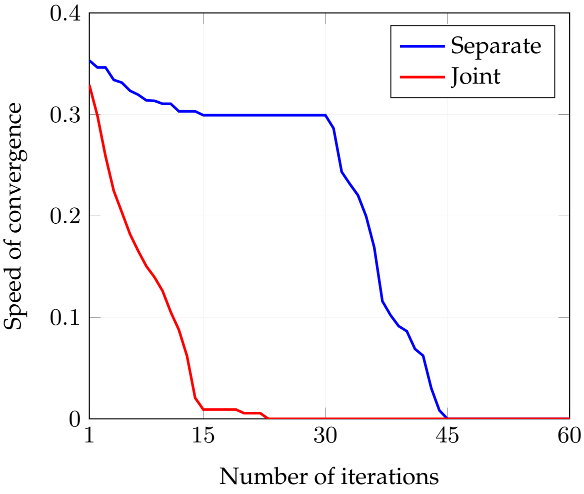

Figure 4.16: Speed of convergence versus the number of iterations.

which relies on successive quadratic upper-bound minimization (SQUM). We can see that this approach shows a behavior similar to (E), and, as before, the NMSE decreases with the correlation degree φ. However, both strategies perform poorly when compared to (S) or (J).

On the other hand, instead of random selection, we also consider the approach where sensors are chosen according to their channel gain. This is included in Figures 4.13 and 4.14. To avoid redundancy, only the cases of 4-bit and 8-bit are shown. We can see that this strategy performs well only when the correlation is high (i.e., $\varphi = 0.99$). The reason is that choosing the devices based on their channel does not consider the quality and correlation of the information that they measure, which ultimately conditions the estimation accuracy.

As discussed in Subsection 4.4.1.2, we also compare the computational complexity of both approaches (S and J). To do so, we show the average execution time required to optimize the selected sensors and the number of quantization bits. The implementation is done using MATLAB and the resulting execution time is illustrated in Figure 4.15.

In Figure 4.16, we depict the corresponding speed of convergence (i.e., the difference w.r.t. the final NMSE) versus the number of iterations. As we can observe, the separate approach requires more iterations ($\boldsymbol{V}$ and $\boldsymbol{b}$ are found separately). However, despite the higher speed of convergence, the joint strategy needs more execution time due to the higher computational complexity (cf. Subsection 4.4.2.2.2). Thus, since the performance of the separate optimization reaches the joint approach in almost all setups[12], the separate approach yields a better strategy. In fact, given the minor improvement achieved with the joint optimization, its formulation can be used to justify the usefulness of the separate approach. Besides that, in Figure 4.15, we also include the average execution time of the aforementioned error-free strategy and that of the approach in [97]. As expected, both methods require similar but smaller values than the separate and joint strategies (which is reasonable given that $\boldsymbol{b}$ is not optimized).

Finally, regarding the system with memory, we consider different degrees of temporal correlation, namely, $\psi = 0.1$, $\psi = 0.9$, $\psi = 0.95$, and $\psi = 0.99$. The different cases are depicted in Figures 4.17, 4.18, 4.19, and 4.20, respectively, where we use the previous values for φ, $N/M = 0.2$, and $M = 30$. For the sake of clarity, only the case of 4-bit quantization and $\varphi = 0.9$ is included as a reference. Besides, like in the memoryless case, only the separate optimization is shown.

As we can see, leveraging the temporal correlation can also help to reduce the NMSE substantially. Obviously, this behavior is more notorious when the coefficients φ and ψ are higher. However, even in the case of low spatial correlation (i.e., $\varphi = 0.1$), a large temporal correlation still improves the estimation performance. This can be easily seen in Figures 4.18, 4.19, and 4.20, where the NMSE decreases more rapidly with high values of ψ. In fact, note that when ψ is very low (e.g., 0.1), the NMSE barely decreases in time (even if $\varphi \to 1$). For instance, in Figure 4.17 we can see that the NMSE is almost constant over the different frames. Overall, compared to the 4-bit case, our approach yields better gains when the data is highly correlated.

4.6.2.5 Sensor Selection and Distributed Quantization with Real Data

Following the discussion above, now we study the performance of our estimation when the measurements are obtained from the Intel database [129] described in Subsection 4.6.2.2. However, in order to avoid redundancy, in this subsection, we omit the analysis of the accuracy of the upper bound $\bar{\varepsilon}_G$ from (4.35) since the previous reasoning is still valid (cf. Figure 4.8).

Thereby, considering the memoryless case, we show the NMSE $\varepsilon/\text{tr}(\boldsymbol{C}_{\boldsymbol{\theta}})$ w.r.t. the percentage of active sensors. This is depicted in Figure 4.21. As before, the performance improves when more sensors are allowed to transmit. In fact, we can observe the same behavior as that with a high correlation factor (cf. Figure 4.12): a small error is attained with few sensors. Thus, since almost all measurements are identical, our approach retrieves most of the information

---

[12] The main reason behind is that in the scenario under study, the impact of the quantization bits on the NMSE is smaller than that of the device selection since removing information (i.e., silencing a certain sensor) degrades more the estimation accuracy than reducing the quantization precision. Thus, both approaches distinguish the optimal devices (those with better channel conditions and good observations) independently of their quantization level.

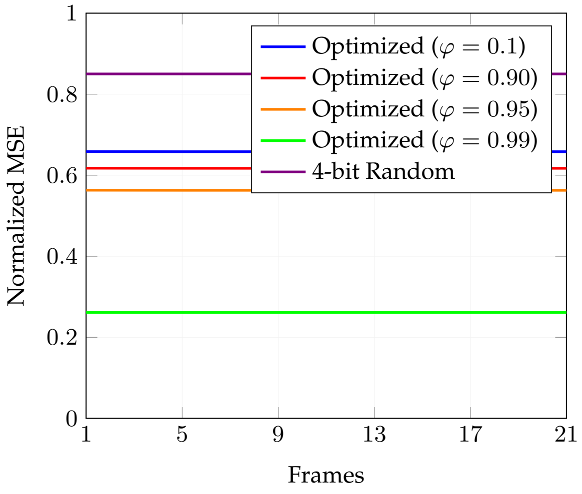

Figure 4.17: Evolution of NMSE $\varepsilon(t)/\mathrm{tr}(\boldsymbol{C}_{\boldsymbol{\theta}}(t))$ with $\psi = 0.1$.

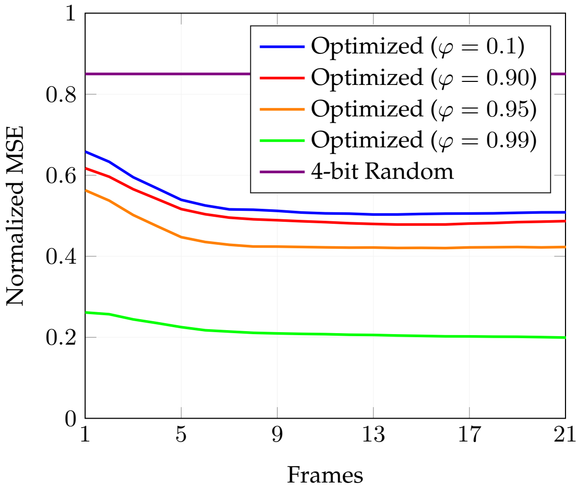

Figure 4.18: Evolution of NMSE $\varepsilon(t)/\mathrm{tr}(\boldsymbol{C}_{\boldsymbol{\theta}}(t))$ with $\psi = 0.9$.

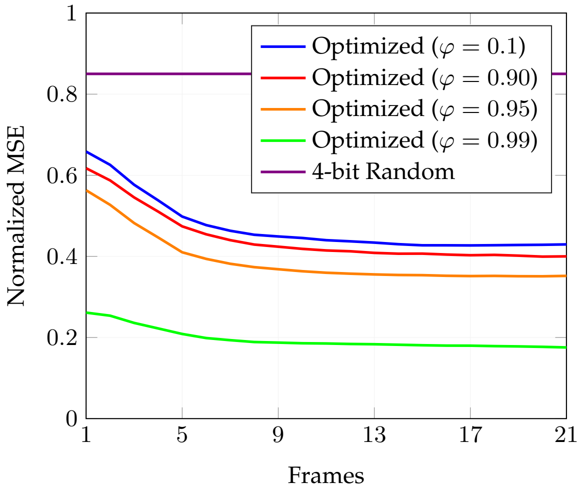

Figure 4.19: Evolution of NMSE $\varepsilon(t)/\mathrm{tr}(\boldsymbol{C}_{\boldsymbol{\theta}}(t))$ with $\psi = 0.95$.

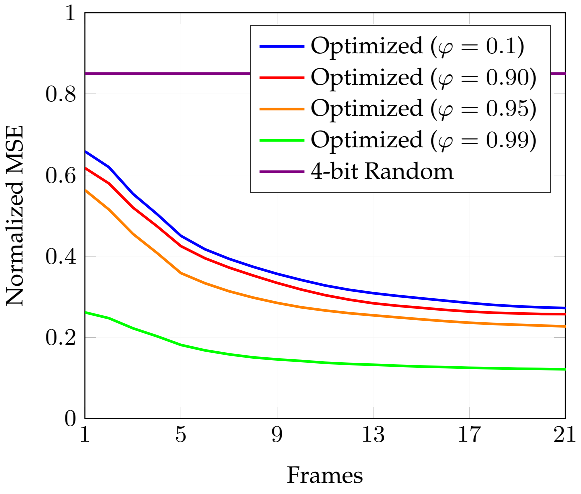

Figure 4.20: Evolution of NMSE $\varepsilon(t)/\mathrm{tr}(\boldsymbol{C}_{\boldsymbol{\theta}}(t))$ with $\psi = 0.99$.

with 10% of active sensors (equivalent to a power reduction of 90%). Contrarily, although the random selection does not yield poor results, it needs a considerably larger number of active sensors to attain the same performance (around 50% is needed to obtain the same error as the optimized case with 10% of active sensors, i.e., a NMSE of 0.1).

Additionally, for the sake of clarity in the explanation, in Figure 4.22 we present the NMSE w.r.t. the number of quantization bits b_i and different percentages of active sensors. Similar behavior can be observed when the number of bits is small (e.g., 1 bit) or high (e.g., 8 bits). This is because too few bits imply a low precision (or high quantization noise) for the parameter estimation and too many bits represent small message protection (or high error probability). This reveals the need for choosing the proper number of quantization bits.

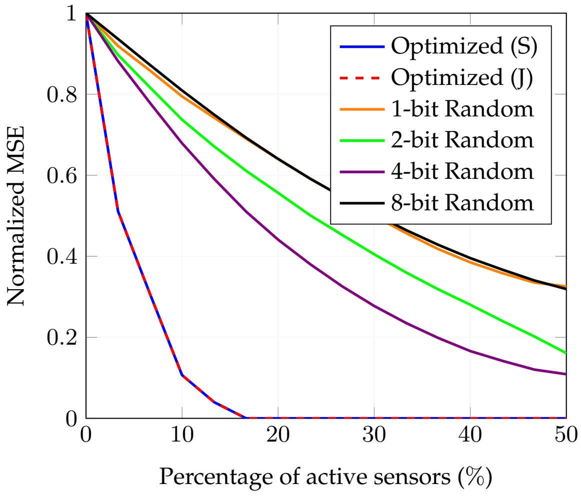

Figure 4.21: NMSE $\varepsilon/\text{tr}(\boldsymbol{C}_{\boldsymbol{\theta}})$ versus the percentage of active sensors $N/M \cdot 100$ (Intel database).

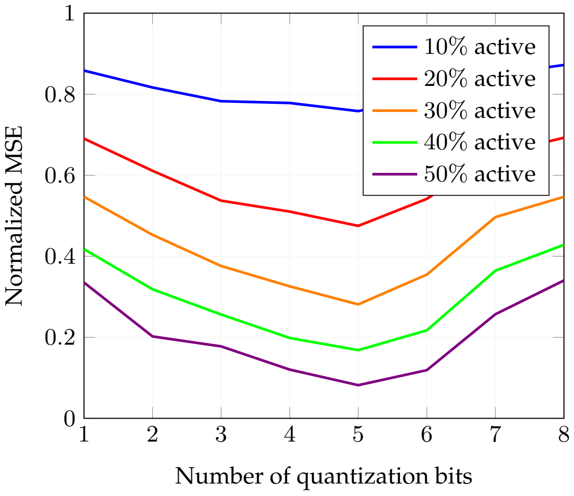

Figure 4.22: NMSE $\varepsilon/\text{tr}(\boldsymbol{C}_{\boldsymbol{\theta}})$ versus the number of quantization bits b_i (Intel database).

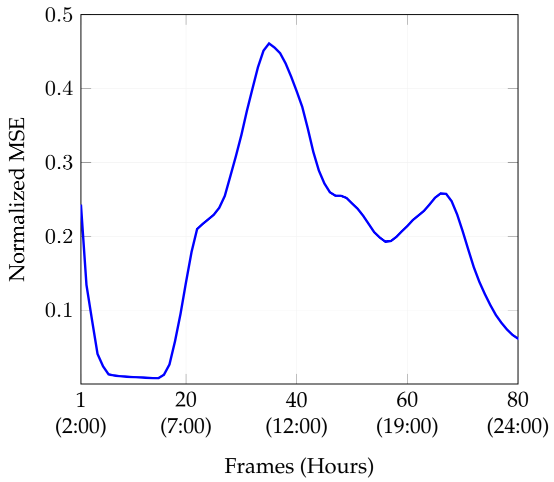

Figure 4.23: Evolution of NMSE $\varepsilon(t)/\text{tr}(\boldsymbol{C}_{\boldsymbol{\theta}}(t))$ (Intel database).

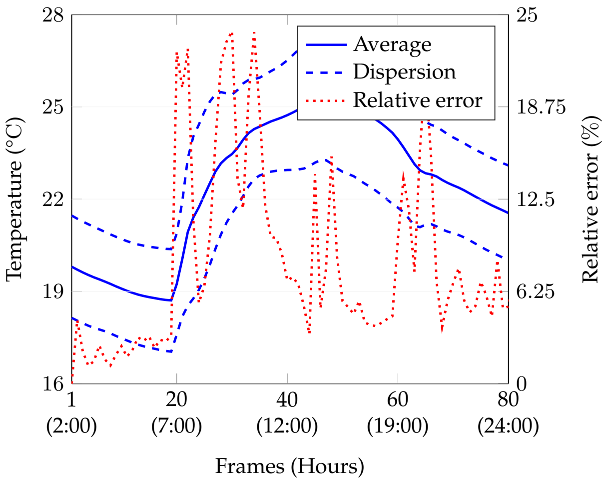

Figure 4.24: Average temperature $\bar{\theta}(t)$, dispersion $\bar{\theta}(t) \pm \hat{\theta}(t)$ and relative error $\zeta(t)$ over the day (Intel database).

On the other hand, the evolution of the NMSE over time is depicted in Figure 4.23 for 3.33% of active sensors. Here the different frames indicate consecutive time periods of the day. Note that, different from before, the error does not always decrease monotonically. Instead, there are some frames where there is a huge increase. The reason behind this behavior is the dynamical modeling of $\boldsymbol{\theta}(d,t)$, presented in (4.69), in which we assume a common transition matrix over the days. However, this model does not capture entirely the nature of the measurements in [129], i.e., there are some instants where evolution is not common over the days.

In order to illustrate this, in Figure 4.24 we show the sensors average temperature during the day $\bar{\theta}(t)$, the standard deviation $\hat{\theta}(t)$ over the days, and the relative error in the second-order statistics of the dynamical model $\zeta(t)$:

$$\bar{\theta}(t) = \frac{1}{D}\sum_{d=1}^{D} \mathbf{1}_M^{\mathrm{T}}\boldsymbol{\theta}(d,t)/M, \tag{4.73}$$

$$\hat{\theta}(t) = \sqrt{\frac{1}{D}\sum_{d=1}^{D}\left(\mathbf{1}_M^{\mathrm{T}}\boldsymbol{\theta}(d,t)/M\right)^2 - \bar{\theta}(t)^2}, \tag{4.74}$$

$$\zeta(t) = \| \underbrace{\tau(t)^2\boldsymbol{C}_{\boldsymbol{\theta}}(t-1) + \boldsymbol{C}_{\boldsymbol{\nu}}(t)}_{\text{model}} - \underbrace{\boldsymbol{C}_{\boldsymbol{\theta}}(t)}_{\text{reality}} \|_{\mathrm{F}}/\|\boldsymbol{C}_{\boldsymbol{\theta}}(t)\|_{\mathrm{F}}. \tag{4.75}$$

Note that a rapid change in the temperature and a large dispersion (e.g., in frame 20) result in poor dynamical modeling (i.e., a single $\tau(t)$ per time instant does not capture properly the statistical evolution of $\boldsymbol{\theta}(d,t)$ across the days) and, thus, the estimation fails. Despite that, the proposed approach is able to adapt to these changes as the resulting NMSE is reduced after the peaks. Whenever the relative error is small, our estimation scheme yields a good accuracy.

4.7 Summary and Conclusions

In this chapter, we have addressed the problem of inferring a set of measured parameters in an UL mMTC network. In a scenario where a group of sensors sends their spatially (and temporally) correlated observations to a single CN, we have contemplated two different perspectives to measure the decoded (or available) information: source entropy and estimation error.

In the first setup, we have designed a selection strategy that minimizes the loss of information to be transmitted (or sensed data entropy) through a noiseless channel subject to power-related constraints, i.e., minimize the loss of information when some of the sensors do not collect or report the collected information. A degenerate Gaussian distribution has been employed as a model to measure the correlation in the information. Given the discrete nature of the optimization problem, some steps have been taken to find a sub-optimal solution. Results have proven that most of the information can be retrieved with a smaller number of active devices. This effect is more pronounced in larger networks, where a higher correlation is experienced.

In the parameter estimation error setup, we have derived a strategy based on the MMSE estimate and Kalman filters that also take into consideration the energy restrictions of the sensing devices. Given that communication errors may compromise the estimation performance, we have averaged the MSE over the decoding error probabilities and proposed a device selection scheme and quantization approach that minimize the resulting MSE. This way, since the number of active sensors and the information to be transmitted are significantly reduced, we have been able to decrease the data traffic and improve the power consumption. Our approach has been evaluated in several scenarios with synthetic and real data. Numerical simulations have shown that in the case of synthetically generated data, our scheme can reduce the power consumption by 50% (i.e., the number of silent sensors) without a significant increase in the NMSE. This behavior is more notorious in the case of real data, where the spatial correlation is significantly higher. With only 10% of active sensors, we have attained a performance in NMSE of 0.1. In both cases, better performance is observed when including temporal correlation.

Appendix 4.A Entropy of the Quantized Source

According to [116], the entropy of the quantized source $\boldsymbol{Z} = \mathcal{Q}(\boldsymbol{Y})$ already defined in (4.3) can also be written in the following way:

$$H(\boldsymbol{Z}) = -\int_{\boldsymbol{y}} f_{\boldsymbol{Y}}(\boldsymbol{y}) \log \bar{f}(\boldsymbol{y}) d\boldsymbol{y} - M \log \Delta, \tag{4.76}$$

where $\bar{f}(\boldsymbol{y})$ is the average value of $f_{\boldsymbol{Y}}(\boldsymbol{y})$ over each quantization cell of side Δ. Therefore, it can be seen that (4.76) can be lower bounded by (4.4). In fact, this bound is tight for $\Delta \to 0$, i.e., when $f_{\boldsymbol{Y}}(\boldsymbol{y}) \approx \bar{f}(\boldsymbol{y})$ is valid (high-rate assumption).

For simplicity, we continue with the one-dimensional case (equivalent to the uniform scalar quantization), although the same discussion holds for higher dimensions. Thereby, for $M = 1$, the difference between both entropies, now $\widetilde{H}(Z)$ and $H(Z)$, is always non-positive:

$$\begin{aligned} \widetilde{H}(Z) - H(Z) &= \int_{y} f_{Y}(y) \log \bar{f}(y)/f_{Y}(y) dy \leq \left(\int_{y} f_{Y}(y)(\bar{f}(y)/f_{Y}(y) - 1) dy\right) \log e \\ &= \left(\int_{y} \bar{f}(y) dy - \int_{y} f_{Y}(y) dy\right) \log e = (1-1) \log e = 0, \end{aligned} \tag{4.77}$$

which follows from the logarithm inequality $\ln x \leq x - 1$ [75].

Note that the previous reasoning holds irrespective of the selection strategy, i.e., is valid for any continuous source $\boldsymbol{Y}$ (or Y).

Appendix 4.B Convexity of the Entropy-Based Selection Problem

In order to derive the convex problem in $\boldsymbol{T}$, i.e., (4.33), starting from (4.32), we need to find a new concave objective function and all constraints must be convex. Note that as we are dealing with norm-constraints, they are convex. For the l_0 quasi-norm, convexity is preserved through the l_1 norm relaxation. In addition, the constraint $\boldsymbol{t} \in [0,1]^M$ defines a convex set. The same holds for $\boldsymbol{t} \in [\xi, 1]^M$, which is forced with $\boldsymbol{T} - \xi \mathbf{I}_M \succeq \mathbf{0}$. Recall that the latter condition implies $\boldsymbol{T} \succ \mathbf{0}$, which does not define a convex cone as the origin is not included [123].

The objective function $\widetilde{H}(\boldsymbol{Z})$ in (4.32) can be approximated by a lower bound. To that end, as discussed in [120], we bound the rank function $r(\boldsymbol{X})$ of a symmetric positive semi-definite matrix $\boldsymbol{X}$ by its convex envelope, i.e., the nuclear norm $\|\boldsymbol{X}\|_* \triangleq \text{tr}(\sqrt{\boldsymbol{X}^{\mathrm{T}}\boldsymbol{X}})$[13]$= \text{tr}(\boldsymbol{X})$. This bound is valid if the spectral norm (maximum eigenvalue) of $\boldsymbol{X}$ is smaller than 1, i.e., $\|\boldsymbol{X}\|_2 \triangleq \lambda_{\max}(\boldsymbol{X}) \leq 1$. Note that $\|\boldsymbol{X}\|_*$ and $\|\boldsymbol{X}\|_2$ are two different norms and can take different values.

By defining the normalized matrix $\overline{\boldsymbol{C}}$ as $\overline{\boldsymbol{C}} = \boldsymbol{C}/\|\boldsymbol{C}\|_2$, we ensure that $\|\sqrt{\boldsymbol{T}}\,\overline{\boldsymbol{C}}\sqrt{\boldsymbol{T}}\|_2 \leq 1$. This comes from the fact that $\|\boldsymbol{T}\|_2 \leq 1$ and that for two symmetric positive semi-definite matrices $\boldsymbol{A}$ and $\boldsymbol{B}$, it can be proved that $\|\boldsymbol{A}\boldsymbol{B}\|_2 \leq \|\boldsymbol{A}\|_2 \|\boldsymbol{B}\|_2$ [130].

---

[13] The matrix square root operation $\sqrt{\boldsymbol{Y}} = \boldsymbol{X}$ implies that $\boldsymbol{Y} = \boldsymbol{X}^2$. Note that although this operation is different from the element-wise square root operation, both operations coincide when applied to diagonal matrices.

Hence, given that $r(\sqrt{\boldsymbol{T}}\boldsymbol{C}\sqrt{\boldsymbol{T}}) = r(\sqrt{\boldsymbol{T}}\,\overline{\boldsymbol{C}}\sqrt{\boldsymbol{T}})$, the objective function $\widetilde{H}(\boldsymbol{Z})$ in (4.32) can be lower bounded as:

$$\begin{aligned}
\widetilde{H}(\boldsymbol{Z}) &= \frac{1}{2}\left(r\left(\sqrt{\boldsymbol{T}}\,\boldsymbol{C}\sqrt{\boldsymbol{T}}\right)\log\left(\frac{2\pi e}{\Delta^2}\right) + \log\det\left(\boldsymbol{L}_r^{\mathrm{T}}\boldsymbol{T}\boldsymbol{L}_r\right)\right) \\
&= \frac{1}{2}\left(r\left(\sqrt{\boldsymbol{T}}\,\overline{\boldsymbol{C}}\sqrt{\boldsymbol{T}}\right)\log\left(\frac{2\pi e}{\Delta^2}\right) + \log\det\left(\boldsymbol{L}_r^{\mathrm{T}}\boldsymbol{T}\boldsymbol{L}_r\right)\right) \\
&\geq \frac{1}{2}\left(\|\sqrt{\boldsymbol{T}}\,\overline{\boldsymbol{C}}\sqrt{\boldsymbol{T}}\|_*\log\left(\frac{2\pi e}{\Delta^2}\right) + \log\det\left(\boldsymbol{L}_r^{\mathrm{T}}\boldsymbol{T}\boldsymbol{L}_r\right)\right) \\
&\overset{\text{(a)}}{=} \frac{1}{2}\left(\mathrm{tr}(\boldsymbol{T}\overline{\boldsymbol{C}})\log\left(\frac{2\pi e}{\Delta^2}\right) + \log\det(\boldsymbol{L}_r^{\mathrm{T}}\boldsymbol{T}\boldsymbol{L}_r)\right) \\
&\triangleq \widetilde{H}_{lb}(\boldsymbol{Z}),
\end{aligned} \tag{4.78}$$

where (a) follows from the definition of nuclear norm and the fact that $\mathrm{tr}(\sqrt{\boldsymbol{T}}\,\overline{\boldsymbol{C}}\sqrt{\boldsymbol{T}}) = \mathrm{tr}(\boldsymbol{T}\overline{\boldsymbol{C}})$, which results from the trace property $\mathrm{tr}(\boldsymbol{A}\boldsymbol{B}) = \mathrm{tr}(\boldsymbol{B}\boldsymbol{A})$ for any matrices $\boldsymbol{A}$ and $\boldsymbol{B}$.

It is important to highlight that the lower bound in (4.78) is concave in $\boldsymbol{T}$ because $\mathrm{tr}(\boldsymbol{T}\overline{\boldsymbol{C}})$ is linear in $\boldsymbol{T}$ and $\log\det(\boldsymbol{L}_r^{\mathrm{T}}\boldsymbol{T}\boldsymbol{L}_r)$ is concave in $\boldsymbol{T}$ for $\boldsymbol{T} \succ \boldsymbol{0}$ [123]. Therefore, replacing the objective function in (4.32) by its lower bound, we obtain the convex problem defined in (4.33): maximization of a concave function subject to convex constraints.

Besides, for our analysis to be consistent, the approximation in (4.9) must be accurate. Accordingly, the quantization interval Δ must be close to the minimum eigenvalues $\lambda_{\min}(\boldsymbol{C})$ and $\lambda_{\min}(\boldsymbol{T}\boldsymbol{C})$. For symmetric positive semi-definite matrices, we have that $\lambda_{\min}(\boldsymbol{T}\boldsymbol{C}) \geq \lambda_{\min}(\boldsymbol{T})\lambda_{\min}(\boldsymbol{C})$ [130], and, since $\lambda(\boldsymbol{T}) \leq 1$, it holds that $\lambda_{\min}(\boldsymbol{T})\lambda_{\min}(\boldsymbol{C}) \leq \lambda_{\min}(\boldsymbol{C})$. Thus, $\Delta \leq \lambda_{\min}(\boldsymbol{T})\lambda_{\min}(\boldsymbol{C})$ with $\lambda_{\min}(\boldsymbol{T}) = \xi$ satisfies both conditions.

Chapter 5

Robust Design of Reconfigurable Intelligent Surfaces

5.1 Introduction

Following the discussion in the previous chapter, in scenarios where the quality of the channel between the sensors and the CN is poor, the transmission of the measurements taken by the mMTC devices might be difficult. Some examples could be setups with: (1) a strong Rayleigh fading, or a Rician fading with a weak LoS [36], and (2) large propagation losses due to the use of millimeter wave (mmWave) [131] or terahertz (THz) [132] bands. In these cases, the resulting decoding error probability can be too large to ensure reliable communication. Additionally, the retransmissions needed in the case of transmission failure can be fatal in terms of latency and power consumption, which are key factors in mMTC networks [21].

To improve the system performance, in this chapter, we will explore the use of reconfigurable intelligent surfaces (RISs) [133, 134]. A RIS is a large passive surface that allows the adaptation to the wireless environment. In essence, these types of structures act as reflectors that, for example, can be used to point the signals toward the target destination to enhance the signal strength. This gain in received power, together with their low cost and easy deployment, makes RISs one of the potential technologies for the evolution of future mobile networks [135].

Channel state information (CSI) becomes essential to achieve these high beamforming gains. However, given the passive nature of RISs and their large number of elements, channel estimation represents a challenging problem [136]. That is why we will also study different strategies for feasibly acquiring CSI knowledge. Accordingly, the RIS will be designed to minimize the parameter estimation error while contemplating the impact of imperfect CSI (I-CSI) and communication errors. Hence, our proposal will be robust against these uncertainties.

Finally, in contrast with Chapter 4, here we will contemplate multiple access (MA) channels with non-orthogonal resources [41–43] (cf. Subsection 2.3.2). As a result, the received signals of the different sensors will be also affected by interference (cf. Chapter 3). To cope with this issue, we will consider successive interference cancelation (SIC) as a decoding procedure and analyze different proposals for choosing the decoding order [44–46]. In that sense, the role of the RIS will be also to adapt the channel to the SIC procedure, which can help to significantly reduce the impact of the interference (along with the mitigation of channel quality drawbacks) [137, 138].

5.1.1 Related Work

RISs are currently drawing a lot of attention among both academic and industrial communities. Recent studies have shown that incorporating these structures in wireless networks can help to improve performance significantly [133, 139]. However, most works focus on the optimization of the data rate. For instance, the authors of [140] maximized the sum rate w.r.t. the RIS response in the context of device-to-device (D2D) communications. Based on block coordinate descent methods, the BS beamforming, power allocation, and user pairing were also derived. In [141], authors investigated the use of RIS to support NOMA-based transmissions with the help of SIC decoding schemes. A series of convex approximations and relaxations were used to jointly design the RIS and BS configurations that maximize the total throughput. Similarly, the ergodic rate in presence of correlated Rician fading was characterized in [142], and later optimized by means of alternating optimization techniques.

On the other hand, regarding channel knowledge acquisition, several approaches have been proposed within the literature. As an example, in [143], authors presented an estimation and transmission protocol relying on orthogonal frequency-division multiplexing (OFDM) and overhead reduction for frequency-selective channels. The lack of CSI was also contemplated in [144], where authors employed deep reinforcement learning to obtain the channel estimate.

5.1.2 Contributions

The main contributions of this chapter are listed in the following:

- A MMSE parameter estimation scheme for NOMA-based mMTC in RIS-aided environments. The estimate is derived assuming I-CSI and communication errors.
- A tractable decoding strategy relying on SIC and different protocols to obtain the channel estimate: binary and non-binary.
- An iterative algorithm to optimize the RIS and the SIC decoding order. Simulation results justify the use of RIS to support mMTC transmissions.

5.1.3 Organization

The remainder of this chapter is structured as follows. Section 5.2 describes the system model. In Section 5.3, we discuss the channel estimation, while the SIC decoding procedure is presented in Section 5.4. Section 5.5 is devoted to the robust design of the RIS, while numerical simulations are shown in Section 5.6. Finally, conclusions are presented in Section 5.7.

5.2 System Model

Throughout this chapter, we consider a scenario similar to that described in Chapter 4 where a set of M sensors are connected to a CN. Each of these sensors observes a parameter θ_i, subject to a measurement noise η_i with $i \in \{1, \dots, M\}$. Thus, the information to be transmitted is

$$\boldsymbol{x} = \boldsymbol{\theta} + \boldsymbol{\eta} \in \mathbb{R}^M, \tag{5.1}$$

where $\boldsymbol{x} = [x_1, \dots, x_M]^{\mathrm{T}}$ is the set of observations, $\boldsymbol{\theta} = [\theta_1, \dots, \theta_M]^{\mathrm{T}} \in \mathbb{R}^M$ is the parameter vector, Gaussian distributed with mean $\boldsymbol{\mu_\theta} \in \mathbb{R}^M$ and covariance matrix $\boldsymbol{C_\theta} \in \mathbb{R}^{M \times M}$, i.e., $\boldsymbol{\theta} \sim \mathcal{N}(\boldsymbol{\mu_\theta}, \boldsymbol{C_\theta})$, and $\boldsymbol{\eta} = [\eta_1, \dots, \eta_M]^{\mathrm{T}} \in \mathbb{R}^M$ is set of observation noises, mutually independent and Gaussian distributed with zero mean and covariance matrix $\boldsymbol{C_\eta} \in \mathbb{R}^{M \times M}$, i.e., $\boldsymbol{\eta} \sim \mathcal{N}(\boldsymbol{0}_M, \boldsymbol{C_\eta})$. Denoting the individual noise powers as $\sigma^2_{\eta_i}$, we have $\boldsymbol{C_\eta} = \mathrm{diag}(\sigma^2_{\eta_1}, \dots, \sigma^2_{\eta_M})$.

Accordingly, each sensor maps the individual x_i into a transmit symbol $s_i \in \mathbb{C}$ through an encoder represented by $\mathcal{G}_i(\cdot)$, i.e., $s_i = \mathcal{G}_i(x_i)$. Also, we further assume that these symbols have zero mean and transmit power P_i. Note that the function $\mathcal{G}_i(\cdot)$ includes the error correcting code and the modulation scheme, i.e., the MCS (cf. Chapter 2).

Considering a NOMA communication, the received signal at the CN yields

$$y \triangleq \sum_{i=1}^{M} q_i s_i + w \in \mathbb{C}, \tag{5.2}$$

where $q_i \in \mathbb{C}$ is the direct channel between sensor i and the CN, and $w \in \mathbb{C}$ is the complex AWGN with zero mean and power σ^2_w, i.e., $w \sim \mathcal{CN}(0, \sigma^2_w)$.

Unlike Chapter 3, we consider a regular data traffic. Thereby, the SINR of the signal received from sensor i can be expressed as follows (cf. (2.9)):

$$\rho_i = \frac{P_i |q_i|^2}{\sigma^2_w + \sum_{j \neq i} P_j |q_j|^2}, \tag{5.3}$$

where we have omitted the super-index *NOMA, regular* to ease of notation.

As mentioned, in real scenarios, the received power $P_i |q_i|^2$ can be quite small compared to the noise and interference levels. That is why in this chapter, to support the transmission from the sensors to the CN, we incorporate the use of a RIS. By means of phase-shifters, the RIS will be responsible for pointing the different signals towards the CN as needed [145,146].

An illustrative example of a setup with $M = 4$ and $L = 9$ is shown in Figure. 5.1, where the direct path is blocked by a certain object (critical when considering mmWave and THz bands), and the RIS is used to create an additional path to reach the CN.

With the above considerations, the response of a RIS with L elements reads as [147,148]

$$\boldsymbol{\Psi} \triangleq \mathrm{diag}\left(\lambda_1 e^{j\phi_1}, \dots, \lambda_L e^{j\phi_L}\right), \tag{5.4}$$

where $\lambda_l \in \{0, 1\}$ are the set of amplitude reflection coefficients that represent the on/off states of each element[1] and ϕ_l are the different phase-shifts (both configurable).

The received signal from (5.2) can then be expressed in the following way:

$$y = \sum_{i=1}^{M} \left(q_i + \boldsymbol{g}_{\mathrm{R}}^{\mathrm{T}} \boldsymbol{\Psi} \boldsymbol{g}_i\right) s_i + w, \tag{5.5}$$

where $\boldsymbol{g}_{\mathrm{R}} \in \mathbb{C}^L$ is the channel between the RIS and the CN, and $\boldsymbol{g}_i \in \mathbb{C}^L$ is the channel between sensor i and the RIS. This way, the effective channel from Section 2.3 results $h_i = q_i + \boldsymbol{g}_{\mathrm{R}}^{\mathrm{T}} \boldsymbol{\Psi} \boldsymbol{g}_i \in \mathbb{C}$.

---

[1] The off state means that the incident electromagnetic wave is perfectly absorbed and there is no reflection [147]. For further information on practical implementations, please refer to [136] and references therein.

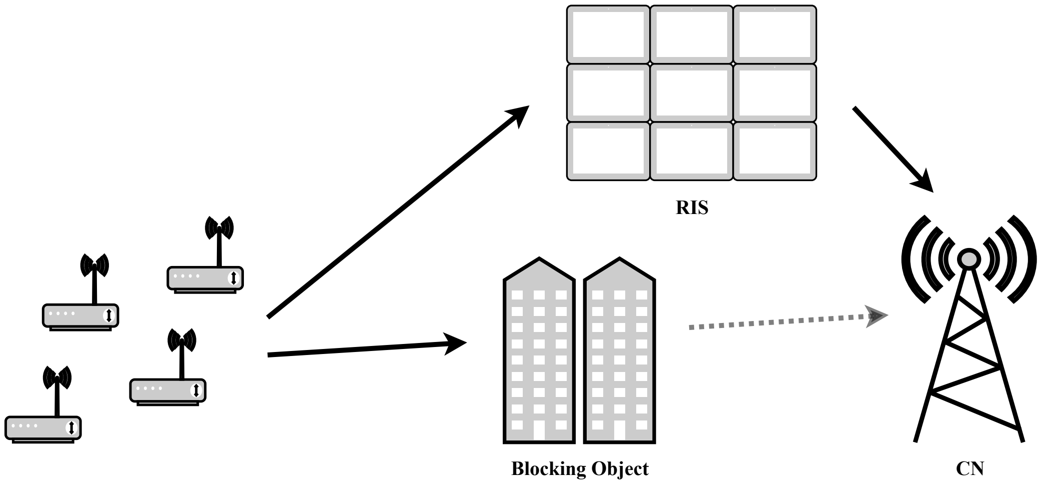

Figure 5.1: Illustrative scenario with $M = 4$ and $L = 9$. Solid and dotted lines indicate strong and weak paths, respectively.

In addition, defining $\boldsymbol{\psi} \triangleq [\psi_1, \ldots, \psi_L]^{\mathrm{T}} \in \mathbb{C}^L$ as the diagonal entries of $\boldsymbol{\Psi}$ (i.e., $\psi_l = \lambda_l e^{j\phi_l}$), this expression yields $h_i = q_i + \boldsymbol{\psi}^{\mathrm{T}} \boldsymbol{g}_{\mathrm{C},i}$, with $\boldsymbol{g}_{\mathrm{C},i} \triangleq \mathrm{diag}(\boldsymbol{g}_R)\boldsymbol{g}_i \in \mathbb{C}^L$ the cascaded channel. From now on, we assume that $\boldsymbol{g}_{\mathrm{C},i}$ has mean $\boldsymbol{\mu}_{\boldsymbol{g}_{\mathrm{C},i}} \in \mathbb{C}^L$ and covariance matrix $\boldsymbol{C}_{\boldsymbol{g}_{\mathrm{C},i}} \in \mathbb{C}^{L \times L}$.

5.3 Channel Estimation

In most scenarios, the CSI is assumed to be perfectly known at the CN. This knowledge can be easily acquired through (orthogonal) training pilots. Nevertheless, as mentioned before, when considering RIS-aided networks, this procedure presents some drawbacks [133].

First, given that these structures are passive, the acquisition of CSI has to be performed at the CN. This task involves the estimation of the cascaded channel of the link sensors-RIS-CN, which is non-trivial due to the underdetermination of the system. Second, since the overhead size required by this operation (i.e., number of pilot symbols) is proportional to the number of reflecting elements, the estimation results prohibitive for large surfaces.

To overcome these issues, during the training stage we design the RIS matrix $\boldsymbol{\Upsilon}$ (different from $\boldsymbol{\Psi}$, used for data transmission), where the reflection coefficients and phase-shifts are chosen to minimize the channel estimation error. We will consider two different protocols, namely, binary and non-binary, which rely on exhaustive searches [136, 149].

In line with some recent findings in the literature [150, 151], we later reduce the resulting overhead by grouping adjacent elements of the RIS and performing joint estimations. Besides, considering the use of machine learning techniques, the estimation process could be further improved (even if the number of pilots is limited) [152, 153].

Each sensor will sequentially send a training sequence of length W repeated over T training periods towards the CN. As depicted in Figure 5.2, after the T training periods, we will have T copies of M different training sequences of length W (one per sensor). Based on that, at each training period, we will tune the response of the RIS so that the CN can calculate the channel estimates using the aforementioned strategies.

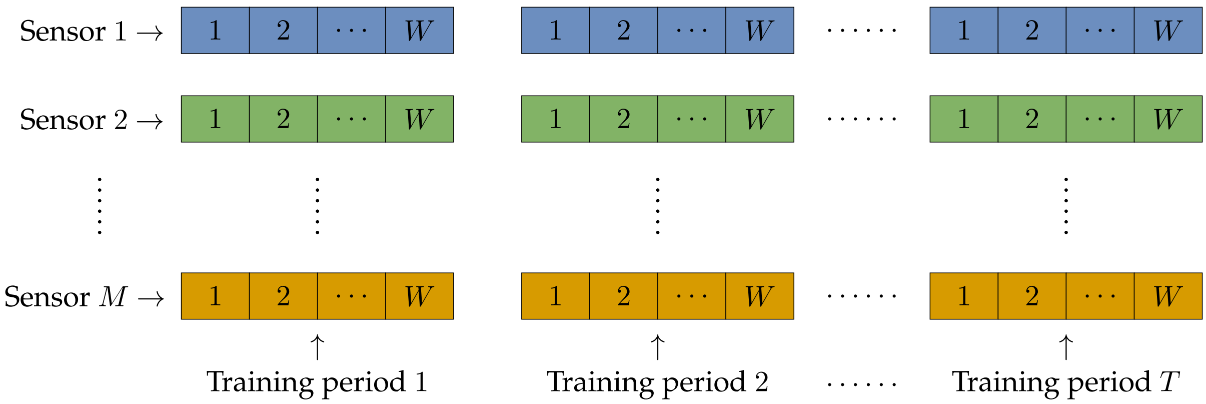

Figure 5.2: Training phase of the channel estimation (different colors represent different pilot sequences).

Note that, since this information will be sent sequentially, we will end up with T different received signals (one for each training period). Accordingly, the received signal associated with training period t can be written as [149]

$$\boldsymbol{y}_t \triangleq \sum_{i=1}^{M} \left(q_i + \boldsymbol{v}_t^{\mathrm{T}} \boldsymbol{g}_{\mathrm{C},i}\right) \boldsymbol{p}_i + \boldsymbol{w}_t \in \mathbb{C}^W, \quad t \in \{1, \dots, T\}, \tag{5.6}$$

where $\boldsymbol{p}_i = [p_{i,1}, \dots, p_{i,W}]^{\mathrm{T}} \in \mathbb{C}^W$ is the (known) UL pilot of sensor i with $|p_{i,m}|^2 = P_i \ \forall m$, W is the length of each training sequence $\boldsymbol{p}_i$, and $\boldsymbol{w}_t \in \mathbb{C}^W$ is the noise defined in (5.2) at training period t, i.e., $\boldsymbol{w}_t \sim \mathcal{CN}(\mathbf{0}, \sigma_w^2 \mathbf{I}_W)$. Note that $\boldsymbol{v}_t \in \mathbb{C}^L$ is the vector containing the elements of the RIS matrix at training period t, which depends on the channel estimation approach.

Both channels (q_i and $\boldsymbol{g}_{\mathrm{C},i}$) can be obtained through conventional MMSE estimation after correlating $\boldsymbol{y}_t$ with each pilot. For the sake of simplicity, we will consider that the direct link q_i can be perfectly estimated and removed from the received signal [147]. This way, we can concentrate on the estimation of the cascaded channel $\boldsymbol{g}_{\mathrm{C},i}$.

By means of pilot correlation[2], we obtain the sufficient estimation statistic for sensor i at training period t:

$$z_{i,t} \triangleq \frac{\boldsymbol{p}_i^{\mathrm{H}}}{\|\boldsymbol{p}_i\|_2^2} \boldsymbol{y}_t = \boldsymbol{v}_t^{\mathrm{T}} \boldsymbol{g}_{\mathrm{C},i} + \frac{\boldsymbol{p}_i^{\mathrm{H}}}{W P_i} \boldsymbol{w}_t. \tag{5.7}$$

The whole set of sufficient statistics $\boldsymbol{z}_i = [z_{i,1}, \dots, z_{i,T}]^{\mathrm{T}} \in \mathbb{C}^T$ for sensor i can then be written as

$$\boldsymbol{z}_i \triangleq \boldsymbol{\Upsilon} \boldsymbol{g}_{\mathrm{C},i} + \left(\frac{\boldsymbol{p}_i^{\mathrm{H}}}{W P_i} [\boldsymbol{w}_1, \dots, \boldsymbol{w}_T]\right)^{\mathrm{T}}, \tag{5.8}$$

where $\boldsymbol{\Upsilon} = [\boldsymbol{v}_1, \dots, \boldsymbol{v}_T]^{\mathrm{T}} \in \mathbb{C}^{T \times L}$ is the RIS response matrix during the estimation process and will be discussed in the upcoming subsections.

---

[2] The training pilots are considered to be mutually orthogonal such that no interference (contamination) is experienced after correlation, i.e., $\boldsymbol{p}_i^{\mathrm{H}} \boldsymbol{p}_i = W P_i$ and $\boldsymbol{p}_i^{\mathrm{H}} \boldsymbol{p}_j = 0$ for $j \neq i$ [149]. This can be ensured as long as $W \geq M$. Note that, for scenarios with too many sensors, M could be reduced with device selection techniques (cf. Chapter 4).

Based on that, the linear MMSE estimate of the cascaded channel reads as follows [95]:

$$\begin{aligned}\hat{\boldsymbol{g}}_{\mathrm{C},i} \triangleq \mathbb{E}[\boldsymbol{g}_{\mathrm{C},i}|\boldsymbol{z}_i] &= \underbrace{\boldsymbol{C}_{\boldsymbol{g}_{\mathrm{C},i}}\boldsymbol{\Upsilon}^{\mathrm{H}}\left(\boldsymbol{\Upsilon}\boldsymbol{C}_{\boldsymbol{g}_{\mathrm{C},i}}\boldsymbol{\Upsilon}^{\mathrm{H}} + \frac{\sigma_w^2}{WP_i}\mathbf{I}_T\right)^{-1}}_{\triangleq \boldsymbol{A}_i}\left(\boldsymbol{z}_i - \boldsymbol{\Upsilon}\boldsymbol{\mu}_{\boldsymbol{g}_{\mathrm{C},i}}\right) + \boldsymbol{\mu}_{\boldsymbol{g}_{\mathrm{C},i}} \\ &= \boldsymbol{A}_i\boldsymbol{z}_i + \underbrace{(\mathbf{I}_L - \boldsymbol{A}_i\boldsymbol{\Upsilon})\boldsymbol{\mu}_{\boldsymbol{g}_{\mathrm{C},i}}}_{\triangleq \boldsymbol{b}_i} = \boldsymbol{A}_i\boldsymbol{z}_i + \boldsymbol{b}_i,\end{aligned} \tag{5.9}$$

where $\boldsymbol{A}_i \in \mathbb{C}^{L\times T}$ and $\boldsymbol{b}_i \in \mathbb{C}^L$ are defined for the sake of clarity in the notation. In addition, we denote $\tilde{\boldsymbol{g}}_{\mathrm{C},i} = \boldsymbol{g}_{\mathrm{C},i} - \hat{\boldsymbol{g}}_{\mathrm{C},i}$ as the resulting uncorrelated estimation error with zero mean and covariance matrix $\boldsymbol{C}_{\tilde{\boldsymbol{g}}_{\mathrm{C},i}} \triangleq \mathbb{E}\left[\tilde{\boldsymbol{g}}_{\mathrm{C},i}\tilde{\boldsymbol{g}}_{\mathrm{C},i}^{\mathrm{H}}|\boldsymbol{z}_i\right] = \boldsymbol{C}_{\boldsymbol{g}_{\mathrm{C},i}} - \boldsymbol{A}_i\boldsymbol{\Upsilon}\boldsymbol{C}_{\boldsymbol{g}_{\mathrm{C},i}}$. As we will see in Section 5.4, this I-CSI knowledge will affect the SIC decoding procedure.

Overall, as discussed in the forthcoming sections, in both strategies (binary and non-binary RIS matrices), there will exist a trade-off between the channel estimation error and the required overhead training, i.e., smaller T and W yield a higher error but a smaller overhead. This will have an impact on the MSE of the parameter estimation (further studied in Section 5.6).

5.3.1 Binary Protocol

A common procedure is the so-called on/off (or binary) protocol [136], in which all RIS elements are sequentially turned off except for one (or more) reflector(s). This way, at each training period, the CN will estimate the effective channel(s) corresponding to the active element(s). Recall that we distinguish between two setups: no grouping and grouping.

5.3.1.1 No Grouping

In this case, the RIS response at training period t is directly $\boldsymbol{v}_t = \boldsymbol{e}_t$, where $\{\boldsymbol{e}_t\}$ refers to the set of canonical vectors, i.e., $[\boldsymbol{e}_t]_t = 1$ and $[\boldsymbol{e}_t]_{t'} = 0\,\forall t' \neq t$.. This means that, when the t-th element is on (and all the other ones are off), it is used for estimating the t-th element of the cascaded channel $\boldsymbol{g}_{\mathrm{C},i}$. As a result, we have $\boldsymbol{\Upsilon} = \mathbf{I}_T$ with $T = L$.

5.3.1.2 Grouping

As the previous procedure entails a prohibitive number of pilots for large surfaces, a possible alternative is to group adjacent elements and, for each training period, activate the corresponding reflectors simultaneously [150]. This way, considering a group size G, the number of training sequences is given by $T = L/G$. Accordingly, the RIS estimation matrix can be expressed as $\boldsymbol{\Upsilon} \triangleq \mathbf{I}_T \otimes \mathbf{1}_G^{\mathrm{T}}$, which represents the activation of the different groups. For instance, if $G = 2$ and $L = 6$, two adjacent elements will be simultaneously activated and, thus, this matrix results

$$\boldsymbol{\Upsilon} = \begin{bmatrix} 1 & 1 & 0 & 0 & 0 & 0 \\ 0 & 0 & 1 & 1 & 0 & 0 \\ 0 & 0 & 0 & 0 & 1 & 1 \end{bmatrix}. \tag{5.10}$$

5.3.2 Non-Binary Protocol

Instead of considering a binary matrix RIS (i.e., $\lambda_l = 0$, off-state, or $\lambda_l = 1$, on-state), another approach is to consider all reflectors to be active and design the set of phase-shifts at each training period [149]. In other words, we can define the RIS response as $\boldsymbol{v}_t = [\lambda_{t,1} e^{j\phi_{t,1}}, \ldots, \lambda_{t,L} e^{j\phi_{t,L}}]^{\mathrm{T}}$ with amplitude coefficients $\lambda_{t,l} = 1$ (activated) and phase-shifts $\phi_{t,l} \in [0, 2\pi]$ for estimating the cascaded channel at period t. Note that this reasoning holds for both cases, grouping and no grouping, yet in the latter we will have $T = L$. As an example, when considering $G = 1$ (i.e., no grouping), the authors of [149] discussed a discrete Fourier transform (DFT)-based approach where the elements of $\boldsymbol{\Upsilon}$ are given by $[\boldsymbol{\Upsilon}]_{t,l} = \exp\left(-\mathrm{i}2\pi(t-1)(l-1)/L\right)$.

5.4 SIC Decoding

As mentioned before, in this chapter, we consider the use of SIC to mitigate the impact of the interference during the communication stage of the devices [137]. In SIC, the different signals are decoded sequentially following a certain order (as later discussed in Section 5.5) and, at each step, the previously decoded signals are canceled i.e., their contributions are removed.

Without loss of generality, let us consider a decoding order $\mathcal{S}$, which can be easily defined by the function $o(\cdot)$ applied to the sensor's index, i.e., $o(i)$ is the step at which sensor i is decoded. Thereby, the SINR for the received signal of sensor i results [44,45]

$$\rho_i^{\text{CSI}} \triangleq \frac{P_i |h_i|^2}{\sigma_w^2 + \sum\limits_{\substack{j=1 \\ o(j)<o(i)}}^{M} \gamma_j P_j |h_j|^2 + \sum\limits_{\substack{j=1 \\ o(j)>o(i)}}^{M} P_j |h_j|^2}, \tag{5.11}$$

where γ_j is a binary RV that accounts for the cancelation failure of the previous signals due to communication errors, i.e., $\gamma_j \sim \mathit{Ber}(\text{PER}_j)$ with PER_j the decoding error probability of sensor j [36] (cf. Subsection 2.2.2.2). However, when considering I-CSI acquisition, there will still be a residual power due to imperfect cancelation, i.e.,

$$\rho_i^{\text{I-CSI}} \triangleq \frac{P_i |\hat{h}_i|^2}{\sigma_w^2 + P_i|\tilde{h}_i|^2 + \sum\limits_{\substack{j=1 \\ o(j)<o(i)}}^{M} (1-\gamma_j) P_j |\tilde{h}_j|^2 + \sum\limits_{\substack{j=1 \\ o(j)<o(i)}}^{M} \gamma_j P_j |h_j|^2 + \sum\limits_{\substack{j=1 \\ o(j)>o(i)}}^{M} P_j |h_j|^2}, \tag{5.12}$$

where $\hat{h}_i \triangleq q_i + \boldsymbol{\psi}^{\mathrm{T}} \hat{\boldsymbol{g}}_{\mathrm{C},i}$ is the estimated effective channel[3] and $\tilde{h}_i \triangleq h_i - \hat{h}_i = \boldsymbol{\psi}^{\mathrm{T}} \tilde{\boldsymbol{g}}_{\mathrm{C},i}$ is the corresponding channel estimation error. Thus, the terms $|\tilde{h}_j|^2 \triangleq |\boldsymbol{\psi}^{\mathrm{T}} \tilde{\boldsymbol{g}}_{\mathrm{C},i}|^2$ represent the residual powers that originate from the imperfect channel knowledge (i.e., parts of $\{h_{j:o(j)<o(i)}\}$ that are not completely suppressed after decoding).

It can be shown that, for a proper performance of the SIC procedure, it is imperative to have unbalanced received powers in order to separate the signals of the different devices (i.e., power-domain NOMA [154]).

---

[3] Recall that we assume that the direct channel q_i is perfectly known (estimated) at the CN.

As an example, for the case of equal QoS requirements, the optimal distribution of the received power follows an exponential profile [155]. However, since our goal is to minimize the MSE in the estimation of $\boldsymbol{\theta}$, the optimal distribution might be different.

In conventional wireless networks, the difference in received powers can be attained by modifying the sensors' transmit powers, or by designing spatial filters at the CN (when equipped with multiple-antenna technology) [156]. Nevertheless, in mMTC scenarios, power allocation mechanisms are not feasible due to the large number of devices involved. In fact, even when available, the simplicity of the sensors limits the number of power levels and their adjustment. That is why the set of powers P_i is normally considered to be fixed.

In our case, given the presence of the RIS, the different channel gains can be adapted. Thus, the role of the RIS is two-fold: (1) to improve the quality of the received signals, and (2) to adapt the effective channels to the SIC procedure.

Recall that in order to find the decoding error probability, which is a function of the SINR, we need to establish a certain MCS (cf. Subsection 2.2.2.2). Given that an analytic closed-form expression for each PER$_i$ is usually available in the case of only modulation and no coding (e.g., QPSK without error protection), in this chapter, we employ the approximation in (2.7):

$$\mathrm{PER}_i \approx Q\left(\sqrt{n_i}\frac{C(\rho_i) - R_i}{\sqrt{V(\rho_i)}}\right), \tag{5.13}$$

where n_i is the number of transmit symbols (or packet length), $Q(\cdot)$ is the Gaussian Q-function, $C(x) = \log(1 + x)$ is the AWGN channel capacity, and $V(x) = (1 - (1 + x)^{-2}) \log^2 e$ is the so-called channel dispersion [39]. In line with Chapter 2, the term $R_i = l_i/n_i$ represents the (coded) data rate (with l_i the number of information bits). Besides, we will consider the same number of symbols for all sensors, which is determined by the product of the total bandwidth B_s and the packet (or slot) duration T_s, i.e., $n_i = n_s = B_sT_s$ (cf. Section 4.2).

Unfortunately, due to the presence of I-CSI and decoding errors in (5.12), the resulting SINR is random. It depends on the previously decoded sensors through their RVs γ_j with parameter PER$_j$. Hence, since the decoding system is dynamic, there is a statistical dependence between the SINRs (the different Bernoulli RVs γ_j are dependent).

As a result, the joint distribution of the SINRs becomes difficult to compute (the number of required terms grows exponentially with the number of sensors [157]). That is why in this section, in order to deal with tractable statistics, we will use a different SIC decoding procedure [158]. More specifically, now sensor i can only be decoded when the previous ones are correctly decoded (but not completely canceled due to I-CSI errors), i.e., $\gamma_j = 0$ with $j : o(j) < o(i)$, which represents a worse-case and more conservative scenario.

Based on that, the SINR for each sensor becomes a binary RV of value

$$\rho_i^{\text{SIC,I-CSI}} \triangleq \frac{P_i|\hat{h}_i|^2}{\sigma_w^2 + \sum\limits_{\substack{j=1\\o(j)<o(i)}}^{M} P_j|\tilde{h}_j|^2 + \sum\limits_{\substack{j=1\\o(j)>o(i)}}^{M} P_j|h_j|^2}, \tag{5.14}$$

with probability $\varphi_i \triangleq \Pr\{\gamma_j = 0, \forall j : o(j) < o(i)\}$ and 0 (no decoding) with probability $1 - \varphi_i$.

As a result, in this case, errors can be due to actual decoding failure of the sensor of interest, or to incorrectly decoded packets of previous sensors (i.e., error propagation). Since these events might not be disjoint (or mutually exclusive), we could use the following bounds [158]:

$$\max\left(\mathrm{PER}_i^{\mathrm{SIC,\,I\text{-}CSI}}, \mathrm{PER}_{i-1}\right) \leq \mathrm{PER}_i \leq \mathrm{PER}_i^{\mathrm{SIC,\,I\text{-}CSI}} + \mathrm{PER}_{i-1}, \tag{5.15}$$

where $\mathrm{PER}_i^{\mathrm{SIC,I\text{-}CSI}}$ refers to the PER of sensor i when the previous sensors are perfectly decoded but not completely canceled due to I-CSI knowledge. In fact, this probability is given by the approximation in (5.13) with SINR $\rho_i^{\mathrm{SIC,I\text{-}CSI}}$.

Nevertheless, given the presence of the estimation errors $\tilde{h}_j$, the SINR in (5.14) is still random. As discussed in Appendix 5.A, to overcome this issue, we consider the approach derived in [159], i.e., condition on the set of observations $\boldsymbol{z} = [\boldsymbol{z}_1^{\mathrm{T}}, \ldots, \boldsymbol{z}_M^{\mathrm{T}}]^{\mathrm{T}}$:

$$\rho_i^{\mathrm{SIC,I\text{-}CSI}}|\boldsymbol{z} \triangleq \frac{P_i|\hat{h}_i|^2}{\sigma_w^2 + \sum\limits_{j=1}^{M} P_j \boldsymbol{\psi}^{\mathrm{T}} \boldsymbol{C}_{\tilde{\boldsymbol{g}}_{\mathrm{C}},j} \boldsymbol{\psi}^* + \sum\limits_{\substack{j=1 \\ o(j)>o(i)}}^{M} P_j |\hat{h}_j|^2}. \tag{5.16}$$

Consequently, the error probability in (5.15) is also conditioned on $\boldsymbol{z}$, i.e., $\mathrm{PER}_i|\boldsymbol{z}$. Hence, we only need to average over the distribution of $\boldsymbol{z}$. This is discussed in the upcoming section.

5.5 Robust RIS Design

The purpose of this chapter is to design the RIS in order to minimize the parameter estimation error, taking into account I-CSI. For that task, the CN needs to estimate the cascaded channel (prior to transmission). That is why in the present section, apart from the optimization of the matrix $\boldsymbol{\Psi}$ for data transmission, we will also include the optimization of the RIS matrix $\boldsymbol{\Upsilon}$ (only in the non-binary case) and group size G for the training phase.

As discussed in Section 5.3, considering perfect CSI knowledge is not a realistic assumption and estimating the channel becomes a challenging task in a RIS-aided environment (especially for large L, where the size of the required overhead is prohibitive). In fact, the number of pilot symbols $n_p = WT = WL/G$ and the number of transmitted symbols n_s are both limited by the temporal variation of the channel [160]:

$$n_p + n_s = n_c, \tag{5.17}$$

where n_c is the number of symbols equivalent to the coherence time [36]. Accordingly, a larger training stage will improve the channel estimation error, but compromise the parameter estimation accuracy (few symbols will be available for data transmission). Contrarily, when n_p is small, the channel estimation will be poor in exchange for more transmit symbols n_s (although the resulting CSI errors might also limit the parameter estimation). Therefore, finding the right balance between n_p and n_s will be crucial for a good performance.

Under the decoding procedure from Section 5.4 and a decoding order $\mathcal{S}$, the MSE (conditioned on $\boldsymbol{z}$) of the parameter estimation can be written as follows:

$$\varepsilon_{\boldsymbol{z}} \triangleq \varepsilon|\boldsymbol{z} = \sum_{i\in\mathcal{S}} \varrho_{\boldsymbol{z},i}\varepsilon_i + \varrho_{\boldsymbol{z},0}\varepsilon_0, \tag{5.18}$$

where ε_i is the MSE when the information of the sensors in the set $\{j : o(j) \leq o(i)\}$ is available (i.e., correctly decoded) and $\varrho_{\boldsymbol{z},i} \triangleq \Pr\{\gamma_j = 0, \forall j : o(j) \leq o(i) \,\text{and}\, \gamma_{j:o(j)=o(i)+1} = 1|\boldsymbol{z}\}$ is the corresponding probability[4]. Note that ε_0 is the case of complete communication failure (i.e., no sensors can be correctly decoded) and $\varrho_{\boldsymbol{z},0} \triangleq \Pr\{\gamma_{j:o(j)=1} = 1|\boldsymbol{z}\} = 1 - \sum_{i\in\mathcal{S}} \varrho_{\boldsymbol{z},i}$.

Considering a linear MMSE estimate for the parameter $\boldsymbol{\theta}$, the individual ε_i are given by [95]

$$\varepsilon_i \triangleq \mathrm{tr}\left(\boldsymbol{C}_{\boldsymbol{\theta}} - \boldsymbol{C}_{\boldsymbol{\theta}}\boldsymbol{V}_i^{\mathrm{T}}\left(\boldsymbol{V}_i\left(\boldsymbol{C}_{\boldsymbol{\theta}} + \boldsymbol{C}_{\boldsymbol{\eta}}\right)\boldsymbol{V}_i^{\mathrm{T}}\right)^{-1}\boldsymbol{V}_i\boldsymbol{C}_{\boldsymbol{\theta}}\right), \tag{5.19}$$

where $\boldsymbol{V}_i \in \{0,1\}^{i\times M}$ is a binary matrix indicating the correctly decoded messages (equivalent to matrix $\boldsymbol{A}_{\mathcal{I}}$ from Subsection 4.3.2.2).

This way, the overall MSE can be obtained by averaging $\varepsilon_{\boldsymbol{z}}$ w.r.t. the statistics of $\boldsymbol{z}$, i.e.,

$$\varepsilon = \mathbb{E}_{\boldsymbol{z}}\left[\varepsilon|\boldsymbol{z}\right] = \int_{\mathcal{Z}} \varepsilon_{\boldsymbol{z}} f_{\boldsymbol{z}}(\boldsymbol{z}) d\boldsymbol{z}, \tag{5.20}$$

where $f_{\boldsymbol{z}}(\boldsymbol{z}) : \mathbb{C}^{LM} \to \mathbb{R}$ is the joint distribution of the observations with support $\mathcal{Z}$, which depends on the channel estimation method (cf. Section 5.3). This is further discussed in Section 5.6, where we focus on particular channel models. Besides, given the combinatorial nature of $\varepsilon_{\boldsymbol{z}}$, the integral in (5.20) can only be solved numerically (see Appendix 5.C).

Depending on the decoding order $\mathcal{S}$, the performance of the SIC procedure can be considerably affected [155]. Hence, its impact has to be also contemplated in the minimization of ε. As a result, considering the constraint in (5.17), and the fact that $W \geq M$ to ensure orthogonality among training pilots[5], the optimization problem reads as

$$\{\boldsymbol{\Upsilon}^\star, G^\star, \boldsymbol{\Psi}^\star, \mathcal{S}^\star\} = \mathrm{argmin}\ \varepsilon \quad \text{s.t.} \quad ML/G = n_c - n_s, \tag{5.21}$$

which can be solved separately [161], i.e., decompose the joint optimization into separate problems, find each variable when the rest are fixed, and alternate the searches until convergence is reached (cf. Subsection 4.4.2.2.1). Since at each iteration we keep the same MSE or improve its value, convergence is always assured. This results into a feasible, yet sub-optimal approach (the alternating optimization does not guarantee to attain the global optimum solution). For the sake of clarity in the explanation, we dedicate separate subsections for each sub-problem.

5.5.1 RIS Matrices

For a fixed group size G, decoding order $\mathcal{S}$, and RIS estimation matrix $\boldsymbol{\Upsilon}$, we have

$$\boldsymbol{\Psi}^\star = \mathrm{argmin}\ \varepsilon, \tag{5.22}$$

---

[4] Please refer to Appendix 5.B for the exact expression of $\varrho_{\boldsymbol{z},i}$.

[5] In this section, we further assume that $W = M$.

which can be solved sequentially. In short, given that $\boldsymbol{\Psi}$ contains variable elements $\phi_l \in [0, 2\pi]$, each of them can be found through the bisection method [123] when the rest are fixed. This operation is then repeated until convergence is reached (guaranteed since each iteration yields the same or a lower MSE). The same procedure can also be used for optimizing $\boldsymbol{\Upsilon}$ (although the search space increases from L to TL elements). Recall that such a problem is only formulated for the case of non-binary channel estimation protocols (cf. Section 5.3).

5.5.2 Group Size

To find the optimal group size, problem (5.21) yields

$$G^\star = \text{argmin } \varepsilon \quad \text{s.t.} \quad ML/G = n_c - n_s, \tag{5.23}$$

which can be solved by one-dimensional search since $1 \leq G \leq L$.

5.5.3 Decoding Order

Contrarily, when $\boldsymbol{\Upsilon}$, G, and $\boldsymbol{\Psi}$ are given, the problem in (5.21) can be written as

$$\{\mathcal{S}^\star\} = \text{argmin } \varepsilon, \tag{5.24}$$

which has a combinatorial nature with complexity $\mathcal{O}(M!)$. Thus, exhaustive search is not bearable (even for a small number of sensors M). In fact, although the number of active sensors can be reduced with the device selection techniques from Chapter 4, the computational cost is still unfeasible. That is why we will present some heuristic strategies to obtain the decoding order.

5.5.3.1 Gain-Based Solution

As the PER increases with the deterioration of the SINR (cf. (5.13)), a typical way of determining the decoding order is through the (estimated) channel gains of the different sensors.

In particular, when decoded first, the CN can struggle to decode the signals of the devices with poor channels because they are largely affected by the high interference (no cancelation is performed) [158]. On the contrary, the devices with better conditions can be decoded more easily. Then, we can consider that $\mathcal{S}$ is given by the descending order of the gains of the (estimated) effective channels $\hat{h}_i$ [154].

5.5.3.2 Measurement-Based Solution

The strategy above does not contemplate the quality of the observations, which affect the individual MSEs ε_i (cf. (5.19)) and can be measured through the ratio $[\boldsymbol{C_\theta}]_{i,i}/[\boldsymbol{C_\eta}]_{i,i}$. Hence, another approach can be to order the sensors according to their measurements. Different from before, this ordering does not affect $\boldsymbol{\Psi}$, $\boldsymbol{\Upsilon}$, nor G (ρ_i is fixed and independent of the RIS matrices and group size) and, thus, no alternating optimization is needed.

Algorithm 5.1 Greedy sensor ordering [162]

```
Initialize orders: $\mathcal{S}^m(1) = m \, \forall m$
for $m = 1 : M$ do
    for $s = 2 : M$ do
        Find next sensor: $j_s^m = \underset{j \notin \mathcal{S}_{s-1}^m}{\text{argmin}} \, \varepsilon_s^m$
        Add next sensor: $\mathcal{S}^m(s) = j_s^m$
    end for
end for
Select best order: $\mathcal{S} = \underset{\{\mathcal{S}^m\}}{\text{argmin}} \, \varepsilon_M^m$
```

5.5.3.3 Combined Solution

The previous approaches can be combined to consider both, channel gain and measurement quality. In particular, in this subsection, we first propose a greedy-based approach similar to that described in [162]. The main idea is to construct the vector $\mathcal{S}$ sequentially so that at each stage we choose the sensing device minimizing the estimation error from (5.20), which includes transmission quality (through the PERs) and estimation performance (through the MSEs ε_i).

Let us denote $\mathcal{S}^m \in \mathbb{N}^M$ as the decoding order when starting with sensor m and $\mathcal{S}_{s-1}^m \triangleq [\mathcal{S}^m(1), \ldots, \mathcal{S}^m(s-1)] \in \mathbb{N}^{s-1}$ as the vector containing the first $s-1$ elements of $\mathcal{S}^m$. Then, at stage $s \in \{1, \ldots, M\}$ we will select the device $j_s^m \notin \mathcal{S}_{s-1}^m$ that minimizes the average MSE

$$\varepsilon_s^m = \mathbb{E}\left[\sum_{i \in \mathcal{S}_s^{m,j}} \varrho_{\boldsymbol{z},i} \varepsilon_i + \varrho_{\boldsymbol{z},0} \varepsilon_0 \middle| \boldsymbol{z} \right], \tag{5.25}$$

where $\mathcal{S}_s^{m,j} \triangleq [\mathcal{S}_s^m : \mathcal{S}^m(s) = j_s^m]$ is the corresponding order when inserting sensor j_s^m. As a result, the ultimate decoding order (i.e., the one at stage $s = M$) when starting with sensor m will be $\mathcal{S}^m = [m, j_2^m, \ldots, j_M^m]$. Finally, in order to find the optimal $\mathcal{S}$, we need to evaluate over all the possible initial sensors and select the one minimizing the total MSE ε_M^m. The whole procedure is summarized in Algorithm 5.1.

Alternatively, we can also select the decoding order sequentially, but considering the complete MSE ε. To do so, we initialize $\mathcal{S}$ randomly and, for each position, we try all the available possibilities. At stage s, we discard the sensors decoded up to stage $s-1$, i.e., those in $\mathcal{S}_{s-1} \triangleq [\mathcal{S}(1), \ldots, \mathcal{S}(s-1)] \in \mathbb{N}^{s-1}$, and select the best one among the remaining devices (the sensor minimizing ε that has not been decoded yet). For instance, if $M = 3$ and the initial order is $\mathcal{S} = [3, 1, 2]$, we can choose between sensors 1, 2 and 3 for the first position ($\mathcal{S}_0$ has no elements). Accordingly, the positions of the devices involved must be swapped (e.g., sensor 3 changes to the position of the sensor under evaluation). Then, considering 2 is the selected terminal, at stage 2 the available devices are only 1 and 3 (i.e., $\mathcal{S}_1 = 2$). Finally, assuming we choose sensor 3, at the last stage the available option is terminal 1 because $\mathcal{S}_2 = [2, 3]$. Hence, the decoding order would result $\mathcal{S} = [2, 3, 1]$. This is detailed in Algorithm 5.2.

Algorithm 5.2 Combined sensor ordering

```
Initialize $\mathcal{S}$
for $s = 1 : M$ do
    Find next sensor: $j = \underset{j \notin \mathcal{S}_{s-1}}{\text{argmin}}\ \varepsilon$
    Update order: $\mathcal{S}(s, s') = [j, j']$ s.t. $\mathcal{S}(s) = j'$ and $\mathcal{S}(s') = j$
end for
```

5.6 Numerical Simulations

In this section, the resulting MSE ε (cf. (5.20)) after the RIS optimization is analyzed for different setups. To that end, we will consider a realistic mMTC network for our study. In particular, we will use the parameters and guidelines specified by the 3GPP and ITU standards [35, 90]. As in Section 4.6, we will consider that the set of measurements is obtained from the database collected by the Intel Berkeley Research Lab with $M = 30$ [129]. That is why in the following, we dedicate an initial subsection to discussing these practical issues.

5.6.1 Practical Issues

In all simulations, we consider the micro-urban scenario described in [90] with $P_i = P = 0$ dBm and $\sigma_w^2 = N_o B_s$ with $N_o = -174$ dBm/Hz and $B_s = 180$ kHz (cf. NB-IoT [22]). Besides, we further assume a coherence block of n_c OFDMA (sub-carrier) symbols, each of duration $T_o \approx 71.4$ μs [35] and spacing $B_o = 15$ kHz [40].

Note that n_c (later defined) depends on the sensors' mobility and will condition the tuple n_s and n_p (cf. (5.17)). The packet duration results $T_s = n_s T_o$ and will vary according to the group size G (or, equivalently, the number of training pilots n_p). The individual data rates $R_i = l_i / n_s$ from (5.13) are extracted from Table 5.2.2.1 in [35]. In order to meet all these temporal requirements, the number of information bits l_i will be adapted (which ultimately affect the parameter estimation accuracy).

Regarding the channels between sensors and CN, we assume a power-law path loss, i.e.,

$$q_i = d_i^{-\alpha/2} \chi_i, \tag{5.26}$$

where d_i is the distance from sensor i to the CN, $\chi_i \sim \mathcal{CN}(0, 1)$ is the fading coefficient, and $\alpha = 3$ is the decay exponent. The spatial distribution is given by the deployment in [129].

On the other hand, the channels between sensors and RIS can be described by the well-known Saleh-Valenzuela model [163, 164]:

$$\boldsymbol{g}_i = \delta_i^{-\alpha/2} \underbrace{\frac{1}{\sqrt{D}} \sum_{k=1}^{D} \tau_{i,k} \boldsymbol{v}(\vartheta_{i,k})}_{\triangleq \boldsymbol{v}_i}, \tag{5.27}$$

where δ_i is the distance from sensor i to the RIS, D is the number of (dominant) paths, $\tau_{i,k} \sim \mathcal{CN}(0, 1)$ is the (uncorrelated) fading coefficient of path k (independent among the sensors), $\boldsymbol{v}(\cdot) = [v_1, \ldots, v_L]^{\mathrm{T}} \in \mathbb{C}^L$ is the steering vector, and $\vartheta_{i,k}$ is the steering direction of path k [89].

Likewise, the channel between RIS and CN can be written as follows [165]:

$$\boldsymbol{g}_{\mathrm{R}} = \delta_{\mathrm{R}}^{-\alpha/2} \left(\sqrt{\frac{1}{1+F}} \boldsymbol{\tau}_{\mathrm{R}} + \sqrt{\frac{F}{F+1}} \underbrace{\frac{1}{\sqrt{U}} \sum_{k=1}^{U} \boldsymbol{v}(\vartheta_{\mathrm{R},k})}_{\triangleq \boldsymbol{v}_{\mathrm{R}}} \right), \tag{5.28}$$

where δ_{R} is the distance from the RIS to the CN, F is the Rician factor, $\boldsymbol{\tau}_{\mathrm{R}} \sim \mathcal{CN}(\mathbf{0}_L, \mathbf{I}_L)$ are the NLoS components (assumed to be Rayleigh distributed), U is the number of paths (or taps), and $\vartheta_{\mathrm{R},k}$ is the steering direction corresponding to path k.

Throughout all simulations, we consider that the RIS is equipped with a uniform planar array (UPA) of L elements and we set the reflection coefficients λ_l from the RIS data matrix $\boldsymbol{\Psi}$ to 1 [134]. Additionally, we assume that the angles $\vartheta_{i,k}$ and $\vartheta_{\mathrm{R},i}$ are generated according to Von Mises distributions with means $\vartheta_{i,0}$ and $\vartheta_{\mathrm{R},0}$ and spread $\zeta = 6$ [166]. Both azimuth directions $\vartheta_{i,0}$ and $\vartheta_{\mathrm{R},0}$ refer to the AoA of the sensors and RIS signals, respectively. Finally, the number of paths D and U are proportional to L [167].

Given that the RIS will be usually deployed in a position that ensures a strong LoS with the CN, the NLoS components might be considered negligible ($F \to \infty$) and, therefore, the channel $\boldsymbol{g}_{\mathrm{R}}$ can be approximated by a constant, i.e., $\boldsymbol{g}_{\mathrm{R}} \approx \delta_{\mathrm{R}}^{-\alpha/2} \boldsymbol{v}_{\mathrm{R}}$. In this particular (simple) case[6], the cascaded channel $\boldsymbol{g}_{\mathrm{C},i} \approx (\delta_R \delta_i)^{-\alpha/2} \mathrm{diag}(\boldsymbol{v}_{\mathrm{R}}) \boldsymbol{v}_i$ is uniquely determined by the statistics of the sensor-to-RIS channel $\boldsymbol{g}_i$.

This way, the set of observations $\boldsymbol{z}$ is distributed as

$$\boldsymbol{z} \sim \mathcal{CN} \left(\begin{bmatrix} \boldsymbol{\mu}_{\boldsymbol{z}_1} \\ \vdots \\ \boldsymbol{\mu}_{\boldsymbol{z}_M} \end{bmatrix}, \begin{bmatrix} \boldsymbol{C}_{\boldsymbol{z}_1} & \dots & \mathbf{0}_{T\times T} \\ \vdots & \ddots & \vdots \\ \mathbf{0}_{T\times T} & \dots & \boldsymbol{C}_{\boldsymbol{z}_M} \end{bmatrix} \right), \tag{5.29}$$

where the different statistical moments $\boldsymbol{\mu}_{\boldsymbol{z}_i} \triangleq \mathbb{E}[\boldsymbol{z}_i] \in \mathbb{C}^T$ and $\boldsymbol{C}_{\boldsymbol{z}_i} \triangleq \mathbb{E}[\boldsymbol{z}_i \boldsymbol{z}_i^{\mathrm{H}}] \in \mathbb{C}^{T\times T}$ are directly defined by the channel estimation strategy (cf. (5.9)), i.e.,

$$\boldsymbol{\mu}_{\boldsymbol{z}_i} = \boldsymbol{\Upsilon} \boldsymbol{\mu}_{\boldsymbol{g}_{\mathrm{C},i}}, \quad \boldsymbol{C}_{\boldsymbol{z}_i} = \boldsymbol{\Upsilon} \boldsymbol{C}_{\boldsymbol{g}_{\mathrm{C},i}} \boldsymbol{\Upsilon}^{\mathrm{H}} + \frac{\sigma_w^2}{W P_i} \mathbf{I}_T, \tag{5.30}$$

with $\boldsymbol{\mu}_{\boldsymbol{g}_{\mathrm{C},i}} \approx \mathbf{0}$ and $\boldsymbol{C}_{\boldsymbol{g}_{\mathrm{C},i}} \approx (\delta_{\mathrm{R}} \delta_i)^{-\alpha} \mathrm{diag}(\boldsymbol{v}_{\mathrm{R}}) \mathbb{E}[\boldsymbol{v}_i \boldsymbol{v}_i^{\mathrm{H}}] \mathrm{diag}(\boldsymbol{v}_{\mathrm{R}})^{\mathrm{H}}$. The remaining expectations $\mathbb{E}[\boldsymbol{v}_i \boldsymbol{v}_i^{\mathrm{H}}] = 1/D \sum_k \mathbb{E}[\boldsymbol{v}(\vartheta_{i,k}) \boldsymbol{v}(\vartheta_{i,k})^{\mathrm{H}}]$ are calculated following the derivations in [168].

5.6.2 Robust RIS Design

In this subsection, we present several results to assess the performance of our estimation approach. For that task, the average MSE ε is evaluated w.r.t. the number of reflecting elements L, number of coherence symbols n_c, and number of sensors M. This is done for different setups, where we analyze the channel estimation protocols and SIC decoding orders $\mathcal{S}$.

---

[6] Note that the assumption of a deterministic RIS-to-CN channel $\boldsymbol{g}_{\mathrm{R}}$ is used here as a first approach to solve the problem. The analysis of more complex models will be object of study of future works.

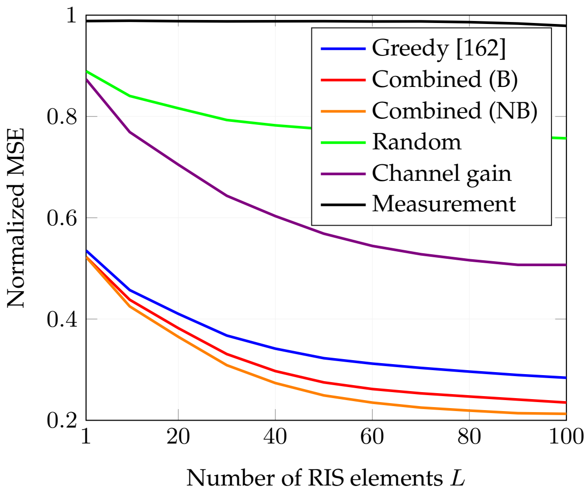

Figure 5.3: Normalized MSE $\varepsilon/\mathrm{tr}(\boldsymbol{C}_{\boldsymbol{\theta}})$ versus the number of reflecting elements L.

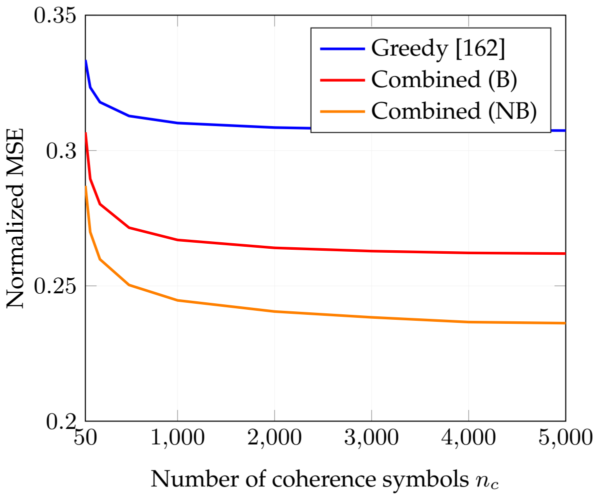

Figure 5.4: Normalized MSE $\varepsilon/\mathrm{tr}(\boldsymbol{C}_{\boldsymbol{\theta}})$ versus the number of coherence symbols n_c.

First, we will focus on the parameter estimation accuracy w.r.t. the size of the surface. This is illustrated in Figure 5.3 for $n_c = 1000$ and the decoding orders described in Subsection 5.5.3. For a broader comparison, the case of a random device ordering is also depicted. In order to avoid redundancy, the non-binary channel estimation protocol (NB) is only included with the combined decoding order. The rest of the curves are computed considering the binary approach (B). Note that, as in Subsection 4.6.2, we show the normalized MSE (NMSE) $\varepsilon/\mathrm{tr}(\boldsymbol{C}_{\boldsymbol{\theta}})$.

In most cases, the error decreases with the number of RIS elements because the surface gain can increase the resulting SINR. However, as discussed in Section 5.5, the performance of the SIC system depends greatly on $\mathcal{S}$. For instance, in the case of the measurement-based strategy, the decoding order yields an almost total error (i.e., NMSE close to 1) due to the high communication errors. In short, the selected order leads to large PERs (i.e., devices with poor channel quality are decoded first), preventing any decoding at the CN.

As expected, the non-binary approach provides better results than the binary case. Moreover, for larger values of L, both binary and non-binary protocols, together with the combined decoding order, surpass the performance of [162]. Overall, these simulations highlight the importance of choosing a suitable decoding order.

On the other hand, in Figure 5.4 we show the NMSE w.r.t. the number of coherence symbols. Recall that n_c is given by the product of system bandwidth B_s and coherence time T_c. In that sense, given the low mobility of sensors, a coherence time up to 50 ms might be considered (e.g., EPA-5 standard [11]). As we can observe, a larger coherence block yields a smaller error since we can dedicate more resources to channel knowledge and parameter estimation. In other words, more training pilots allow a better CSI acquisition, and $\mathrm{PER}_i \to 0$ with the number of transmit symbols (cf. (5.13)). Like before, the non-binary protocol with the combined decoding outperforms all the other schemes. For the sake of clarity in the explanation, the results of the random, gain-based, and measurement-based decoding orders have been omitted.

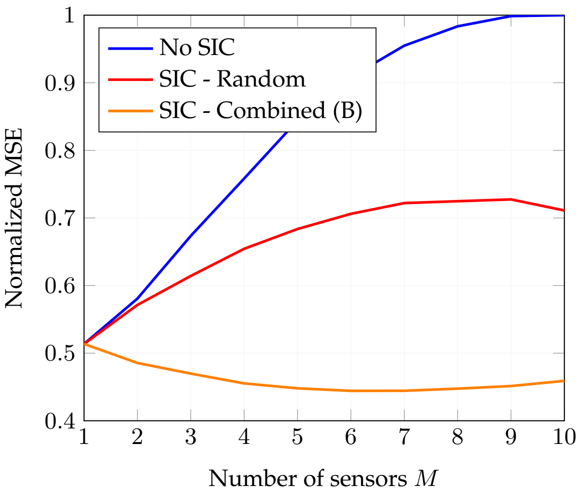

Figure 5.5: Normalized MSE $\varepsilon/\mathrm{tr}(\boldsymbol{C}_{\boldsymbol{\theta}})$ versus the number of sensors M.

Finally, in this subsection, we also study the accuracy of our proposal in terms of the number of sensors. This is depicted in Figure 5.5, where we also include the case of no SIC decoding (which can be calculated following the derivations in Chapter 4). For a fair comparison, only 1 incorrectly decoded packet is allowed in the expression from Subsection 4.4.2. It is easy to see that this last case performs poorly when increasing M (the NMSE tends to one). The reason behind this is that, as interference is not suppressed, the resulting decoding error probabilities are too large for reliable communication. This justifies the use of interference cancelation methods to avoid the saturation of the NMSE. However, only when the SIC decoding order is properly chosen (e.g., combined strategy), a decreasing behavior is obtained.

5.7 Summary and Conclusions

In this chapter, we have addressed the problem of designing a RIS to support the parameter estimation in a mMTC network. Considering a scenario where a set of sensors transmit their correlated measurements to a serving CN on a NOMA basis, we have presented an estimation scheme based on the MMSE criterion. The resulting estimate is derived taking into account communication and I-CSI errors. Accordingly, to overcome the lack of channel knowledge, we have studied different methods for acquiring that information feasibly. In addition, to cope with the interference among devices, we have also considered the use of SIC and optimized the decoding order. Based on that, the RIS is optimized to minimize the average MSE under channel variation (i.e., coherence time) constraints.

In order to assess the performance of our approach, we have conducted numerical simulations with real databases. Results have shown that incorporating the RIS can reduce the MSE significantly, especially with a large number of reflecting elements. However, when considering fast varying channels, the parameter estimation accuracy can be compromised. Finally, the use of SIC decoding becomes essential for proper performance, as long as the decoding order is correctly chosen.

Appendix 5.A SINR Expression

To derive the expression in (5.10), let us define the following system model. Considering the (ultimate) decoding procedure described in Section 5.4, the equivalent signal of sensor i yields

$$\hat{s}_i^{\text{SIC,I-CSI}} \triangleq \hat{h}_i s_i + \tilde{h}_i s_i + \underbrace{\sum_{\substack{j=1 \\ o(j)<o(i)}}^{M} \tilde{h}_j s_j + \sum_{\substack{j=1 \\ o(j)>o(i)}}^{M} h_j s_j + w}_{\triangleq w_{\text{eff},i}}, \tag{5.31}$$

where $\hat{h}_i s_i$ is now the desired signal and $w_{\text{est},i} \triangleq \tilde{h}_i s_i$ is treated as an additional (estimation) noise. In that sense, following the worst-case scenario described in [159], the estimation noise $w_{\text{est},i}$ and the effective noise $w_{\text{eff},i}$ are considered to be uncorrelated and Gaussian distributed with variances $\text{var}\left(w_{\text{est},i}\right)$ and $\text{var}\left(w_{\text{eff},i}\right)$, respectively.

As a result, when conditioning on the observation $\boldsymbol{z}$, the SINR reads as

$$\rho_i^{\text{SIC,I-CSI}}|\boldsymbol{z} = \frac{\text{var}\left(\hat{h}_i s_i|\boldsymbol{z}\right)}{\text{var}\left(w_{\text{est},i}|\boldsymbol{z}\right) + \text{var}\left(w_{\text{eff},i}|\boldsymbol{z}\right)}, \tag{5.32}$$

where, due to the MMSE channel estimation, $\hat{h}_i$ become deterministic functions of $\boldsymbol{z}$. Hence, given that the transmit signals are independent of $\boldsymbol{z}$, have zero mean, and power P_i, we have

$$\text{var}(\hat{h}_i s_i|\boldsymbol{z}) \triangleq \mathbb{E}\left[|\hat{h}_i s_i|^2|\boldsymbol{z}\right] = P_i|\hat{h}_i|^2. \tag{5.33}$$

Since the errors $\tilde{h}_j$ have zero mean and variance $\kappa_j \triangleq \boldsymbol{\psi}^{\text{T}} \boldsymbol{C}_{\tilde{\boldsymbol{g}}_{\text{C},j}} \boldsymbol{\psi}^*$, the other terms result

$$\text{var}\left(w_{\text{est},i}|\boldsymbol{z}\right) \triangleq \mathbb{E}\left[|w_{\text{est},i}|^2|\boldsymbol{z}\right] = P_i\kappa_i, \tag{5.34}$$

$$\text{var}\left(w_{\text{eff},i}|\boldsymbol{z}\right) \triangleq \mathbb{E}\left[|w_{\text{eff},i}|^2|\boldsymbol{z}\right] = \sum_{\substack{j=1 \\ o(j)<o(i)}}^{M} P_j\kappa_j + \sum_{\substack{j=1 \\ o(j)>o(i)}}^{M} P_j(|\hat{h}_j|^2 + \kappa_j) + \sigma_w^2. \tag{5.35}$$

In this last expectation, the terms $\mathbb{E}\left[|h_j s_j|^2|\boldsymbol{z}\right]$ become $P_j(|\hat{h}_j|^2 + \kappa_j)$ since the cross products disappear, i.e., $\mathbb{E}\left[\hat{h}_j\tilde{h}_j^*|s_j|^2|\boldsymbol{z}\right] = \hat{h}_j\mathbb{E}\left[\tilde{h}_j^*|\boldsymbol{z}\right]\mathbb{E}\left[|s_j|^2|\boldsymbol{z}\right] = P_j\hat{h}_j\mathbb{E}\left[\tilde{h}_j^*|\boldsymbol{z}\right] = 0$. Finally, by substituting all variances into expression (5.32), we obtain the SINR defined in (5.10).

Appendix 5.B Intersection Probability

The derivation of the probability $\varrho_{\boldsymbol{z},i} = \Pr\{\gamma_j = 0, \forall j : o(j) \leq o(i) \,\text{and}\, \gamma_{j:o(j)=o(i)+1} = 1|\boldsymbol{z}\}$ is non trivial given the statistical dependence between γ_j. In particular, since these RVs are functions of the SINRs in (5.10), apart from the noise w, they share a part of the interference coming from I-CSI. For simplicity, in the following we assume a decoding order $\mathcal{S} = \{1, \ldots, M\}$.

In line with that, when considering $M = 3$, the signals coming from sensors 1 and 2 will be affected by the (same) component of sensor 3 (i.e., $\tilde{h}_3 s_3$). Similarly, sensors 2 and 3 will be affected by $\tilde{h}_1 s_1$ (cf. Appendix 5.A).

As a result, $\varrho_{\boldsymbol{z},i}$ can be expressed as

$$\varrho_{\boldsymbol{z},i} = \Pr\{\gamma_1 = 0 | \gamma_2 = 0, \dots, \gamma_i = 0, \gamma_{i+1} = 1, \boldsymbol{z}\} \times \cdots \times \Pr\{\gamma_{i+1} = 1 | \boldsymbol{z}\}, \tag{5.36}$$

where $\Pr\{\gamma_{i+1} = 1|\boldsymbol{z}\}$ is directly $\mathrm{PER}_{i+1}^{\mathrm{SIC,I\text{-}CSI}}|\boldsymbol{z}$, yet the rest of the conditional probabilities depend on the MCS and an analytic closed-form expression is not usually available. Note that, for the case of continuous communications, the condition $\gamma_j = 0$ translates into the SINR being above a certain threshold (cf. Subsection 2.2.2.1). Nevertheless, in the packet-based setup, finding an analog statement might be difficult [158].

Alternatively, we can consider that all the previous events are statistically independent provided that, in many realistic scenarios, each sensor will use a different coding scheme (i.e., rate and/or structure). Thereby, we can assume that the CN observes a different realization of this shared interference when decoding each sensor (e.g., the portion of the signal from sensor 3 will be different for sensors 1 and 2). Intuitively, the different codes see this common part from different points of view and, thus, the interference is virtually randomized. In fact, the same effect could be achieved with the help of an interleaver.

This way, thanks to the presence of the channel decoder, the set of probabilities $\varrho_{\boldsymbol{z},i}$ result

$$\varrho_{\boldsymbol{z},i} \approx \left(\mathrm{PER}_{i+1}^{\mathrm{SIC,\,I\text{-}CSI}}|\boldsymbol{z}\right) \prod_{j=1}^{i} \left(1 - \mathrm{PER}_{j}^{\mathrm{SIC,\,I\text{-}CSI}}|\boldsymbol{z}\right), \tag{5.37}$$

which essentially represents the decoding procedure described in Section 5.4, i.e., sensor i can only be decoded if (and only if) the previous sensors are correctly decoded (but not completely suppressed due to I-CSI errors). Otherwise, we consider that the decoding is not possible and, thus, the information from that sensor cannot be retrieved.

Appendix 5.C Average MSE

To solve the integral in (5.20), we will focus on the channel models described in Subsection 5.6.1. For simplicity, let us first consider again a decoding order $\mathcal{S} = \{1, \dots, M\}$ with $M = 3$ sensors. In that sense, the conditional MSE $\varepsilon_{\boldsymbol{z}}$ yields

$$\varepsilon_{\boldsymbol{z}} = \varrho_{\boldsymbol{z},1}\varepsilon_1 + \varrho_{\boldsymbol{z},2}\varepsilon_2 + \varrho_{\boldsymbol{z},3}\varepsilon_3 + \varrho_{\boldsymbol{z},0}\varepsilon_0, \tag{5.38}$$

where ε_i are given in (5.19) and $\varrho_{\boldsymbol{z},i}$ follow from the derivations in Appendix 5.B. Accordingly, considering the independence approximation, we have $\varrho_{\boldsymbol{z},0} \approx \mathrm{PER}_1^{\mathrm{SIC,\,I\text{-}CSI}}|\boldsymbol{z}$ and

$$\varrho_{\boldsymbol{z},1} \approx (1 - \mathrm{PER}_1^{\mathrm{SIC,\,I\text{-}CSI}}|\boldsymbol{z}) \cdot \mathrm{PER}_2^{\mathrm{SIC,\,I\text{-}CSI}}|\boldsymbol{z}, \tag{5.39}$$

$$\varrho_{\boldsymbol{z},2} \approx (1 - \mathrm{PER}_1^{\mathrm{SIC,\,I\text{-}CSI}}|\boldsymbol{z}) \cdot (1 - \mathrm{PER}_2^{\mathrm{SIC,\,I\text{-}CSI}}|\boldsymbol{z}) \cdot \mathrm{PER}_3^{\mathrm{SIC,\,I\text{-}CSI}}|\boldsymbol{z}, \tag{5.40}$$

$$\varrho_{\boldsymbol{z},3} \approx (1 - \mathrm{PER}_1^{\mathrm{SIC,\,I\text{-}CSI}}|\boldsymbol{z}) \cdot (1 - \mathrm{PER}_2^{\mathrm{SIC,\,I\text{-}CSI}}|\boldsymbol{z}) \cdot (1 - \mathrm{PER}_3^{\mathrm{SIC,\,I\text{-}CSI}}|\boldsymbol{z}). \tag{5.41}$$

The average MSE ε can then be decomposed as the sum of the following expectations:

$$\varepsilon = \mathbb{E}_{\boldsymbol{z}}[\varrho_{\boldsymbol{z},1}]\varepsilon_1 + \mathbb{E}_{\boldsymbol{z}}[\varrho_{\boldsymbol{z},2}]\varepsilon_2 + \mathbb{E}_{\boldsymbol{z}}[\varrho_{\boldsymbol{z},3}]\varepsilon_3 + \mathbb{E}_{\boldsymbol{z}}[\varrho_{\boldsymbol{z},0}]\varepsilon_0. \tag{5.42}$$

Without loss of generality, we concentrate on the first expectation, i.e., $\mathbb{E}_{\boldsymbol{z}}[\varrho_{\boldsymbol{z},1}]$. The associated decoding error probabilities are a function of the (known) effective channel gains $|\hat{h}_i|^2$:

$$|\hat{h}_i|^2 = |q_i + \boldsymbol{\psi}^{\mathrm{T}}(\boldsymbol{A}_i\boldsymbol{z}_i + \boldsymbol{b}_i)|^2, \tag{5.43}$$

which ultimately determine all the randomness in our scenario (cf. (5.16)).

Defining $\boldsymbol{a}_i \triangleq \boldsymbol{\psi}^T\boldsymbol{A}_i$, we have $(\boldsymbol{a}_i\boldsymbol{z}_i + \boldsymbol{\psi}^{\mathrm{T}}\boldsymbol{b}_i) \sim \mathcal{CN}(\mu_i, \sigma_i^2)$ with $\mu_i = 0$ and $\sigma_i^2 \triangleq \boldsymbol{a}_i\boldsymbol{C}_{\boldsymbol{z}_i}\boldsymbol{a}_i^{\mathrm{H}}$ (cf. (5.29)). Also, due to the independence between the direct channel q_i and the cascaded channel $\boldsymbol{g}_{\mathrm{C},i}$, the estimated coefficients $\hat{h}_i$ will follow a complex Gaussian distribution with zero mean and variance $\varsigma_i^2 + \sigma_i^2$, i.e., $\hat{h}_i \sim \mathcal{CN}(0, \varsigma_i^2 + \sigma_i^2)$, where $\varsigma_i = d_i^{-\alpha/2}\sqrt{0.1}$ is the standard deviation of q_i (cf. (5.26)). Therefore, the set of gains $|\hat{h}_i|^2$ will be Gamma RVs with shape parameter $1/2$ and scale parameter $2(\varsigma_i^2 + \sigma_i^2)$ i.e., $|\hat{h}_i|^2 \sim \Gamma(1/2, 2(\varsigma_i^2 + \sigma_i^2))$.

As a result, the first expectation in (5.42) now depends on $c_i \triangleq |\hat{h}_i|^2$ with $i \in \{1, 2, 3\}$, which yields the following one-dimensional triple integral:

$$\mathbb{E}_{\boldsymbol{c}}\left[\varrho_{\boldsymbol{c},1}\right] \triangleq \iiint \varrho_{\boldsymbol{c},1} f_{\boldsymbol{c}}(c_1, c_2, c_3)dc_1dc_2dc_3, \tag{5.44}$$

where $\boldsymbol{c} = [c_1, c_2, c_3]$ is used for the sake of brevity in the notation. Consequently, given that all c_i are independent[7], we can rewrite the previous integral as

$$\mathbb{E}_{\boldsymbol{c}}\left[\varrho_{\boldsymbol{c},1}\right] = \int \left(\int \left(\int (1-\xi_1|c_2,c_3) f_{c_1}(c_1)dc_1\right)(\xi_2|c_3) f_{c_2}(c_2)dc_2\right) f_{c_3}(c_3)dc_3, \tag{5.45}$$

where $\xi_i \triangleq \mathrm{PER}_i^{\text{SIC, I-CSI}}$ only depends on $\boldsymbol{z}_i, \dots, \boldsymbol{z}_M$ (or, equivalently, on $c_i, \dots, c_M$) and not the whole vector $\boldsymbol{z}$ (or $\boldsymbol{c}$). Then, we condition on c_2, c_3 to average over c_1, and later on c_3 to average over c_2. This way, the previous integrals can be solved through (one-dimensional) numerical evaluations. A similar reasoning can be used for the rest of the expectations in (5.42).

Overall, according to the previous derivations, we can express the average MSE ε for the general case of M sensors in the following way:

$$\varepsilon = \sum_{i=1}^{M} \mathbb{E}_{\boldsymbol{c}}\left[\varrho_{\boldsymbol{c},i}\right]\varepsilon_i + \mathbb{E}_{\boldsymbol{c}}\left[\varrho_{\boldsymbol{c},0}\right]\varepsilon_0, \tag{5.46}$$

where the expectations

$$\mathbb{E}_{\boldsymbol{c}}\left[\varrho_{\boldsymbol{c},i}\right] = \int\cdots\int \left(\int \left(\int \left(\int \dots \left(\int I_1 dc_1\right)\dots\right) I_i dc_i\right) J_{i+1}dc_{i+1}\right) \prod_{j=i+2}^{M} f_{c_j}(c_j)dc_j, \tag{5.47}$$

with $I_i \triangleq (1-\xi_i|c_{i+1}, \dots c_M)\, f_{c_i}(c_i)$ and $J_i \triangleq (\xi_i|c_{i+1}, \dots c_M)\, f_{c_i}(c_i)$, are solved numerically[8]. In practice, since the design variables (e.g., RIS matrices) affect the PERs ξ_i but also the statistical distributions $f_{c_i}(c_i)$, this procedure has to be performed in an offline basis at the CN. Finally, note that the last expectation in (5.46) can be obtained as $\mathbb{E}_{\boldsymbol{c}}[\varrho_{\boldsymbol{c},0}] = 1 - \sum_i \mathbb{E}_{\boldsymbol{c}}[\varrho_{\boldsymbol{c},i}]$.

---

[7] This is true under the assumption of independent cascaded channels (see Subsection 5.6.1), which translates into independent observations $\boldsymbol{z}_i$ (cf. (5.8)). Since c_i are functions of $\boldsymbol{z}_i$, they are also independent.

[8] To reduce the computational complexity, this method can be implemented through Monte-Carlo evaluations as we average the expressions I_i and J_i over all possible values from the set of RVs $c_1, \dots, c_M$.

Part III

Techniques in the Downlink

Chapter 6

Energy Transfer

6.1 Introduction

As mentioned in the introduction, in most mMTC networks, the devices involved are usually battery constrained. Apart from reducing power consumption in the UL, as we considered in Chapters 3, 4 and 5, another possible strategy to increase the lifetime of the mMTC terminals is to provide energy supply mechanisms. For that task, two interesting candidates emerge: wireless power transfer (WPT) and energy harvesting (EH), among others.

WPT represents the transfer of energy to sensors through dedicated signals from the CN, whereas EH consists in collecting energy from the signals transmitted by other devices coexisting in the same geographical region. As a result, these two approaches can allow mMTC terminals to be powered remotely and, thus, lead the way to WPNs [169, 170].

In this chapter, we will consider a setup with a set of sensors and a serving CN equipped with multiple antennas. Accordingly, the CN will be in charge of the WPT in the DL and, given the high spatial density of the sensing devices [12], each terminal will harvest energy from the signals coming from other sensors when they transmit (TX) in the UL, i.e., they will recycle the power of the perceived ambient interference; hence, leveraging the size of mMTC systems.

Since in mMTC networks the positions of the devices are considered to be random and normally unknown, we will use stochastic geometry to model their spatial distribution [26]. In particular, we will consider that they are represented by repulsive MCPs. Also, for a more realistic analysis, the intermittent activities of the sensors will be modeled with Bernoulli RVs. This will allow us to derive and statistically characterize both harvested and transferred energies.

Finally, in order to optimize the collected energy within the network, in this chapter, we will design an energy allocation scheme with a proportional fair (PF) policy through the WPT. This way, sensors will receive a similar amount of energy over time.

6.1.1 Related Work

The rise of WPNs shed light on the need for novel solutions that meet the energy demands [171, 172]. Several resource allocation (RA) schemes have been proposed in [173–176]. In [173], authors presented a protocol for HTC where users employ the energy harvested from the BSs to transmit their information in a time-division manner. Based on that, the RAs maximizing the sum rate or ensuring a minimum throughput are found using convex optimization techniques.

In the presence of a sustainable relay powering the users and with the help of successive approximations, the sum rate was also optimized w.r.t. the RA in [174]. Considering the circuit power consumption within the system, the authors of [175] designed the time and power allocations that maximize the energy efficiency under QoS constraints by means of fractional programming. In [176], authors tackled the doubly near-far problem[1] in OMA and NOMA environments and derived the Pareto-optimal solution. Other works like [177] focused on device selection strategies to reduce power consumption, taking into account channel knowledge and complexity requirements. The use of WPT for energy-efficient mobile cloud computing was also investigated in [178]. A survey with more (cooperative) approaches can be found in [179].

6.1.2 Contributions

The main contributions of this chapter are listed in the following:

- Characterization of the energies collected from WPT and EH, taking into consideration the random positions and sporadic activity of the sensors.
- Derivation of an energy allocation scheme with a PF policy that ensures that all devices have a sufficient (and fair) battery level over time.

6.1.3 Organization

The remainder of this chapter is structured as follows. Section 6.2 describes the system model. In Section 6.3, the WPT and EH collected energies are statistically characterized. Section 6.4 is devoted to the design of the WPT scheme and numerical simulations are shown in Section 6.5. Some final thoughts and concluding remarks are presented in Section 6.6.

6.2 System Model

Throughout this chapter, we consider a scenario with a set of sensors randomly located in space and served by a CN. Following the discussion in Section 2.4, we consider that these devices are grouped together in K clusters represented by disks of radius r_k centered at $\boldsymbol{c}_k \in \mathbb{R}^2$, with $k \in \{1, \ldots, K\}$. Recall that each cluster has a density of sensors λ_k and sensors in the same cluster are at a minimum distance d_{min} between each other.

Assuming a uniform distribution within each cluster, the positions of the sensors can be represented by repulsive MCPs Υ_k of intensities λ_k and minimum distance d_{min} (cf. Section 2.4). Each of these processes is defined from a general MCP Ψ_k of intensity δ_k and without minimum distance, where devices are uniformly distributed in the circle of radius r_k around the center $\boldsymbol{c}_k$. Accordingly, to ensure the minimum sensor distance, a dependent thinning is applied to each MCP Ψ_k [53], leading to the repulsive process Υ_k with a density of devices (cf. (2.14)):

$$\lambda_k = \frac{1 - \exp(-\delta_k \pi d_{\text{min}}^2)}{\pi d_{\text{min}}^2}. \tag{6.1}$$

---

[1] Due to the high propagation losses, users that are located far away from the BS will receive less energy but also have to transmit with more power in order to ensure reliable communication.

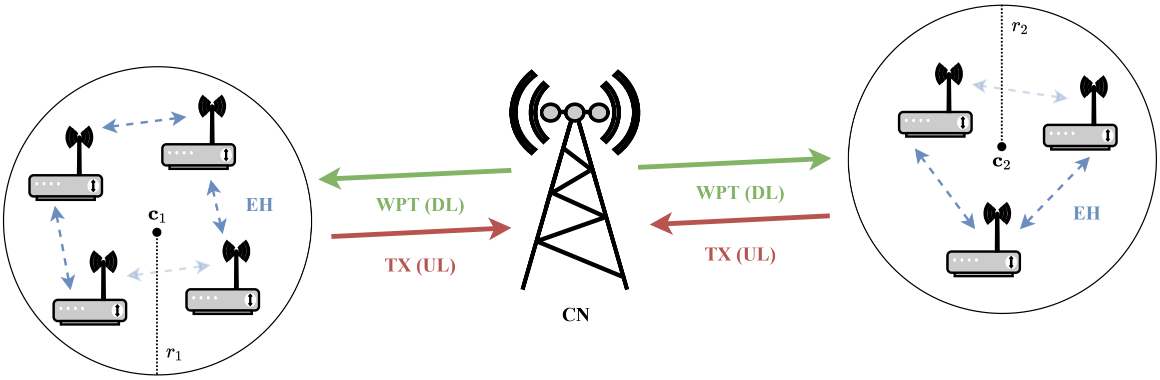

Figure 6.1: Illustrative scenario with $K = 2$ and $L = 3$. Solid lines represent intended power transfer (or data transmission), whereas dashed lines refer to energy recycling.

For a sufficiently small minimum distance, Υ_k can be approximated by a MCP Φ_k with the same boundaries and density of sensors λ_k [49]. This was introduced in Subsection 2.4.4 and is known as the PPP approximation (valid as long as $d_{\min} \to 0$). As a result, we end up with a set of independent processes Φ_k modeling the sensors' positions in a cluster-basis manner.

As in Chapter 3, here we also consider the use of multiple-antenna technology. In that sense, the CN will be equipped with L antennas, the array gain of which can counteract the high propagation losses and better direct the energy to where it is needed when WPT is applied. In addition, we assume that sensors are single-antenna devices due to the required simplicity and low cost. An illustrative example of a setup with $K = 2$ and $L = 3$ is depicted in Figure 6.1.

Given the limited capability of the sensors, we assume that WPT and EH are not performed simultaneously but in a half-duplex (HD) way. Considering that time is divided into frames of duration T_f (cf. Chapter 2), WPT will occupy the first T_d seconds and TX/EH will occupy the other T_u such that $T_f = T_d + T_u$. Besides, whenever a sensor is transmitting, it will be unable to harvest energy from the signals transmitted by other active sensors, i.e., TX and EH are not simultaneous. That is why the period T_u is also divided into the N slots[2] of duration T_s such that $T_u = NT_s$. Hence, during one slot, some sensors will transmit and the rest will harvest.

Finally, in this chapter, we focus on event-driven mMTC networks. Since sensors transmit sporadically [22], we consider the probability of being active at any time slot to be p_{act} (cf. Section 2.2). An example of the frame structure is shown in Figure 6.2. Recall that, for these types of systems, a NOMA scheme is normally used (although in this chapter, we focus on the collection of energy, not on the transmission of the sensed parameters).

With the above considerations, the average energy that the sensors in cluster k will receive from WPT and EH at the end of each frame can be written as

$$\bar{E}_k = \bar{E}_{k,\text{WPT}} + \bar{E}_{k,\text{EH}}, \tag{6.2}$$

where $\bar{E}_{k,\text{WPT}}$ refers to the average energy obtained from WPT and $\bar{E}_{k,\text{EH}}$ is the average energy collected from EH thanks to the other active sensors that are transmitting.

---

[2] Given the low data traffic of mMTC networks in the DL (which is mostly composed by signaling), this phase is not included in the slot division (yet considered apart and common for all sensors).

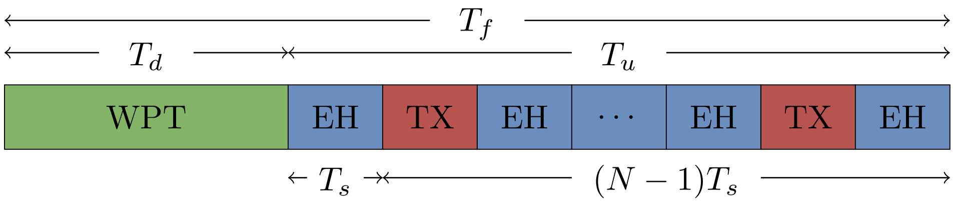

Figure 6.2: Example of a frame structure for a given sensor. Colors differentiate separate time instants.

6.3 Energy Characterization

In order to statistically characterize $\bar{E}_{k,\text{WPT}}$ and $\bar{E}_{k,\text{EH}}$, we first model the received signals at the sensors side. Later, by means of stochastic geometry tools, we derive the expressions for both average energies. Based on that, in Section 6.4, we design an energy allocation scheme for WPT where the average energies $\bar{E}_k$ are maximized under a CN's total power constraint and a PF policy [180]. This way, we are able to evenly improve the battery level of all sensors and approach a wireless powered mMTC network.

6.3.1 Energy Received from WPT

The signal received from the CN by a sensor randomly chosen in the set of cluster k and located at $\hat{\boldsymbol{x}}_k \in \Phi_k$ can be expressed as

$$\hat{y}_k^{\text{WPT}} \triangleq \hat{\boldsymbol{h}}_k^{\text{H}} \boldsymbol{s} + \hat{w}_k \in \mathbb{C}, \tag{6.3}$$

where $\hat{\boldsymbol{h}}_k \in \mathbb{C}^L$ is the channel of the sensor w.r.t. the CN (equivalent to h_i in Section 2.3), $\boldsymbol{s} \in \mathbb{C}^L$ is the CN's transmit signal with zero mean and covariance $\boldsymbol{Q} \triangleq \mathbb{E}[\boldsymbol{s}\boldsymbol{s}^{\text{H}}] \in \mathbb{C}^{L\times L}$, and $\hat{w}_k \in \mathbb{C}$ is the corresponding AWGN with zero mean and power σ_w^2.

Ignoring the negligible energy coming from the noise term [170,181], and assuming a linear harvesting model, the received energy can be written as follows:

$$\bar{E}_{k,\text{WPT}} \triangleq \zeta_k T_d \mathbb{E}\left[\hat{\boldsymbol{h}}_k^{\text{H}} \boldsymbol{Q} \hat{\boldsymbol{h}}_k\right] = \zeta_k T_d \text{tr}\left(\boldsymbol{Q}\mathbb{E}\left[\hat{\boldsymbol{h}}_k \hat{\boldsymbol{h}}_k^{\text{H}}\right]\right) = \zeta_k T_d \text{tr}\left(\boldsymbol{Q}\boldsymbol{C}_k\right), \tag{6.4}$$

where ζ_k is the energy conversion efficiency [169]. The entries of $\boldsymbol{C}_k \triangleq \mathbb{E}[\hat{\boldsymbol{h}}_k \hat{\boldsymbol{h}}_k^{\text{H}}] \in \mathbb{C}^{L\times L}$ are

$$[\boldsymbol{C}_k]_{l,l'} \triangleq \mathbb{E}\left[\hat{h}_{k,l}\hat{h}_{k,l'}^*\right], \quad 1 \le l \le L, \quad 1 \le l' \le L, \tag{6.5}$$

which average the (random) sensor selection over the process Φ_k.

When considering a power-law path loss, the sensor's channel in (6.3) yields

$$\hat{\boldsymbol{h}}_k \triangleq \hat{d}_k^{-\alpha/2} \hat{g}_k \boldsymbol{v}(\hat{\theta}_k), \tag{6.6}$$

where $\hat{d}_k$ is the distance of the sensor located at $\hat{\boldsymbol{x}}_k \in \Phi_k$ to the CN, α is the path-loss exponent, $\hat{g}_k$ is the fading coefficient with zero mean and variance σ_g^2, $\boldsymbol{v}(\cdot) = [v_1(\cdot), \ldots, v_L(\cdot)]^{\text{T}} \in \mathbb{C}^L$ is the steering vector with elements $v_l(\cdot)$, and $\hat{\theta}_k$ is the steering direction pointing at the sensor [89].

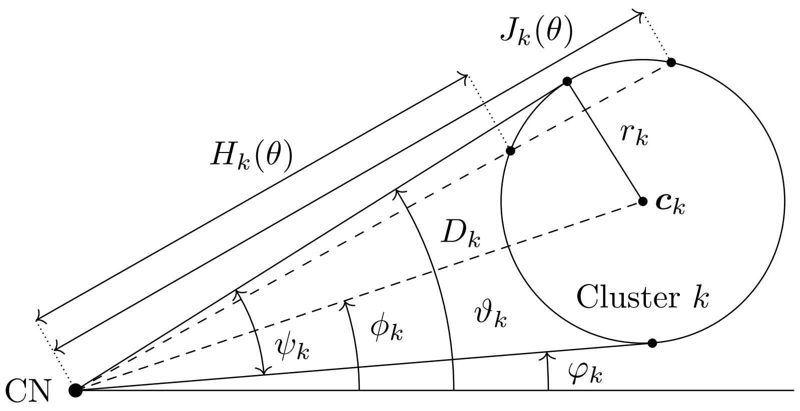

Figure 6.3: Geometry between the CN and cluster k.

As a result, the entries of $\boldsymbol{C}_k$ defined in (6.5) read as

$$\begin{aligned}[\boldsymbol{C}_k]_{l,l'} &= \mathbb{E}\left[\hat{d}_k^{-\alpha}\hat{g}_k^2 v_l(\hat{\theta}_k)v_{l'}(\hat{\theta}_k)^*\right] \\ &\overset{\text{(a)}}{=} \sigma_g^2\mathbb{E}\left[\hat{d}_k^{-\alpha}v_l(\hat{\theta}_k)v_{l'}(\hat{\theta}_k)^*\right] \\ &\overset{\text{(b)}}{=} \frac{\sigma_g^2}{\pi r_k^2}\int_{\varphi_k}^{\vartheta_k}\left(\int_{H_k(\theta)}^{J_k(\theta)}\frac{z}{z^\alpha}dz\right)v_l(\theta)v_{l'}(\theta)^*d\theta \\ &= \frac{\sigma_g^2}{\pi r_k^2}\int_{\varphi_k}^{\vartheta_k} I_k(\theta)v_l(\theta)v_{l'}(\theta)^*d\theta,\end{aligned} \tag{6.7}$$

where (a) follows from assuming independence between fading and spatial process, and (b) from the sensors uniform distribution and the change to polar coordinates (i.e., $\boldsymbol{x} = [x_1, x_2] = [z\cos(\theta), z\sin(\theta)]$, with $z = \sqrt{x_1 + x_2}$ and $\theta = \arctan(x_2, x_1)$).

As depicted in Figure 6.3, φ_k and ϑ_k are the two angles corresponding to the tangent lines from the CN to cluster k, i.e.,

$$\begin{aligned}\varphi_k &\triangleq \phi_k - \psi_k/2, \\ \vartheta_k &\triangleq \phi_k + \psi_k/2,\end{aligned} \tag{6.8}$$

where $\psi_k \triangleq 2\arcsin(r_k/D_k)$ is the angle between these two tangent lines, D_k is the distance between the cluster center $\boldsymbol{c}_k$ and the CN, and ϕ_k is the associated angle, as shown in Figure 6.3.

Note that the integral term $I_k(\theta)$ in (6.7) depends on the decay exponent α and reads as

$$I_k(\theta) \triangleq \int_{H_k(\theta)}^{J_k(\theta)}\frac{z}{z^\alpha}dz = \begin{cases}\ln\left(J_k(\theta)/H_k(\theta)\right), & \alpha = 2, \\ (J_k(\theta)^{2-\alpha} - H_k(\theta)^{2-\alpha})/(2-\alpha), & \alpha > 2,\end{cases} \tag{6.9}$$

where $H_k(\theta) \leq J_k(\theta)$ are the distances to the CN of the intersections between the lines determined by φ_k and ϑ_k, and the boundaries of cluster k. They are computed as the roots of the following polynomial:

$$p(\theta) \triangleq z^2 - 2D_k z\cos(\theta - \phi_k) + D_k^2 - r_k^2. \tag{6.10}$$

Finally, as there is no analytic closed-form expression for the integral in (6.7), it is computed numerically. This way, we can obtain the values for the matrix $\boldsymbol{C}_k$ formulated in (6.5).

6.3.2 Energy Received from EH

Regarding the received signal from the other sensors, we need to take into account their spatial distribution. To ease of notation, we also consider that the sensor under study is located at $\hat{\boldsymbol{x}}_k$ inside cluster $k \in \{1, \dots, K\}$. For a power-law path loss, the received signal at a given slot $m \in \{1, \dots, N\}$ (assuming one symbol per slot) is given by

$$\hat{y}_k^{\text{EH}}[m] \triangleq \sum_{l=1}^{K} \hat{y}_{k,l}^{\text{EH}}[m](1 - \beta_{\hat{\boldsymbol{x}}_k}[m]) + \hat{\omega}_k \in \mathbb{C}, \tag{6.11}$$

with $\hat{y}_{k,l}^{\text{EH}}[m]$ the signal coming from cluster l at slot m:

$$\hat{y}_{k,l}^{\text{EH}}[m] \triangleq \sum_{\boldsymbol{x} \in \Phi_l \setminus \{\hat{\boldsymbol{x}}_k\}} \hat{u}_{k,\boldsymbol{x}}^{-\alpha/2} \hat{\gamma}_{k,\boldsymbol{x}}[m] \tau_{\boldsymbol{x}}[m] \beta_{\boldsymbol{x}}[m] \in \mathbb{C}, \tag{6.12}$$

where $\hat{u}_{k,\boldsymbol{x}}$ is the distance between $\boldsymbol{x}$ and $\hat{\boldsymbol{x}}_k$, $\hat{\gamma}_{k,\boldsymbol{x}}[m] \in \mathbb{C}$ is the fading coefficient with zero mean and variance σ_γ^2, $\tau_{\boldsymbol{x}}[m] \in \mathbb{C}$ is the sensor's transmit signal with zero mean and power P_τ (assumed equal for all devices), and $\hat{\omega}_k[m]$ is the AWGN noise with zero mean and power σ_ω^2. $\beta_{\boldsymbol{x}}[m] \sim$ *Ber*(p_{act}) are the set of independent Bernoulli RVs introduced to account for the random activity of the sensors located at $\boldsymbol{x}$, i.e., p_{act} (equivalent to p_i) is the probability that a sensor is active and transmitting during the time slot m (cf. Section 2.2). In that sense, $1 - \beta_{\hat{\boldsymbol{x}}_k}[m]$, with $\beta_{\hat{\boldsymbol{x}}_k}[m] \sim$ *Ber*(p_{act}) independent of the rest, represents the fact that the sensor located at $\hat{\boldsymbol{x}}_k$ can only harvest energy from the other active devices when it is not transmitting.

As a result, neglecting again the noise term, the average energy harvested by a sensor at cluster k reads as [52]

$$\bar{E}_{k,\text{EH}} \triangleq \zeta_k \mathbb{E}\left[\sum_{m=1}^{N} T_s \left(\hat{y}_k^{\text{EH}}[m]\right)^2\right] = \zeta_k N T_s P_\tau \sigma_\gamma^2 p_{\text{act}}(1 - p_{\text{act}})\, \underbrace{\mathbb{E}\left[\sum_{l=1}^{K} \sum_{\boldsymbol{x} \in \Phi_l \setminus \{\hat{\boldsymbol{x}}_k\}} \hat{u}_{k,\boldsymbol{x}}^{-\alpha}\right]}_{\triangleq \eta_k}, \tag{6.13}$$

which follows from the independence of fading, transmit signal and activity RVs. Note that the sum of path loss η_k can be decomposed as follows:

$$\eta_k = \mathbb{E}\left[\sum_{l=1}^{K} \sum_{\boldsymbol{x} \in \Phi_l \setminus \{\hat{\boldsymbol{x}}_k\}} \hat{u}_{k,\boldsymbol{x}}^{-\alpha}\right] = \sum_{l=1}^{K} \mathbb{E}\left[\sum_{\boldsymbol{x} \in \Phi_l \setminus \{\hat{\boldsymbol{x}}_k\}} \hat{u}_{k,\boldsymbol{x}}^{-\alpha}\right] = \underbrace{\mathbb{E}\left[\sum_{\boldsymbol{x} \in \Phi_k \setminus \{\hat{\boldsymbol{x}}_k\}} \hat{u}_{k,\boldsymbol{x}}^{-\alpha}\right]}_{\triangleq \eta_{k,\text{intra}}} + \underbrace{\sum_{l \neq k} \mathbb{E}\left[\sum_{\boldsymbol{x} \in \Phi_l} \hat{u}_{k,\boldsymbol{x}}^{-\alpha}\right]}_{\triangleq \eta_{k,\text{inter}}}, \tag{6.14}$$

where $\eta_{k,\text{intra}}$ is the expected value of the sum of path loss within the same cluster (i.e., intra-cluster) and $\eta_{k,\text{inter}}$ is the expected value of the sum of path loss coming from the rest of the clusters (i.e., inter-cluster). As discussed below, the former can be expressed in an analytic closed form, yet an approximation is used for the latter.

With the help of Campbell's theorem [53], the sum of intra-cluster path loss (without the harvesting sensor) can be written as

$$\eta_{k,\text{intra}} = (\lambda_k \pi r_k^2 - 1) \int_{d_{\min}}^{2r_k} u^{-\alpha} f_k(u) du, \tag{6.15}$$

where $f_k(u)$ is the distance distribution in cluster k [52]:

$$f_k(u) \triangleq \frac{4u}{A_k \pi r_k^2} \left(\arccos\left(\frac{u}{2r_k}\right) - \frac{u}{2r_k}\sqrt{1 - \frac{u^2}{4r_k^2}} \right), \tag{6.16}$$

in the interval $d_{\min} \leq u \leq 2r_k$ and 0 otherwise. Note that A_k is the normalization factor that ensures the distribution has unit area.

On the other hand, the sum of inter-cluster path loss can be difficult to model as the position of the sensor under study is also random, i.e., $\hat{\boldsymbol{x}}_k \in \Phi_k$. That is why, instead of focusing on the energy harvested by a sensor located in cluster k, we concentrate on the energy received at the cluster center, i.e., $\hat{\boldsymbol{x}}_k = \boldsymbol{c}_k$, and used it as an approximation for the inter-cluster energy.

This way, in line with the discussion in Subsection 6.3.1, by means of Campbell's theorem, $\eta_{k,\text{inter}}$ can be approximated as [49]

$$\eta_{k,\text{inter}} \approx \tilde{\eta}_{k,\text{inter}} = \sum_{l \neq k} \lambda_l \int_{\varphi_{k,l}}^{\vartheta_{k,l}} I_{k,l}(\theta) d\theta. \tag{6.17}$$

As shown in Figure 6.4, the angles $\varphi_{k,l}$ and $\vartheta_{k,l}$ follow the definitions in (6.8), but now from the point of view of the cluster center $\boldsymbol{c}_k$, i.e.,

$$\begin{aligned} \varphi_{k,l} &\triangleq \phi_{k,l} - \psi_{k,l}/2, \\ \vartheta_{k,l} &\triangleq \phi_{k,l} + \psi_{k,l}/2, \end{aligned} \tag{6.18}$$

where the angles $\psi_{k,l}$ and $\phi_{k,l}$ are also illustrated in Figure 6.4.

Similarly, given the distances $H_{k,l}(\theta)$ and $J_{k,l}(\theta)$, $I_{k,l}(\theta)$ reads as (cf. (6.9)):

$$I_{k,l}(\theta) \triangleq \int_{H_{k,l}(\theta)}^{J_{k,l}(\theta)} \frac{z}{z^\alpha} dz = \begin{cases} \ln\left(J_{k,l}(\theta)/H_{k,l}(\theta)\right), & \alpha = 2, \\ (J_{k,l}(\theta)^{2-\alpha} - H_{k,l}(\theta)^{2-\alpha})/(2-\alpha), & \alpha > 2. \end{cases} \tag{6.19}$$

The use of the approximation in (6.17) can be justified by the small channel gains and high attenuation in the sensor-to-sensor link. In that sense, clusters far apart can be seen approximately as a point and, thus, the energy that a sensor harvests from other clusters will be similar over its own cluster. This is verified through simulations in Section 6.5, where we compare the actual value $\eta_{k,\text{inter}}$ and the approximation $\tilde{\eta}_{k,\text{inter}}$ to prove its accuracy.

6.4 Energy Allocation

The previous analysis can be useful in the design of mMTC systems. As an example, in this section, we present the design of an energy allocation scheme for WPT from the CN under a PF policy that can lead to a WPN.

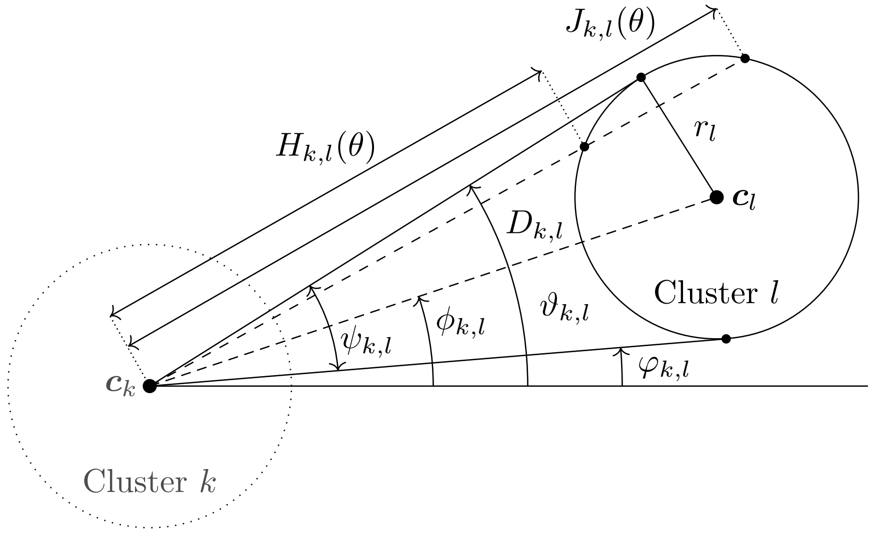

Figure 6.4: Geometry between cluster k and cluster l.

To that aim, we maximize the sum of the logarithm of the sensors' long-term collected energy under a CN's total power constraint [180]. Note that this is equivalent to maximizing the product (or geometric mean) of the sensors' received energy, which results in a more fair distribution of energy within the network [36].

We start by considering an observation time of T frames. Accordingly, the average received energy $\bar{E}_k$ in (6.2) now depends on the frame index $t \in \{1, \dots, T\}$, i.e., $\bar{E}_k(t)$ is the received energy at cluster k after frame t. Following the previous analysis, we have

$$\bar{E}_k(t) \triangleq \zeta_k T_d \text{tr}(\boldsymbol{Q}(t)\boldsymbol{C}_k) + \zeta_k T_u P_\tau \sigma_\gamma^2 p_{\text{act}}(1 - p_{\text{act}})\eta_k, \tag{6.20}$$

where the covariance matrix $\boldsymbol{Q}(t)$ is allowed to change over the frames to optimize the accumulated energy. In fact, this matrix determines the energy coming from the CN that arrives at the different sensors of each cluster and, thus, it will be the design variable of the system.

As a result, given that received energies are linear functions of $\boldsymbol{Q}(t)$ and are monotonically increasing, maximizing the product is equivalent to maximizing the logarithm of the product. Consequently, the optimization problem can be defined as [182]

$$\boldsymbol{Q}^\star(t) = \underset{\boldsymbol{Q}(t)\succeq \boldsymbol{0}}{\text{argmax}} \sum_{k=1}^{K} \ln T_k(t) \quad \text{s.t.} \quad \text{tr}(\boldsymbol{Q}(t)) \leq P_{\text{tx}}, \tag{6.21}$$

where $\boldsymbol{Q}(t) \succeq \boldsymbol{0}$ expresses that the matrix $\boldsymbol{Q}(t)$ must be positive semi-definite by definition, and P_{tx} is the total transmit power available at the CN. The terms $T_k(t)$ are the received energies averaged over an exponentially weighted window of length T_c frames [36, 183], i.e.,

$$T_k(t) \triangleq \left(1 - \frac{1}{T_c}\right) T_k(t-1) + \frac{1}{T_c}\bar{E}_k(t). \tag{6.22}$$

As shown in Appendix 6.A, for a sufficiently large window duration T_c, the problem defined in (6.21) is equivalent to the following optimization [184]:

$$\boldsymbol{Q}^{\star}(t) = \underset{\boldsymbol{Q}(t)\succeq\boldsymbol{0}}{\operatorname{argmax}} \sum_{k=1}^{K} \nu_k(t)\bar{E}_k(t) \quad \text{s.t.} \quad \operatorname{tr}(\boldsymbol{Q}(t)) \leq P_{\text{tx}}, \tag{6.23}$$

where the weights $\nu_k(t) \triangleq \frac{1}{T_k(t-1)}$ scale the individual $\bar{E}_k(t)$ such that a higher priority is given to sensors with less accumulated energy during past frames.

The solution to the previous problem is given by [36]

$$\boldsymbol{Q}^{\star}(t) = P_{\text{tx}}\boldsymbol{\varpi}_{\max}(t)\boldsymbol{\varpi}_{\max}^{\mathrm{H}}(t), \tag{6.24}$$

where $\boldsymbol{\varpi}_{\max}(t)$ is the eigenvector of the largest eigenvalue of the matrix

$$\boldsymbol{C}(t) = T_d \sum_{k=1}^{K} \nu_k(t)\boldsymbol{C}_k \in \mathbb{C}^{L\times L}. \tag{6.25}$$

Note that, although the energy harvested from the signals of other sensors $\bar{E}_{k,\text{EH}}$ does not depend on $\boldsymbol{Q}(t)$, it is taken into account in the optimization through to the weights $\nu_k(t)$. More importantly, the proposed scheme depends only on the channel statistics, the spatial distribution of sensors, and their activity. Therefore, since this information is usually known (or can be estimated) in realistic scenarios, a practical implementation of the energy allocation is feasible.

6.5 Numerical Simulations

In this section, several numerical simulations are presented to evaluate the performance of the previous approach. To that end, we consider the micro-urban scenario in [90] with $K = 10$, $r_k = 10$ m, $d_{\min} = 0.1$ m, $T_f = 1$ s, $T_d = 0.5$ s, $P_{\text{tx}} = 40$ dBm, $P_{\mathcal{T}} = 20$ dBm, $\sigma_\gamma^2 = \sigma_g^2 = 1$, $\alpha = 2$, $\zeta_k = 1$, and $p_{\text{act}} = 0.1$. The steering vectors $\boldsymbol{v}(\cdot)$ are computed for a UCA [89] with $L = 100$ antennas. Regarding the density of the sensors, we will study three different cases: (i) $\lambda_k = \lambda = 0.1\ \text{m}^{-2}\ \forall k \in \{1,\ldots,K\}$, (ii) λ_k that are equispaced in the interval $[0.5\lambda, 2\lambda]$, and (iii) λ_k that are equispaced in the interval $[0.1\lambda, \lambda]$. For the sake of brevity in the notation, cases (ii) and (iii) are denoted by $\lambda_k \in [0.5\lambda, 2\lambda]$ and $\lambda_k \in [0.1\lambda, \lambda]$, respectively.

We start by validating the approximation of the sum of inter-cluster path loss in (6.17), i.e., the assumption that the sum of path loss at the cluster center is similar over the cluster. For this task, in Figure 6.5, we illustrate the histogram of the sum of inter-cluster path loss together with the approximation $\tilde{\eta}_{k,\text{inter}}$ and the actual value $\eta_{k,\text{inter}}$. It can be observed that as $\tilde{\eta}_{k,\text{inter}} = -47.94$ dB is quite close to $\eta_{k,\text{inter}} = -47.80$ dB, it can be used as a suitable approximation.

To assess the results of the proportional fairness, we consider $T = 1000$ frames with an averaging filter of length $T_c = 50$ frames. In that sense, we make use of Jain's fairness index (FI) to measure the fairness within the system [182, 184]:

$$\text{FI}(t) \triangleq \left(1 - \frac{1}{T_c}\right)\text{FI}(t-1) + \frac{1}{T_c}\frac{(\sum_{k=1}^{K}\bar{E}_k(t))^2}{K\sum_{k=1}^{K}\bar{E}_k(t)^2}. \tag{6.26}$$

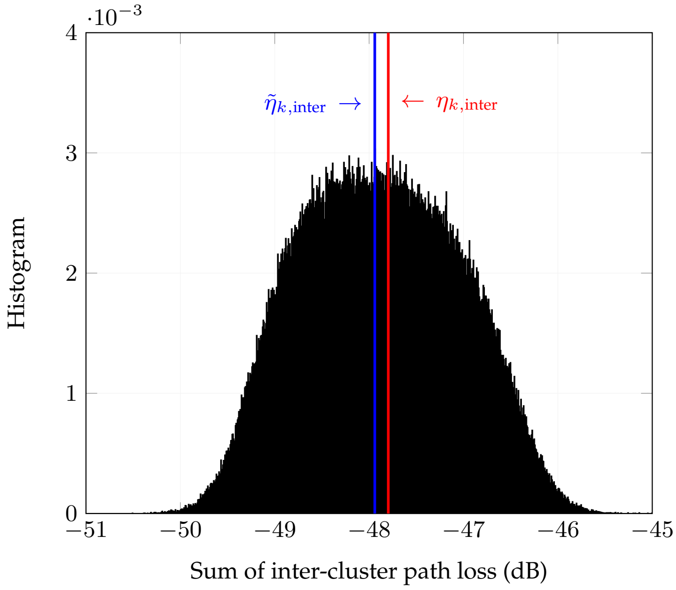

Figure 6.5: Histogram of the sum of inter-cluster path loss.

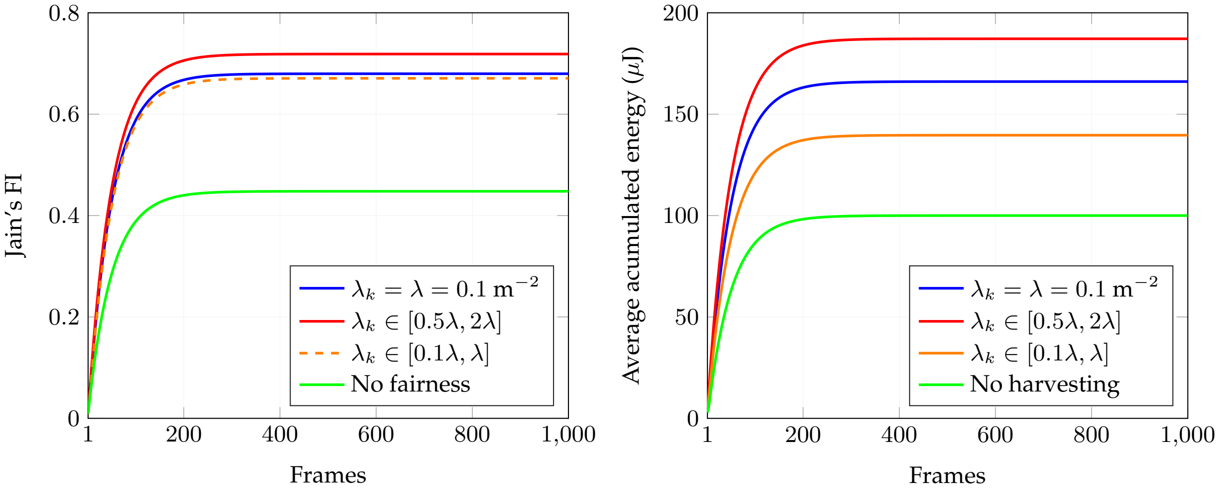

Figure 6.6: Evolution of Jain's index in time.

Figure 6.7: Evolution of average energy in time.

Moreover, regarding the accumulated energy, we also measure the average w.r.t. the different frames, which can be defined as

$$\bar{T}(t) \triangleq \frac{1}{K}\sum_{k=1}^{K} T_k(t). \tag{6.27}$$

Metrics FI and $\bar{T}$ are depicted in Figure 6.6 and 6.7, respectively. Note that, to appreciate the effect of the proportional fairness, in Figure 6.6 we also include the case where the sum of stored energies is maximized without a fair policy ($\nu_k(t) = 1$). Similarly, regarding the impact of the EH, the case with WPT and no EH (i.e., no harvesting) is also shown in Figure 6.7.

As illustrated in Figure 6.6, the dispersion diminishes (i.e., FI increases) over time thanks to the PF policy. This means that most of the sensing devices will receive a similar amount of power. In fact, after a first transitory period, Jain's index converges to a constant value and, as expected, a poor value is obtained in the case of no fairness in the optimization.

Finally, in Figure 6.7 we can observe that the case of no harvesting entails a smaller amount of average accumulated energy $\bar{T}$. This is not surprising and can be easily seen in the cases with a higher density, namely, (ii), where the contribution of the harvested energy is larger. Hence, a considerable improvement is attained when collecting energy from the signals transmitted by other sensors. Besides, note that since the average of (iii) is approximately 0.5λ, this case results in the lowest energy obtained from the signals of other sensors.

6.6 Summary and Conclusions

In this chapter, we have addressed the problem of wireless powering a mMTC network. Given the energy limitations of the devices, WPT and EH are considered as feasible options to enlarge their battery lifetimes. In that sense, we have considered a scenario where clusters of sensors are served by a multiple-antenna CN, which is responsible for the WPT. Additionally, EH has been used to collect energy from the signals transmitted by the other active terminals.

To characterize the energy obtained from both procedures, we have modeled the sporadic activity of sensors as Bernoulli RVs and their positions with repulsive MCPs. This way, the random activity and spatial distribution of the terminals are introduced in the analysis of the energy statistics. This can be useful for system key aspects such as energy allocation protocols or optimization of idle-active periods, among others. As an example of application of the developed analysis, we have included the design of a WPT scheme under a PF policy.

Simulation results have shown that, over time, most mMTC devices (i.e., high FI values) can recharge their batteries with a (more) fair amount of power. In fact, this behavior is more notorious in highly dense setups, where the contribution of EH is higher.

Appendix 6.A Equivalence between Optimization Problems

In order to show that problems (6.21) and (6.23) are equivalent, we make use of the first-order Taylor series expansion of the logarithm, i.e.,

$$\begin{aligned}
\underset{\boldsymbol{Q}(t)\succeq\mathbf{0}}{\operatorname{argmax}} \sum_{k=1}^{K} \ln T_k(t) &= \underset{\boldsymbol{Q}(t)\succeq\mathbf{0}}{\operatorname{argmax}} \sum_{k=1}^{K} \ln\left(\left(1-\frac{1}{T_c}\right)T_k(t-1)+\frac{1}{T_c}\bar{E}_k(t)\right) \\
&= \underset{\boldsymbol{Q}(t)\succeq\mathbf{0}}{\operatorname{argmax}} \sum_{k=1}^{K} \ln\left(T_k(t-1)+\frac{1}{T_c}\left(\bar{E}_k(t)-T_k(t-1)\right)\right) \\
&\overset{\text{(a)}}{\approx} \underset{\boldsymbol{Q}(t)\succeq\mathbf{0}}{\operatorname{argmax}} \sum_{k=1}^{K} \ln T_k(t-1)+\frac{1}{T_c}\sum_{k=1}^{K}\frac{\partial \ln T_k(t-1)}{\partial T_k(t-1)}\left(\bar{E}_k(t)-T_k(t-1)\right) \\
&= \underset{\boldsymbol{Q}(t)\succeq\mathbf{0}}{\operatorname{argmax}} \sum_{k=1}^{K} \ln T_k(t-1)+\frac{1}{T_c}\sum_{k=1}^{K}\frac{\bar{E}_k(t)-T_k(t-1)}{T_k(t-1)} \\
&= \underset{\boldsymbol{Q}(t)\succeq\mathbf{0}}{\operatorname{argmax}} \sum_{k=1}^{K} \frac{\bar{E}_k(t)}{T_k(t-1)},
\end{aligned} \tag{6.28}$$

where the approximation in (a) follows from $\ln(x+c) \approx \ln x + \frac{1}{x}c$ for a sufficiently small c. In fact, note that (a) becomes equality for an infinite averaging time, i.e., $T_c \to \infty$.

Chapter 7

Information and Power Transfer

7.1 Introduction

In networks where mMTC and HTC coexist using the same cellular links, suitable transmission schemes and communication policies might be difficult to find. In the former, a large number of battery-constrained devices try to communicate autonomously and usually require a low power consumption. Contrarily, HTC terminals are driven by high data rates.

To properly meet both requirements, strategies based on simultaneous wireless information and power transfer (SWIPT) have emerged as promising candidates [185,186]. SWIPT consists in sending information and power to (possibly) different targets through the same signals, e.g., data is transmitted to user terminals (UTs) and energy to mMTC devices at the same time. Contrarily, another possibility is to transmit information and energy separately through dedicated data transmission (TX) and wireless power transfer (WPT) signals, respectively [170]. As we will see in this chapter, this separation will allow the communication protocol to be more flexible thanks to having different frame structures for HTC and mMTC. In both cases, when taking into account energy harvesting (EH), mMTC terminals can also leverage other transmit signals in the environment to extend their battery lifetime [187].

In this chapter, we will consider a setup where a set of sensors and UTs are connected to a serving CN equipped with multiple antennas. The CN will be responsible for the design of information and power transfer in the DL, considering the capability of the sensors to harvest energy from other active devices. This is of special interest in networks with a high concentration of sensors transmitting in the UL, i.e., in mMTC. Besides, since their locations are random and unknown, we will rely on stochastic geometry tools to model their spatial distribution and the impact on the collected energy (cf. Chapter 6).

Finally, we will also explore the use of block diagonalization (BD) to eliminate HTC interference in the DL [188]. Based on that, transmission strategies will be designed to maximize the sum rate of the UTs while guaranteeing that a sufficient amount of energy is received at the sensors' side. Accordingly, depending on the type of HTC, half duplex (HD) or full duplex (FD), different communication schemes will be presented. The resulting optimization problems, which are non-convex, can be formulated through difference of convex programming (DCP) [189] and semi-definite programming (SDP) [123], for which feasible techniques able to find a local optimum will be proposed.

7.1.1 Related Work

Coexistence has a prominent role in the next generation of mobile systems [28]. The inclusion of mMTC into cellular networks is a challenging problem given the requirements of the devices involved. That is why approaches providing a common solution have been extensively sought within the literature. For instance, the authors of [190] considered the use of massive multiple-input multiple-output (MIMO) technology for joint signal detection, activity identification, and channel estimation. To that aim, they proposed a statistical model including the sporadic traffic and channel sparsity, which allowed the emergence of an inferring receiver scheme. Similarly, by means of stochastic geometry tools, a multiple association strategy that takes into account the capacity limitations of the backhaul in ultra-dense networks was derived in [191].

In that sense, as pointed out before, SWIPT can be a reasonable solution for enabling heterogeneous networks. Some approaches can be found in [192] and references therein. In fact, it has also been widely used for other similar purposes. As an example, in [193], authors analyzed the use of SWIPT in a NOMA-based network with imperfect channel knowledge for D2D communications. Within that framework, they characterized the outage probability and the ergodic capacity of the different terminals. More recently, the authors of [194] presented a beamforming and waveform optimization in a RIS-aided system. The problem is first solved by means of block coordinate descent methods and later using low-complexity approaches.

7.1.2 Contributions

With the above considerations, this chapter can be seen as an extension of Chapter 6, where we maximized the average received energy in a (pure) mMTC setup where no UTs were coexisting. Thereby, the main contributions are the following:

- Inclusion of HTC[1] devices (both in HD and FD configurations), their throughput requirements, and their contribution to the energy harvested by the sensors.
- Derivation of the variance of the sensors' collected energy, the maximum value of which is constrained in the design of transmission schemes maximizing the UTs' rate. This allows us to limit the dispersion of the received energy around the average value (i.e., control the number of depleted batteries) while also meeting the HTC demands.

7.1.3 Organization

The remainder of this chapter is structured as follows. Section 7.2 describes the system model. In Section 7.3, we characterize the statistics of the energy received by the sensors and the data rate of the UTs. Section 7.4 is devoted to the design of the transmission schemes, while numerical simulations are shown in Section 7.5. Conclusions are presented in Section 7.6.

---

[1] Note that HTC can be used to refer to (personal) mobile communications, i.e., eMBB.

7.2 System Model

Throughout this chapter, we consider a scenario similar to that described in Chapter 6, where a single CN serves a group of randomly located sensors and now, additionally, a set of D UTs. The sensors are organized in K clusters [50], each one defined by a disk of radius r_k located at a center $\boldsymbol{c}_k \in \mathbb{R}^2$, with $k \in \{1, \ldots, K\}$.

Like before, the positions of the sensors in cluster k can be represented by repulsive MCPs Φ_k of densities (or intensities) λ_k and a minimum distance between sensing devices d_{min} [49,51]. Regarding the UTs, we consider that they are located at fixed positions and their channels w.r.t. CN to be known. Hence, all the uncertainty comes exclusively from the sensors, the concrete positions of which are considered to be unknown.

We also consider that the CN is equipped with L antennas. This allows the use of linear processing methods, such as BD, that can mitigate the interference among UTs transmitting in the DL simultaneously. In addition to that, this technology can be used to enhance the transfer of energy thanks to the array gain. For simplicity, we assume that sensors and UTs are single-antenna devices. Once again, following the 5G standard [21], we adopt a time-division basis with frames of duration T_f. Depending on the type of HTC communication, we distinguish the different scenarios, HD and FD, and the corresponding frame structures.

In both HD and FD configurations, the energy received by a sensor in cluster k at the end of each frame is

$$E_k \triangleq E_k^{\text{CN}} + E_k^{\text{EH}_\text{S}} + E_k^{\text{EH}_\text{U}}, \tag{7.1}$$

where E_k^{CN} refers to the energy obtained from the CN (either through SWIPT or WPT), $E_k^{\text{EH}_\text{S}}$ is the energy collected from EH thanks to the other active sensors (EH$_\text{S}$), and $E_k^{\text{EH}_\text{U}}$ is that received from the transmitting UTs (EH$_\text{U}$).

7.2.1 HD Configuration

In the HD case, the CN, UTs, and sensors share the same frame structure. More specifically, the first T_d seconds are reserved to SWIPT in the DL and the next T_u seconds are scheduled for UL data transmission, such that $T_f = T_u + T_d$.

During the DL phase, sensors are not allowed to transmit and will simply collect energy from the transmit signal from the CN (SWIPT). Thus, they will be able to transmit data only in the UL. As in Chapter 6, the period T_u will be also divided into N slots of duration T_s such that $T_u = NT_s$. In that sense, each sensing device will transmit information (TX$_\text{S}$) in some of the UL slots, while it will be able to collect energy through EH in the remaining ones. This energy will come from the signals sent by the UTs (EH$_\text{U}$) and the other sensors (EH$_\text{S}$) in the UL. Besides, considering an event-driven mMTC network, the probability of being active at any time slot is p_{act}. Regarding the UTs, we assume that they are (continuously) transmitting (TX$_\text{U}$) during the UL and that they receive data from the CN in the DL (SWIPT).

An illustrative example of a setup with $K = 2$, $D = 5$, and $L = 3$ is shown in Figure 7.1, where different colors represent separate time instants. Accordingly, in Figure 7.2, we depict the (shared) frame structures of sensors and UTs, where EH refers to EH$_\text{S}$ and EH$_\text{U}$.

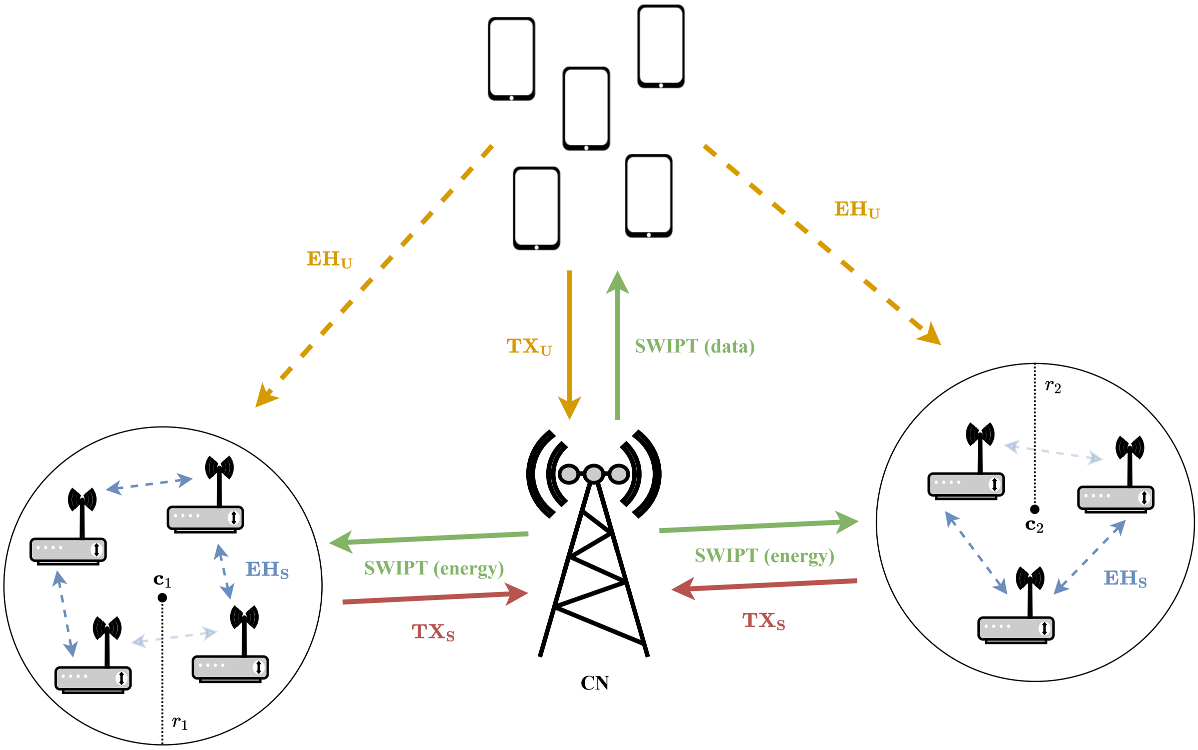

Figure 7.1: Illustrative scenario with $K = 2$, $D = 5$ (HD), and $L = 3$. Solid lines represent intended power transfer (or data transmission), whereas dashed lines refer to energy recycling.

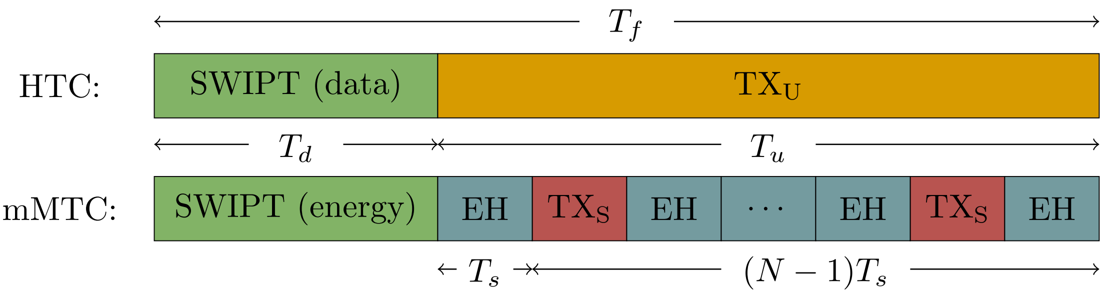

Figure 7.2: Example of frame structures as seen by a HD UT and a particular sensor. Different colors indicate separate time instants and EH denotes the combination of both $\mathrm{EH_S}$ and $\mathrm{EH_U}$.

7.2.2 FD Configuration

When considering the scenario where the HTC devices operate in a FD manner, the data transmission of the CN ($\mathrm{TX_C}$) and UTs ($\mathrm{TX_U}$) are performed simultaneously in time through different frequencies or PRBs (cf. Section 2.3). However, since this configuration does not affect the communication of the sensors, the mMTC terminals maintain the same frame structure. In line with that, sensors will receive energy from the CN (WPT) and UTs ($\mathrm{EH_U}$) during the whole frame, whereas they will only collect energy from the other active devices ($\mathrm{EH_S}$) in the UL.

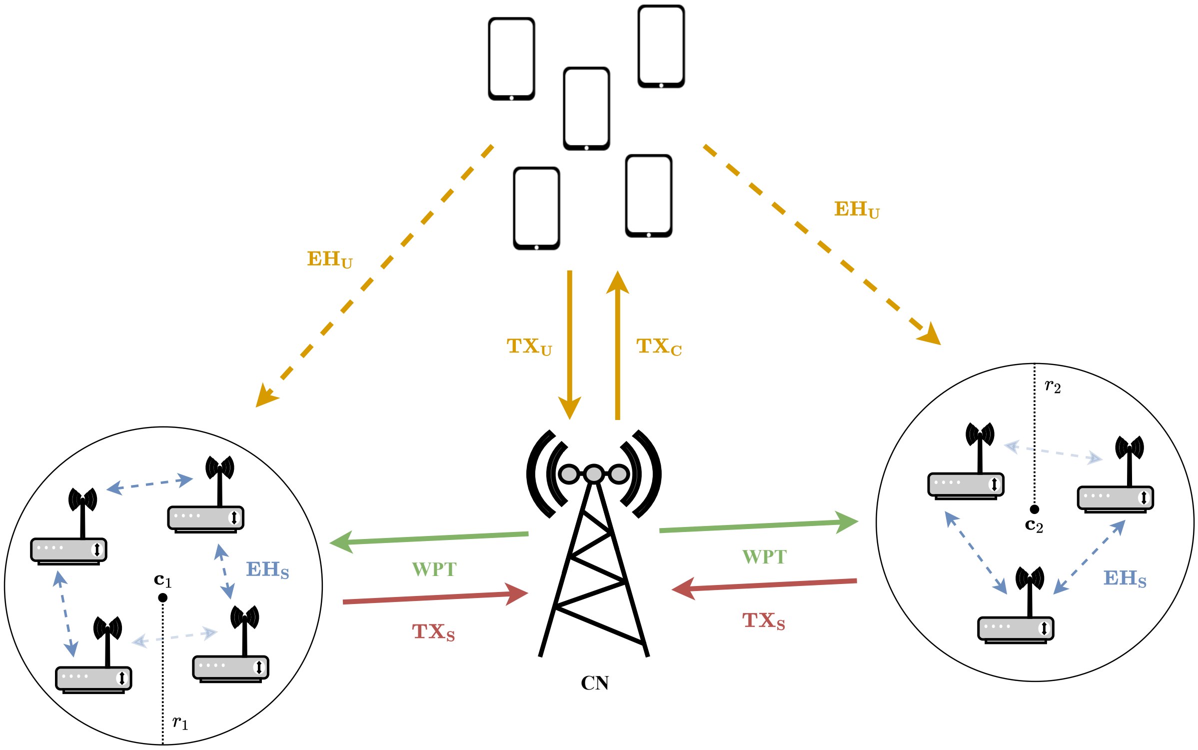

Figure 7.3: Illustrative scenario with $K = 2$, $D = 5$ (FD), and $L = 3$. Solid lines represent intended power transfer (or data transmission), whereas dashed lines refer to energy recycling.

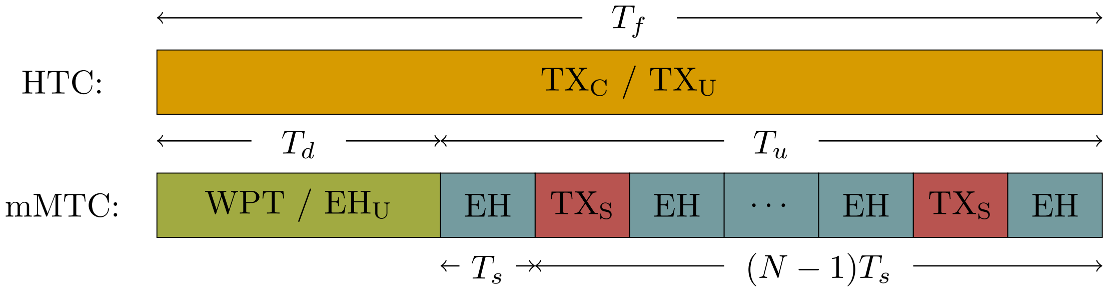

Figure 7.4: Example of frame structures as seen by a FD UT and a particular sensor. Different colors indicate separate time instants and EH denotes the combination of both EH_{S} and EH_{U}.

Similar to before, an illustrative example of a setup with $K = 2$, $D = 5$, and $L = 3$ is shown in Figure 7.3, and the (independent) frame structures are shown in Figure 7.4. Note that simultaneous transmissions (i.e., TX_{C} and TX_{U}) share the same color. Also, in comparison to the HD case, where the DL communication is shared (i.e., SWIPT), here the DL transmission from the CN is dedicated to TX_{C} and WPT.

7.3 Energy and Data Rate Characterization

In this section, we describe the energy collected by the sensors, which is random, and focus on its mean and variance. Later, we provide an expression for the throughput received by the UTs. Based on that, in Section 7.4, we design transmission strategies with BD to maximize the data rate while guaranteeing a similar level of energy is received among all mMTC devices.

7.3.1 Energy Received in the DL

Following the discussion in Subsection 6.3.1, the signal received from the CN in the DL (SWIPT or WPT) by a sensor randomly chosen in cluster k and located at $\hat{\boldsymbol{x}}_k \in \Phi_k$ is given by

$$\hat{y}_k^{\text{CN (DL)}} \triangleq \hat{\boldsymbol{h}}_k^{\text{H}} \boldsymbol{s} + \hat{w}_k \in \mathbb{C}, \tag{7.2}$$

where $\hat{\boldsymbol{h}}_k \in \mathbb{C}^L$ is the UL channel between the sensor and the CN, $\boldsymbol{s} \in \mathbb{C}^L$ is the CN's transmit signal with zero mean and covariance matrix $\boldsymbol{U} \triangleq \mathbb{E}[\boldsymbol{s}\boldsymbol{s}^{\text{H}}] \in \mathbb{C}^{L\times L}$, and $\hat{w}_k \in \mathbb{C}$ is the AWGN with zero mean and power σ_w^2. Considering a linear harvesting model[2] and a negligible noise energy [181], the received energy yields (cf. Subsection 6.3.1)

$$E_k^{\text{CN (DL)}} \triangleq \zeta_k T_d \hat{\boldsymbol{h}}_k^{\text{H}} \boldsymbol{U} \hat{\boldsymbol{h}}_k = \zeta_k T_d \text{tr}\left(\hat{\boldsymbol{h}}_k \hat{\boldsymbol{h}}_k^{\text{H}} \boldsymbol{U}\right), \tag{7.3}$$

with ζ_k the energy conversion efficiency [192]. In addition, considering a power-law path loss, the channel reads as follows:

$$\hat{\boldsymbol{h}}_k \triangleq \hat{d}_k^{-\alpha/2} \hat{\chi}_k \boldsymbol{v}(\hat{\theta}_k), \tag{7.4}$$

where $\hat{d}_k$ is the distance of the randomly selected sensor to the CN, α is the path-loss exponent, $\hat{\chi}_k \sim \mathcal{CN}(0, \sigma_\chi^2)$ is the fading coefficient, $\boldsymbol{v}(\cdot) = [v_1(\cdot), \ldots, v_L(\cdot)]^{\text{T}} \in \mathbb{C}^L$ is the steering vector, and $\hat{\theta}_k$ is the associated steering direction [89].

In the case of HD HTC, the CN's transmit signal is designed to transmit both data to UTs and energy to sensors (SWIPT), and can be decomposed as

$$\boldsymbol{s} \triangleq \sum_i^D \boldsymbol{s}_i, \tag{7.5}$$

where $\boldsymbol{s}_i \in \mathbb{C}^L$ are the independent zero-mean signals for the different UTs with covariance matrix $\boldsymbol{Q}_i \triangleq \mathbb{E}[\boldsymbol{s}_i \boldsymbol{s}_i^{\text{H}}] \in \mathbb{C}^{L\times L}$, with $i \in \{1, \ldots, D\}$[3]. To ease of notation, from now on we define the matrix $\boldsymbol{Q} \triangleq \sum_{i=1}^D \boldsymbol{Q}_i$. Note that, in this case, we have $\boldsymbol{U} = \boldsymbol{Q}$.

Contrarily, when considering FD HTC, sensors and UTs have separate dedicated signals. Thus, the CN's transmit signal can be constructed as the following superposition:

$$\boldsymbol{s} = \boldsymbol{p} + \sum_i^D \boldsymbol{s}_i, \tag{7.6}$$

---

[2] The analysis of non-linear models will be object of study of future works (cf. [195]).

[3] In the previous chapters, the index i has been used to enumerate the mMTC terminals. However, here it will represent the indexes of the UTs (the sensors under study are already described by the locations $\hat{\boldsymbol{x}}_k$).

where $\boldsymbol{p} \in \mathbb{C}^L$ is the WPT signal with zero mean and covariance matrix $\boldsymbol{W} = \mathbb{E}[\boldsymbol{p}\boldsymbol{p}^{\mathrm{H}}] \in \mathbb{C}^{L\times L}$, and independent from all $\boldsymbol{s}_i$ such that $\boldsymbol{U} = \boldsymbol{W} + \boldsymbol{Q}$. In this chapter, we also assume $\boldsymbol{p}$ is a known pseudo-random pilot sequence that can be suppressed at the UTs' side. Hence, it will not interfere in the DL communication.

In the FD case, sensors also receive energy from the HTC terminals. In particular, the energy received from the UTs ($\mathrm{EH_U}$) is

$$E_k^{\mathrm{EH_U(DL)}} \triangleq \zeta_k T_d \sum_{i=1}^{D} \hat{\varrho}_{k,i}^{-\alpha} |\hat{\xi}_{k,i}|^2 |z_i|^2, \tag{7.7}$$

where $\hat{\varrho}_{k,i}$ is the distance between UT i and $\hat{\boldsymbol{x}}_k$, $\hat{\xi}_{k,i} \sim \mathcal{CN}(0, \sigma_\xi^2)$ is the fading coefficient, and $z_i \sim \mathcal{CN}(0, P_z)$ are the independent transmit signals of the UTs.

It is noteworthy to mention that, even though sensors and UTs actually transmit through different carriers, both signals are located at the same band and, therefore, the sensing devices are able to collect the energy of the signals coming from these UTs [21].

7.3.2 Energy Received in the UL

Likewise, the received energy from the CN (only in the FD case) by the sensor randomly chosen in cluster k (located at $\hat{\boldsymbol{x}}_k \in \Phi_k$) can be expressed as

$$E_k^{\mathrm{CN(UL)}} \triangleq \zeta_k T_s \mathrm{tr}\left(\hat{\boldsymbol{h}}_k \hat{\boldsymbol{h}}_k^{\mathrm{H}} \boldsymbol{Q}\right) \sum_{m=1}^{N} (1 - \beta_{\hat{\boldsymbol{x}}_k}[m]), \tag{7.8}$$

where $\beta_{\hat{\boldsymbol{x}}_k}[m] \sim$ *Ber*(p_{act}) is the Bernoulli RV describing the sporadic activity of the sensor located at $\hat{\boldsymbol{x}}_k$, i.e., p_{act} is the probability that the sensor is transmitting during the time slot m. Accordingly, $(1 - \beta_{\hat{\boldsymbol{x}}_k}[m])$ accounts for the fact that the sensor can collect energy only when it is not transmitting (cf. Subsection 6.3.2).

On the other hand, the energy received from the other active sensors ($\mathrm{EH_S}$) is given by

$$E_k^{\mathrm{EH_S}} \triangleq \zeta_k T_s \sum_{m=1}^{N} \sum_{\boldsymbol{x}\in\hat{\Phi}_k} \hat{\tau}_{k,\boldsymbol{x}}^{-\alpha} |\hat{\gamma}_{k,\boldsymbol{x}}[m]|^2 |\kappa_{\boldsymbol{x}}[m]|^2 \beta_{\boldsymbol{x}}[m] (1 - \beta_{\hat{\boldsymbol{x}}_k}[m]), \tag{7.9}$$

where $\hat{\tau}_{k,\boldsymbol{x}}$ is the distance between $\boldsymbol{x}$ and $\hat{\boldsymbol{x}}_k$, $\hat{\gamma}_{k,\boldsymbol{x}}[m] \sim \mathcal{CN}(0, \sigma_\gamma^2)$ is the fading coefficient[4], and $\kappa_{\boldsymbol{x}}[m] \sim \mathcal{CN}(0, P_\kappa)$ is the sensor's transmit signal during time slot m. Note that $\beta_{\boldsymbol{x}}[m] \sim$ *Ber*(p_{act}) (assumed to be independent) represents the activity of the sensor located at $\boldsymbol{x}$. In addition to that, $\hat{\Phi}_k = \cup_l \Phi_l \backslash \{\hat{\boldsymbol{x}}_k\}$ is used to denote the set of positions of all mMTC devices excluding the location of the sensor under study.

Finally, the energy received from the UTs ($\mathrm{EH_U}$) is

$$E_k^{\mathrm{EH_U(UL)}} \triangleq \zeta_k T_s \sum_{i=1}^{D} \hat{\varrho}_{k,i}^{-\alpha} |\hat{\xi}_{k,i}|^2 |z_i|^2 \sum_{m=1}^{N} (1 - \beta_{\hat{\boldsymbol{x}}_k}[m]). \tag{7.10}$$

---

[4] For the sake of generality, here we have considered that the fading coefficient can vary over time (between slots) since its impact can be critical in the sensor-to-sensor links (where the channel quality is usually poor).

As a result, depending on the UTs communication, we have the following received energies:

- HD: $E_k^{\text{CN}} \triangleq$ (7.3), and $E_k^{\text{EH}_{\text{U}}} \triangleq$ (7.10).
- FD: $E_k^{\text{CN}} \triangleq$ (7.3) + (7.8), and $E_k^{\text{EH}_{\text{U}}} \triangleq$ (7.7) + (7.10).

It is noteworthy to mention that the energy coming from the sensors is the same in both configurations. Besides, note that for the derivations of the FD case, we consider that the signals carrying information from the CN, i.e., the set $\{\boldsymbol{s}_i\}$ (TX$_{\text{C}}$), and those from the UTs, i.e., the set $\{z_i\}$ (TX$_{\text{U}}$), are the same during the entire frame.

7.3.3 Mean and Variance of the Received Energy

As previously mentioned, the received energy in (7.1) is random due to the fading, activities, and positions of the sensors. That is why in the following analysis, we characterize its statistics. In particular, we focus on the first- and second-order moments:

$$\bar{E}_k \triangleq \mathbb{E}[E_k], \quad \bar{V}_k \triangleq \text{Var}[E_k]. \tag{7.11}$$

The mean in (7.11) can be rewritten as follows:

$$\bar{E}_k = \mathbb{E}\left[E_k^{\text{CN}}\right] + \mathbb{E}\left[E_k^{\text{EH}_{\text{S}}}\right] + \mathbb{E}\left[E_k^{\text{EH}_{\text{U}}}\right]. \tag{7.12}$$

In the HD case, the first two terms can be found in Section 6.3:

$$\mathbb{E}\left[E_k^{\text{CN}}\right] = \zeta_k T_d \text{tr}\left(\boldsymbol{C}_k \boldsymbol{Q}\right) \triangleq \bar{E}_k^{\text{CN}}, \tag{7.13}$$

$$\mathbb{E}\left[E_k^{\text{EH}_{\text{S}}}\right] = \zeta_k T_u P_\kappa \sigma_\gamma^2 p_{\text{act}}(1-p_{\text{act}})\eta_k \triangleq \bar{E}_k^{\text{EH}_{\text{S}}}, \tag{7.14}$$

where $\boldsymbol{C}_k$ is the covariance matrix of the channel between the sensor in cluster k and the CN, and η_k is the sum of intra-cluster and inter-cluster path loss. Their analytic closed-form expressions are already derived in Chapter 6. Please refer to (6.7) and (6.14), respectively.

Likewise, it can be shown that the third addend yields [52]

$$\mathbb{E}\left[E_k^{\text{EH}_{\text{U}}}\right] = \zeta_k T_u P_z \sigma_\xi^2 (1-p_{\text{act}}) \sum_{i=1}^{D} \mathbb{E}\left[\hat{\varrho}_{k,i}^{-\alpha}\right] \triangleq \bar{E}_k^{\text{EH}_{\text{U}}}, \tag{7.15}$$

where $\mathbb{E}\left[\hat{\varrho}_{k,i}^{-\alpha}\right]$ is a particular case of equation (6.7) for $L = 1$ (single-antenna transmitter).

When considering the FD scenario, we need to include some additional terms in the expressions (7.13) and (7.15), namely, the energy collected from the UTs during the first T_d seconds and that coming from the CN in the other T_u seconds (cf. Figure 7.4), i.e.,

$$\mathbb{E}\left[E_k^{\text{CN}}\right] = \zeta_k T_d \text{tr}\left(\boldsymbol{C}_k \boldsymbol{W}\right) + \zeta_k \left(T_f - p_{\text{act}} T_u\right) \text{tr}\left(\boldsymbol{C}_k \boldsymbol{Q}\right) \triangleq \bar{E}_k^{\text{CN}}, \tag{7.16}$$

$$\mathbb{E}\left[E_k^{\text{EH}_{\text{U}}}\right] = \zeta_k P_z \sigma_\xi^2 \left(T_f - p_{\text{act}} T_u\right) \sum_{i=1}^{D} \mathbb{E}\left[\hat{\varrho}_{k,i}^{-\alpha}\right] \triangleq \bar{E}_k^{\text{EH}_{\text{U}}}. \tag{7.17}$$

On the other hand, the variance can be difficult to obtain given the statistical dependence between the three terms. In this chapter, we opt for using the following upper bound [75]:

$$\bar{V}_k \leq 3\left(\text{Var}\left[E_k^{\text{CN}}\right] + \text{Var}\left[E_k^{\text{EH}_\text{S}}\right] + \text{Var}\left[E_k^{\text{EH}_\text{U}}\right]\right). \tag{7.18}$$

As discussed in Section 7.4, the variance will be constrained to a maximum value when designing the transmission strategy. This way, we control the situations in which the batteries of the sensors drain (although the mean energy $\bar{E}_k$ is positive) due to the randomness of the energy evolution. Consequently, this upper bound will result in a more restrictive design. Its impact will be further discussed through numerical simulations in Section 7.5.

To find a more tractable expression, the first term in (7.18) is also upper bounded. In particular, in the HD case, we have

$$\begin{aligned}
\text{Var}\left[E_k^{\text{CN}}\right] &= \mathbb{E}\left[\zeta_k^2 T_d^2 \text{tr}\left(\hat{\boldsymbol{h}}_k \hat{\boldsymbol{h}}_k^{\text{H}} \boldsymbol{Q}\right)^2\right] - \left(\bar{E}_k^{\text{CN}}\right)^2 \\
&\overset{\text{(a)}}{\leq} \zeta_k^2 T_d^2 \mathbb{E}\left[\text{tr}\left(\left(\hat{\boldsymbol{h}}_k \hat{\boldsymbol{h}}_k^{\text{H}}\right)^2\right) \text{tr}\left(\boldsymbol{Q}^2\right)\right] - \left(\bar{E}_k^{\text{CN}}\right)^2 \\
&\overset{\text{(b)}}{=} \zeta_k^2 3 T_d^2 L^2 \sigma_\chi^4 \mathbb{E}\left[\hat{d}_k^{-2\alpha}\right] \|\boldsymbol{Q}\|_\text{F}^2 - \left(\bar{E}_k^{\text{CN}}\right)^2 \\
&\triangleq f_{k,1}(\boldsymbol{Q}) - f_{k,2}(\boldsymbol{Q}),
\end{aligned} \tag{7.19}$$

where (a) follows from the fact that $\hat{\boldsymbol{h}}_k \hat{\boldsymbol{h}}_k^{\text{H}}$ and $\boldsymbol{Q}$ are positive semi-definite matrices, and (b) follows from the 4-th order moment of the fading coefficient $\hat{\chi}_k$. Note that $\mathbb{E}\left[\hat{d}_k^{-2\alpha}\right]$ can be derived from equation (6.7) by substituting the decay factor for 2α.

Regarding the FD configuration, we have

$$\text{Var}\left[E_k^{\text{CN}}\right] \leq \zeta_k^2 3 L^2 \sigma_\chi^4 \mathbb{E}\left[\hat{d}_k^{-2\alpha}\right] t(\boldsymbol{W}, \boldsymbol{Q}) - \left(\bar{E}_k^{\text{CN}}\right)^2 \triangleq f_{k,1}\left(\boldsymbol{W}, \boldsymbol{Q}\right) - f_{k,2}\left(\boldsymbol{W}, \boldsymbol{Q}\right), \tag{7.20}$$

where $t(\boldsymbol{W}, \boldsymbol{Q}) \triangleq a_1 \|\boldsymbol{Q}\|_\text{F}^2 + a_2 \|\boldsymbol{W}\|_\text{F}^2 + 2a_3 \text{tr}\left(\boldsymbol{W}\boldsymbol{Q}\right)$ with

$$a_1 \triangleq T_d^2 + T_u(1 - p_\text{act})\left(T_s\left(1 + (N-1)(1-p_\text{act})\right) + 2T_d\right), \quad a_2 \triangleq T_d^2, \quad a_3 \triangleq T_d^2 + T_d T_u (1 - p_\text{act}). \tag{7.21}$$

Finally, the variance of $E_k^{\text{EH}_\text{S}}$ can be obtained by including the cross products in (6.14) [49]:

$$\begin{aligned}
\text{Var}\left[E_k^{\text{EH}_\text{S}}\right] &= \zeta_k^2 T_u T_s P_\kappa^2 \sigma_\gamma^4 p_\text{act}(1 - p_\text{act}) \\
&\times \left(b_1 \mathbb{E}\left[\sum_{\boldsymbol{x} \in \hat{\Phi}_k} \hat{\tau}_{k,\boldsymbol{x}}^{-2\alpha}\right] + b_2 \mathbb{E}\left[\sum_{\boldsymbol{x}_1, \boldsymbol{x}_2 \in \hat{\Phi}_k}^{\boldsymbol{x}_1 \neq \boldsymbol{x}_2} \hat{\tau}_{k,\boldsymbol{x}_1}^{-\alpha} \hat{\tau}_{k,\boldsymbol{x}_2}^{-\alpha}\right]\right) - \left(\bar{E}_k^{\text{EH}_\text{S}}\right)^2,
\end{aligned} \tag{7.22}$$

with $b_1 \triangleq 9 + 3(N-1)(1-p_\text{act})p_\text{act}$ and $b_2 \triangleq p_\text{act} + (N-1)(1-p_\text{act})p_\text{act}$.

Likewise, the variance of the energy harvested from the UTs' signals yields

$$\text{Var}\left[E_k^{\text{EH}_\text{U}}\right] = \zeta_k^2 P_z^2 \sigma_\xi^4 \left(c_1 \sum_{i=1}^{D} \mathbb{E}\left[\hat{\varrho}_{k,i}^{-2\alpha}\right] + c_2 \sum_{i,j}^{j \neq i} \mathbb{E}\left[\hat{\varrho}_{k,i}^{-\alpha} \hat{\varrho}_{k,j}^{-\alpha}\right]\right) - \left(\bar{E}_k^{\text{EH}_\text{U}}\right)^2, \tag{7.23}$$

where $c_1 \equiv c_1^{\mathrm{HD}} \triangleq 9T_uT_s(1-p_{\mathrm{act}})\,(1+(N-1)(1-p_{\mathrm{act}}))$ and $c_2 \equiv c_2^{\mathrm{HD}} \triangleq T_uT_s(1-p_{\mathrm{act}}) + T_uT_s(N-1)(1-p_{\mathrm{act}})^2$ in the HD scenario, while $c_1 \equiv c_1^{\mathrm{FD}} \triangleq c_1^{\mathrm{HD}} + 9T_d^2 + 18T_dT_u(1-p_{\mathrm{act}})$ and $c_2 \equiv c_2^{\mathrm{FD}} \triangleq c_2^{\mathrm{HD}} + T_d^2 + 2T_dT_u(1-p_{\mathrm{act}})$ in the FD configuration.

As before, the remaining expectations in (7.22) and (7.23) can be computed following similar derivations to those in Subsection 6.3.2. For more details, refer to equations (6.15) and (6.17).

7.3.4 Data Rate of the UTs

In the HD case, the signal received from the CN by UT i is

$$y_i \triangleq \boldsymbol{g}_i^{\mathrm{H}} \sum_{i=1}^{D} \boldsymbol{s}_i + \omega_i \in \mathbb{C}, \tag{7.24}$$

where $\boldsymbol{g}_i \in \mathbb{C}^L$ is the (known) channel of the UT w.r.t. the CN and $\omega_i \in \mathbb{C}$ is the noise with zero mean and power σ_ω^2. Thereby, when considering Gaussian distributed noise and signals, the data rate of UT i yields (cf. Subsection 2.2.2)

$$\Gamma_i \triangleq \log(1+\rho_i) = \log\left(1 + \frac{\boldsymbol{g}_i^{\mathrm{H}}\boldsymbol{Q}_i\boldsymbol{g}_i}{\sigma_\omega^2 + \sum_{j\neq i} \boldsymbol{g}_i^{\mathrm{H}}\boldsymbol{Q}_j\boldsymbol{g}_i}\right), \tag{7.25}$$

where ρ_i is the SINR corresponding to the received signal at UT i (cf. (2.9)). Besides, note that these expressions also hold for the FD configuration since the pilot sequence $\boldsymbol{p}$ (sent through WPT) is known and can be suppressed at the UTs' side (cf. Subsection 7.3.1). That is why the covariance matrix $\boldsymbol{W}$ does not affect the throughput Γ_i.

7.4 Transmission Optimization

The purpose of this chapter is to design transmission strategies that maximize the (weighted) sum rate while ensuring a sufficient amount of energy for the sensors in the network. For that task, we formulate different problems depending on the UTs communication (HD or FD).

7.4.1 HD Configuration: SWIPT Optimization

In the HD case, the optimization problem reads as follows:

$$\begin{aligned} \{\boldsymbol{Q}_i^\star\} = \underset{\{\boldsymbol{Q}_i\}}{\operatorname{argmax}} \; & \sum_{i=1}^{D} \nu_i \log(1+\rho_i) \\ \text{s.t.} \quad & C1 : \boldsymbol{Q}_i \succeq \mathbf{0}, \quad \forall i \\ & C2 : \sum_{i=1}^{D} \operatorname{tr}(\boldsymbol{Q}_i) \leq P_{\mathrm{tx}} \\ & C3 : \bar{E}_k \geq \delta, \quad \forall k \\ & C4 : \bar{V}_k \leq \mu, \quad \forall k, \end{aligned} \tag{7.26}$$

where the design parameters are the covariance matrices $\{\boldsymbol{Q}_i\}$, which must be positive semi-definite ($C1$), and ν_i is the set of (fixed) weights to achieve some fairness [36]. In addition, $C2$ represents the total power constraint at the CN and P_{tx} is the available transmit power. $C3$ guarantees that the sensors receive (on average) a sufficient amount of energy δ. Nevertheless, given the randomness of the collected energy, even if $C3$ is satisfied, there might be situations in which sensors do not have enough energy. That is why, to limit the energy dispersion to μ, $C4$ is introduced in (7.26). This will reduce the number of sensors with depleted batteries.

Due to the interfering terms in Γ_i, the objective function in (7.26) is not concave in $\{\boldsymbol{Q}_i\}$ and, therefore, the problem in (7.26) results non-convex. To overcome this issue, we can impose a new constraint in (7.26) so that all interference is eliminated. The previous constraint can be achieved by forcing $\boldsymbol{g}_j^{\mathrm{H}}\boldsymbol{Q}_i\boldsymbol{g}_j = 0 \; \forall j \neq i$ in problem (7.26):

$$\begin{aligned} \{\boldsymbol{Q}_i^\star\} = \underset{\{\boldsymbol{Q}_i\}}{\operatorname{argmax}} \quad & \sum_{i=1}^{D} \nu_i \log(1+\rho_i) \\ \text{s.t.} \quad & C1 - C4 \\ & C5: \boldsymbol{g}_j^{\mathrm{H}}\boldsymbol{Q}_i\boldsymbol{g}_j = 0, \quad \forall j \neq i. \end{aligned} \tag{7.27}$$

In this chapter, to account for constraint $C5$, we make use of BD [188]. More specifically, under the assumption of a large number of transmitting antennas[5] such that $L > D-1$, we can construct the covariance matrices as

$$\boldsymbol{Q}_i = \tilde{\boldsymbol{V}}_i \tilde{\boldsymbol{Q}}_i \tilde{\boldsymbol{V}}_i^{\mathrm{H}}, \tag{7.28}$$

where $\tilde{\boldsymbol{V}}_i \in \mathbb{C}^{L\times(L-D+1)}$ represent the right singular vectors associated to the zero singular values (i.e., row null space) of the following matrix $\tilde{\boldsymbol{G}}_i$:

$$\tilde{\boldsymbol{G}}_i = [\boldsymbol{g}_1, \ldots, \boldsymbol{g}_{i-1}, \boldsymbol{g}_{i+1}, \ldots, \boldsymbol{g}_N]^{\mathrm{H}} \in \mathbb{C}^{(D-1)\times L}. \tag{7.29}$$

This way, constraint $C5$ in (7.27) is satisfied and (7.27) can be written in terms of the variables $\tilde{\boldsymbol{Q}}_i \in \mathbb{C}^{(L-D+1)\times(L-D+1)}$:

$$\begin{aligned} \left\{\tilde{\boldsymbol{Q}}_i^\star\right\} = \underset{\{\tilde{\boldsymbol{Q}}_i\}}{\operatorname{argmax}} \quad & \sum_{i=1}^{D} \nu_i \log\left(1 + \frac{1}{\sigma_\omega^2}\tilde{\boldsymbol{g}}_i^{\mathrm{H}}\tilde{\boldsymbol{Q}}_i\tilde{\boldsymbol{g}}_i\right) \\ \text{s.t.} \quad & C1: \tilde{\boldsymbol{Q}}_i \succeq \boldsymbol{0}, \quad \forall i \\ & C2: \sum_{i=1}^{D} \operatorname{tr}(\tilde{\boldsymbol{Q}}_i) \leq P_{\text{tx}} \\ & C3: \bar{E}_k \geq \delta, \quad \forall k \\ & C4: \bar{V}_k \leq \mu, \quad \forall k, \end{aligned} \tag{7.30}$$

with $\tilde{\boldsymbol{g}}_i \triangleq \tilde{\boldsymbol{V}}_i^{\mathrm{H}}\boldsymbol{g}_i$. Note that constraints $C1 - C3$ define a convex set on $\left\{\tilde{\boldsymbol{Q}}_i\right\}$ (cf. (7.13) or (7.16)),

---

[5] This condition can be easily met in current deployments, where a massive number of antennas is usually considered (i.e., massive MIMO) [196].

whereas constraint $C4$ yields a difference of convex functions:

$$\begin{aligned}\bar{V}_k &\overset{\text{(a)}}{\leq} 3\underbrace{\left(\mathrm{Var}\left[E_k^{\mathrm{EH_U}}\right]+\mathrm{Var}\left[E_k^{\mathrm{EH_S}}\right]\right)}_{\triangleq\tilde{V}_k}+3\mathrm{Var}\left[E_k^{\mathrm{CN}}\right]\\ &\overset{\text{(b)}}{\leq} 3\tilde{V}_k+3\left(f_{k,1}\left(\left\{\tilde{\boldsymbol{Q}}_i\right\}\right)-f_{k,2}\left(\left\{\tilde{\boldsymbol{Q}}_i\right\}\right)\right),\end{aligned} \tag{7.31}$$

where (a) and (b) follow from the bounds in (7.18) and (7.19), respectively.

Recall that $f_{k,1}$ and $f_{k,2}$ are already defined in (7.19) and can be shown to be convex in $\left\{\tilde{\boldsymbol{Q}}_i\right\}$. As mentioned before, in comparison with limiting $\bar{V}_k$, constraining the maximum value of the upper bound from (7.31) will represent a more restrictive use case scenario.

In general, these problems do not have an analytic closed-form solution leading to a global optimum. However, with the help of DCP, we are able to find a local optimum with still good performance [189]. In short, (7.30) is decomposed into a sequence of convex sub-problems that are solved iteratively (at each stage, we update the solution based on the previous outcomes). To that end, $f_{k,2}$ is approximated by an affine function so that $C4$ is convexified.

In our case, for any feasible initial point in the constraint set $\mathcal{S}\triangleq\{C1,\dots,C4\}$, denoted by $\{\tilde{\boldsymbol{Q}}_i^{(0)}\}$, the first-order approximation of the function $f_{k,2}$ in (7.19) reads as follows:

$$\begin{aligned}f_{k,2}\left(\left\{\tilde{\boldsymbol{Q}}_i\right\}\right) &\approx f_{k,2}\left(\{\tilde{\boldsymbol{Q}}_i^{(0)}\}\right)+\mathrm{tr}\left(\left(\nabla f_{k,2}\left(\{\tilde{\boldsymbol{Q}}_i^{(0)}\}\right)\right)^{\mathrm{T}}\left(\sum_{i=1}^{D}\tilde{\boldsymbol{V}}_i\tilde{\boldsymbol{Q}}_i\tilde{\boldsymbol{V}}_i^{\mathrm{H}}-\sum_{i=1}^{D}\tilde{\boldsymbol{V}}_i\tilde{\boldsymbol{Q}}_i^{(0)}\tilde{\boldsymbol{V}}_i^{\mathrm{H}}\right)\right)\\ &\overset{\text{(a)}}{=}\zeta_k^2T_d^2\mathrm{tr}\left(\boldsymbol{C}_k\sum_{i=1}^{D}\tilde{\boldsymbol{V}}_i\tilde{\boldsymbol{Q}}_i^{(0)}\tilde{\boldsymbol{V}}_i^{\mathrm{H}}\right)^2\\ &\quad+2\zeta_k^2T_d^2\mathrm{tr}\left(\boldsymbol{C}_k\sum_{i=1}^{D}\tilde{\boldsymbol{V}}_i\tilde{\boldsymbol{Q}}_i^{(0)}\tilde{\boldsymbol{V}}_i^{\mathrm{H}}\right)\mathrm{tr}\left(\boldsymbol{C}_k\left(\sum_{i=1}^{D}\tilde{\boldsymbol{V}}_i\tilde{\boldsymbol{Q}}_i\tilde{\boldsymbol{V}}_i^{\mathrm{H}}-\sum_{i=1}^{D}\tilde{\boldsymbol{V}}_i\tilde{\boldsymbol{Q}}_i^{(0)}\tilde{\boldsymbol{V}}_i^{\mathrm{H}}\right)\right)\\ &\triangleq\tilde{f}_{k,2}\left(\left\{\tilde{\boldsymbol{Q}}_i\right\},\{\tilde{\boldsymbol{Q}}_i^{(0)}\}\right),\end{aligned} \tag{7.32}$$

where (a) follows from the fact that $\nabla_{\boldsymbol{A}}\mathrm{tr}\left(\boldsymbol{A}\boldsymbol{B}\right)^2=2\mathrm{tr}\left(\boldsymbol{A}\boldsymbol{B}\right)\boldsymbol{B}^{\mathrm{T}}$ for any two matrices $\boldsymbol{A}$ and $\boldsymbol{B}$. In this case, it suffices to particularize this operation for $\boldsymbol{A}=\sum_{i=1}^{D}\tilde{\boldsymbol{V}}_i\tilde{\boldsymbol{Q}}_i^{(0)}\tilde{\boldsymbol{V}}_i^{\mathrm{H}}$ and $\boldsymbol{B}=\boldsymbol{C}_k$.

At each step of the iterative algorithm, denoted by u as for $\{\tilde{\boldsymbol{Q}}_i^{(u)}\}$, we focus on the following convex optimization sub-problem:

$$\begin{aligned}\left\{\tilde{\boldsymbol{Q}}_i^{\star}\right\}=\underset{\{\tilde{\boldsymbol{Q}}_i\}}{\mathrm{argmax}}\;&\sum_{i=1}^{D}\nu_i\log\left(1+\frac{1}{\sigma_\omega^2}\tilde{\boldsymbol{g}}_i^{\mathrm{H}}\tilde{\boldsymbol{Q}}_i\tilde{\boldsymbol{g}}_i\right)\\ \text{s.t.}\quad&C1-C3\\ &C4:\tilde{V}_k+f_{k,1}\left(\left\{\tilde{\boldsymbol{Q}}_i\right\}\right)-\tilde{f}_{k,2}\left(\left\{\tilde{\boldsymbol{Q}}_i\right\},\{\tilde{\boldsymbol{Q}}_i^{(u)}\}\right)\leq\mu/3,\quad\forall k,\end{aligned} \tag{7.33}$$

which can be solved numerically with standard optimization methods [123]. Then, since the solution $\left\{\tilde{\boldsymbol{Q}}_i^{\star}\right\}$ of (7.33) converges to a local optimum of (7.30), it can be used as a sub-optimal approach with still good performance [188, 189].

Algorithm 7.1 Iterative solution to problem (7.30)

```
Initialize $\{\tilde{\boldsymbol{Q}}_i^{(0)}\} \in \mathcal{S}$ and set $u = 0$
Compute $\sum_{i=1}^{D} \nu_i \Gamma_i \left(\tilde{\boldsymbol{Q}}_i^{(0)}\right)$
repeat
    Solve (7.33) with $\{\tilde{\boldsymbol{Q}}_i^{(u)}\}$ to find $\left\{\tilde{\boldsymbol{Q}}_i^{\star}\right\}$ using [124]
    Set $\tilde{\boldsymbol{Q}}_i^{(u+1)} = \tilde{\boldsymbol{Q}}_i^{\star}$ $\forall i$ and $u \leftarrow u + 1$
    Compute $\sum_{i=1}^{D} \nu_i \Gamma_i \left(\tilde{\boldsymbol{Q}}_i^{(u)}\right)$
until Convergence (7.34) is reached.
```

Accordingly, to address the problem in (7.33), we make use of the successive approximation method with the SeDuMi solver of the CVX software package, for which we set the precision parameter to high [124]. The entire procedure is described in Algorithm 7.1, where the stopping criterion is given by the following condition:

$$\sum_{i=1}^{D} \nu_i \Gamma_i \left(\tilde{\boldsymbol{Q}}_i^{(u)}\right) - \sum_{i=1}^{D} \nu_i \Gamma_i \left(\tilde{\boldsymbol{Q}}_i^{(u-1)}\right) \leq \epsilon, \tag{7.34}$$

for some $\epsilon \geq 0$ and $\Gamma_i \left(\tilde{\boldsymbol{Q}}_i^{(u)}\right) \triangleq \log\left(1 + \frac{1}{\sigma_\omega^2} \tilde{\boldsymbol{g}}_i^{\mathrm{H}} \tilde{\boldsymbol{Q}}_i^{(u)} \tilde{\boldsymbol{g}}_i\right)$, which refer to the stopping threshold (later defined) and the data rate of UT i obtained at the u-th iteration, respectively.

7.4.2 FD Configuration: WPT and TX Optimization

Similar to before, when considering FD UTs, the problem can be formulated as follows:

$$\begin{aligned} \{\boldsymbol{W}^{\star}, \{\boldsymbol{Q}_i^{\star}\}\} = \underset{\boldsymbol{W}, \{\boldsymbol{Q}_i\}}{\operatorname{argmax}} \ & \sum_{i=1}^{D} \nu_i \log(1 + \rho_i) \\ \text{s.t.} \quad & C1 : \boldsymbol{W} \succeq \boldsymbol{0}, \quad \boldsymbol{Q}_i \succeq \boldsymbol{0}, \quad \forall i \\ & C2 : T_d \mathrm{tr}\left(\boldsymbol{W}\right) + T_f \sum_{i=1}^{D} \mathrm{tr}\left(\boldsymbol{Q}_i\right) \leq T_f P_{\mathrm{tx}} \\ & C3 : \bar{E}_k \geq \delta, \quad \forall k \\ & C4 : \bar{V}_k \leq \mu, \quad \forall k, \end{aligned} \tag{7.35}$$

where the CN's power constraint $C3$ is replaced for an energy constraint to account for the different duration of the transmit signals.

Given the nature of the previous problem, even with the help of BD processing, the joint optimization of the $\boldsymbol{W}$ and $\{\boldsymbol{Q}_i\}$ is still non-convex (cf. (7.20)) and finding an analytic closed-form solution is a challenging task. That is why in this chapter, to reduce complexity, we consider the separate (alternating) optimization of these covariance matrices [197].

Algorithm 7.2 Alternating solution to problem (7.35)

```
Initialize $\boldsymbol{W} \in \mathcal{S}$ and $\{\boldsymbol{Q}_i\} \in \mathcal{S}$
repeat
    Solve (7.36) with $\boldsymbol{W}$ to find $\{\boldsymbol{Q}_i^\star\}$ using Algorithm 7.1
    Set $\boldsymbol{Q}_i = \boldsymbol{Q}_i^\star \ \forall i$
    Solve (7.37) with $\{\boldsymbol{Q}_i\}$ to find $\boldsymbol{W}^\star$ using [124]
    Set $\boldsymbol{W} = \boldsymbol{W}^\star$
until Convergence is reached.
```

Considering a fixed WPT covariance matrix $\boldsymbol{W}$, problem (7.35) can be rewritten as

$$\begin{aligned} \{\boldsymbol{Q}_i^\star\} = \underset{\{\boldsymbol{Q}_i\}}{\text{argmax}} \ & \sum_{i=1}^{D} \nu_i \log(1+\rho_i) \\ \text{s.t.} \ & C1 : \boldsymbol{Q}_i \succeq \boldsymbol{0}, \quad \forall i \\ & C2 - C4, \end{aligned} \tag{7.36}$$

which can be solved following the procedure described in Subsection 7.4.1. Different from the joint optimization in (7.35), now the function $f_{k,1}(\boldsymbol{W}, \boldsymbol{Q}) = f_{k,1}(\{\boldsymbol{Q}_i\})$ defined in (7.20) is convex in $\{\boldsymbol{Q}_i\}$ since it is composed by the sum of two convex functions, i.e., squared Frobenius norm and trace [123]. Likewise, the function $f_{k,2}(\boldsymbol{W}, \boldsymbol{Q}) = f_{k,2}(\{\boldsymbol{Q}_i\})$ is given by the sum of a convex function (i.e., squared trace), which can be approximated by an affine function as before (cf. (7.32)), and a linear function (i.e., trace). As a result, constraint $C4$ can still be convexified and a sub-optimal solution of (7.36) can be found. The same applies for the optimization of $\boldsymbol{W}$.

Accordingly, given that $\boldsymbol{W}$ does not affect the data rate of the UTs (cf. (7.25)), when the set $\{\boldsymbol{Q}_i\}$ is fixed, the optimization in (7.35) can be written as the following feasibility problem [123]:

$$\begin{aligned} \left\{\boldsymbol{W}^\star, \bar{P}_{\text{tx}}^\star\right\} = \underset{\boldsymbol{W}, \bar{P}_{\text{tx}}}{\text{argmin}} \ & T_f \bar{P}_{\text{tx}} \\ \text{s.t.} \ & C1 : \boldsymbol{W} \succeq \boldsymbol{0} \\ & C2 : T_d \text{tr}(\boldsymbol{W}) + T_f \sum_{i=1}^{D} \text{tr}(\boldsymbol{Q}_i) \leq T_f \bar{P}_{\text{tx}} \\ & C3 - C4, \end{aligned} \tag{7.37}$$

where $\bar{P}_{\text{tx}}$ is used as an auxiliary optimization variable that does not affect the optimal covariance matrix $\boldsymbol{W}^\star$. The previous problem can be solved numerically through SDP [123]. In particular, we make use of the interior point method of the CVX software package with the SeDuMi solver and the high precision [124]. Note that if the problem above is infeasible (i.e., $\bar{P}_{\text{tx}}^\star > P_{\text{tx}}$), the constraint set should be loosen until feasibility is ensured (i.e., $\bar{P}_{\text{tx}}^\star \leq P_{\text{tx}}$). However, this analysis is beyond the scope of this chapter.

Finally, to find a suitable solution of $\boldsymbol{W}$ and $\{\boldsymbol{Q}_i\}$, both procedures are alternated until convergence is reached, e.g., until the increase in (weighted) sum rate is below a certain threshold (cf. (7.34)). This is summarized in Algorithm 7.2, where the constraint set is represented by $\mathcal{S}$.

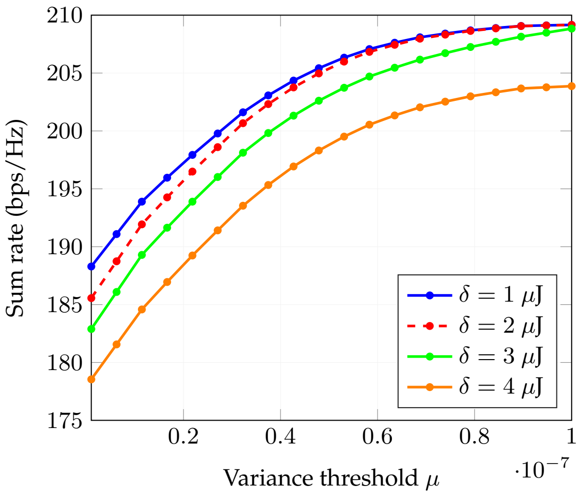

Figure 7.5: Sum rate of HD UTs versus the variance threshold μ for case (i).

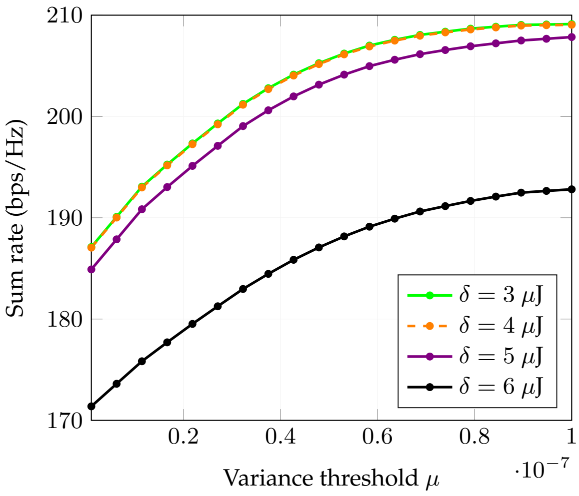

Figure 7.6: Sum rate of HD UTs versus the variance threshold μ for case (ii).

7.5 Numerical Simulations

We have conducted extensive simulations to evaluate the performance of our approach. We present the results in this section, where we consider the micro-urban scenario in [90] with $K = 10$, $D = 10$, $r_k = r = 40$ m, $d_{\min} = 1$ m, $T_f = 1$ s, $T_u = 0.5$ s, $N = 10$, $P_{\text{tx}} = 40$ dBm, $P_\kappa = 10$ dBm, $P_z = 24$ dBm, $\sigma_\chi^2 = \sigma_\gamma^2 = \sigma_\xi^2 = 1$, $\alpha = 2$, and $p_{\text{act}} = 0.1$. The steering vectors $\boldsymbol{v}(\cdot)$ are computed for a UCA [89] with $L = 20$ antennas. We also assume that clusters have densities λ_k regularly taken within the intervals (i) $[0.005, 0.05]$ m^{-2} and (ii) $[0.025, 0.1]$ m^{-2}. Besides, the stopping threshold ϵ is set to 10^{-6} and, without loss of generality, all weights ν_i and all energy conversion efficiencies ζ_k are considered to be 1.

In order to assess the results obtained with the transmission strategies, we show the total throughput of the UTs for the cases (i) and (ii). Both cases are depicted w.r.t. the threshold μ and for different values of δ in Figure 7.5 and 7.6 for the HD configuration, respectively, and in Figure 7.7 and 7.8 for the FD configuration, respectively.

Recall that these thresholds, δ and μ, constrain the mean $\bar{E}_k$ and variance $\bar{V}_k$ of the received energy, which in turn reveal the ability of the system to provide enough energy to avoid drained batteries. That is why in this chapter, to model this behavior and ensure proper distribution of energy, we have incorporated these statistical moments in the constraint set.

As illustrated in all figures, there is a trade-off between the UTs' data rates and the sensors' received energies. The demand for less depleted batteries, which translates into high values of δ and small values of μ, entails a smaller throughput. Contrarily, the system provides higher data rates when a larger number of drained batteries can be tolerated and these constraints can be relaxed, i.e., whenever δ decreases and/or μ increases. Finding the optimal balance between rate and energy distribution is a challenging task and will be considered in future works.

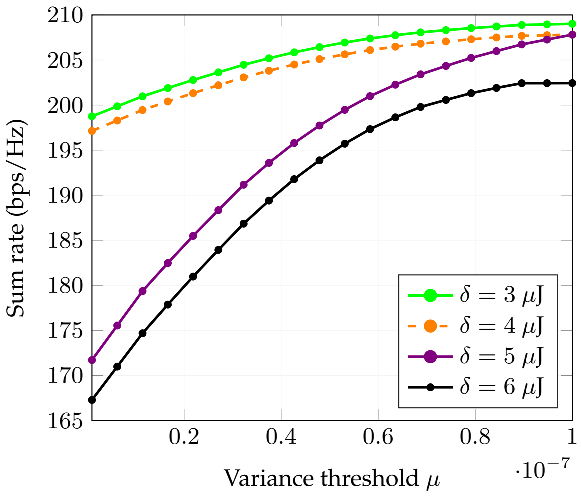

Figure 7.7: Sum rate of FD UTs versus the variance threshold μ for case (i).

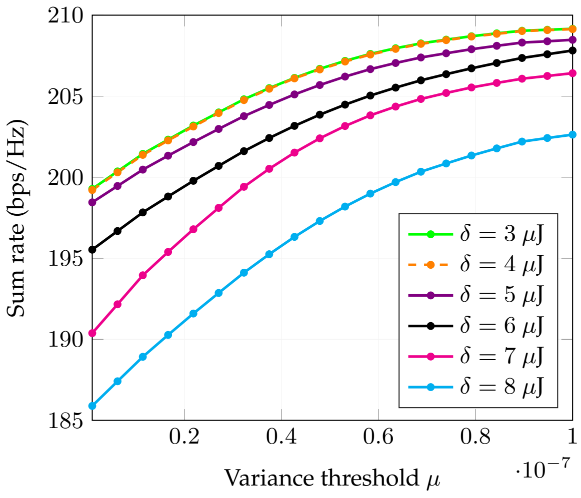

Figure 7.8: Sum rate of FD UTs versus the variance threshold μ for case (ii).

It can be easily seen that the data rate increases with the threshold μ since we allow a larger dispersion in the received energy. On the other hand, when imposing a higher δ, the system reduces the UTs' data rates to meet the harder energy requirements. As an example, in Figure 7.5 (HD), for $\mu = 1 \cdot 10^{-9}$ J^2, the sum rate decreases from 185.6 bps/Hz to 178.5 bps/Hz for $\delta = 2\ \mu$J and $\delta = 4\ \mu$J, respectively. The same reasoning holds for Figure 7.7 (FD), where the sum rate decreases from 197.1 bps/Hz to 167.3 bps/Hz for $\delta = 4\ \mu$J and $\delta = 6\ \mu$J, respectively.

Note that the FD case yields better performance than the HD configuration. This is not surprising as sensors are able to harvest more energy from the environment (i.e., from the CN in the UL and from the UTs in the DL). For instance, in Figure 7.5 and 7.7, the sum rate increases from 178.5 bps/Hz to 197.1 bps/Hz for $\mu = 1 \cdot 10^{-9}$ J^2 and $\delta = 4\ \mu$J. Actually, in both cases, (i) and (ii), the FD setup allows feasible solutions with larger values of δ (up to 8 μJ).

Finally, it is important to highlight that, in case (ii), a larger throughput is obtained for the same values of δ. For $\delta = 4\ \mu$J and $\mu = 1 \cdot 10^{-9}$ J^2, the rate increases from 178.5 bps/Hz in Figure 7.5 to 187 bps/Hz in Figure 7.6 (HD). Note that the same behavior can be observed in the FD configuration. This is because in case (ii) the density of sensors is higher and more energy can be harvested from their transmitted signals.

As a result, the energy constraints in (ii) can be satisfied more easily and the CN can dedicate more resources to the UTs. In fact, in comparison with case (i), the threshold δ can be increased up to 6 μJ (HD) and 8 μJ (FD) with similar performance. Therefore, harvesting energy from other transmitted signals in the environment, especially those coming from other sensors, can help the transmission strategy.

7.6 Summary and Conclusions

In this chapter, we have addressed the problem of designing transmission strategies that meet the requirements of both mMTC and HTC: large battery lifetimes and high data rates, respectively. Considering a cellular network where sensors coexist with UTs (HD or FD), all of them served by a multiple-antenna CN, we have presented the statistics of the energy collected by the sensors and the UTs' data rate. EH has been employed to recycle energy from other devices (i.e., to collect energy from the active sensors and UTs), whereas SWIPT and WPT have been used to transfer energy from the CN to the mMTC terminals. Accordingly, SWIPT and dedicated (separate) signals are used to transmit information to the HTC devices.

All processes have been modeled through repulsive MCPs and Bernoulli RVs, which represent the random positions and the sporadic activity of the sensors, respectively. In order to mitigate the DL interference of the UTs, we have also considered the use of BD techniques. Based on that, we have derived a set of transmission strategies that maximize the HTC weighted sum rate while ensuring a sufficient amount of energy is received at the sensors' side. The proposed strategies have been mathematically formulated as non-convex optimization problems and a local optimum has been found with the help of DCP and SDP.

Simulation results have shown that there is a trade-off between the sum rate and received energies. Higher and non-dispersed collected powers compromise the data transmission. As in Chapter 6, larger concentrations of sensors can improve the total DL throughput of the UTs.

Part IV

Conclusions

Chapter 8

Conclusions

This dissertation has focused on the design of energy-driven techniques for mMTC networks. Special emphasis has been put on the reduction of power consumption in the UL and the wireless supply of energy in the DL. Additionally, given the large number of active devices in the UL, several interference management approaches have been proposed to ensure reliable communication. On the other hand, in order to enable more sustainable WPNs, different transmission schemes have been also derived in the DL. Both setups have been formulated taking into account practical implementation aspects and standard recommendations.

In the following, we summarize the main conclusions of each chapter.

In **Chapter 1**, we have presented the general motivation and main outline of this thesis, as well as the different relationships between the constituting parts. Accordingly, the list of research contributions and corresponding publications has been shortly described.

In **Chapter 2**, we have introduced the system overview upon which the whole dissertation is built. In particular, the types of traffic models that encompass data transmission (event-driven or regular) and network communication (continuous or packet-based), have been discussed. In line with that, the different MA schemes used throughout this thesis, both orthogonal and non-orthogonal, have been also reviewed. Finally, a brief summary of the stochastic geometry tools and processes (CPPs and HCPPs) employed to characterize the spatial distribution of the sensors has been developed.

In **Chapter 3**, we have addressed the problem of modeling the aggregate interference statistics by means of Gram-Charlier series expansions of truncated Gaussian kernels. This has allowed us to derive an analytic closed-form expression for the outage probability, which has been later minimized through a graph-based RA approach that uses coloring techniques. In addition, we have presented a MAC protocol relying on spatial beamforming to overcome the collisions that arise in dedicated scheduling mechanisms. Numerical simulations have shown that our proposal provides an accurate approximation of the interference distribution and that our RA method reduces the outage probability within the system.

In **Chapter 4**, we have addressed the problem of inferring the measured parameters from two different points of view: source data entropy and parameter estimation error. In the first scenario, we have designed a device selection strategy minimizing the loss of information to be transmitted through a noiseless channel when the correlation in the information is modeled through degenerate Gaussian distributions. Due to the discrete nature of the problem, convex relaxations and approximations have been used to find a sub-optimal and feasible solution.

In the parameter estimation error setup, we have derived a strategy based on the MMSE estimate and Kalman filters that take into consideration the possible communication errors and temporal correlation. For that task, we have averaged the MSE over the different PERs and proposed a device selection scheme and quantization approach that minimize the resulting MSE. Numerical simulations have shown that most of the (relevant) information can be retrieved with a smaller number of active devices. Therefore, the power consumption and data traffic within the network can be significantly reduced with still good performance.

In **Chapter 5**, we have introduced the use of RIS to assess the communication of the sensors in the UL when they transmit on a NOMA basis. Taking into account communication and I-CSI errors, we have presented an estimation scheme also based on the MMSE criterion. In that sense, we have studied different approaches for acquiring channel knowledge. Finally, incorporating SIC as a decoding procedure, the RIS is designed to minimize the parameter estimation error while considering the temporal variations of the channel. Numerical simulations have shown that a smaller MSE can be obtained with large reflective surfaces and that choosing a suitable decoding order is essential for proper accuracy.

In **Chapter 6**, we have addressed the problem of wireless powering a mMTC network when considering WPT and EH as feasible options to improve the battery lifetime of the sensors. The positions of the devices have been modeled with repulsive MCPs and, as in Chapter 3, their sporadic activity has been included through Bernoulli RVs. Based on that, we have characterized the collected energy from both processes, WPT and EH, and designed an energy allocation scheme with proportional fairness. Numerical simulations have shown that, over time, most mMTC devices can recharge their batteries with a fairer amount of power.

In **Chapter 7**, we have addressed the problem of designing transmission strategies that meet the requirements of both mMTC and HTC: large battery lifetimes and high data rates, respectively. Following the modeling from Chapter 6, we have derived the first and second-order statistics of the energy collected from EH, WPT, and SWIPT. With the help of BD processing, we have presented several transmission strategies that maximize the sum rate of the coexisting UTs while ensuring sensors receive a sufficient amount of energy. To find a local optimum of the resulting non-convex problems, we have used DCP and SDP techniques. Numerical simulations have shown that there is a trade-off between the sum rate and received energies, concluding that higher and non-dispersed collected powers compromise the data transmission.

Chapter 9

Future Work

Many research lines could be considered to extend the results presented in this dissertation. In the following, we provide some ideas that could contribute to the state of the art of mMTC networks and that, to the best of our knowledge, have not been conducted yet.

In **Chapter 3**, the spatial distribution of the sensors and the lack of perfect CSI could also be included to better characterize the uncertainties within the system. For a broader vision, the approximations of the interference statistics could be applied to other metrics (e.g., throughput and coverage). Apart from that, instead of minimizing the average outage probability, we could focus on other problems such as the minimax optimization.

In **Chapter 4**, the presence of communication errors and measurement noise could be introduced in the entropy analysis to better describe a more realistic scenario. Additionally, the case of temporal correlation could be derived to further reduce the payload.

On the other hand, in the estimation approach, the study of non-uniform scalar quantizers could be useful to improve the distribution of quantization bits. In addition, for a more faithful representation of practical deployments, MA channels with non-orthogonal resources could be investigated. Moreover, vector quantization techniques could be employed in two scenarios: i) setups where each sensor measures multiple phenomena simultaneously, and ii) multi-hop networks where the CN quantizes the decoded messages before retransmission.

In **Chapter 5**, apart from the randomness coming from the estimation and communication errors, we could also consider the sporadic activity of the devices (i.e., *NOMA, sporadic* transmission). Regarding the accuracy of the channel estimation, machine learning techniques could be incorporated. Besides, to further improve the quality of the channel and increase the degrees of freedom, the CN could be equipped with multiple antennas. In line with that, another possibility could be to optimize the location of the RIS (cf. [198]).

In **Chapter 6**, the analysis of other stochastic geometry models for the position of the mMTC terminals could be useful. It would allow the extension to other types of network topologies. Additionally, considering the limiting effects of non-linear harvesting could help in the design of more appropriate and realistic strategies.

In **Chapter 7**, the analysis of the percentage of depleted batteries of the sensors w.r.t. the throughput of the UTs could be addressed. This would provide better insights into the impact that the presented power supply mechanisms have on WPN. Besides, we could also include multiple CNs to enhance the transfer of data and energy.

Finally, there are some other future and promising directions that affect the general overview of this thesis. First, it would be interesting to compare the performance of the proposed methods in terms of power consumption. Second, the combination of all these energy-driven techniques could potentially lead to more sustainable mMTC networks. Third, given its relevance in many applications, the impact on the energy efficiency within the system could be reviewed. Accordingly, novel solutions could also be formulated to optimize this new metric. Like before, few or even no similar studies have been reported in the current state of the literature so far.

Bibliography

[1] *Ericsson mobility report*, Ericsson, Document EAB-21:005137, Jun. 2021. [Online]. Available: https://www.ericsson.com/en/reports-and-papers/mobility-report/reports/june-2021

[2] F. Boccardi *et al.*, "Five disruptive technology directions for 5G," *IEEE Commun. Mag.*, vol. 52, no. 2, pp. 74–80, Feb. 2014.

[3] J. G. Andrews *et al.*, "What will 5G be?" *IEEE J. S. Areas Commun.*, vol. 32, no. 6, pp. 1065–1082, Jun. 2014.

[4] *IMT Vision – Framework and overall objectives of the future development of IMT for 2020 and beyond*, Radiocommunication Sector of International Telecommunication Union, Recommendation ITU-R M.2083-0, Sep. 2015. [Online]. Available: https://www.itu.int/rec/R-REC-M.2083-0-201509-I/en

[5] J. Navarro-Ortiz *et al.*, "A survey on 5G usage scenarios and traffic models," *IEEE Commun. Surveys Tuts.*, vol. 22, no. 2, pp. 905–929, 2nd Quart., 2020.

[6] A. Ghosh, A. Maeder, M. Baker, and D. Chandramouli, "5G evolution: A view on 5G cellular technology beyond 3GPP release 15," *IEEE Access*, vol. 7, pp. 127 639–127 651, Sep. 2019.

[7] M. Shafi *et al.*, "5G: A tutorial overview of standards, trials, challenges, deployment, and practice," *IEEE J. Sel. Areas Commun.*, vol. 35, no. 6, pp. 1201–1221, Jun. 2017.

[8] *Study on scenarios and requirements for next generation access technologies*, 3rd Generation Partnership Project, Document 3GPP TR 38.913 v16.0.0, Jul. 2020. [Online]. Available: https://portal.3gpp.org/desktopmodules/Specifications/SpecificationDetails.aspx?specificationId=2996

[9] *5G wireless access: An overview*, Ericsson, White Paper 1/28423-FGB1010937, Apr. 2020. [Online]. Available: https://www.ericsson.com/en/reports-and-papers/white-papers/5g-wireless-access-an-overview

[10] M. R. Palattella *et al.*, "Internet of things in the 5G era: Enablers, architecture, and business models," *IEEE J. Sel. Areas Commun.*, vol. 34, no. 3, pp. 510–527, Mar. 2016.

[11] M. Elsaadany, A. Ali, and W. Hamouda, "Cellular LTE-A technologies for the future internet-of-things: Physical layer features and challenges," *IEEE Commun. Surveys Tuts.*, vol. 19, no. 4, pp. 2544–2572, 4th Quart., 2017.

[12] C. Bockelmann *et al.*, "Massive machine-type communications in 5G: Physical and MAC-layer solutions," *IEEE Commun. Mag.*, vol. 54, no. 9, pp. 59–65, Sep. 2016.

[13] S. Chen *et al.*, “Machine-to-machine communications in ultra-dense networks—A survey,” *IEEE Commun. Surveys Tuts.*, vol. 19, no. 3, pp. 1478–1503, 3rd Quart., 2017.

[14] U. Raza, P. Kulkarni, and M. Sooriyabandara, “Low power wide area networks: An overview,” *IEEE Commun. Surveys Tuts.*, vol. 19, no. 2, pp. 855–873, 2nd Quart., 2017.

[15] G. A. Akpakwu, B. J. Silva, G. P. Hancke, and A. M. Abu-Mahfouz, “A survey on 5G networks for the internet of things: Communication technologies and challenges,” *IEEE Access*, vol. 6, pp. 3619–3647, Feb. 2018.

[16] M. Agiwal, A. Roy, and N. Saxena, “Next generation 5G wireless networks: A comprehensive survey,” *IEEE Commun. Surveys Tuts.*, vol. 18, no. 3, pp. 1617–1655, 3rd Quart., 2016.

[17] *Detailed specifications of the terrestrial radio interfaces of international mobile telecommunications-2020 (IMT-2020)*, Radiocommunication Sector of International Telecommunication Union, Recommendation ITU-R M.2150-0, Feb. 2021. [Online]. Available: https://www.itu.int/rec/R-REC-M.2150-0-202102-I/en

[18] A. Laya, L. Alonso, and J. Alonso-Zarate, “Is the random access channel of LTE and LTE-A suitable for M2M communications? A survey of alternatives,” *IEEE Commun. Surveys Tuts.*, vol. 16, no. 1, pp. 4–16, 1st Quart., 2014.

[19] *NR; Physical layer procedures for control*, 3rd Generation Partnership Project, Document 3GPP TS 38.213 v16.7.0, Sep. 2021. [Online]. Available: https://portal.3gpp.org/desktopmodules/Specifications/SpecificationDetails.aspx?specificationId=3215

[20] *Study on new radio (NR) access technology*, 3rd Generation Partnership Project, Document 3GPP TR 38.912 v16.0.0, Jul. 2020. [Online]. Available: https://portal.3gpp.org/desktopmodules/Specifications/SpecificationDetails.aspx?specificationId=3059

[21] C. Bockelmann *et al.*, “Towards massive connectivity support for scalable mMTC communications in 5G networks,” *IEEE Access*, vol. 6, pp. 28 969–28 992, Jun. 2018.

[22] *Cellular system support for ultra low complexity and low throughput internet of things (CIoT)*, 3rd Generation Partnership Project, Document 3GPP TR 45.820 v13.1.0, Dec. 2015. [Online]. Available: https://portal.3gpp.org/desktopmodules/Specifications/SpecificationDetails.aspx?specificationId=2719

[23] T. N. Weerasinghe, V. Casares-Giner, I. A. M. Balapuwaduge, and F. Y. Li, “Priority enabled grant-free access with dynamic slot allocation for heterogeneous mMTC traffic in 5G NR networks,” *IEEE Trans. Commun.*, vol. 69, no. 5, pp. 3192–3206, May 2021.

[24] R. Jurdi *et al.*, “Outage of periodic downlink wireless networks with hard deadlines,” *IEEE Trans. Commun.*, vol. 67, no. 2, pp. 1238–1253, Feb. 2019.

[25] R. K. Shakya, Y. N. Singh, and N. K. Verma, “Generic correlation model for wireless sensor network applications,” *IET Wireless Sensor Syst.*, vol. 3, no. 4, pp. 266–276, Dec. 2013.

[26] H. ElSawy, E. Hossain, and M. Haenggi, “Stochastic geometry for modeling, analysis, and design of multi-tier and cognitive cellular wireless networks: A survey,” *IEEE Commun. Surveys Tuts.*, vol. 15, no. 3, pp. 996–1019, 3rd Quart., 2013.

[27] Y. Hmamouche *et al.*, "New trends in stochastic geometry for wireless networks: A tutorial and survey," *Proc. IEEE*, vol. 109, no. 7, pp. 1200–1252, Jul. 2021.

[28] Z. Dawy *et al.*, "Toward massive machine type cellular communications," *IEEE Wireless Commun.*, vol. 24, no. 1, pp. 120–128, Feb. 2017.

[29] H. Wang and A. O. Fapojuwo, "A survey of enabling technologies of low power and long range machine-to-machine communications," *IEEE Commun. Surveys Tuts.*, vol. 19, no. 4, pp. 2621–2639, 4th Quart., 2017.

[30] W. Yang *et al.*, "Narrowband wireless access for low-power massive internet of things: A bandwidth perspective," *IEEE Wireless Commun.*, vol. 24, no. 3, pp. 138–145, Jun. 2017.

[31] J. Xu *et al.*, "Narrowband internet of things: Evolutions, technologies, and open issues," *IEEE Internet Things J.*, vol. 5, no. 3, pp. 1449–1462, Jun. 2018.

[32] V. Gazis, "A survey of standards for machine-to-machine and the internet of things," *IEEE Commun. Surveys Tuts.*, vol. 19, no. 1, pp. 482–511, 1st Quart., 2017.

[33] M. B. Shahab, R. Abbas, M. Shirvanimoghaddam, and S. J. Johnson, "Grant-free non-orthogonal multiple access for IoT: A survey," *IEEE Commun. Surveys Tuts.*, vol. 22, no. 3, pp. 1805–1838, 3rd Quart., 2020.

[34] T. Cover and J. Thomas, *Elements of Information Theory*. John Wiley & Sons, 2006.

[35] *NR; Physical layer procedures for data*, 3rd Generation Partnership Project, Document 3GPP TS 38.214 v16.7.0, Sep. 2021. [Online]. Available: https://portal.3gpp.org/desktopmodules/Specifications/SpecificationDetails.aspx?specificationId=3216

[36] D. Tse and P. Viswanath, *Fundamentals of Wireless Communication*. Cambridge University Press, 2005.

[37] J. Proakis and M. Salehi, *Digital Communications*. McGraw-Hill, 2008.

[38] Y. Cai *et al.*, "Modulation and multiple access for 5G networks," *IEEE Commun. Surveys Tuts.*, vol. 20, no. 1, pp. 629–646, 1st Quart., 2018.

[39] Y. Polyanskiy, H. V. Poor, and S. Verdu, "Channel coding rate in the finite blocklength regime," *IEEE Trans. Inf. Theory*, vol. 56, no. 5, pp. 2307–2359, May 2010.

[40] *LTE evolution for IoT connectivity*, Nokia, White Paper SR1702006775EN, Dec. 2016. [Online]. Available: https://onestore.nokia.com/asset/200178

[41] Y. Liu *et al.*, "Nonorthogonal multiple access for 5G and beyond," *Proc. IEEE*, vol. 105, no. 12, pp. 2347–2381, Dec. 2017.

[42] K. Yang *et al.*, "Non-orthogonal multiple access: Achieving sustainable future radio access," *IEEE Commun. Mag.*, vol. 57, no. 2, pp. 116–121, Feb. 2019.

[43] M. Elbayoumi, M. Kamel, W. Hamouda, and A. Youssef, "NOMA-assisted machine-type communications in UDN: State-of-the-art and challenges," *IEEE Commun. Surveys Tuts.*, vol. 22, no. 2, pp. 1276–1304, 2nd Quart., 2020.

[44] S. Verdú, *Multiuser Detection*. Cambridge University Press, 1998.

[45] L. Dai *et al.*, "A survey of non-orthogonal multiple access for 5G," *IEEE Commun. Surveys Tuts.*, vol. 20, no. 3, pp. 2294–2323, 3rd Quart., 2018.

[46] Z. Ding, R. Schober, and H. V. Poor, "Unveiling the importance of SIC in NOMA systems—part 1: State of the art and recent findings," *IEEE Commun. Lett.*, vol. 24, no. 11, pp. 2373–2377, Nov. 2020.

[47] C. Namislo, "Analysis of mobile radio slotted ALOHA networks," *IEEE J. Sel. Areas Commun.*, vol. 2, no. 4, pp. 583–588, Jul. 1984.

[48] M. Schwartz and N. Abramson, "The ALOHAnet - Surfing for wireless data," *IEEE Commun. Mag.*, vol. 47, no. 12, pp. 21–25, Dec. 2009.

[49] H. ElSawy, A. Sultan-Salem, M.-S. Alouini, and M. Z. Win, "Modeling and analysis of cellular networks using stochastic geometry: A tutorial," *IEEE Commun. Surveys Tuts.*, vol. 19, no. 1, pp. 167–203, 1st Quart., 2017.

[50] J.-S. Leu, T.-H. Chiang, M.-C. Yu, and K.-W. Su, "Energy efficient clustering scheme for prolonging the lifetime of wireless sensor network with isolated nodes," *IEEE Commun. Lett.*, vol. 19, no. 2, pp. 259–262, Feb. 2015.

[51] Y. J. Chun, M. O. Hasna, and A. Ghrayeb, "Modeling heterogeneous cellular networks interference using Poisson cluster processes," *IEEE J. Sel. Areas Commun.*, vol. 33, no. 10, pp. 2182–2195, Oct. 2015.

[52] S. N. Chiu, D. Stoyan, W. S. Kendall, and J. Mecke, *Stochastic Geometry and its Applications*. John Wiley & Sons, 2013.

[53] J. G. Andrews, A. K. Gupta, and H. S. Dhillon, "A primer on cellular network analysis using stochastic geometry," *arXiv preprint*, arXiv:1604.03183, Oct. 2016. [Online]. Available: https://arxiv.org/abs/1604.03183

[54] F. Baccelli and B. Błaszczyszyn, *Stochastic Geometry and Wireless Networks*. Now Publishers, 2009.

[55] M. Haenggi, *Stochastic Geometry for Wireless Networks*. Cambridge University Press, 2012.

[56] A. Rabbachin, T. Q. Quek, H. Shin, and M. Z. Win, "Cognitive network interference," *IEEE J. Sel. Areas Commun.*, vol. 29, no. 2, pp. 480–493, Feb. 2011.

[57] S. Kusaladharma and C. Tellambura, "Aggregate interference analysis for underlay cognitive radio networks," *IEEE Wireless Commun. Lett.*, vol. 1, no. 6, pp. 641–644, Dec. 2012.

[58] G. C. Alexandropoulos, P. Ferrand, J.-M. Gorce, and C. B. Papadias, "Advanced coordinated beamforming for the downlink of future LTE cellular networks," *IEEE Commun. Mag.*, vol. 54, no. 7, pp. 54–60, Jul. 2016.

[59] R. W. Heath Jr, T. Wu, Y. H. Kwon, and A. C. K. Soong, "Multiuser MIMO in distributed antenna systems with out-of-cell interference," *IEEE Trans. Signal Process.*, vol. 59, no. 10, pp. 4885–4899, Oct. 2011.

[60] P. Cardieri, "Modeling interference in wireless ad hoc networks," *IEEE Commun. Surveys Tuts.*, vol. 12, no. 4, pp. 551–572, 4th Quart., 2010.

[61] M. Haenggi *et al.*, "Stochastic geometry and random graphs for the analysis and design of wireless networks," *IEEE J. Sel. Areas Commun.*, vol. 27, no. 7, pp. 1029–1046, Sep. 2009.

[62] J. G. Andrews *et al.*, "A primer on spatial modeling and analysis in wireless networks," *IEEE Commun. Mag.*, vol. 48, no. 11, pp. 156–163, Nov. 2010.

[63] T. Kwon and J. M. Cioffi, "Random deployment of data collectors for serving randomly-located sensors," *IEEE Trans. Wireless Commun.*, vol. 12, no. 6, pp. 2556–2565, Jun. 2013.

[64] K. Senel and E. G. Larsson, "Grant-free massive MTC-enabled massive MIMO: A compressive sensing approach," *IEEE Trans. Commun.*, vol. 66, no. 12, pp. 6164–6175, Dec. 2018.

[65] P. Kela *et al.*, "Connectionless access for massive machine type communications in ultra-dense networks," in *2017 IEEE Int. Conf. Commun. (ICC)*, May 2017, pp. 1–6.

[66] C.-Y. Oh, D. Hwang, and T.-J. Lee, "Joint access control and resource allocation for concurrent and massive access of M2M devices," *IEEE Trans. Wireless Commun.*, vol. 14, no. 8, pp. 4182–4192, Aug. 2015.

[67] P. Si, J. Yang, S. Chen, and H. Xi, "Adaptive massive access management for QoS guarantees in M2M communications," *IEEE Trans. Veh. Technol.*, vol. 64, no. 7, pp. 3152–3166, Jul. 2015.

[68] S. Lagen *et al.*, "Long-term provisioning of radio resources based on their utilization in dense OFDMA networks," in *2016 IEEE 27th Ann. Int. Symp. Pers. Indoor Mob. Radio Commun. (PIMRC)*, Sep. 2016, pp. 1–7.

[69] T. Salam, W. U. Rehman, and X. Tao, "Cooperative data aggregation and dynamic resource allocation for massive machine type communication," *IEEE Access*, vol. 6, pp. 4145–4158, Jan. 2018.

[70] O. L. Alcaraz López, H. Alves, P. H. Juliano Nardelli, and M. Latva-Aho, "Aggregation and resource scheduling in machine-type communication networks: A stochastic geometry approach," *IEEE Trans. Wireless Commun.*, vol. 17, no. 7, pp. 4750–4765, Jul. 2018.

[71] J. Guo, S. Durrani, X. Zhou, and H. Yanikomeroglu, "Massive machine type communication with data aggregation and resource scheduling," *IEEE Trans. Commun.*, vol. 65, no. 9, pp. 4012–4026, Sep. 2017.

[72] N. Xia, H.-H. Chen, and C.-S. Yang, "Radio resource management in machine-to-machine communications—A survey," *IEEE Commun. Surveys Tuts.*, vol. 20, no. 1, pp. 791–828, Oct. 2018.

[73] S. Liesegang, O. Muñoz, and A. Pascual-Iserte, "Interference statistics approximations for data rate analysis in uplink massive MTC," in *2018 IEEE Glob. Conf. Signal Inf. Process. (GlobalSIP)*, Nov. 2018, pp. 176–180.

[74] P. Raghavan, "Probabilistic construction of deterministic algorithms: Approximating packing integer programs," *J. Comput. Syst. Sci.*, vol. 37, no. 2, pp. 130–143, Oct. 1988.

[75] A. Papoulis and S. U. Pillai, *Probability, Random Variables, and Stochastic Processes*. McGraw-Hill, 2002.

[76] T. Brenn and S. N. Anfinsen, “A revisit of the Gram-Charlier and Edgeworth Series expansions,” *Department of Physics and Technology, UiT The Arctic University of Norway*, Jul. 2017. [Online]. Available: https://munin.uit.no/bitstream/handle/10037/11261/article.pdf?sequence=1&isAllowed=y

[77] L. Comtet, *Advanced Combinatorics: The Art of Finite and Infinite Expansions*. Springer Science & Business Media, 2012.

[78] P. J. Smith, “A recursive formulation of the old problem of obtaining moments from cumulants and vice versa,” *Am. Stat.*, vol. 49, no. 2, pp. 217–218, May 1995.

[79] K. Knight, *Mathematical Statistics*. CRC Press, 1999.

[80] J. Burkardt, “The truncated normal distribution,” *Department of Scientific Computing Website, Florida State University*, Oct. 2014. [Online]. Available: https://people.sc.fsu.edu/~jburkardt/presentations/truncated_normal.pdf

[81] K. Zheng *et al.*, “Radio resource allocation in LTE-advanced cellular networks with M2M communications,” *IEEE Commun. Mag.*, vol. 50, no. 7, pp. 184–192, Jul. 2012.

[82] F. Ghavimi and H.-H. Chen, “M2M communications in 3GPP LTE/LTE-A networks: Architectures, service requirements, challenges, and applications,” *IEEE Commun. Surveys Tuts.*, vol. 17, no. 2, pp. 525–549, 2nd Quart., 2015.

[83] D. B. Owen, “A table of normal integrals,” *Commun. Stat. Simul. Comput.*, vol. 9, no. 4, pp. 389–419, Jan. 1980.

[84] R. Balakrishnan and K. Ranganathan, *A Textbook of Graph Theory*. Springer Science & Business Media, 2012.

[85] L. Cowen, W. Goddard, and C. E. Jesurum, “Defective coloring revisited,” *J. Graph Theory*, vol. 24, no. 3, pp. 205–219, Mar. 1997.

[86] M. Grötschel, L. Lovász, and A. Schrijver, *Geometric Algorithms and Combinatorial Optimization*. Springer Science & Business Media, 2012.

[87] S.-Y. Lien, K.-C. Chen, and Y. Lin, “Toward ubiquitous massive accesses in 3GPP machine-to-machine communications,” *IEEE Commun. Mag.*, vol. 49, no. 4, pp. 66–74, Apr. 2011.

[88] A. Ghosh and R. Ratasuk, *Essentials of LTE and LTE-A*. Cambridge University Press, 2011.

[89] H. L. Van Trees, *Optimum Array Processing: Part IV of Detection, Estimation, and Modulation Theory*. John Wiley & Sons, 2004.

[90] *Guidelines for evaluation of radio interface technologies for IMT-Advanced*, Radiocommunication Sector of International Telecommunication Union, Report ITU-R M.2135-1, Dec. 2009. [Online]. Available: https://www.itu.int/pub/R-REP-M.2135-1-2009

[91] J. Lin, “Divergence measures based on the Shannon entropy,” *IEEE Trans. Inf. Theory*, vol. 37, no. 1, pp. 145–151, Jan. 1991.

[92] Y. Zhu, E. Song, J. Zhou, and Z. You, “Optimal dimensionality reduction of sensor data in multisensor estimation fusion,” *IEEE Trans. Signal Process.*, vol. 53, no. 5, pp. 1631–1639, May 2005.

[93] J. Li and G. AlRegib, "Distributed estimation in energy-constrained wireless sensor networks," *IEEE Trans. Signal Process.*, vol. 57, no. 10, pp. 3746–3758, Oct. 2009.

[94] S. Talarico, N. A. Schmid, M. Alkhweldi, and M. C. Valenti, "Distributed estimation of a parametric field: Algorithms and performance analysis," *IEEE Trans. Signal Process.*, vol. 62, no. 5, pp. 1041–1053, Mar. 2014.

[95] S. M. Kay, *Fundamentals of Statistical Signal Processing: Estimation Theory*. Prentice-Hall, Inc., 1993.

[96] J. Fang and H. Li, "Optimal/near-optimal dimensionality reduction for distributed estimation in homogeneous and certain inhomogeneous scenarios," *IEEE Trans. Signal Process.*, vol. 58, no. 8, pp. 4339–4353, Aug. 2010.

[97] L. Zhang *et al.*, "Joint optimization of dimension assignment and compression in distributed estimation fusion," *IEEE Trans. Signal Process.*, vol. 67, no. 9, pp. 2453–2468, May 2019.

[98] H. Rowaihy *et al.*, "A survey of sensor selection schemes in wireless sensor networks," *Proc. SPIE*, vol. 6562, pp. 1–13, May 2007.

[99] S. Joshi and S. Boyd, "Sensor selection via convex optimization," *IEEE Trans. Signal Process.*, vol. 57, no. 2, pp. 451–462, Feb. 2009.

[100] S. P. Chepuri and G. Leus, "Sparsity-promoting sensor selection for non-linear measurement models," *IEEE Trans. Signal Process.*, vol. 63, no. 3, pp. 684–698, Feb. 2015.

[101] A. Scaglione and S. Servetto, "On the interdependence of routing and data compression in multi-hop sensor networks," *Wireless Netw.*, vol. 11, no. 1, pp. 149–160, Jan. 2005.

[102] A. Dabirmoghaddam, M. Ghaderi, and C. Williamson, "Cluster-based correlated data gathering in wireless sensor networks," in *2010 IEEE Int. Symp. Model. Anal. Simul. Comput. Telecommun. Syst. (MASCOTS)*, Aug. 2010, pp. 163–171.

[103] C. Studer and G. Durisi, "Quantized massive MU-MIMO-OFDM uplink," *IEEE Trans. Commun.*, vol. 64, no. 6, pp. 2387–2399, Jun. 2016.

[104] P. L. Dragotti and M. Gastpar, *Distributed Source Coding: Theory, Algorithms and Applications*. Academic Press/Elsevier, 2009.

[105] M. C. Vuran, Ö. B. Akan, and I. F. Akyildiz, "Spatio-temporal correlation: Theory and applications for wireless sensor networks," *Comput. Netw.*, vol. 45, no. 3, pp. 245–259, Jan. 2004.

[106] E. J. Msechu, S. I. Roumeliotis, A. Ribeiro, and G. B. Giannakis, "Decentralized quantized Kalman filtering with scalable communication cost," *IEEE Trans. Signal Process.*, vol. 56, no. 8, pp. 3727–3741, Aug. 2008.

[107] Ó. Fresnedo, P. Suárez-Casal, and L. Castedo, "Transmission of spatio-temporal correlated sources over fading multiple access channels with DQLC mappings," *IEEE Trans. Commun.*, vol. 67, no. 8, pp. 5604–5617, Aug. 2019.

[108] J. Fang and H. Li, "Power constrained distributed estimation with cluster-based sensor collaboration," *IEEE Trans. Wireless Commun.*, vol. 8, no. 7, pp. 3822–3832, Jul. 2009.

[109] E. J. Msechu and G. B. Giannakis, “Sensor-centric data reduction for estimation with WSNs via censoring and quantization,” *IEEE Trans. Signal Process.*, vol. 60, no. 1, pp. 400–414, Jan. 2012.

[110] P. Giménez-Febrer, A. Pagès-Zamora, and G. B. Giannakis, “Matrix completion and extrapolation via kernel regression,” *IEEE Trans. Signal Process.*, vol. 67, no. 19, pp. 5004–5017, Oct. 2019.

[111] J.-J. Xiao, A. Ribeiro, Z.-Q. Luo, and G. Giannakis, “Distributed compression-estimation using wireless sensor networks,” *IEEE Signal Process. Mag.*, vol. 23, no. 4, pp. 27–41, Jul. 2006.

[112] J. Fang and H. Li, “Distributed adaptive quantization for wireless sensor networks: From delta modulation to maximum likelihood,” *IEEE Trans. Signal Process.*, vol. 56, no. 10, pp. 5246–5257, Oct. 2008.

[113] M. Nikolov and Z. J. Haas, “Encoded sensing for energy efficient wireless sensor networks,” *IEEE Sensors J.*, vol. 18, no. 2, pp. 875–889, Jan. 2018.

[114] J.-J. Xiao and Z.-Q. Luo, “Decentralized estimation in an inhomogeneous sensing environment,” *IEEE Trans. Inf. Theory*, vol. 51, no. 10, pp. 3564–3575, Oct. 2005.

[115] S. Khobahi, M. Soltanalian, F. Jiang, and A. L. Swindlehurst, “Optimized transmission for parameter estimation in wireless sensor networks,” *IEEE Trans. Signal Inf. Process. Netw.*, vol. 6, pp. 35–47, Oct. 2020.

[116] R. G. Gallager, *Principles of Digital Communication*. Cambridge University Press, 2008.

[117] O. Knill, “Cauchy-Binet for pseudo-determinants,” *Linear Algebra Appl.*, vol. 459, pp. 522–547, Oct. 2014.

[118] B. Widrow and I. Kollar, *Quantization Noise: Roundoff Error in Digital Computation, Signal Processing, Control, and Communications*. Cambridge University Press, 2008.

[119] K. B. Petersen and M. S. Pedersen, *The Matrix Cookbook*. Technical University of Denmark, 2012.

[120] F. J. Iglesias *et al.*, “Demixing and blind deconvolution of graph-diffused sparse signals,” in *2018 IEEE Int. Conf. Acoust. Speech Signal Process. (ICASSP)*, Apr. 2018, pp. 4189–4193.

[121] J. Tropp, “Just relax: Convex programming methods for identifying sparse signals in noise,” *IEEE Trans. Inf. Theory*, vol. 52, no. 3, pp. 1030–1051, Mar. 2006.

[122] S. P. Chepuri, G. Leus *et al.*, “Sparse sensing for statistical inference,” *Found. Trends Signal Process.*, vol. 9, no. 3-4, pp. 233–368, 2016.

[123] S. Boyd, S. P. Boyd, and L. Vandenberghe, *Convex Optimization*. Cambridge University Press, 2004.

[124] M. Grant and S. Boyd, “CVX: MATLAB software for disciplined convex programming, version 2.1,” http://cvxr.com/cvx, Mar. 2014.

[125] L. F. O. Chamon, G. J. Pappas, and A. Ribeiro, “Approximate supermodularity of Kalman filter sensor selection,” *IEEE Trans. Autom. Control*, vol. 66, no. 1, pp. 49–63, Jan. 2021.

[126] J. Fang and H. Li, "Joint dimension assignment and compression for distributed multisensor estimation," *IEEE Signal Process. Lett.*, vol. 15, pp. 174–177, Jan. 2008.

[127] X. Shen and P. K. Varshney, "Sensor selection based on generalized information gain for target tracking in large sensor networks," *IEEE Trans. Signal Process.*, vol. 62, no. 2, pp. 363–375, Jan. 2014.

[128] S. Das and J. M. F. Moura, "Distributed Kalman filtering with dynamic observations consensus," *IEEE Trans. Signal Process.*, vol. 63, no. 17, pp. 4458–4473, Sep. 2015.

[129] P. Bodik *et al.*, "Intel lab data," *Online dataset*, Mar. 2004. [Online]. Available: http://db.csail.mit.edu/labdata/labdata.html

[130] B.-Y. Wang and M.-P. Gong, "Some eigenvalue inequalities for positive semidefinite matrix power products," *Linear Algebra Appl.*, vol. 184, pp. 249–260, Apr. 1993.

[131] I. A. Hemadeh, K. Satyanarayana, M. El-Hajjar, and L. Hanzo, "Millimeter-wave communications: Physical channel models, design considerations, antenna constructions, and link-budget," *IEEE Commun. Surveys Tuts.*, vol. 20, no. 2, pp. 870–913, 2nd Quart., 2018.

[132] M. Polese, J. M. Jornet, T. Melodia, and M. Zorzi, "Toward end-to-end, full-stack 6G terahertz networks," *IEEE Commun. Mag.*, vol. 58, no. 11, pp. 48–54, Nov. 2020.

[133] M. Di Renzo *et al.*, "Smart radio environments empowered by reconfigurable intelligent surfaces: How it works, state of research, and the road ahead," *IEEE J. Sel. Areas Commun.*, vol. 38, no. 11, pp. 2450–2525, Nov. 2020.

[134] P. Wang, J. Fang, L. Dai, and H. Li, "Joint transceiver and large intelligent surface design for massive MIMO mmWave systems," *IEEE Trans. Wireless Commun.*, vol. 20, no. 2, pp. 1052–1064, Feb. 2021.

[135] N. Rajatheva *et al.*, "Scoring the terabit/s goal: Broadband connectivity in 6G," *arXiv preprint*, arXiv:2008.07220, Feb. 2021. [Online]. Available: https://arxiv.org/abs/2008.07220

[136] X. Wei, D. Shen, and L. Dai, "Channel estimation for RIS assisted wireless communications—Part I: Fundamentals, solutions, and future opportunities," *IEEE Commun. Lett.*, vol. 25, no. 5, pp. 1398–1402, May 2021.

[137] Y. Liu *et al.*, "Reconfigurable intelligent surface (RIS) aided multi-user networks: Interplay between NOMA and RIS," *arXiv preprint*, arXiv:2011.13336, Oct. 2021. [Online]. Available: https://arxiv.org/abs/2011.13336

[138] Y. Li, M. Jiang, Q. Zhang, and J. Qin, "Joint beamforming design in multi-cluster MISO NOMA reconfigurable intelligent surface-aided downlink communication networks," *IEEE Trans. Commun.*, vol. 69, no. 1, pp. 664–674, Jan. 2021.

[139] E. Björnson, Ö. Özdogan, and E. G. Larsson, "Intelligent reflecting surface versus decode-and-forward: How large surfaces are needed to beat relaying?" *IEEE Wireless Commun. Lett.*, vol. 9, no. 2, pp. 244–248, Feb. 2020.

[140] Y. Cao, T. Lv, W. Ni, and Z. Lin, "Sum-rate maximization for multi-reconfigurable intelligent surface-assisted device-to-device communications," *IEEE Trans. Commun.*, vol. 69, no. 11, pp. 7283–7296, Nov. 2021.

[141] X. Mu *et al.*, "Exploiting intelligent reflecting surfaces in NOMA networks: Joint beamforming optimization," *IEEE Trans. Wireless Commun.*, vol. 19, no. 10, pp. 6884–6898, Oct. 2020.

[142] K. Xu *et al.*, "On the sum-rate of RIS-assisted MIMO multiple-access channels over spatially correlated Rician fading," *IEEE Trans. Commun.*, vol. 69, no. 12, pp. 8228–8241, Dec. 2021.

[143] Y. Yang, B. Zheng, S. Zhang, and R. Zhang, "Intelligent reflecting surface meets OFDM: Protocol design and rate maximization," *IEEE Trans. Commun.*, vol. 68, no. 7, pp. 4522–4535, Jul. 2020.

[144] C. Huang, R. Mo, and C. Yuen, "Reconfigurable intelligent surface assisted multiuser MISO systems exploiting deep reinforcement learning," *IEEE J. Sel. Areas Commun.*, vol. 38, no. 8, pp. 1839–1850, Aug. 2020.

[145] C. Huang *et al.*, "Reconfigurable intelligent surfaces for energy efficiency in wireless communication," *IEEE Trans. Wireless Commun.*, vol. 18, no. 8, pp. 4157–4170, Aug. 2019.

[146] E. Björnson, Ö. Özdogan, and E. G. Larsson, "Reconfigurable intelligent surfaces: Three myths and two critical questions," *IEEE Commun. Mag.*, vol. 58, no. 12, pp. 90–96, Dec. 2020.

[147] Z.-Q. He and X. Yuan, "Cascaded channel estimation for large intelligent metasurface assisted massive MIMO," *IEEE Wireless Commun. Lett.*, vol. 9, no. 2, pp. 210–214, Feb. 2020.

[148] E. Björnson and L. Sanguinetti, "Rayleigh fading modeling and channel hardening for reconfigurable intelligent surfaces," *IEEE Wireless Commun. Lett.*, vol. 10, no. 4, pp. 830–834, Apr. 2021.

[149] Q.-U.-A. Nadeem *et al.*, "Intelligent reflecting surface-assisted multi-user MISO communication: Channel estimation and beamforming design," *IEEE Open J. Commun. Soc.*, vol. 1, pp. 661–680, May 2020.

[150] C. You, B. Zheng, and R. Zhang, "Channel estimation and passive beamforming for intelligent reflecting surface: Discrete phase shift and progressive refinement," *IEEE J. Sel. Areas Commun.*, vol. 38, no. 11, pp. 2604–2620, Nov. 2020.

[151] B. Zheng and R. Zhang, "Intelligent reflecting surface-enhanced OFDM: Channel estimation and reflection optimization," *IEEE Wireless Commun. Lett.*, vol. 9, no. 4, pp. 518–522, Apr. 2020.

[152] D. Neumann, T. Wiese, and W. Utschick, "Learning the MMSE channel estimator," *IEEE Trans. Signal Process.*, vol. 66, no. 11, pp. 2905–2917, Jun. 2018.

[153] A. Zappone, M. Di Renzo, and M. Debbah, "Wireless networks design in the era of deep learning: Model-based, AI-based, or both?" *IEEE Trans. Commun.*, vol. 67, no. 10, pp. 7331–7376, Oct. 2019.

[154] S. M. R. Islam, N. Avazov, O. A. Dobre, and K.-S. Kwak, "Power-domain non-orthogonal multiple access (NOMA) in 5G systems: Potentials and challenges," *IEEE Commun. Surveys Tuts.*, vol. 19, no. 2, pp. 721–742, 2nd Quart., 2017.

[155] J. Andrews and T. Meng, "Optimum power control for successive interference cancellation with imperfect channel estimation," *IEEE Trans. Wireless Commun.*, vol. 2, no. 2, pp. 375–383, Mar. 2003.

[156] J. Andrews, "Interference cancellation for cellular systems: A contemporary overview," *IEEE Wireless Commun.*, vol. 12, no. 2, pp. 19–29, Apr. 2005.

[157] B. Dai, S. Ding, and G. Wahba, "Multivariate Bernoulli distribution," *Bernoulli*, vol. 19, no. 4, pp. 1465–1483, Sep. 2013.

[158] S. Schiessl, M. Skoglund, and J. Gross, "NOMA in the uplink: Delay analysis with imperfect CSI and finite-length coding," *IEEE Trans. Wireless Commun.*, vol. 19, no. 6, pp. 3879–3893, Jun. 2020.

[159] B. Hassibi and B. Hochwald, "How much training is needed in multiple-antenna wireless links?" *IEEE Trans. Inf. Theory*, vol. 49, no. 4, pp. 951–963, Apr. 2003.

[160] T. L. Marzetta, "Noncooperative cellular wireless with unlimited numbers of base station antennas," *IEEE Trans. Wireless Commun.*, vol. 9, no. 11, pp. 3590–3600, Nov. 2010.

[161] Q. Wu and R. Zhang, "Intelligent reflecting surface enhanced wireless network via joint active and passive beamforming," *IEEE Trans. Wireless Commun.*, vol. 18, no. 11, pp. 5394–5409, Nov. 2019.

[162] L. P. Qian *et al.*, "Optimal SIC ordering and computation resource allocation in MEC-aware NOMA NB-IoT networks," *IEEE Internet Things J.*, vol. 6, no. 2, pp. 2806–2816, Apr. 2019.

[163] A. Forenza, D. J. Love, and R. W. Heath, "Simplified spatial correlation models for clustered MIMO channels with different array configurations," *IEEE Trans. Veh. Technol.*, vol. 56, no. 4, pp. 1924–1934, Jul. 2007.

[164] E. Björnson, J. Hoydis, and L. Sanguinetti, "Massive MIMO networks: Spectral, energy, and hardware efficiency," *Found. Trends Signal Process.*, vol. 11, no. 3-4, pp. 154–655, 2017. [Online]. Available: http://dx.doi.org/10.1561/2000000093

[165] H. Guo, Y.-C. Liang, J. Chen, and E. G. Larsson, "Weighted sum-rate maximization for reconfigurable intelligent surface aided wireless networks," *IEEE Trans. Wireless Commun.*, vol. 19, no. 5, pp. 3064–3076, May 2020.

[166] Q.-U.-A. Nadeem, A. Kammoun, M. Debbah, and M.-S. Alouini, "Design of 5G full dimension massive MIMO systems," *IEEE Trans. Commun.*, vol. 66, no. 2, pp. 726–740, Feb. 2018.

[167] J. Hoydis, S. ten Brink, and M. Debbah, "Massive MIMO in the UL/DL of cellular networks: How many antennas do we need?" *IEEE J. Sel. Areas Commun.*, vol. 31, no. 2, pp. 160–171, Feb. 2013.

[168] M. Shafi *et al.*, "Polarized MIMO channels in 3-D: Models, measurements and mutual information," *IEEE J. Sel. Areas Commun.*, vol. 24, no. 3, pp. 514–527, Mar. 2006.

[169] S. Bi, C. K. Ho, and R. Zhang, "Wireless powered communication: Opportunities and challenges," *IEEE Commun. Mag.*, vol. 53, no. 4, pp. 117–125, Apr. 2015.

[170] K. W. Choi *et al.*, "Wireless-powered sensor networks: How to realize," *IEEE Trans. Wireless Commun.*, vol. 16, no. 1, pp. 221–234, Jan. 2017.

[171] Y. Zeng, B. Clerckx, and R. Zhang, "Communications and signals design for wireless power transmission," *IEEE Trans. Commun.*, vol. 65, no. 5, pp. 2264–2290, May 2017.

[172] B. Clerckx *et al.*, "Wireless power transfer for future networks: Signal processing, machine learning, computing, and sensing," *IEEE J. Sel. Topics Signal Process.*, vol. 15, no. 5, pp. 1060–1094, Aug. 2021.

[173] H. Ju and R. Zhang, "Throughput maximization in wireless powered communication networks," *IEEE Trans. Wireless Commun.*, vol. 13, no. 1, pp. 418–428, Jan. 2014.

[174] Z. Chen, L. X. Cai, Y. Cheng, and H. Shan, "Sustainable cooperative communication in wireless powered networks with energy harvesting relay," *IEEE Trans. Wireless Commun.*, vol. 16, no. 12, pp. 8175–8189, Dec. 2017.

[175] Q. Wu *et al.*, "Energy-efficient resource allocation for wireless powered communication networks," *IEEE Trans. Wireless Commun.*, vol. 15, no. 3, pp. 2312–2327, Mar. 2016.

[176] P. S. Bouzinis, P. D. Diamantoulakis, L. Fan, and G. K. Karagiannidis, "Pareto-optimal resource allocation in decentralized wireless powered networks," *IEEE Trans. Commun.*, vol. 69, no. 2, pp. 1007–1020, Feb. 2021.

[177] M. Dimitropoulou, C. Psomas, and I. Krikidis, "Generalized selection in wireless powered networks with non-linear energy harvesting," *IEEE Trans. Commun.*, vol. 69, no. 8, pp. 5634–5648, Aug. 2021.

[178] C. You, K. Huang, and H. Chae, "Energy efficient mobile cloud computing powered by wireless energy transfer," *IEEE J. Sel. Areas Commun.*, vol. 34, no. 5, pp. 1757–1771, May 2016.

[179] H. Chen, C. Zhai, Y. Li, and B. Vucetic, "Cooperative strategies for wireless-powered communications: An overview," *IEEE Wireless Commun.*, vol. 25, no. 4, pp. 112–119, Aug. 2018.

[180] P. Viswanath, D. Tse, and R. Laroia, "Opportunistic beamforming using dumb antennas," *IEEE Trans. Inf. Theory*, vol. 48, no. 6, pp. 1277–1294, Jun. 2002.

[181] X. Zhou, R. Zhang, and C. K. Ho, "Wireless information and power transfer: Architecture design and rate-energy tradeoff," *IEEE Trans. Commun.*, vol. 61, no. 11, pp. 4754–4767, Nov. 2013.

[182] N. Tekbiyik, T. Girici, E. Uysal-Biyikoglu, and K. Leblebicioglu, "Proportional fair resource allocation on an energy harvesting downlink," *IEEE Trans. Wireless Commun.*, vol. 12, no. 4, pp. 1699–1711, Apr. 2013.

[183] J. Rubio and A. Pascual-Iserte, "Energy-aware user scheduling for downlink multiuser-MIMO systems," in *2014 IEEE 25th Ann. Int. Symp. Pers. Indoor Mob. Radio Commun. (PIMRC)*, Sep. 2014, pp. 965–969.

[184] T.-D. Nguyen and Y. Han, "A proportional fairness algorithm with QoS provision in downlink OFDMA systems," *IEEE Commun. Lett.*, vol. 10, no. 11, pp. 760–762, Nov. 2006.

[185] R. Zhang and C. K. Ho, "MIMO broadcasting for simultaneous wireless information and power transfer," *IEEE Trans. Wireless Commun.*, vol. 12, no. 5, pp. 1989–2001, May 2013.

[186] X. Lu *et al.*, "Wireless networks with RF energy harvesting: A contemporary survey," *IEEE Commun. Surveys Tuts.*, vol. 17, no. 2, pp. 757–789, 2nd Quart., 2015.

[187] S. Bi, Y. Zeng, and R. Zhang, "Wireless powered communication networks: An overview," *IEEE Wireless Commun.*, vol. 23, no. 2, pp. 10–18, Apr. 2016.

[188] J. Rubio, A. Pascual-Iserte, D. P. Palomar, and A. Goldsmith, "Joint optimization of power and data transfer in multiuser MIMO systems," *IEEE Trans. Signal Process.*, vol. 65, no. 1, pp. 212–227, Jan. 2017.

[189] T. Lipp and S. Boyd, "Variations and extension of the convex-concave procedure," *Optim. Eng.*, vol. 17, no. 2, pp. 263–287, Jan. 2016.

[190] X. Kuai, X. Yuan, W. Yan, and Y.-C. Liang, "Coexistence of human-type and machine-type communications in uplink massive MIMO," *IEEE J. Sel. Areas Commun.*, vol. 39, no. 3, pp. 804–819, Mar. 2021.

[191] M. Elbayoumi, W. Hamouda, and A. Youssef, "Multiple-association supporting HTC/MTC in limited-backhaul capacity ultra-dense networks," *IEEE Trans. Commun.*, vol. 69, no. 6, pp. 4113–4127, Feb. 2021.

[192] T. D. Ponnimbaduge Perera *et al.*, "Simultaneous wireless information and power transfer (SWIPT): Recent advances and future challenges," *IEEE Commun. Surveys Tuts.*, vol. 20, no. 1, pp. 264–302, 1st Quart., 2018.

[193] I. Budhiraja *et al.*, "SWIPT-enabled D2D communication underlaying NOMA-based cellular networks in imperfect CSI," *IEEE Trans. Veh. Technol.*, vol. 70, no. 1, pp. 692–699, Jan. 2021.

[194] Y. Zhao, B. Clerckx, and Z. Feng, "IRS-aided SWIPT: Joint waveform, active and passive beamforming design under nonlinear harvester model," *IEEE Trans. Commun.*, vol. 70, no. 2, pp. 1345–1359, Feb. 2022.

[195] B. Clerckx *et al.*, "Fundamentals of wireless information and power transfer: From RF energy harvester models to signal and system designs," *IEEE J. Sel. Areas Commun.*, vol. 37, no. 1, pp. 4–33, Jan. 2019.

[196] J. Zhang *et al.*, "Prospective multiple antenna technologies for beyond 5G," *IEEE J. Sel. Areas Commun.*, vol. 38, no. 8, pp. 1637–1660, Aug. 2020.

[197] S. S. Christensen, R. Agarwal, E. De Carvalho, and J. M. Cioffi, "Weighted sum-rate maximization using weighted MMSE for MIMO-BC beamforming design," *IEEE Trans. Wireless Commun.*, vol. 7, no. 12, pp. 4792–4799, Dec. 2008.

[198] S. Zeng *et al.*, "Reconfigurable intelligent surface (RIS) assisted wireless coverage extension: RIS orientation and location optimization," *IEEE Commun. Lett.*, vol. 25, no. 1, pp. 269–273, Jan. 2021.